Proton conductivity and local structures of oxide compounds for use as electrolytes in fuel cells by ab initio simulations

Karsten Rasim

To cite this version:

Karsten Rasim. Proton conductivity and local structures of oxide compounds for use as electrolytes in fuel cells by ab initio simulations. Material chemistry. Université de Nantes, 2011. English. NNT : . tel-00983483

HAL Id: tel-00983483
https://theses.hal.science/tel-00983483

Submitted on 25 Apr 2014

UNIVERSITÉ DE NANTES
FACULTÉ DES SCIENCES ET TECHNIQUES

ECOLE DOCTORALE 3MPL
MATÉRIAUX, MATIÈRES, MOLÉCULES EN PAYS DE LA LOIRE

Année 2011

Conductivité protonique et structures locales par simulations *ab initio* d'oxydes utilisés comme électrolyte dans les piles à combustible

THÈSE DE DOCTORAT
Discipline : Sciences des Matériaux
Spécialité : Physico-Chimie Théorique

Présentée et soutenue publiquement par
Karsten RASIM
Le 22 mars 2011, devant le jury ci-dessous

Président	M. Guy OUVRARD, *professeur* • Université de Nantes
Rapporteurs	M. Truls NORBY, *professeur* • Université d'Oslo, Norvège
	M. Fabrizio CLERI *professeur* • Université de Lille
Examinateurs	Mme Deborah JONES *directeur de recherche CNRS* • Université de Montpellier II
	M. Philippe BARANEK *ingénieur de recherche* • EDF R&D, Moret sur Loing
	M. Florent BOUCHER *chargé de recherche CNRS HDR* • IMN, Nantes
	M. Olivier JOUBERT *maître de conférences HDR* • Université de Nantes
Invité	M. Mathieu MARRONY *ingénieur de recherche* • EIfER, Karlsruhe, Allemagne

Directeur de thèse : M. Florent BOUCHER
Co-directeur de thèse : M. Olivier JOUBERT

Contents

List of abbreviations

(PC)-SOFC	(proton conducting) solid oxide fuel cell
MD	molecular dynamics
MC	Monte Carlo
MSD	mean square displacement
NEB	nudged elastic band
PCF	pair correlation function
VAF	velocity autocorrelation function
EN	electronegativity
DOS	density of states
PES	potential energy surface
TS	transition state
GS	ground state
ZPE	zero point energy
NMA	normal mode analysis
RB	random barrier
RT	random trap
AIBx	shorthand for dehydrated compounds A={**B**a,**S**r}; I=**I**n; B={**T**i,**Z**r,**Y**}; x = % substitution of In with B
AIBhx	shorthand for fully hydrated compounds; A,B,x, as above

Resumé

Cette thèse porte sur une étude de matériaux oxydes fortement désordonnés de type Brownmillerite et présentant diverses substitutions. Les aspects les plus étudiés sont la conductivité protonique des phases hydratées ainsi que les propriétés structurales des composés anhydres. L'étude repose majoritairement sur des calculs de type DFT (réalisés de manière statique à 0 K et à haute température en utilisant la dynamique moléculaire *ab initio*). Elle est complétée de mesures XANES (spectroscopie d'absorption des rayons X) qui ont permi de confirmer certains résultats issus des calculs DFT. Ces approches combinées ont fourni des informations cruciales sur la préférence de coordination chimique de plusieurs substituants, sur la mobilité des protons dans divers composés en fonction de leur contenu cationique ainsi que sur les propriétés vibrationnelles. Le matériau $Ba_2In_{2(1-x)}Ti_{2x}O_{5+x}$ (BITx) a été le centre d'intérêt de cette thèse, au vu des performances prometteuses dans des piles à combustible de type PC-SOFC. Dans une optique de comparaison et de rationalisation, des composés de formulation voisine $Sr_2In_{2(1-x)}Ti_{2x}O_{5+x}$ (SITx), $Ba_2In_{2(1-x)}Zr_{2x}O_{5+x}$ (BIZx) et $Ba_2In_{2(1-x)}Y_{2x}O_5$ (BIYx) ont été également étudiés pour préciser le rôle des différents substituants sur le comportement de la conductivité protonique (e.g. les effets de piégeage, la force des liaisons hydrogène, la distinction entre plusieurs arrangements protoniques etc...). Tous ces aspects ont été obtenus grâce à la dynamique moléculaire qui intègre naturellement les effets de température et d'entropie.

Abstract

This thesis gives a detailed study of heavily cation-substituted, disordered Brownmillerite based compounds. The focus is on their proton conduction behaviour when being hydrated as well as their structural properties in the dry state. The study is predominantly conducted by DFT calculations (both static and Born-Oppenheimer molecular dynamics) combined with XANES experiments which confirmed certain theoretical results. Amongst others, by means of these techniques, the coordination preference of different substituents, the protonic mobility and vibrational spectra can be obtained and compared to experimental evidence. The focus lies on the $Ba_2In_{2(1-x)}Ti_{2x}O_{5+x}$ (BITx) family, proven to be a well suited electrolyte material for proton conducting solid-oxide fuel cells (PC-SOFC). Moreover, neighbouring compounds, such as $Sr_2In_{2(1-x)}Ti_{2x}O_{5+x}$ (SITx), $Ba_2In_{2(1-x)}Zr_{2x}O_{5+x}$ (BIZx) and $Ba_2In_{2(1-x)}Y_{2x}O_5$ (BIYx), are being considered as they prove useful to systematically clarify the influence of different chemical environments on proton diffusivity (e.g. different ”proton affinities” of the Ti- or Zr-substituents, more or less pronounced hydrogen bonding, distinction between extra- and intra-octahedrally bonded protons, etc.). All those aspects are obtained in the molecular dynamics framework, naturally integrating temperature or entropic effects.

Introduction

0.1 The fuel cell

Fuel cells represent an extremely promising way to establish a non fossil fuel based energy system. Their merit is due to their electrochemical nature, which enables them to reach theoretical fuel efficiencies of 90% which exceeds by far the theoretical limit of any Carnot process. Even in realistic working conditions their performances can be as high as 50-60% electrical plus 20-30% thermal efficiency, when the use of the ”waste heat” is possible. Furthermore the actual electricity generation is rather elegant, as no moving parts are involved anywhere, leading to the absence of any noise, mechanical vibrations and fatigue problems linked to that.

Another important feature is the environmental aspect, stating that ideally the only direct reaction product would be water in case the fuel consisted of pure hydrogen. Noting however, that hydrogen does not represent a primary energy resource, its production would have to be taken into account. Therefore the environmental aspect has necessarily to be looked at in a global manner, which however is not in the scope of this introduction.

As electrochemical reaction system, fuel cells canalize the electron transfer process of the oxidation reaction of a gaseous fuel (ideally pure hydrogen gas, but also methane - natural gas is possible). This is achieved by the spatial separation of fuel and oxygen by an electronically insulating but ion-conducting electrolyte which is covered by a cathode material (on the oxygen side) and an anode material (on the fuel side). Those two electrodes are interconnected by an external electrical circuit. Given the electrochemical potential difference of the fuel-oxygen couple, a steady electronic current across the external circuit as well as a counterbalancing ionic current across the electrolyte eventually leads to the formation of the reaction product and the generation of electrical power.

Different kinds of fuel cells do already exist, however their degree of actual use is rather different. Two of the most predominant types of fuel cells can be subdivided according to the nature of their electrolyte:

(I) The polymer exchange membrane fuel cells (PEMFCs) and

(II) solid oxide fuel cells (SOFC) both oxygen- and proton-conducting.

In the following, the two types will be shortly described, however focusing on the SOFC type fuel cell, being the subject of interest for this thesis.

(I) PEMFCs operate at temperatures as low as 80°C and the migrating species are protons that diffuse across a polymer electrolyte. In most cases this electrolyte is based on a fluorinated ionomer (Nafion) discovered in the 1960s and in use ever since. The low operating temperatures are necessary, because at temperatures above 100°C the electrolyte would dry out and cease to be proton conducting. Linked to the low operating temperature are the two major problems of this technology, being the presence of liquid water as reaction product and the necessity to use expensive platinum based catalyst materials to enable the electrode reactions at such low temperatures. These two disadvantages are immediately remedied by the use of SOFCs, that operate at significantly higher temperatures.

(II): The classic (here: oxygen-conducting) SOFC operates at temperatures between 700°C and 900°C and can use both hydrogen-gas or methane as a fuel. For the latter case, methane gas can either be steam-reformed before it gets into actual contact with the anode, or by choice of an appropriate anode material, it can directly be dissociated at the electrode. The relevant transport reaction is the transfer of oxygen-anions from the cathode-side to the anode-side of the cell, where they form water by reaction with the dissociated hydrogen (or methane). Oxygen-anions are the migrating species and therefore the electrolyte has to be a good oxygen-ion conductor. This for example is realized by yttrium-stabilized zirconia (YSZ) electrolytes at the aforementioned rather high temperatures of 700°-900°C. This kind of cell is already relatively mature concerning its development, and numerous (however not yet really market introduced) applications exist.

This mode of action however has some disadvantages, which can partly be avoided by the introduction of a substantial new concept to the SOFC type cell: the proton-conducting SOFC (PC-SOFC). As indicated in the designation, although remaining a solid-oxide electrolyte, the migrating species now will be the protons, that diffuse/drift from the anode-side of the cell to the cathode side to accomplish the water-forming reaction. The major advantage of this approach is that those electrolytes that are proton-conducting can do that at considerably lower temperatures in the range of 500°C-600°C. Due to this lower operating temperature, for example material fatigue issues are less severe than for the classic SOFC. The direction of proton transport is from the anode to the cathode-side of the cell and therefore the water forming reaction takes place at the "air-side". This in turn is an advantage with respect to the water-management. When produced at the hydrogen-side (as for classic SOFCs) it dilutes the fuel concentration and therefore lowers the chemical potential-difference (Nernst-voltage) between hydrogen and oxygen. Produced at the air-side, the water vapour can much more easily be removed by floating the compartment.

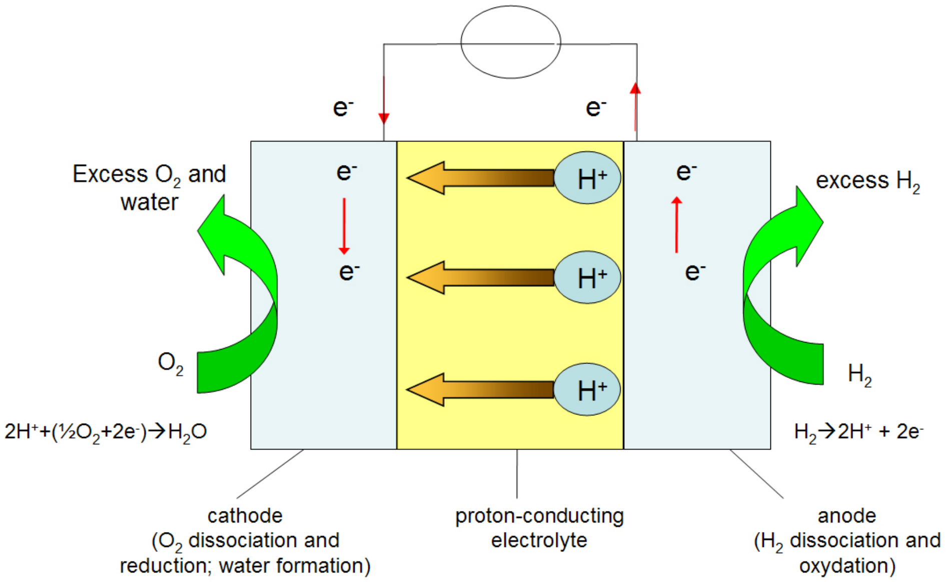

Figure 1: Rough sketch of a proton conducting solid-oxide fuel cell indicating the direction of charge transport, reactants and products.

The electrochemical performance of a fuel cell in terms of electrical power output is determined by the combination of each component's resistivity. Those are determined both by chemical reaction barriers at the gas-solid interfaces (catalytic surface properties of the anode and the cathode), the solid-solid interfacial charge transfers as well as the charge transport within the electrolyte (the conduction of the mobile ionic species). The lower those resistivities the higher the potential power output per surface area.

This thesis deals with one particular aspect of the fuel cell system, which is the solid oxide electrolyte and its ionic-transport properties. More in detail the study focuses on a part of the very large family of perovskite related compounds, that have proven to show very high possible proton-conductivities when used as electrolyte. In contrast to many other treatments of proton conductivity however the point of departure is not a slightly doped perovskite structure but significantly substituted disordered materials. The reference material here is an $A_2^{(II)}B_2^{(III)}O_5$ compound crystallizing in the Brownmillerite structure.

From the viewpoint of a to-be-minimized electrolyte-resistivity, its most important figure of merit is its protonic conductivity, which is composed of the possible content of protons at a given temperature and their mobility. It is the focus of this thesis to elucidate conductivity mechanisms and chemical properties that influence it as well as to microscopically determine or confirm trends concerning the hydration energies.

0.2 Density functional theory modeling of proton conducting oxides

DFT based studies of chemically relevant compounds and substances have gotten more and more useful during the last years. Despite the existence of the theoretical foundations of density functional theory since the publication of the groundbreaking papers of HOHENBERG, KOHN, SHAM and others in the 1960s, advances in computational performance only recently allowed to actually study systems, that are of a genuine chemical interest. Moreover, the degree to which more or less quantitative predictions of relevant compounds can be made has risen steadily. So the investigation of a mesoscopic property such as the bulk protonic diffusion coefficient in a disordered material is not yet a standard procedure. Relevant ab-initio molecular dynamics studies published in the literature are very often restricted to significantly smaller (and therefore less disordered) systems. In this thesis, it is tried to gain systematic insight into the proton-conduction mechanisms in disordered perovskite related systems by observations made in reasonably large simulation cells.

From a structure-chemical viewpoint, both the pure $Ba_2In_2O_5$ and its substituted versions are very interesting. Generally speaking, the structure is rather open due to the presence of the intrinsic oxygen voids, as well as the large ionic-radii differences between the cations Ba^{II}, In^{III} and some substituents. Especially titanium as the smallest of the cations under scrutiny here plays a special role, as its size will eventually lead to a special behaviour concerning its local coordination structure. In any case, large radii-differences lead to large local distortions which render an accurate description rather difficult. Therefore it was decided to consequently work with relatively large simulation cells of 140 up to 192 atoms (depending on degree of

substitution and state of hydration). They are used for the entire set of molecular dynamics runs and for most of the static calculations.
This approach is therefore somewhat particular, as due to the relatively large systems, local structures and other properties will mostly *not* be investigated ”one by one”, but rather in an spatially and temporally averaged manner what is made possible by the molecular dynamics approach. An immediate advantage to that is the easier transferability to macroscopic terms as well as the intrinsic thermodynamic plausibility. This means that one obtains an actual structural observation rather than a snapshot-description of one single configuration of a disordered structure. This for example is especially true for the statistical measures of the distribution of different coordination polyhedra in the dehydrated compounds in chapter 3 or the question of proton trapping next to particular cations, the vibrational spectra or the overall diffusion coefficients.

0.3 General Thesis layout

The thesis is made up of four main chapters, which focus on the entirely dry compounds (chap. 3), the structure of the completely hydrated compounds (chap. 4), a supporting Monte Carlo study (chap. 5) and finally the protonic transport properties in the fully hydrated state (chap. 6).

Those main chapters are preceded by chapters containing a general introduction of the Brownmillerite class of materials, an overview of the most relevant literature studies on the subject and methods-section with the introduction of the used computational tools.

Apart from the computational aspect in general, the thesis has a strong focus on comparison concerning a selection of different model compounds, which are generated by substituting the metal cations in $Ba_2In_2O_5$. Each of them does represent a certain differing parameter with respect to the reference $Ba_2In_2O_5$ or its hydrated counterpart, respectively. Investigated were (I) the influence of the degree of In/Ti-substitution being represented by compounds containing 0, 6.25, 25, 50 and 75% titanium, (II) the influence of different substituents, studied by the comparison of 25% substitution with Ti, Zr, Y and (III) the influence of the A-site cation which for a single composition of 25%Ti-75%In was switched from Ba to Sr. The last aspect does mainly probe the influence of an overall smaller lattice onto the protonic properties.

This thesis shall contribute to a better understanding of proton structures and mobility in

Brownmillerite and related materials. A special focus is on the Ti-substituted $Ba_2In_2O_5$ compounds which show promising performances as electrolyte in proton-conducting SOFCs [1].

The major novelty in studying these materials with respect to their proton conductivity is their heavily disordered character and their potentially very high proton content. Both points represent fundamental contrasts to the treatment of acceptor-doped perovskite which are exceedingly well studied concerning their proton transport properties, both experimentally and by calculations (see literature section 1.3).

To conclude, the most important problem fields which will be addressed in the thesis are given in the following:

- The local coordination structure of the completely dehydrated phases that due to their locally disordered character are not accessible via diffraction methods.
- The trends that various substituents are responsible for concerning the vibrational properties of the dry compounds.
- Tendencies concerning the energies of hydration obtained by comparing molecular dynamics simulations of dry and hydrated compounds; their relation to solid-state chemistry concepts such as electronegativity
- The investigation of local structures in fully hydrated compounds with regard to the impact of the cation substituents: stability of the extra-octahedral proton site, trapping or repulsion effects of a given substituent, vibrational properties of protons
- The actual mobility of protons in the fully hydrated compounds seen by direct ”observation” via the molecular dynamics approach in relation to the structural aspects just mentioned.

Chapter 1

Existing studies on Brownmillerite materials

This chapter introduces the pure (i.e. unsubstituted) reference compound both in its dry and hydrated state which the thesis is focused on. Their principal structural and conductivity properties are presented first. The second section gives an overview of how the key topic of the thesis - ionic/protonic diffusion in solids - can be described. After that the most relevant literature sources are briefly introduced which are more specifically related to the computational description of perovskite/brownmmillerite compounds and their proton-conductivity properties.

1.1 General properties of the Brownmillerite material family

1.1.1 The dehydrated case

Throughout the thesis the family of compounds that will be studied are based on the Brownmillerite structure and their hydrated counterparts. The name Brownmillerite was initially given to the substance $Ca_2Fe_2O_5$. The structure is closely related to the well known perovskite structure, as the basic framework is identical. Therefore the A-site and B-site nomenclature for the cations will be used throughout. The Brownmillerite is one of the possible realizations of an $A^{(II)}B^{(III)}O$ structure, with the A-cation being an earth-alkaline metal and the B-cation one of the (III)-valent metals. The most striking particularity is to have this B-cation in two different coordinative situations. Focusing on $Ba_2In_2O_5$, which will be the reference material throughout this work, the structure consists of a layered arrangement of In-octahedra and In-tetrahedra. Its room-temperature crystal structure exhibits a Ima2 (46) or Icmm (74) orthorhombic spacegroup (depending on the degree of refinement) with cell constants of a=6.095 Å , b=16.727 Å and c=5.96 Å obtained by XRD in the Icmm spacegroup [2]. The particularity for the Icmm Rietveld-refined structure is a slight orientational disorder of the In-O tetrahedra in their respective layer, which appears to be a static (domain-wise) disorder for which the Ima2 group is excluded. However this kind of disorder can be safely thought of to be rather sensitive towards differing preparation routes and temperature of investigation itself.

Figure 1.1 shows the ideal Brownmillerite structure in a four times larger super-cell than the minimal representation of the Ima2 spacegroup. This simulation cell is representative of the cells which are going to be used for the entire molecular dynamics runs throughout the thesis. For the $Ba_2In_2O_5$ case it consists of 144 atoms and considers four independent layers, two tetragonal and two octahedral in the direction of the c-axis.

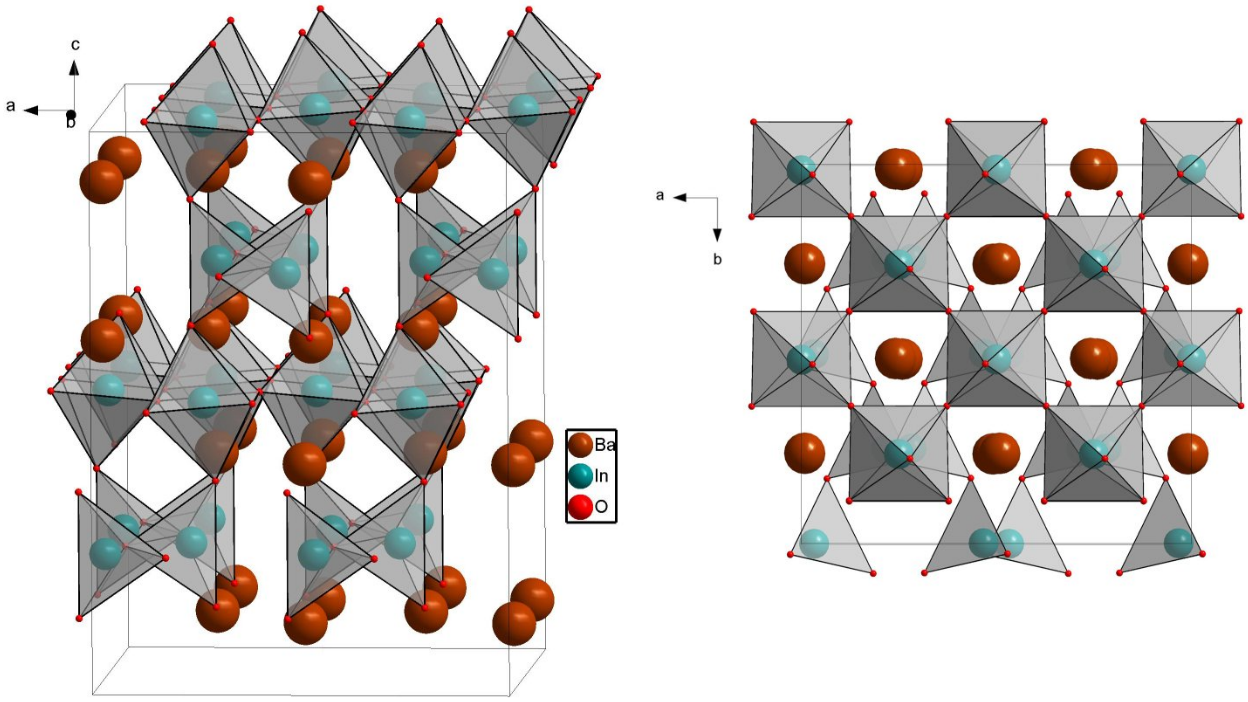

Figure 1.1: Side and top view of the ordered Brownmillerite structure of $Ba_2In_2O_5$ as used for all calculations throughout this work. 144 ions in total correspond to 32 indium(III)-polyhedra and 32 Ba(II) ions.

Conceptually the structure could also be seen as a 100% B-site substituted perovskite, where the (IV)-valent cation on the pervoskite B-site is completely substituted by a (III)-valent element, indium in this case. However the well established considerations based on the notion of slighly doped-perovskite compounds are not necessarily useful in this case, as many implications are based on a rather dilute situation which does not hold for substitutions in the entire compositional range, as they are investigated here. Especially this becomes evident, on adressing the structurally present (and stoichiometrical) oxygen vacancies as double-positively charged defects. In doing so, one would in turn be obliged to designate every In(III) B-site cation as a negatively charged defect as well, which obviously is not quite useful. Utilizing the charged defect notion is indeed very useful in deciding, whether or not some given defect acts as a "trap" for a moving ionic species in a compound (this can be O^{-II}-ions, protons or even electrons as is the case for F-centers in strongly ionic materials). In the case of a (II-III)-Brownmillerite structure however, the "defect" - In - occupies all existing B-sites and therefore rather *defines* the potential energy surface than perturbing it, as a real defect does. Related to that, the notion of a defect formation enthalpy loses its sense when describing the oxygen voids in $Ba_2In_2O_5$ and related compounds. In (proton)-"acceptor" *doped* perovskites this enthalpy can be attributed to the creation of two dangling bonds (distributed on two adjacent former B-site octahedra) per oxygen vacancy. In first place however the vacancy had to be created to ensure stoichiometry. So given the fact that an acceptor dopant (a (III)-valent cation on a (IV)-valent B-site) *is* integrated in the perovskite structure, the energetic situation is less favourable than in the ideal lattice.

For what the defect structure is concerned, pure $Ba_2In_2O_5$ can be considered a mixed ionic/electronic conductor with a moderate overall level of conductivity. For temperatures below 950°C it shows ionic/electronic transference numbers between 0.2 and 0.8 depending on temperature and oxygen partial pressure [3]. Although the electronic band-gap is quite large (in the region around 2-3 eV), this behaviour is mainly determined by two aspects:

(I) By rather high ionic-migration enthalpies due to the very ordered oxygen-void structure in the tetrahedral layer (which leads to a very low oxygen ion conductivity level) and

(II) a rather easy incorporation of *non-stoichiometric* oxygen ions due to the relatively open structure which at high $p(O_2)$ gives rise to p-type conduction via $\frac{1}{2}\,O_2 + V_o^{\bullet\bullet} \rightarrow O_o + 2h^{\bullet}$ (as there is no easily oxidizable cation present)

For practical application as an ion conductor pure barium indate is not well suited due to the overall low conductivity level. However its temperature behaviour around 950°C is very interesting, as the (by perovskite standards) extremely high oxygen vacancy concentration eventually becomes mobile. The effect is caused by an order disorder transition which changes the orthorhombic ordered phase into an averaged cubic phase having the oxygen vacancies randomly distributed over all perovskite oxygen sites. This is illustrated in figure 1.2 a) taken from YOSHINAGA and coworkers, where at around 933°C a very sharp increase of ionic conductivity is observed. As the concentration of oxygen ions remains rather constant, this conductivity-change therefore reflects a mobility- or diffusivity change.

An immensely important aspect linked to that is the partial substitution of cations which induces a disorder that is capable of stabilizing the aforementioned high temperature cubic structure even down to room temperature. This will be the major topic of chapter 3 where the impact of several substituents will be studied by DFT calculations.

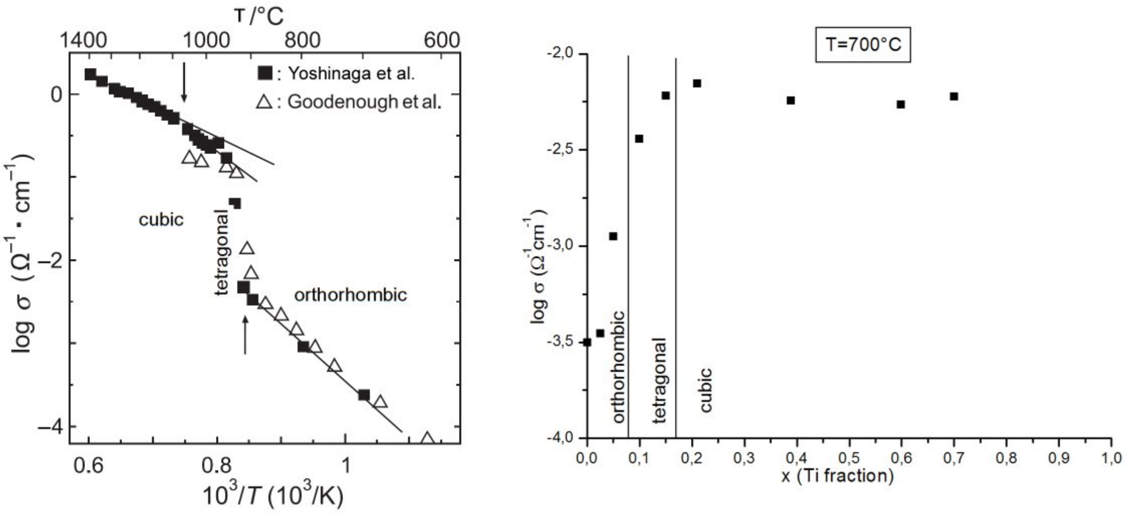

Figure 1.2: a) Electrical conductivity of $Ba_2In_2O_5$ over temperature [4, 5], b) Electrical conductivity at 700°C for various degrees of In-substitution with Ti [6]

An idea of a substituent's effect is given in figure 1.2 b) where for several Ti-substituted compounds already at 700°C the conductivity is about one order of magnitude larger than for pure barium indate.

Given the fact that by substituting with cations having a stable valence state (however either iso- or aliovalent to In), the electronic properties are not altered substantially, the ionic conductivity will be largely dominating the overall conductivity. This indicates the drastic influence of a substituent onto a collective property such as the ionic mobility. A more structural manifestation of this influence is supplied by XRD-experiments [1, 2, 7, 8], which confirm the "stabilization" of cubic (disordered) structures at room temperature for degrees of substitution >20% for Ti, Zr, Y, W and others.

An interesting issue, which however is a bit out of scope of this work, is the question at which scale those cubic phases are actually disordered. Adler and co-workers [9] for example suggest the presence of nanometer-sized regions in cation-substituted $Ba_2In_2O_5$-based compounds which nevertheless are ordered inside. Those domains would then fall below the resolution of an X-ray or neutron scattering experiment and therefore not be seen. Unfortunately, this type of structural investigation can (at the moment) not yet be tackled directly by DFT (or even DFT-based molecular dynamics) since it concerns a length scale of the order of many nanometers.

1.1.2 The hydrated case

The completely hydrated equivalent compound $Ba_2In_2O_4(OH)_2$ which will be the basis of the "Hydrated" part of the thesis, is formed by the uptake of the equivalent of one water-molecule per formula unit described by the reaction $H_2O(g) + O_o + V_o^{\bullet\bullet} \rightarrow 2OH^{\bullet}$ which is a pure acid-base reaction without electronic defect contribution given in Kröger-Vink notation here.

Structurally the coordination of the Brownmillerite simplifies towards a nominally 6-fold coordination of all indium cations, now qualitatively identical to a perovskite structure. The major particularity is the high concentration of protons, which are covalently bonded to one oxygen ion and hydrogen-bonded to a neighbouring one. Moreover they are distributed on two distinct crystallographic sites. Those sites will be called intra- and extra-octahedral throughout this work[1]. Their designation is rather self-explanatory with the intra-octahedral protons being bonded to two oxygen ions belonging to the same B-site octahedron, and the extra-octahedral protons to two oxygen ions belonging to two different cation-polyhedra.

The overall crystallographic structure is tetrahedral and can be described in spacegroup P4/mmm [10] or P4/mbm [11] depending on the degree of diffraction data refinement. Similar to the dry compound, the structure has a layered character, this time however very much related to the protonic arrangement. It is the extra-octahedral protons (see figure 1.3) that give rise to a pronounced in-plane tilt of the indicated layer in order to accommodate one extra-octahedral proton per rhombus-shaped interstice. Energetically this enables the formation of very strong hydrogen bonds, as can be seen by the short distance to the second-next nearest oxygen. The rest of the protons are distributed between the extra-layers (marked as intra-octahedral region) as intra-octahedral protons, i.e. as in protonated perovskite materials. In contrast to the extra-octahedral protons their crystallographic site is not well defined; they are distributed over a rather large number of possible intra-sites.
Inferred from bond-valence sum considerations based on XRD studies, it has been excluded that those intra-octahedral protons be associated to the particular group of oxygen ions being the in-plane oxygens belonging to the In(1)-site (see figure 1.3)[11].

A DFT-based study on the hydrated compound by Martinez and co-workers [12] entirely confirmed the extra- and intra-octahedral character of the proton sites including their crystal-

---

[1] Slightly more appropriately, many literature sources rather speak of inter- than extra-octahedral. However the "extra-" is retained here for better distinction from "intra-".

lographic sites and number fraction of 50% each.

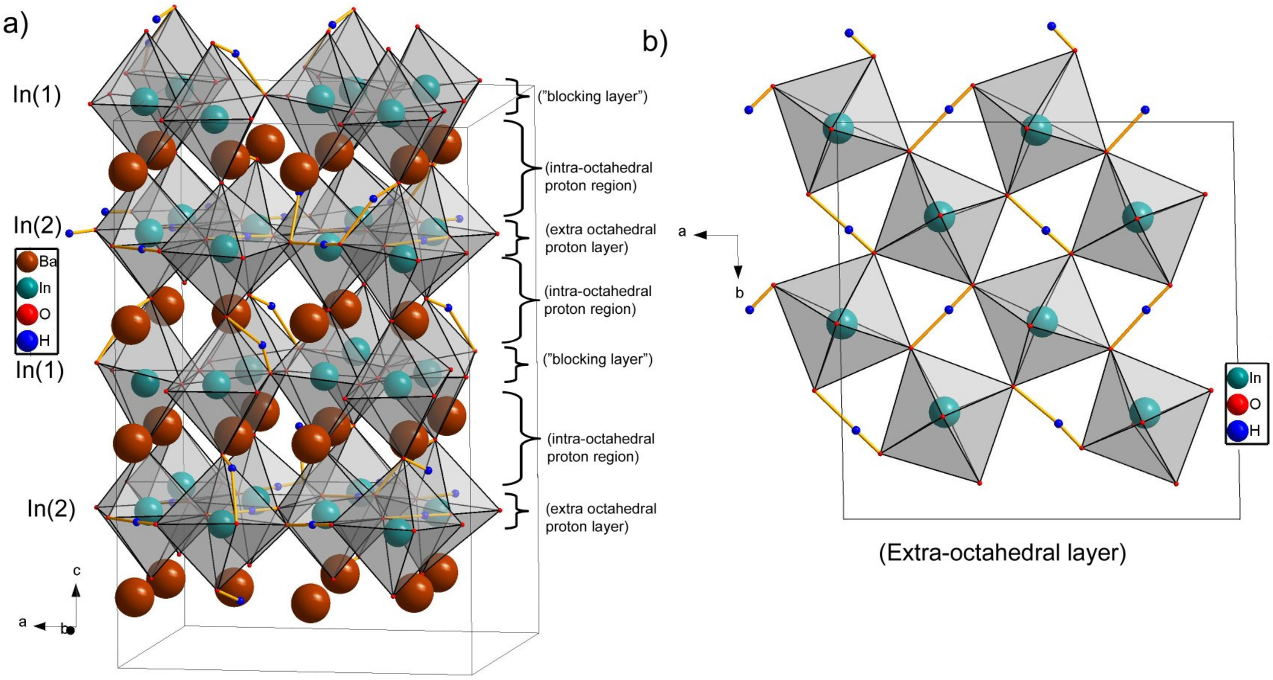

Figure 1.3: a) Tetragonal layered structure and simulation cell of $Ba_2In_2O_4(OH)_2$ containing 192 atoms. Key aspects mentioned in the text are indicated. b) top view of the extra-octahedral proton layer illustrating the particular rhombus like in-plane tilt of the In(2) octahedra (Ba omitted for clarity).

Moreover several permutations of different possible intra-octahedral sites were investigated by them, and it was found that the aforementioned in-plane oxygens bonded to In(1) indeed bind to protons only with substantial energy cost and therefore are not supposed to be occupied, exactly as inferred by the bond-valence calculation. This immediately hints to an interesting diffusional aspect which might be expected, namely the presence of a genuine blocking layer for proton displacement given that the corresponding proton site is significantly higher in energy. It will turn out that this is the case for the temperatures below 800°C but *above* 500°C (see molecular dynamics treatment of $Ba_2In_2O_4(OH)_2$ in section 4.3.3).
So already the unsubstituted reference compound differs tremendously from the usual protonated perovskite structures in having

(I) two distinct stable crystallographic proton sites (including different vibrational and energetic properties both having an impact on diffusivity); see molecular dynamics section on the extra-layer 4.3.1 and

(II) at least one crystallographic oxygen site, to which protons will not easily associate, which however constitutes an entire crystallographic plane; see section 4.3.3

The aforementioned reasoning with respect to the defect-character of high-concentration oxygen vacancies can as well be extended to the completely hydrated state, where it is the protons that are usually considered "defects". Again the same argumentation holds, that in the case of $Ba_2In_2O_4(OH)_2$ the protons rather play the role of a constituent of the structure than that of a defect. For example this is backed by the fact, that the aforementioned tilt of the extra-octahedral layer is a feature that arises *because* of the protons's presence.

1.2 Electrical conduction and Diffusion

As mentioned in the general introduction, the thesis major point of interest is the protonic conductivity, which is an electrical conductivity normally obtained by impedance spectroscopy or simpler DC-measurements at high temperatures. The most important assumption here, is that the conductivity can be described by the simple product of charge-carrier concentration c_i, their effective charge q_i and their mobility μ_i.

$$\sigma_i = c_i q_i \cdot \mu_i \tag{1.1}$$

For fuel cell electrolytes in general we mostly deal with oxygen-ion conductors or proton conductors. For the case of the oxygen conductivity obviously not the entire oxygen concentration can be regarded a charge carrier; the electric conduction is rather realized by only some very few oxygen ions located next to oxygen-vacancies. As a more suitable descriptor it is those vacancies which can be considered charge carriers themselves. Subsequently c_i becomes the concentration of the oxygen vacancies and μ_i their effective mobility. In the case of solid-oxide *proton* conductors we may safely assume that the entire proton content can be considered charge carriers. This for example is obviously no longer true for the proton conduction in liquid water or acids, where again only a small fraction of protons act as charge carriers.

There exists a relation between the empirically easily obtainable d.c.-conductivity σ and the diffusivity of the responsible charge carrier reading. It is based on the expression that relates a particle's mobility (as defined by a force-drift velocity term: $v_d = \mu \cdot F$) and its diffusion coefficient D

$$\mu_i = \frac{q_i \cdot D}{kT} \tag{1.2}$$

and is referred to as Nernst-Einstein relation. It uses the first Fickian equation as well as the applicability of the Boltzmann statistic for the carriers in question (as e.g. presented in

[13].) The electrical conductivity of a pure proton conductor may then be expressed by

$$\sigma_H = \frac{q_h^2 C D}{kT} \tag{1.3}$$

So for the remainder of this work, we are going to be exclusively interested in the mobility term of the protonic conductivity more precisely its diffusivity since for the compounds studied with the molecular dynamics method the proton content will not be changed.

Moreover, dehydrated structures studied by the MD-approach (presented in section 3.6) give an estimation of the oxygen diffusion behaviour, which is characterized by a vacancy-mechanism in an inhomogeneous environment due to the cationic substitution. A complication is introduced by the not-small concentration of oxygen voids for the cases of degrees of substitution from 0 to 25% [2].

The proton diffusion problem addressed is even of a more complex nature. Taking the case of completely hydrated oxides the like of which we are going to be interested in, we essentially deal with an interstitial self-diffusion problem of many protons in a multi-barrier and multi-site potential-energy-surface (PES). Additionally the effective diffusion is accomplished by up to six significantly different elementary steps, each of them characterized by their own migration enthalpies and entropies (as will be presented in section 6.4). Based on partially analytically solvable model systems (of disordered traps and/or barriers), this kind of situation in general leads to a non-Arrhenius behaviour of the net-diffusion coefficient [14, 15]. The distribution of those barriers and traps/sites will determine to what extent a diffusion can be expected to be non-Arrhenian or whether a compensation mechanism gives an effective Arrhenius behaviour. This aspect will be illuminated by a supplementary Monte Carlo study on diffusion problems from a more general point of view. Another issue is the interaction of the diffusing species, which becomes important when this species is not diluted. This will be the case for the treatment of the fully hydrated structures as well where we face a concentration of protons ranging from 32 down to 16 per 96 oxygen sites (32 in case of the unsubstituted $Ba_2In_2O_4(OH)_2$, 16 in case of a 50/50 substitution with an aliovalent cation as in $Ba_2InTiO_5(OH)$). Thus, site-blocking effects or more complex interactions will definitely occur.

---

[2] which corresponds to 16 to 12 oxygen voids distributed on 96 oxygen sites

1.2.1 Diffusivity-conductivity equivalence

In order to justify the use of the Nernst-Einstein relation (equation (1.2)) between the diffusivity and the mobility term of the conduction, an evaluation of the electrical potential gradients are needed. This is because the equivalence between self-diffusion and conduction can only be established when the diffusion is not too easy or the acting electrical fields (the voltage of a conductivity experiment or during fuel-cell operation) are not too high.

The two aspects to be compared are the typical diffusional activation barriers and the electrical potential gradient at the scale of single displacement step of a proton. In order to set up this qualitative comparison, we can safely assume applied or persisting voltages (in conductivity experiments or during fuel-cell operation, respectively) of around 1 V for electrolytes of a minimal thickness of ca. 10 μ m. Furthermore a typical jumping or reorientation distance for a proton will be of the order of 1 Å. Thus the electrical potential gradient for such a 1 Å separation amounts to $\Delta\Phi\cdot \approx U \cdot \frac{1\text{Å}}{10\mu m} = 1 \cdot 10^{-5}$V. For a (protonic) charge of 1e the energy bias is therefore $1 \cdot 10^{-5}$ eV which is to be compared with the typical chemical energy barriers between 0.1 and 1 eV being orders of magnitude bigger. Concluding, the equivalence between conductivity and self-diffusion can safely be applied in this kind of system.

This aspect is also linked to the question of comparability of conductivity diffusion coefficients (D_σ) and self-diffusion coefficients for example obtained by molecular dynamics simulations. Their major difference, is that D_σ is measured on a system that has a (proton)-concentration gradient. The self diffusion as such as well as the molecular dynamics simulations however do not comprise a concentration gradient. However this gradient shall be taken to be sufficiently small not to alter the diffusion mechanism or the activation energy between the proton self-diffusion and the conductivity-diffusion in a conductivity experiment or a working fuel-cell.

1.3 Computational studies on oxide electrolyte materials

This section shall give a quick overview over the most relevant series of literature studies, that have influenced this work. Many details, especially explicit comparisons with own results are given in the corresponding sections later on.

Some of the chronologically first computationally papers were published by Münch, Kreuer and co-workers and directly addressed the proton-conduction properties in $BaCeO_3$, $BaZrO_3$ and $SrTiO_3$. Based on the discovery of a substantial protonic-conduction in perovskite-related materials by the group of IWAHARA in the early 1980s [16, 17] these compounds were investigated experimentally [18, 19, 20, 21, 22] and by means of (first principles) molecular dynamics based on a tight-binding electronic structure calculation approach [23, 24, 25, 26, 27], i.e. already based on quantum chemical grounds.

It was those publications that undoubtedly established the basic microscopic understanding of how protons behave inside solid oxide materials. In this spirit the molecular dynamics work directly showed for the first time the principal mode of diffusion as being a combination of a stretch-jump and a re-orientation mode[3], the latter of which is easy (at times even energetically unhindered) and the first being the rate determining step. One big difference of these MD-calculations compared to this thesis' work is that in their studies the proton diffusion is performed by one isolated protonic "defect". As it is stated several times in the papers mentioned above, the presence of this proton never significantly alters the lattice properties except its immediate surrounding such as the pair correlation functions (PCF) between cations and oxygen, which we will see is not the case for the compounds investigated in this thesis.

In the late 2000s GOMEZ and coworkers revisited the pure perovskites $SrZrO_3$, $CaZrO_3$, $CaTiO_3$, $BaTiO_3$, $BaZrO_3$ [28] with respect to their protonic diffusivity. With a focus on the differences between real cubic and orthorhombic perovskites (i.e. structures made up of tilted octahedra) they performed a comprehensive static VASP study on protonic site energies and migration barriers. In agreement with KREUER and on a more quantitative basis they identify the stretch-activated proton displacement mode to be the rate determining one (with a barrier of 0.25 eV for $BaTiO_3$ *and* $BaZrO_3$ for example) next to a considerably easier reorientation step of around 0.14 eV. These are rather important and very comparable values to this thesis' work where for the compounds in question here the same sort of question will be asked (see the section on the protonic displacement modes 6.4). In later papers [29, 30, 31] they extend their studies also to doped perovskites and the local modifications those dopants cause for the proton energetics. Finally they tackle the single-proton long range diffusivity by the so-called vertex-coding treatment which allows to determine the relative importance of different possible conduction pathways in doped and/or not-cubic perovskites.

Two other very relevant articles on the DFT-based treatment of actual proton conduction

---

[3] For the Brownmillerite materials corresponding results will be given in section 6.4.

in a (doped) non-cubic perovskites come from Bilic and Gale [32, 33]. They treat the long range diffusion of a proton in proton-acceptor-doped $CaZrO_3$ (the dopant is In) by a step-by-step analysis of the potential energy surface (PES), and its subsequent injection into a kinetic Monte Carlo scheme. To this end they calculated the DFT-energy of every possible proton position (48 in total) alongside with every possible migration barrier (a total of 220) using the ”drag method” which means to move the proton along a series of (well chosen) points between an initial and final state and recording the corresponding energies in order to obtain the barrier height. This was done for a supercell containing 4 primitive perovskite unit cells, i.e. 3 Zr and 1 In cation which corresponds to a 25/75 B-site substitution. A serious drawback however, is the necessarily ordered cation-arrangement that comes with such a small supercell. This indeed reflects the huge complexity of a detailed description already in a 4 cation cell[4]. The wealth of activation barriers that are determined for every elementary displacement step is confined between values of almost zero to 0.8 eV. So in order to obtain an idea of the actual diffusion behaviour of one proton in this PES the kinetic Monte Carlo algorithm is used in which the entire set of barriers is integrated. The approach presumably is similar to the one used in this thesis and is described in section 2.3. The outcome of the MC approach in [33] is an approximate intermediate effective activation energy of the order of 0.6 eV however obtained merely by running the MC-routine at two different temperatures. Moreover the role of the ”dopant” turns out to be somewhat ambiguous as for the low temperature it hinders diffusion whereas at the high temperature it improves it (both times compared to MC-simulations in the pure $CaZrO_3$ system). This aspect will be discussed in detail later on in the corresponding MC-section 5.

Another principal source of computational studies, with a focus on vibrational and structural aspects comes from the group around Björketun, Sundell, Wahnström and co-workers. They investigate a great amount of different properties related to doped perovskites (mainly $BaZrO_3$), their structures, vibrational properties, energetics with and without protons. Their effort is entirely based on the charged-defect approach that is capable of supplying meaningful hydration energies for arbitrary perovskites but also for undoped ones (the concept e.g. being explained in [34, 35]). This reduces the computational cost significantly as the calculation of very small (sometimes even elementary) cells with and without a proton is sufficient to describe the hydration.

In one of their most exhaustive studies of 2007 [36] they compare the influence of various (Ga,

---

[4] It is relatively clear, that for the comparative scope of this thesis this approach cannot be pursued being obliged to treat cation-disordered cells of 32 B-sites for several compounds.

In, Sc, Gd) dopants in $BaZrO_3$ and find substantial differences between them. These differences are mainly of structural nature and can relatively reasonably be linked to the ionic-radius match or mis-match between the dopant and Zr. This has profound consequences on the energetic landscape a proton-defect is moving in, which is verified by kinetic Monte Carlo simulations. The concept was introduced in another paper by them [37]. The latter however dealt with the description of the pure $BaZrO_3$ material in a more general way. Concerning the different dopants, they can conclude that Ga, In and Sc will act as traps to the proton migration whereas Y and Gd are either indifferent or obstacles.
Q. Zhang from the same group gave yet another very important contribution to the understanding of proton transport by performing a full quantum mechanical path-integral calculation in $BaZrO_3$ [38]. This sort of approach actually treats also the proton itself as quantum particle, i.e. zero-point energy- and tunnel-effects are included. This work very nicely confirmed the big importance of quantum effects at temperatures below 300°C.

A working group consisting of Mohn, Stolen, Bakken and others based in Oslo also contributed much insight into this kind of material. They do so by employing the so called configurational averaging technique which consists of forming thermodynamically correct partition functions of systems with a large number of possible micro-states, configurations [39]. Not necessarily dependent on DFT calculations, also classic pair potential lattice relaxation techniques supply a total energy for any of the numerous structural varieties, as shown for example for the case of $SrFeO_{2.5}$ in [40]. A configurational partition function would read

$$Z = \sum_{i=1}^{K} \left(g_i \exp\left(\frac{-E_i}{kT} \right) \right) \tag{1.4}$$

which by standard thermodynamic theory can then be used to obtain free energies, enthalpies, entropies and the like. The sum is over all K energetically different microstates and it takes into account the number g_i of crystallographically equivalent configurations (the degeneracy) that are present in the considered simulation cell.

Two of the most relevant papers by them uses this technique to describe the pure $Ba_2In_2O_5$ [41] or Ga-substituted material [42] in terms of some 100 different microstates. By knowledge of their degeneracy g_i and energetical level E_i they manage to determine the temperature region in which a given class of local configurations is realized. These works will be commented on in detail in section 3.2 where the same type of information is obtained by the direct molecular dynamics approach for $Ba_2In_2O_5$.

One of the most drastic shortcomings of this elegant configurational averaging method, is the enormous increase of the number of local configurations when going to bigger simulation cells. By a related approach Martinez [12] from the same group also studied the stability of the fully hydrated $Ba_2In_2O_4(OH)_2$ compound and confirm the experimentally invoked tetragonal layered structures including two different proton sites intra- and extra-octahedral.

Chapter 2

Computational techniques

This chapter gives a short introduction into the theoretical and technical foundations of the key aspects of the thesis. Those include the most important working tool which is the application of density function theory in general and the molecular dynamics (MD) approach based on it. Presented are also the tools and techniques that were used in order to assess the results of the aforementioned MD experiments. Finally the Monte Carlo concept is presented which will later on serve as a means to interpret results.

2.1 Technical parameters of the Density functional theory (DFT) calculations

All calculations that are presented in this thesis were carried out using the *Vienna ab initio simulation package* (VASP) [43, 44, 45]. This implementation of density functional theory uses a plane wave expansion in order to describe the electronic wave functions which is the method of choice for bulk material properties like those this work is interested in. The atomic pseudopotentials that are necessary when planewaves shall be used are generated by means of the so called projector augmented wave (PAW) method as introduced by Blöchl [46, 47].

A generalized gradient approximation as parametrized by Perdew-Burke-Ernzerhof (PBE) is used for electronic exchange and correlation [48]. The PAW-PBE potentials for all the elements studied as supplied by the VASP-POTCAR files are presented in table 2.I including the character and number of explicitly treated electrons.

Table 2.I: Used PAW-PBE elemental potentials including electron configuration and number of electrons as supplied in VASP

Ba_{sv}	5s5p6s (10)	In_d	5s4d5p (13)	Ti_{sv}	3p4s3d (12)
Sr_{sv}	4s4p5s (10)	Zr_{sv}	4s4p5s4d (12)	Y_{sv}	4s4p5s4d (11)
Sc_{sv}	3s3p4s3d (11)	O_s	2s2p (6)	H	1s (1)

Structural relaxation was performed by a standard conjugated gradient routine integrated in the DFT code. Atomic positions as well as cell volume and shapes are allowed to relax. The relaxation is performed until all forces on atoms are smaller than $5 \cdot 10^{-3}$ eV/Å.

For calculations of "smaller" systems (for example some simple trial structures that explore various local oxygen structures as e.g. shown in figure 3.5 on page 51) a cutoff energy of 600 eV was used. A k-point mesh of 2·5·5 proved sufficient for these cells having the approximate dimensions of 16·6·6 Å^3. For the k-point integration the tetrahedron method with Blöchl corrections was chosen [49].

For the much more frequently[1] used 4 times larger cells (12·12·16 Å^3) the cutoff energy could be reduced to 450 eV. Furthermore the calculation was performed only for one k-point (Γ) of the electronic Brillouin zone. Because the aforementioned tetrahedron method does not work for less than three k-points in this case VASP uses a gaussian smearing method to integrate the electron density of each electronic band. Following the recommendations of the VASP authors a very small (0.05) smearing parameter was used for a proper description of the compounds of this study.

Large simulation cells that were relaxed with an energy cutoff of 600 eV were compared to a 450 eV relaxation. They showed an expected but acceptably small decrease of the relaxed lattice constants of about 0.4%. Moreover test calculations on hydration energies[2] yielded deviations of 1-2 % which corresponds to values of -0.61 eV compared to -0.62 eV.

Concerning relaxation in general it has to be stressed that all structures that were used in any way in this thesis (local structure exploration, calculation of mutual energy differences, static hydration energies, vibrational normal mode analysis, Bader-charge analysis, illustration etc.) are always understood to be fully relaxed as just described.

2.1.1 The Bader charge concept

This concept which was brought about by R. Bader [50] is a mathematical method to analyse an arbitrary spatial charge distribution in a way that allows to partition this space into separated sub-volumes. When applied to electronic density distributions that for example may be generated by a converged DFT routine in a solid, these individual Bader-volumes will in general coincide with regions that have an atom in its center. The (Bader)-charge contained in each such region may very often be interpreted as "the charge" associated with the ion in

---

[1] including the molecular dynamics simulations

[2] One of the key properties which will be evaluated in section 4.4.3 describe the energy gain per water molecule for being diluted inside an oxide or in the gas phase.

question, more precisely a sort of physical/spatial charge state. Despite a list of rather fundamental problems with this method [51], it proves rather useful in a comparative sense when for example charge transfer evolutions of different compounds shall be studied as function of dopant concentration or the like. In this thesis it will be employed for the discussion of trends in the energies of hydration as presented in section 4.4.

Technically the Bader analysis is conducted by the openly available software from the groups of Henkelman and Jonsson [52, 53]. A VASP generated CHGCAR-file (containing the spatial charge distribution) serves as input and the routine delivers the effective Bader charge associated to every ion present in the system.

2.2 DFT-based molecular dynamics

2.2.1 The molecular dynamics method

Molecular dynamics (MD) is a rather simple but enormously powerful computational tool to study a great number of material properties. In contrast to pure DFT calculations for example molecular dynamics (MD) simulations focus on properties either heavily influenced or caused by temperature in first place.

It is an iterative and deterministic method that is capable of generating trajectories of an arbitrary number of classical particles that are subject to a known potential energy surface and arbitrary starting conditions. It thus yields an approximate solution of a many body problem which analytically already for three, let alone more particles, is unsolvable. Classical, materials oriented MD searches to describe an ensemble of ”atoms” that are equipped with a mass and that interact with other neighbouring atoms. The most straight-forward approach to describe this interaction is to postulate pair-potentials, i.e. potential-distance curves that will be characterized by a mutual attraction for long distances, an equilibrium distance and a repulsion for shorter distances. Thus when for a given particle all directions and distances to all the surrounding other particles are known the vectorial summation of the corresponding forces gives rise to a net force which is exerted onto this particle at a given instant. This is done for all particles present in the simulation. The remaining task is a mere application of one of the most fundamental relations in physics linking a force to an acceleration by $a = \frac{F}{m}$. In that manner the state-of-motion (i.e. the velocity) of every particle is updated. Simultaneously it is kept track of the actual displacements of every particle due to this velocity. Now, as for all iterative techniques the timestep after which all those procedures are performed has to be

chosen sufficiently small and the outcome will be a trajectory of all particles which depends on the initial conditions and will end up in some collective equilibrium state, e.g. a crystal like close packed vibrating configuration.
Being interested in certain properties at a given temperature the system is coupled to an imaginary thermostat which at every timestep adjusts the total kinetic energy in the particle system given the relations $\langle E_k \rangle_N = 3/2 k_B T$ for N particles.

The particularity of the DFT-based approach lies in the aspect of the aforementioned potentials. For classic MD the particle interaction is modeled by constructed and fitted empirical potentials whereas in the DFT based approach as used in this work the interaction is recalculated at every timestep by performing a new electronic DFT calculation which by virtue of the Hellman-Feynman theorem directly grants access to the forces acting on any particle.
Very conveniently such a direct MD approach is implemented in the VASP DFT-code and very thoroughly explained by KRESSE and co-workers e.g. in [43, 44]. The routine uses a Verlet-Velocity algorithm for the iteration of the newtonian force equations. The temperature can be controlled by a Nosé-Hoover thermostat as described below.

2.2.2 General parameters for the VASP-based MD

The runs were started from completely relaxed initial configurations that correspond to the crystallographically known structures (for BaInO and BaInOH). For the substituted compounds the distribution of the 2^{nd} B-site cation was performed in a "random way" by hand. In order to simulate situations of maximal miscibility for 6.25 and 25% subsitution the substituents were distributed without generating next-nearest neighbours of them.
The time step (as recommended by the VASP-reference) was chosen to be of the order of one tenth of typical vibrating period. For all proton-containing simulations a 1 fs time step was chosen. For the corresponding dehydrated, dry compounds it was augmented to 2 fs due to the lower maximum vibration frequency.

2.2.3 The use of a thermostat

In general there exist different manners to conduct an MD experiment. Commonly either microcanonical (NVE) or canonical ensembles (NVT) are used. For both approaches the particle number (N) and the volume (V) are held constant throughout the MD-run. The simplest

MD-approach is to simulate a NVE ensemble, where it is the total (kinetic plus potential) energy of the system that is kept constant. This translates to the fact that the actual occurring temperature after thermal equilibration will depend on the initial kinetic energy imposed on the particles *and* the structural configuration as well as the system itself. The NVT-ensemble therefore is somewhat more convenient, especially when it comes to comparing averaged energies of several different systems which should be done at a common temperature. In such an NVT ensemble it is an additional routine (the thermostat) that regulates the instantaneous temperature of the system.

The choice to use a thermostat was made, in order to guarantee an easy comparability between structures that contain a different number of particles. This is especially true for the comparison of total cell energies (between hydrated and dry cells for example) that yield direct information on a thermodynamically justified hydration energy.

2.2.4 Data Evaluation

One of the major ”working parts” during the thesis was the elaboration of appropriate routines and criteria that properly characterize the system under scrutiny during an MD-run. This was accomplished by a set of straightforward standard approaches (see the three following subsections) and by system adapted counting algorithms, that allowed to accurately track for example the eight unique modes of proton displacement encountered in the material family as well as the concentration of a given coordination polyhedra of the B-site ions in the dehydrated compounds.

2.2.4.1 Pair correlation functions

The pair correlation functions (PCF) are useful measures to describe time averaged local structural properties during of particles in a MD simulation. For a MD simulation containing several distinguishable species (A and B here) PCFs of the A-A, A-B or the B-B couple may be determined according to the structural information wanted. As will be presented in the section on protonic structures, predominantly we are going to be interested in the couple B-site-cation and proton. The PCFs carry information about the averaged spatial separation of a given particle couple and to what extent this arrangement can be considered ordered or liquid like. For a PCF, which displays the characteristic of becoming 1 for long distances for all but completely static arrangements the definition reads

$$g(r) = \frac{\langle n(r, r + \Delta r)\rangle}{4\pi \Delta r N_A \rho_B r^2} \tag{2.1}$$

for a PCF which is taken for finite spacings Δ r. The $\langle n \rangle$-function indicates a time average over the number of counted A-B distances which are in the range between r and $r + \Delta r$. ρ and N stand for number density (particles per considered volume, i.e. volume of the simulation cell) and absolute number of particles, respectively. The normalization with a factor $1/r^2$ ensures the high distance behaviour to be asymptotically/oscillatorily approaching the value 1. However this somewhat impedes a bit the direct comparison of integrated PCF values in terms of an effective coordination number. A measure which directly yields an expression of the type "particles B per particle A" is given by

$$M = \int_0^{r_{max}} \frac{\langle n(r, r + \Delta r)\rangle}{N_A \Delta r} dr \tag{2.2}$$

in the sense of an effective coordination number with an appropriately chosen r_{max} which may be chosen arbitrarily or better based on obvious structural features of the PCF in question.

Technically the PCFs were obtained by the evaluation of the trajectories of the whole set of particles provided by VASP. The routine was programmed to simply check all the distances around a given ion at any instant of time and to class them into appropriate distance categories (with a cutoff radius of 8 Å and a Δr of 0.01 Å). To correctly treat ions located at the simulation cell's borders the cell is (virtually) repeated 26 times to account for the 6 face-linked, the 12 edge-linked and the 8 corner-linked adjacent cells.

2.2.4.2 Mean-square displacement

One of the most obvious things to track during an MD-experiment is the displacement of a given chemical species. In a random-walk framework, the diffusion coefficient is then given as a linear function of the so called mean-squared displacement (MSD).

$$D = \frac{\langle \Delta^2 \vec{r}(\tau)\rangle}{6\tau} \tag{2.3}$$

Throughout the thesis the MSD is always understood as averaged over all particles n (oxygens for the dehydrated cases, protons for the hydrated ones) and internally averaged. This internal time averaging as e.g. described by SAXTON [54] is an averaging with respect to one single trajectory of length N which is thought of being composed of many runs with different time-origin t_0 which are displaced along the time ordinate.

$$\langle \Delta^2 \vec{r}(\tau) \rangle = \left\langle \left[\vec{R}(t_0+\tau) - \vec{R}(t_0) \right]^2 \right\rangle = \frac{1}{n \cdot (N - N_\tau) + 1} \cdot \sum_{j=0}^{N-N_\tau} \sum_{i=1}^{n} \left(\vec{R}_i(t_j+\tau) - \vec{R}_i(t_j) \right)^2 \quad (2.4)$$

where $t_j = t_0 + j\Delta t$ and $\mathrm{N}_\tau = \frac{\tau}{\Delta t}$

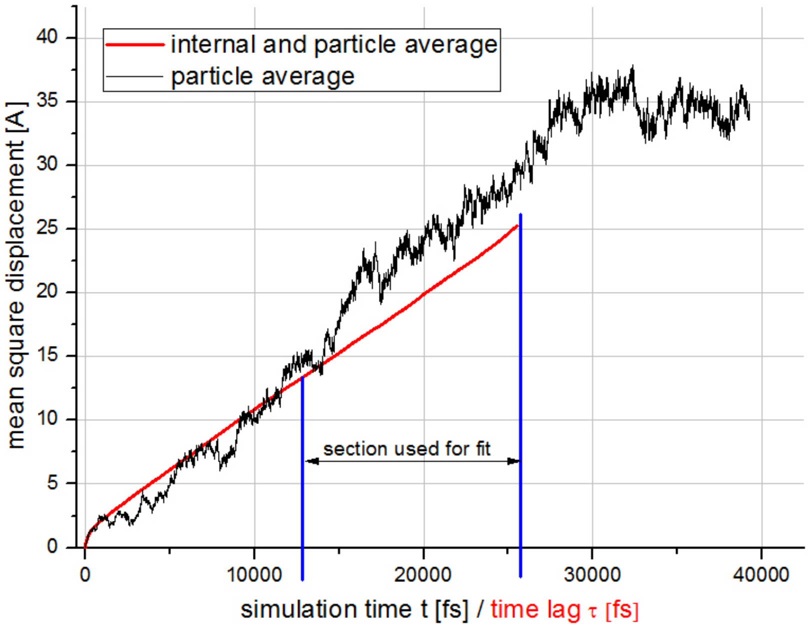

Figure 2.1: Example of a typical proton MSD (here in BIY25) at 800°C. The black line shows the average over the 32 protons present in this systems, whereas the red line additionally is internally averaged. As explained in the text, only the indicated region is used to determine the diffusion coefficient.

So for any new time-origin t_j the trajectory is "restarted" and the displacements $\vec{R}(t_j + \tau)$ for increasing τ are recorded. The internal averaging is therefore performed over (N-N$_\tau$) single trajectories of length τ which implies that with increasing time lag τ the statistical weight decreases.

In practice the MSDs were obtained as follows: (I) The first 1000 steps (= 1000 fs) of any trajectory were arbitrarily cut away completely to avoid possible thermalization effects. (II) The range of τ is restricted to 65% of the simulation time. This ensures that the last point of the MSD which is used to determine the diffusion coefficient is still an average of a number of values corresponding to 35% of the total number of simulation steps. (III) Only the second half of the remaining squared displacement is used to linearly fit the slope (which for the approximate linear behaviour replaces definition 2.3)

A very important issue concerning the MSD is its statistical character and the associated statistical errors or uncertainties. Owed to the relatively large cell size for most cases only one single run of 30-60 ps (30000 to 60000 steps) was performed per compound and temperature. Yet (concerning the proton diffusion) each run included at least 16 diffusing protons, which nevertheless assures a sufficient statistic. An initial idea to obtain the intrinsic statistical spread of the diffusion coefficient is to cut the run into several pieces and to determine their diffusion coefficient separately. This has been done for several runs and yields relative σ-values of about 15%. A more detailed account on the statistical errors in given in the forthcoming section 2.4.

2.2.4.3 Velocity autocorrelation function and normal mode analysis

Given the opportunity to perform DFT-based molecular dynamics simulations the vibrational densities of state (DOS)[3] that can be extracted out of them are of a particular value as in principal the potentials at any MD-time step may be considered chemically correct (i.e. re-evaluated by a complete electronic convergence loop). Therefore bond-properties (e.g. the amount of covalent character and the corresponding bond-stiffness leading to higher vibrational frequencies) are likely to be correctly reproduced even upon changes of local coordination structure and the like. The method to obtain vibrational information out of an MD run is the Fourier transform of the velocity autocorrelation function. It is formulated for any ionic species and describes the degree of correlation of the particles velocity over a time-lag.

$$\Psi(\tau) = \frac{1}{n} \sum_{i}^{n} \frac{\langle \vec{v}_i(t_0 + \tau) \cdot \vec{v}_i(t_0) \rangle}{\langle \vec{v}_i(t_0)^2 \rangle}. \tag{2.5}$$

As it was already performed on the mean-square displacement, the values that constitute the VAF are internally averaged and limited in range, to assure an equal statistical weight for every τ. The practical definition as used in this work reads:

$$\Psi(\tau) = \frac{\sum_{t_j=1}^{N/2} \sum_{i=1}^{n} (\vec{v}_i(t_j + \tau) \cdot \vec{v}_i(t_j))}{\sum_{t_j=1}^{N/2} \sum_{i=1}^{n} (\vec{v}_i(t_j)^2)} \tag{2.6}$$

with $t_j = t_0 + j\Delta t$

The Fourier transform yields a frequency spectrum of all occurring frequencies for the observed ion. They are going to be discussed in the corresponding sections for the dry and

---

[3] Although the equivalent formulation "spectra" will sometimes be used in the text, these are no spectra in the experimental sense, as the actual (IR/Raman)-intensity is combination of the DOS and the dielectric properties of the ions, which has not been simulated in our approach.

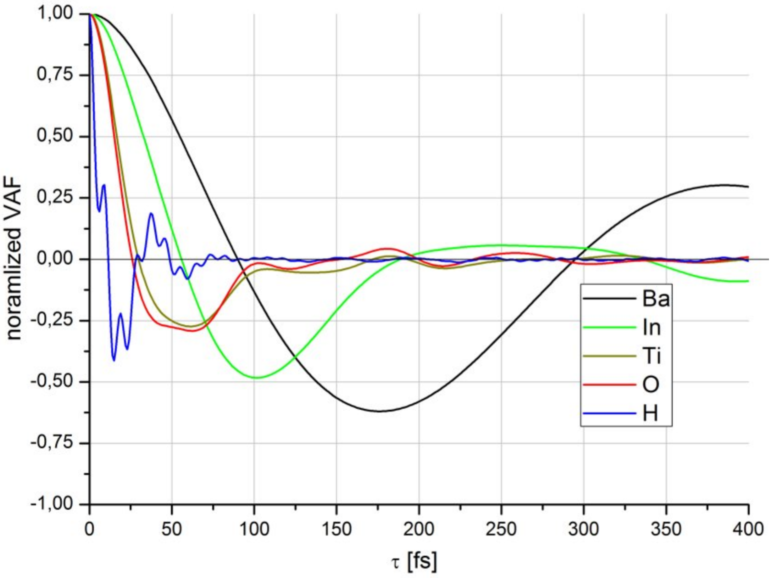

Figure 2.2: Normalized velocity autocorrelation functions for all ionic species in Ba_2InTiO_5OH obtained by a run at 800°C for 50.000 fs

hydrated compounds. The spectra have the character of a vibrational density of states, i.e. a projection of phonon dispersion curves onto the energy scale. They do not contain any information on geometrical aspects like the normal-vectors of a given observed vibrational mode. More precisely, the obtainable density of states is only a portion of the complete phonon spectrum, however limited in low frequencies due to the finite size of the simulation box. This means that acoustic or optic phonons with longer wave lengths than the box dimensions cannot occur during the simulation. Nonetheless the simulation cells used throughout are rather large in having four layers of eight B-site cation polyhedra each. Moreover these long-wave-length effects can supposedly be neglected for what the scope of this work is concerned. HORBACH and co-workers [55] for example argue that predominantly (very) low-temperature thermodynamic properties like the specific heats (*at low temperatures*) are significantly affected.

In a similar spirit as for the MSD evaluation, the calculation of the VAF is based on a truncated MD-run. The first 40% of the run were cut away to allow for a (I) vibrational thermalization and (II) a maximum structural equilibration. Point (I) is a classical MD issue, that is linked to the fact that the particles are abruptly given randomly distributed velocities. This effect is most of the times attenuated within a rather short time of several 100s of MD-steps [56]. Aspect (II) shall ensure that the more or less guessed initial structures correspond to their true configuration to a maximal extent. This concerns the distribution of oxygen vacancies in the dry compounds and the proton locations in the hydrated equivalents.

Another possibility to characterize the vibrational properties is the normal mode analysis (NMA). This is a standard method integrated in the VASP code which allows to obtain the dynamical matrix of a system of nuclei. This dynamical matrix essentially is made up of the second derivatives of forces with respect to positions of ions that successively are slightly displaced in the three directions of space. Based on a very carefully relaxed (force-less) configuration the extent of these arising forces carry information about the stiffness of a given ion with respect to its surrounding, i.e. its vibrational frequency. This method entirely relies on the approximation of these forces to be harmonic. The eigenvalues of this matrix correspond to the 3N-3 (N being the number of considered ions) normal mode frequencies along with the corresponding eigenvectors which indicate the spatial direction of any of these modes. The analysis was conducted without no constraint on any ionic species, i.e. all 144 to 192 ions (depending on the dry or hydrated compound) were displaced by a displacement of 0.02 Å. The cells for which these calculations are carried out were obtained by a full structural relaxation of instantaneous "snap shots" of molecular dynamics runs in order to be close to some structurally meaningful configuration in the spirit of point (II) above.

2.2.4.4 Counting and observation algorithms and Boltzmann statistics evaluation

In order to characterize the elementary steps that constitute the proton diffusion in the compounds, the corresponding rates of each of the six possible elementary displacements are extracted from the MD runs. This is done by keeping track of each proton's first- and second next-nearest neighbour oxygen ions. These two oxygens atoms are the ones which the proton is covalently bonded to and the oxygen with which the proton forms a hydrogen bond. Based on the recorded complete trajectories of an MD run, any change in proton-oxygen association is counted and binned into one of the six categories. This is achieved by a case differentiation on which of the two oxygen neighbours has changed (covalent or hydrogen-bonded) as well as the relation of the previous and current oxygens (e.g. they belong to the same or different cation polyhedron). The so obtained number counts are then normalized with respect to the simulation time and the proton number.

2.3 Kinetic Monte-Carlo algorithm used for the discussion of proton diffusion

During the interpretation process of the obtained MD data concerning the protonic transport properties, a kinetic Monte Carlo modeling scheme proved very useful. Although not having a comprehensive set of every possible proton diffusion barrier or site-energy at hand, it is very illustratively possible to deduce very important aspects of the general behaviour in disordered lattices. Moreover an MC-analysis allows to get insight into the very crucial aspect of the statistic uncertainty of MD-obtained properties as the aforementioned counting rates or the diffusion coefficients (being rather different). Moreover, clear tendencies with respect to random barriers, random traps (or a combination) can be extracted as well as the relation of the elementary step-counting rates with the effective diffusion coefficient.

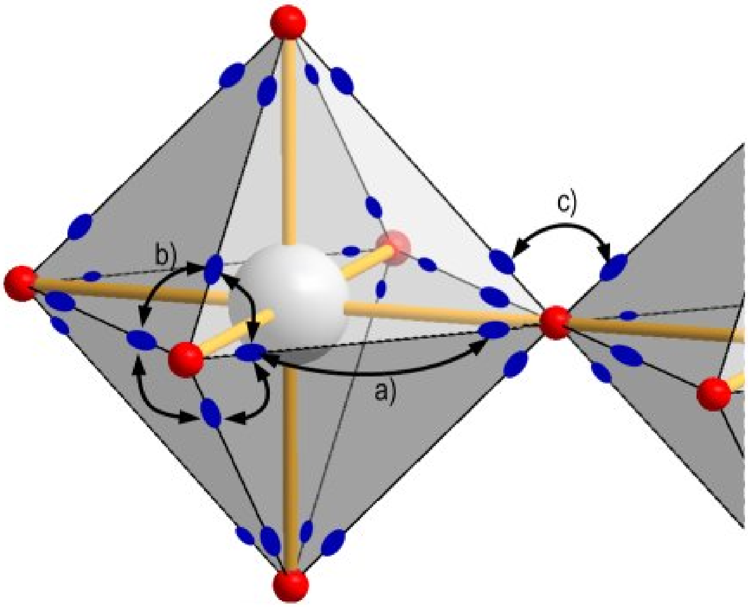

Figure 2.3: The 24 total proton sites at each octahedra which are linked by stretch-hop (a) along the edges), rotations (b) around the summits) and flips (c) changing the octahedron). Each proton site therefore is 4-fold coordinated (1 stretch, 1 flip, 2 rotations)

The proton diffusion was therefore modeled by a topology as shown in fig 2.3. The lattice on which the proton diffusion takes place consists of an arbitrarily large 3-dimensional array of polyhedra having 24 potential protonic sites each. Usually at least 6×6×6 octahedra were used in order to ensure a good trap or barrier distribution. More precisely each polyhedron edge has two proton-sites which are separated by a stretch-hop barrier. Furthermore a proton can diffuse to an adjacent edge of the same polyhedron by a rotation (in two different directions) or to an edge belonging to a neighbouring polyhedron by a flip-motion. Each one of the three displacement modes can be attributed a (randomly distributed or not) activation barrier as well as a prefactor. Moreover any proton-site can be assigned a certain trap-depth (again randomly distributed within certain limits, or fixed). The MC-routine is explicitly considering arbitrarily many protons that diffuse simultaneously. In this manner site-blocking effects are included automatically. More importantly, the presence of many protons influences the overall diffusion in the case of inhomogeneously deep traps, where the deepest traps would preferentially be occupied by protons and therefore leave an effectively smoother ("trap-less") PES for the remaining ones.

The kinetic Monte Carlo scheme itself is kept rather simple. A standard Metropolis algorithm was employed, which compares a Boltzmann factor (containing the trap-depth plus the barrier height) with a pseudo-random number between 0 and 1. A given MC step is effectuated exactly when

$$0 \leq P \leq \exp\left(-\frac{E_{trap} + E_{barrier}}{kT}\right) \tag{2.7}$$

The timestep-definition is based upon observations corresponding to the three kinds of rates that are considered. Typical prefactors of the three relevant modes as they will be identified in section 6.4.1 were used to define a real-time equivalent of the MC-step.

$$\Delta t \equiv \left(\sum_i^3 \nu_i\right)^{-1} = \left(3.0 \cdot 10^{13} s^{-1} \ + 1.6 \cdot 10^{13} s^{-1} \ + 1.8 \cdot 10^{13} s^{-1}\right)^{-1} = 1.47 \cdot 10^{-14} s \tag{2.8}$$

For every MC-step the choice of the subsequent attempt is made according to the relative weights of the three mode prefactors. With this procedure the prefactors obtained by fitting the actual MD-results of the rates (obtained by simple counting) yield the exact values that have been inserted into the routine.

The analysis of the MC-diffusion coefficients is performed the exact same way as already explained for the molecular dynamics runs. The linear slope of the second half of the self averaged mean-square displacement is taken as measure for the diffusion coefficient. However, given the (relative) computational ease of the method, in addition thousands of individual and independent trajectories contribute to this mean-square displacement, for single or multi-particle runs alike. Using a "standard" perovskite cell constant of 4.19 Å $= 4.19 \cdot 10^{-8}$ cm yields diffusion constants in $\mathrm{cm}^2\mathrm{s}^{-1}$.

In analogy to the treatment of MD data, also the three distinct counting-rates of the elementary displacement steps are recorded. All MC-runs that whose rates, diffusion coefficients etc. will be presented are completely equilibrated and consist of run lengths of at least 100000 MC steps, or at least an ensemble displacement 100 Å , i.e. 20 perovskite polyhedra.

2.4 Statistical errors of the diffusivity and the hopping rates

A very convenient ”by product” of the MC studies, is the systematic access to the order of magnitude of the errors of the diffusion coefficient and the aforementioned jumping rates that are intrinsic to the statistical properties of those two properties. In order to get an idea of their extent a series of test calculations was run for a system which contains a barrier and trap-distribution more or less imitating a typical protonic diffusion. The barrier parameters were (0.25 ± 0) eV, (0.1 ± 0.02) eV and (0.08± 0.02) eV as well as also uniformly distributed traps ranging from 0 to -0.1 eV. The lattice (chosen as 6×6×6 polyhedra with 24 sites each) was large enough to ensure no mutual particle-particle blocking effects. Proton number, temperature and length of the run were varied for a set of 2000 individual MC-runs.

According to the theory of the pure random walk the variance of the mean-square displacement $\sigma(msd)^2$ is proportional to its absolute value. As simultaneously the MSD increases linearly in time and given definition 2.3 we see that the diffusivity uncertainty remains constant with respect to (a sufficiently long) simulation time. However this is only true, when the diffusion coefficient is determined strictly by the actual long term behaviour with respect to the simulation time of the run as it has been done for both the MD and MC experiments (e.g. based on the slope of the second half of the linear internally fitted graph, as indicated in figure 2.1).

Put otherwise, the standard-deviation would decrease with total simulation time, if the calculation of the coefficient was performed on the same absolute τ-interval (e.g. always within the blue bounds of figure 2.1 although the actual run-time was longer). The smaller τ the higher the statistical accuracy with respect to the random-walk spread when the internal averaging is performed.

However this criterion can only be applied if the used interval can physically already be considered ”long time behaviour” (i.e. a sufficient sampling of the underlying lattice’s potential energy landscape).

So the absolute and relative error of the diffusion coefficient calculated for the second half of the internally averaged MSD, for the pure random walk is independent of simulation time what (of course) is confirmed by the MC-routine of a diffusion on a completely barrier- and trap-less lattice (2.4 a). The statistical spread of the hopping rates however does depend on both temperature (figure 2.4 b) and simulation time (figure 2.4 d). The relative error here decreases exponentially (as $\propto \exp\left(-\frac{E_a}{2kT}\right)$) with temperature and as the square root of the simulation time.

This is plausible as the statistical spread of such a thermally activated and well defined rate (which additionally is no collective property) in a Monte-Carlo or molecular dynamics experiment does only depend on the absolute number of counted events [57]. In particular the relative error of the rate decreases with the square root of the absolute number of events. Based on that, the behaviour of the stretch-rate error with respect to the temperature and the simulation time is trivial, given that the absolute event number increases exponentially with temperature and linearly with simulation time. Further test calculations with randomly disordered stretch barrier heights ($(0.25 \pm 0.15)\ eV$) show only a minor increase in the relative spread of the rate-count by around one to two points.

Thus, as the net-diffusion is a superposition of a pure random-walk on the protonated perovskite-lattice and the thermally activated hopping rates, it is plausible to state that also the diffusivity error is a combination of the random walk error and the error in the thermally activated hopping rates. As can be seen in figure 2.4 c) (and compared to a)) the relative statistical dispersion behaves indeed as a combination of the relative random-walk spread and the relative spread in the hopping rates. The overall level is rather high and mainly determined by the random-walk uncertainty. However there is a slight temperature dependence present, which is caused by the thermally activated mechanisms that *perform* this random walk.

Both properties do decrease as $\propto 1/\sqrt{N}$ with particle number, where the absolute values imply that the use of at least 16 protons per MD-simulation cell will be necessary in order to observe tendencies with respect to the chemical behaviour of the different compounds. It can be added, that the term particle number is identical to a number of independent runs with appropriately less particles each (for not too strong interaction). Finally, since the random-walk error always outweighs the error in the rates, activation energies and prefactors of the elementary rates observed in the molecular dynamics runs (see section 6.4) are more trustworthy than their

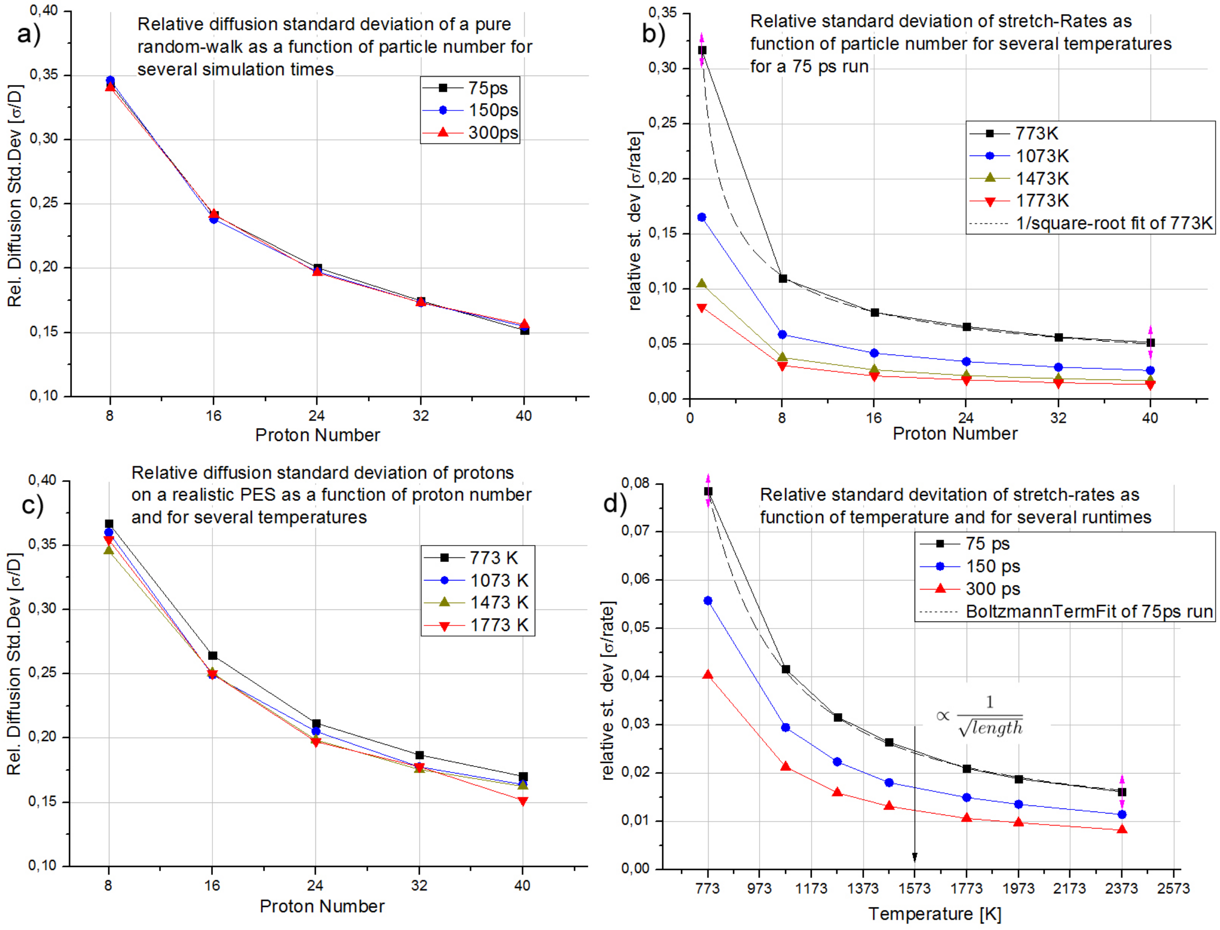

Figure 2.4: Measure of the relative spread of the diffusion coefficient (a) and c)) and the jumping rates (b) and d)). Subfigures a), b) and c) show the dependence on particle number, d) shows the T-dependence for 16 particles. The values are given in terms of σ divided by the mean value of D or the rate. The distribution is based on 2000 independent MC trajectories on the PES given in the text (except for the pure random walk in a) which is barrier- and trap-less).

equivalents extracted out of the mean-square displacement analysis (section 6.3). So for the elementary displacement rates we therefore can establish approximate error bars of less than 10% and for the majority of data points even significantly below (e.g. runs at 1200°C, 1500°C including 32 or 24 protons).

2.5 Statistical errors of the energies

The information on the specific heats and the MD-obtained hydration (see section 4.4.4) energies require the evaluation of the total internal energies per simulation cell which are recorded at every timestep of the MD run. Those energies of course are subject to statistical uncertainties. However the situation here is rather safe, as all MD-runs were performed for at least several

10000 steps. In general the internal energy fluctuates around some well defined mean value, which for very long runs becomes the thermodynamically exact internal energy $\langle U \rangle$. In order to assess the statistical quality of the energy recordings beyond the simple standard deviation of the whole run, a grouping method as described in reference [56] has been used.

The set of energy data of a typical run is regrouped in a manner to obtain subsets of energies within which consecutive values are spaced M steps apart with respect to the real MD-run. To give an example, an index M=100 and a run of 50.000 steps yields M=100 subsets containing 50.000/100=500 data points each. Each subset can now be associated to an own energy mean value along with the corresponding standard deviation, which now is characteristic of a sequence of points that were 100 simulation steps apart in the original run and therefore are less correlated.

So with increasing M this time-correlation will necessarily decrease which is the reason why arguably the simple standard deviation of the entire run is over-optimistic for an MD-experiment.

By performing this operation for step spacings of 40, 80, 200, 400 and 600 fs or steps as shown in figure 2.5 it can however be concluded that the standard deviation in our case is rather insensitive towards this de-correlation procedure. The fragmentation in less and less correlated sets of energy values turns out neither to increase nor decrease their respective standard deviations significantly.

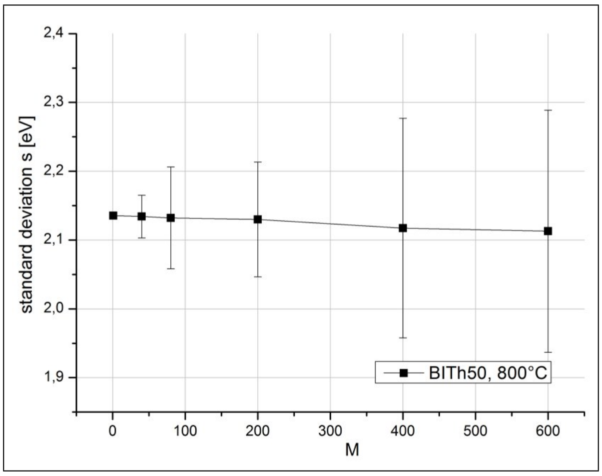

Figure 2.5: Standard deviation (in eV) of the total internal energy (BITh50 at 800°C; ≈ 50.000 MD-steps) as a function of fragmentation parameter M (see text)

It remains of the order of 2 eV for this typical simulation cell of BITh50 at 800°C which corresponds to about 46 eV total internal energy (i.e. an energy level 46 eV higher than the static DFT ionic-electronic total energy). The error-bar *on* the values for M>1 is due to the fact to have more and more groupings of energy values with each of them having their own mean value and standard deviation. This leads to a larger and larger number of energy-standard deviations for which the mean value is represented by the point and *their* standard deviation represented by the error-bar.

This standard deviation itself however is not to be identified with the statistical uncertainty of the arithmetical mean of the energy, as this deviation is determined by the thermal fluctuations *which are a physical property* of any thermodynamic system even in equilibrium of a given size, or equivalently in our case is dominated by the Nosé-Hoover thermostat. They therefore do not have the character of an error or an uncertainty and do not correspond to the error bar on an energy. As given in ref. [58] the real error is of the form

$$\Delta E = a_N \frac{s}{\sqrt{N}} \tag{2.9}$$

where a_N is Student's t-distribution factor being <4 for our case, s the aforementioned standard deviation for the MD-run and N the number of *uncorrelated* data points. The question here is to what extent consecutive values of the total set of energies (where N equals several 10.000) are correlated. According to molecular dynamics literature (e.g. FRENKEL and SMIT [56]) this extent of correlation would manifest itself in a significant dependence of the standard deviation on M, introduced in the previous paragraph. More precisely the standard deviation is supposed to increase significantly (by a factor of order 2) with M to end up in a plateau, which then would correspond to the "true" standard deviation. Here however we find this not being the case. Therefore an alternative measure of correlation, the velocity autocorrelation function is consulted. It has been introduced a previous section (2.2.4.3). The figure presented there (fig. 2.2) was once more obtained from the BITh50 compound and indicated a drop to the zero-correlation value for the slowest ionic species (barium, being the heaviest ion) within 100 fs of simulation time. So taking this decay time as a rough measure as a maximum of correlation time we end up with a ΔE of the order of 0.2 eV for the ensemble internal energy of the MD-calculations of this study. The most interesting property related to the total energies are going to be the hydration energies, i.e. the differences in energy of a fully hydrated compound and its dry counterpart. As this difference concerns two cells, for which the hydrated one has incorporated 4 to 16 water molecules, we can conclude that the error for this property is going to be sufficiently small (as per water molecule it would further be divided by at least 4 - for BITh75 - and at most by 16 for BaInOH).

Dehydrated compounds

3.1 Introduction

This chapter will present the study of the completely dehydrated compounds, as they show many interesting features due to their *disordered* nature, which is caused by a combination of (I) the presence of a high concentration of intrinsic oxygen vacancies, (II) the random distribution of B-site cations, (III) the local preferences in oxygen coordination of any of those B-site cations and (IV) in the case of aliovalent substitution the variation of the vacancy concentration. To study these dry compounds is hereby not only of principal interest, but also do properties of the dry state have an impact on the proton-conductivity of their hydrated counterparts. This is especially true for partially hydrated states where we deal with few protons in a material which still contains a high oxygen-void concentration. But also can information coming out of the study of the dry compounds be helpful to interpret characteristics of the completely hydrated compounds. For the entire molecular dynamics study we will restrain our interest to situations where the two following conditions hold:

(I) The mixed B-site cations themselves are distributed in a random manner on the B-sites and

(II) they are considered immobile.

This is assumed in the MD-treatment of both the dry and fully hydrated compounds later on. Both conditions actually could give rise to entirely independent studies as in related materials (double-perovskites, Ruddlesden-Popper phases) cation-ordering is rather the rule than the exception. Here however, we rely on the experimentally possible way of preparing those compounds in a way that yields cation-disordered materials at room temperature as well the operating temperature of a fuel cell.

The first part (section 3.2) gives an account on the dehydrated reference material $Ba_2In_2O_5$ which has the advantage to consist only of one type of B-site cation and showing a reproducible order-disorder phase transition. To this end many different kinds of approaches (vibrational analysis, pair correlation functions, internal energies) are going to be employed in a synthesized

manner in order to characterize this compound.
The following sections have a more comparative character. They present the properties of the cation-substituted compounds as studied by static DFT calculations, DFT-based molecular dynamics and XANES experiments.

3.2 The $Ba_2In_2O_5$ reference material

The order-disorder transition

The reference structure $Ba_2In_2O_5$ in its dehydrated state plays a special role in the study, as it may serve as ideal ordered system for which there exist several experimental and modeling studies in literature. Although not cation-substituted we are already confronted with the need to properly describe a ”potentially disordered” material given the high concentration of oxygen vacancies. Of particular interest is the existence of two relevant previous studies by classical pair-potential MD [59] and a static computational approach which uses the configurational averaging technique [41]. As already indicated in the ”State-of-the-Art” chapter, the configurational averaging approach is a direct alternative to an MD-treatment concerning the description of equilibrium thermodynamic information[1]. For the case of pure $Ba_2In_2O_5$ MOHN and co-workers created a 2x2x2 supercell containing 36 ions. With respect to an ideal perovskite this structure corresponds to the presence of *four* oxygen vacancies. In the following those vacancies were distributed among the 24 potential oxygen sites resulting in a still treatable number of 81 crystallograhpically inequivalent configurations. Knowing the degree of degeneracy g_i for each configuration i they obtained a closed expression of the configurational partition function Z by performing DFT total-energy calculations for all configurations reading

$$Z = \sum_{i=1}^{K} g_i \exp\left(\frac{-E_i}{k_B T}\right) \tag{3.1}$$

By virtue of this approach they identify a temperature dependent concentration of the polyhedra of coordination of the In(III) ion. This approach yielded a description of the system in terms of its local coordination structures which were found to be essentially tetrahedral and octahedral *up to* temperatures of 2500°C. Only at temperatures higher than that square-pyramidal entities occur to a considerable fraction, which means that up to this very high temperature the overall phase remains essentially similar to the low temperature ordered structure including its layered Brownmillerite character. As given section 1.1 the experimental transition temperature

---

[1] Not for transport or vibrational properties however.

towards a disordered (i.e. pyramid-containing) structure is at around 930°C. This discrepancy with experiment might be due to the fact that their exhaustive analysis of any possible vacancy configuration yielded only one structure which included square-pyramids which however showed a very low degeneracy compared to a very high number of Brownmillerite-like configurations both lower in energy and higher in degeneracy. Such a low degeneracy is linked to a small configurational entropy and therefore leads only to a very small possibility of being actually realized at a given temperature.

Kanzaki and co-workers [59] performed an extensive molecular dynamics study on the compound based on empirical pair-potentials. They in turn find an approximate transition temperature of about 2000°C inferred from jumps in the lattice constants which again is considerably too high compared to experiment, thus representing an inaccuracy in employed empirical pair-potentials. In contrast to what is presented from this work, their MD-routine however allows for a dynamical cell-volume adaption which is entirely absent for the VASP-MD runs. Therefore neither the linear thermal volume expansion as well as phase-transition induced volume changes can be reproduced here.
The conducted MD-experiments nevertheless allow to characterize this phase transition by various different structural and energetic aspects which will be presented in the following. To anticipate results, the phase transition can unambiguously be localized around a temperature region of 1000°C (± 200 K) which satisfactorily lies extremely close to the experimentally obtained value.

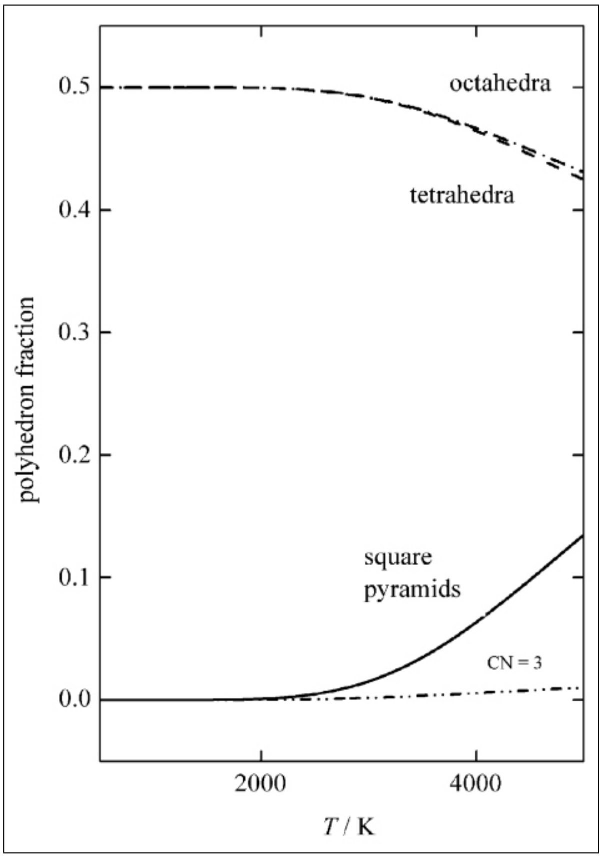

Figure 3.1: Coordination polyhedra for $Ba_2In_2O_5$ as obtained by Mohn et al. (taken from [41])

The first important indicator of such a phase transition behaviour is the temperature evolution of the internal energies. To this end $Ba_2In_2O_5$ was studied intensively in the temperature range from 200°C to 2500°C by molecular dynamics runs. Figure 3.2 a) shows the corresponding internal energies obtained from those simulations. More details with respect to the internal energies are given in the ”Hydration energies” section 4.4.4. Although rather limited in temperature resolution, a numerical derivative taken along all temperatures also gives an idea of the value and temperature-evolution of the specific heat capacity at constant volume defined by

$$c_v = \left(\frac{\partial U(T)}{\partial T}\right)_V \tag{3.2}$$

and which is given in figure a) as well. The two most elevated values (between 800 and 1200°C) represent the region of the phase transition where the internal energy exhibits a clearly visible energy offset. If a finer temperature resolution was available this region would show a singularity at the well defined phase transition temperature, here however we only can state that this temperature is confined within this region. It is remarkably close to the experimental evidence, which states a sequence of phase transitions from orthorhombic to tetragonal to cubic setting in at 930°C up to 1100°C where the final cubic disordered form is adopted (and which was already introduced in section 1.1).

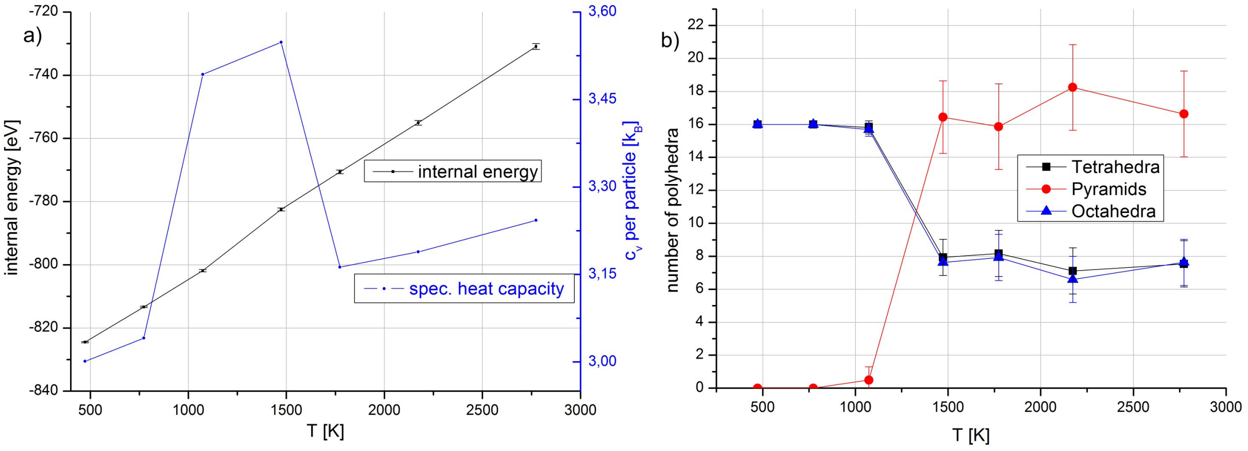

Figure 3.2: a) Internal energy <U> evolution per $Ba_2In_2O_5$ simulation cell (144 atoms, 32 In-polyhedra) at several temperatures (including the small error-bars described in section 2.5) along with its temperature derivative, the specific heat coefficient c_v per atom which shows a considerable temperature dependence; b) time averaged numbers of In-tetrahedra, -octahedra or -pyramids, respectively for temperatures 500°C up to 2500°C

Figure 3.2 b) presents the direct averaged numbercount of the three relevant coordination structures tetrahedra, square-based pyramids and octahedra. They are given with respect to the total number of indium-cations (32) in the simulation cell. The room-temperature structure (consisting of 16 tetrahedra and 16 octahedra) is found to remain strictly stable for the runs at 200°C and 500°C throughout the entire run-time of ≈50 or 70 ps each. Only at 800°C the onset of *temporary* structural changes can be observed which however are strictly reversible and only occasional in character. More precisely these changes can be identified with rotations of the ordered tetrahedra within their tetrahedral layer which render the adjacent octahedra square-based pyramids but leave the actual tetrahedra intact short of being rotated. Figure 3.3 a) illustrates this behaviour. Moreover this behaviour does not lead to any observable permanent oxygen displacement, i.e. the positions of any concerned oxygen merely fluctuate between two sites. Thus, oxygen diffusion in the ordered structure of $Ba_2In_2O_5$ is not directly observable in MD-simulations of this scope, both concerning cell size and simulation times. Fisher and co-workers [60] find (by classical pair-potential calculations) values above 1 eV for a migration energy of oxygen ions within the ordered low-temperature structure and which would be driven by real local thermally activated defect-oxygens.

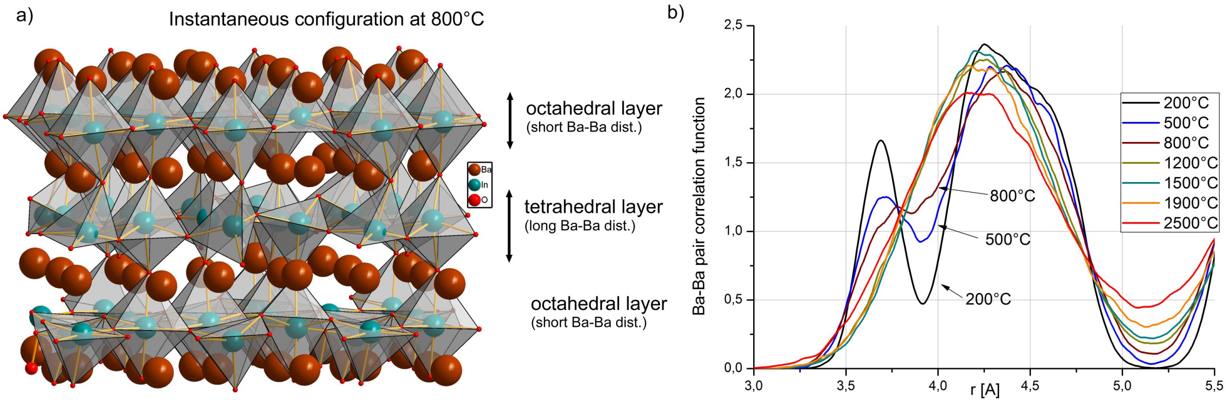

Figure 3.3: a) Illustration of temporary re-arrangements of In-tetrahedra at 800°C (i.e. below the actual phase transition temperature) indicating the still distinguishable tetra- and octahedral layers (now also containing rotated tetrahedra and square-based pyramids) which are related to the characteristic short and long Ba-Ba distances shown in b): pair correlation function for Ba-Ba in $Ba_2In_2O_5$ obtained from MD-runs in the temperature range of 200°C to 2500°C

The observations of the temporarily rotated tetrahedra also indicates the particularly fragile character of the apical oxygen ion, which is the one that links the octahedral and tetrahedral indium-ion in the ideal structure thus showing the onset of the phase transition on a local scale. This is in analogy and close agreement with what was observed by Paulus and co-workers [61] for the isostructural $Sr_2Fe_2O_5$ compound via VASP-based MD-simulations, thus on an identical level of investigation. The apical oxygen atoms are found to be the by far most (locally) mobile ones, in exhibiting the exact same behaviour of rotating the Fe-tetrahedron and thus leaving a square-based pyramid. This however is found to take place at *significantly* lower temperatures of about room temperature owing to the particular Fe-O bonding properties. Making reference to another literature source, again on barium-indate, Zhang and Smyth [3] made an assumption about the predominant intrinsic Frenkel-type oxygen defect. They however postulated the migration of in-plane oxygens out of the octahedral layer into the voids of the tetrahedral layer, a process which at 800°C for 70 ps has not been observed at any moment and may presumably be excluded to be relevant. We stress the striking difference in temperature behaviour compared to what is reported by MOHN and co-workers (and already shown in figure 3.1) mostly with respect to the presence of square-pyramidal entities (linked to the order-disorder transition). Very conveniently the same calculation basis were used in [41] and in this thesis being the PAW-potentials within the VASP DFT-package. Therefore a systematic error concerning the used atomic-potentials or the DFT calculation method can be excluded.

The two crucial differences which in combination are responsible for the discrepancy to the static approach of MOHN ET AL. are: (I) the molecular dynamics approach and (II) the considerably larger simulation cell having a higher atom number by a factor of four. Concerning point (I) the MD approach of course naturally includes the totality of vibration-related effects which may influence the stability of any particular local configurations. A detailed account on that is however outside the scope of this work. The larger unit cell however may probably be more important to the striking difference in the results: A severe drawback of the 2x2x2 perovskite based unit cell of their study, is that in any crystallographic direction there is only one couple of independent nearest neighbour indium-polyhedra whereas in the simulation cell employed here there are four independent In-polyhedra in all four principal directions.

Another structural indicator of this O-D-transition is contained in appropriate pair-correlation functions (PCF). In this case especially the Ba-Ba couple clearly indicates this change above 800°C as the well pronounced first peak at 3.72 Å vanishes completely. This shortest Ba-Ba connection is linked to the vertical Ba-Ba ions that embrace the octahedral layer (as indicated in figure 3.3). Other than the number count of the coordination polyhedra or the energies the PCF however show a somewhat more gradual evolution as indicated for the three lowest temperatures which from 200°C to 800°C smears out the distinction between the two Ba-Ba distances that represent the presence of well defined tetra- or octa-layers. At 1200°C the difference has completely vanished and has the same character as up to the highest temperature of 2500°C.

The specific heat evolution of $Ba_2In_2O_5$

An upcoming section dealing with the hydration energies will elucidate the role and influences of the specific heat coefficient c_v in a comparative manner between dry and hydrated compounds. There an important question addressed will be the origin of the deviation of c_v from its ideal classical value of $3k_B$ per particle which may have configurational (distribution of vacancies or protons) and vibrational (genuine anharmonicity) reasons. Therefore the pure (i.e. unsubstituted) reference compound barium-indate along with another pure reference compound - $BaTiO_3$ may serve as an estimation of this issue. Here we are going to compare the low temperature behaviour for $Ba_2In_2O_5$ and $BaTiO_3$ because as stated before all oxygen ions rest in their equilibrium positions and the heat capacity would exclusively be determined by vibrational aspects. $BaTiO_3$ of course does not have any structural degree of freedom (i.e. structural vacancies) at any temperature, given that the simulations are performed on its cubic phase at temperatures where this latter is stable.

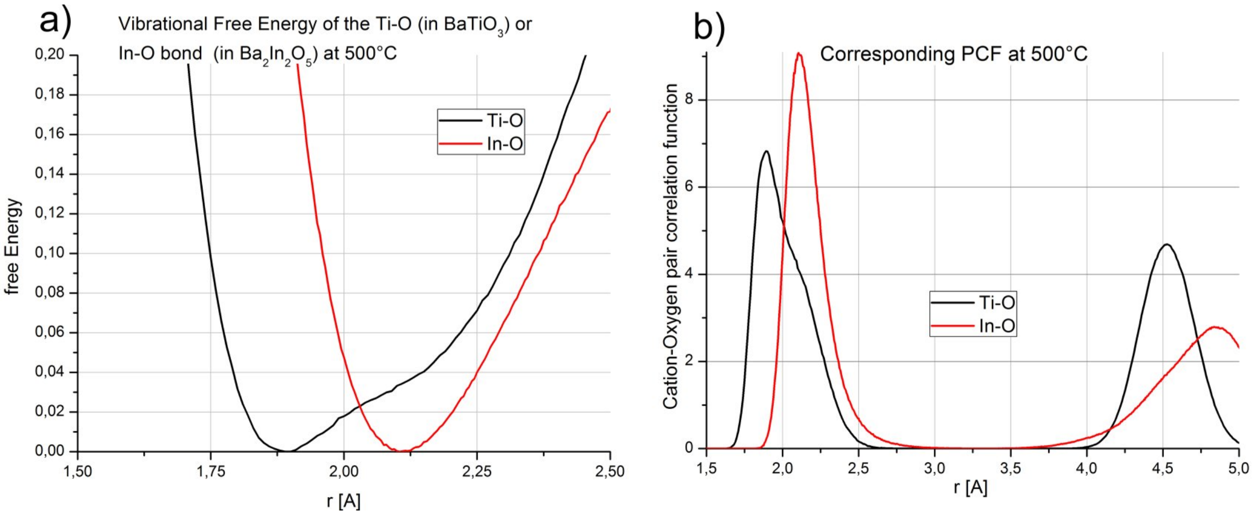

Figure 3.4: a) Free energy profile at 500°C of the pair potential of the B-site cation and their next nearest oxygen for $Ba_2In_2O_5$ and $BaTiO_3$ obtained by equation (3.3)) from the corresponding pair correlation functions presented in b) (all other PCF couples Ba-O, O-O, Ba-In and Ba-Ti show an essentially parabolic free-energy profile)

Figure 3.4 a) shows the In-O or Ti-O vibrational potential as it can be obtained via the equation

$$E(r) = -k_B T \cdot \ln\left(\frac{g(r)}{g(0)}\right) \tag{3.3}$$

from the ratio of the corresponding pair-correlation function $g(r)$ and its value $g(0)$ at the equilibrium distance (the maximum of the PCF). This expression represents the free energy profile with respect to the pair distance cation-oxygen. Figure 3.4 b) shows the actual PCFs. A remarkably different behaviour can be observed for these two reference materials at this low temperature of 500°C. Although by virtue of its structure barium-indate consists of two distinct oxygen environments for indium, even the total In-O PCF (i.e. averaging over the two In-environments) is much more regular (i.e. parabolic) than in for the barium-titanate which is characterized by a pronounced asymmetry in the overall Ti-O potential, albeit being only in one chemical environment inside the oxygen octahedra. More precisely the MD-runs strictly simulate the cubic phase of $BaTiO_3$ and what can easily be seen by optical inspection is that at this temperature, the 32 cation cell shows a distinct dynamical disorder with respect to the Ti-positions relative to their oxygen octahedra. Titanium switches positions within these octahedra on a ps-scale being located temporarily significantly nearer to 2 to 4 oxygen ions whereas the remaining oxygens are about 0.3 Å further away. This is represented by the shoulder in the Ti-O PCF. All the remaining PCF-couplings like Ba-O or O-O are not shown as all of them they show a comparatively regular form of their vibrational potential.

The comparison between the In- and Ti-based reference materials (which do not have any structural degree of freedom at the considered temperature) may serve to characterize the relation of the specific heat coefficient (more precisely its deviation from ideal harmonic behaviour) with the vibrational potentials. For $Ba_2In_2O_5$ the low temperature specific heat is calculated from the averaged internal energies. The value is situated at about 3 k_B per particle with a slight decreasing tendency for decreasing temperatures (see figure 3.2 a). The equivalent value for $BaTiO_3$ obtained from runs at 500°C, 800°C and 1500°C yield a very linear evolution of the internal energy giving 2.87 k_B (graph not shown). Thus it can be stated, that the significantly more anharmonic vibrational potential of the Ti-O couple in $BaTiO_3$ has a detrimental effect onto the specific heat. In contrast, for $Ba_2In_2O_5$ a value very close to what is expected of about 3 k_B is observed, coinciding with a very parabolic vibrational free energy profile. Therefore the conclusion can be drawn that the VASP-based molecular dynamics routine including the Nosé thermostat behaves more or less correctly with respect to the specific heat coefficient for approximately harmonic potentials.

It is important to re-state, that for $Ba_2In_2O_5$ the high temperature behaviour (i.e. the pronounced increase in c_v) is linked to the contribution of the structural degrees of freedom (the redistribution of oxygen vacancies) which are not yet activated at 500°C.

3.3 The disordered state obtained by cation substitution

This section deals with the local coordination structures of the completely dehydrated compounds whose most specific characteristics is their high content of structural oxygen voids. When taking the perovskite structure as a frame of reference one can speak of oxygen vacancies which are present due to the stoichiometry requirement combined with the fact to have an overall perovskite structure maintained. The chemical formula read $Ba_2In_{2(1-x)}(Ti/Zr)_{2x}O_{5+x}$ for the aliovalent substituents and $Ba_2In_{2(1-x)}Y_{2x}O_5$ for the iso-valent Y^{III}, respectively[2]. x is the degree of substitution ranging from 0 ($Ba_2In_2O_5$ reference material) to 1 ($BaTiO_3$).

When one is interested in the local structures of those compounds the obvious question is how ordered those oxygen voids will be. As presented in the previous section the unsubstituted BaInO-compound arranges the oxygen ions in a manner to give rise to a very ordered, layered structure of two different coordination polyhedra (octahedron and tetrahedron) for the same B-site cation In^{III}. Now the doping/substitution with considerable amounts of an aliovalent (Ti and Zr) or isovalent (Y) cation of course supposed to have an impact on this order.

In general there are several approaches to properly describe this kind of disordered state. As stated in the introduction (section 3.1) the two B-site cations are considered to be randomly distributed. Moreover, based only on chemical intuition it is safe to assume, that different cations show more or less pronounced coordination preferences for typical coordination polyhedra such as tetrahedra, pyramids and octahedra. This immediately leads to the obvious question what those preferences look like for the cations in question (In, Ti, Zr, Y) as well as to what extent they are realized depending on controllable parameters. In this work's framework following structural parameters were explored:

- The degree of substitution of the In^{III}-cation with Ti^{IV} from 6.25 up to 75%.
- The type of substituent in BaInO (Ti, Zr, Y) at the level of 25%.
- The influence of the overall lattice constant, which is realized by comparing BIT25 to SIT25 also containing a 75/25 In/Ti mixture but with Sr^{II} completely replacing the larger Ba^{II} on the A-site

---

[2] A shorthand notation which will be used throughout the thesis is BaInO for $Ba_2In_2O_5$ or three letters followed by the percentage of substitution: BIT50 being $Ba_2InTiO_{5.5}$ (50% Ti) or SIT25 for $Sr_2In_{1.5}Ti_{0.5}O_{5.25}$

An interesting method that imposes itself is the configurational averaging which was already introduced in the "Literature" section and the introduction of BaInO (section 3.2). The major disadvantage is the requirement to be in hold of the entire set of possible microscopical configurations of the considered system. To recall, Mohn and co-workers applied this to the 36-atom simulation cell of $Ba_2In_2O_5$ and ended up with around 100 inequivalent arrangements for the oxygen vacancies. Those crystallographically inequivalent configurations had beforehand to be identified out of the set of around 10000 permutations. Concerning the case of substituted Brownmillerites the feasibility of this method is more than questionable mainly just because of the size of the simulation cells used. A simple estimation of the permutations in a 184 atom cell, even without considering the symmetry braking by the cation-substitution places a number of $\approx 1 \cdot 10^{13}$ at the place of the 10000 permutations for BaInO mentioned before.

On the other hand side even only the exact treatment of MD-obtained concentrations, would demand a too a complex equation system. Basically it would have to the describe a delicately coupled multi-energy level system with the energy deltas being the energy differences between the coordination polyhedra. For example such a treatment could be based on rate equations describing the creation/annihilation of every type of polyhedron roughly of the form

$$\frac{dc_{Tet-In}}{dt} = k_1 \cdot c_{Tet-Ti} + k_2 \cdot c_{Pyr-In} + k_3 \cdot c_{Pyr-Ti} + k_4 \cdot c_{Oct-In} + k_5 \cdot c_{Oct-Ti} \tag{3.4}$$

with the set of the c's being the concentrations of the coordination polyhedra and k_i the kinetic factor for each process. This exemplifies that the creation or destruction of any given "species" (here an indium tetrahedron) inevitably may change the concentration of *any* other polyhedron (which means the k-factors can be positive or negative). Each of the six coordination polyhedra would be described by such a rate equation amounting to a total of 30 k-factors, which in turn contain the mutual energy deltas i.e. by how many eV a Ti-tetrahedron is different from all other species. To complicate things even further, these processes depend on details of the local configuration, which could hardly enter into this kind of "mean field" description. For example the balance concerning the creation of a say In-tetrahedron looks different depending on whether or not there are adjacent tetrahedra already present.

Given this complications in describing this kind of disorder in a rigorous manner we will resort to a simpler way of assessing the disordered character by a mere observation approach of the molecular dynamics results which will be presented in section 3.3.2.

3.3.1 Local structures: static DFT calculations

In a preliminary approach several compounds were tested by a number of static energy-calculations. Those are far from being exhaustive for what their permutations are concerned and shall only be regarded as tentative ”trial” configurations. The cation in question (Ti, Zr, Y) was deliberately put in different local oxygen arrangements which correspond to the three usual structural coordinations tetrahedron, square based pyramid and octahedron.

These trial structures are based on the Brownmillerite simulation cell containing 8 A-site cation, 8 B-site cations and 21 (Ti^{IV}, Zr^{IV}) or 20 (Y^{III}) oxygen ions, which accounts for the stoichiometry requirements of the different cations. They all represent a 75/25 cation substitution and contain six indium and two substituents ions. The simulation cells therefore were 4 times smaller than the cells used later on for the MD-simulations.

Figure 3.5 illustrates 4 out of this set of 11 cells that were tested.

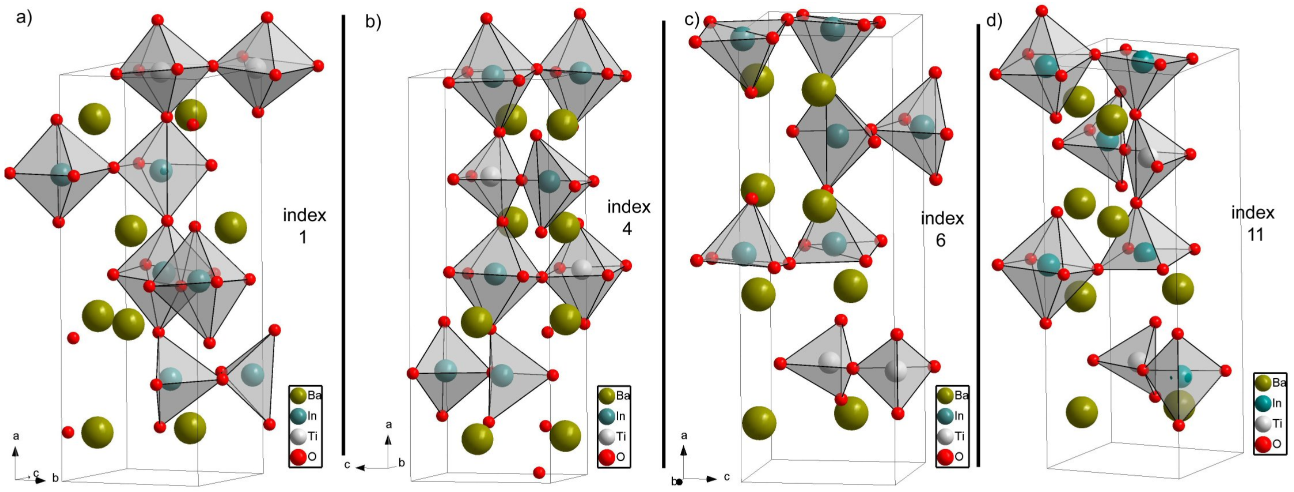

Figure 3.5: Four examples of the 37-ion trial cells with different local structures concerning the (interdependent) substituent (S) and indium-coordination. The indeces given in the four sub-figures correspond to the data points of figure 3.6. Left-to-right goes from unfavourable to favourable for Ti as substituent, whereas the sequence is reversed for both Zr and Y

The main aspect here is the considerable energy differences between certain coordination structures. For BIT (to a lesser extent for SIT) the most favourable configurations have Ti coordinated in tetrahedra or pyramids. On the other hand side, the complete opposite is true for both Zr and Y.

The rather small cell sizes severely constrain the disordered character of the compounds for they inevitably impose a very strict order onto the cationic lattice distributing two substituents on only eight B-sites. Moreover, there exist configurational situations, that are geometrically

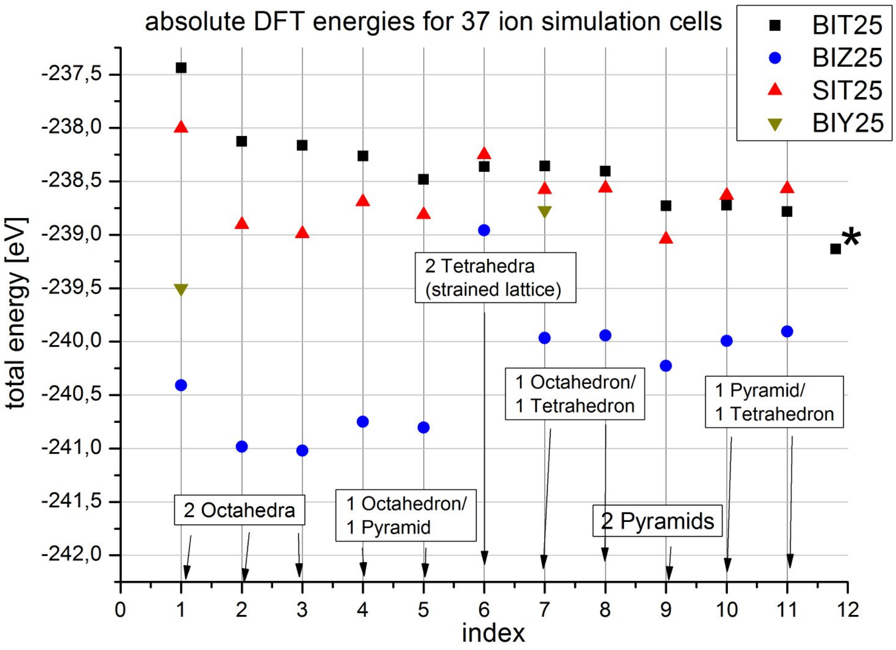

Figure 3.6: Absolute DFT obtained energies in the framework of structural trial calculations. The coordination of the substituent (Ti, Zr, Y) is given in the white boxes accompanying the graph. Only relative energy differences within one group (BIT, BIZ etc.) are meaningful. The index is sorted w.r.t. BIT towards more favourable configurations. The asterisk corresponds to the calculation of a 148 atoms structure as shown in fig. 3.7 below.

not possible to be constructed, e.g. having all substituting cations in a tetrahedral environment without placing them exclusively in one single layer (as it is the case for configuration index 6). This is why the just mentioned configuration 6 has a less favourable energy although nominally the Ti is entirely optimally coordinated.

Nevertheless a quick comparison of the total DFT-energies of a couple of relaxed structures gives access to the order of magnitude of the energy differences of those local coordination entities. The cases of BIT BIZ and BIY were investigated and cells with one oxygen position being different were compared. However it has to be noted that those statements (as they are summarized in table 3.I) is not exhaustive as the presence of either of the three Ti-coordination structures is not independent from further structural aspects. This is because the displacement of an oxygen ion in order to change a Ti-tetrahedron into a Ti-pyramid some other coordination polyhedron has changed as well.
An extension of these static studies enlarged the simulation cell by a factor of four having now (and for the rest of the thesis, notably the molecular dynamics studies) cells with an approximate dimension of 12·12·16 Å^3 containing 140 (dry BaInO) to 192 (hydrated BaInOH) atoms.

Table 3.I: Approximate local energy differences for BIT, BIZ and BIY compounds obtained by comparison of static DFT-calculations

Ti-Tetra	⇒	Ti-Pyra	⇒	Ti-Octa
	+0.35 eV		+0.3 eV	
Zr-Octa	⇒	Zr-Pyra	⇒	Zr-Tetra
	+0.3 eV		+0.7 eV	
Y-Octa	⇒	Y-Tetra		
	+0.5 eV			

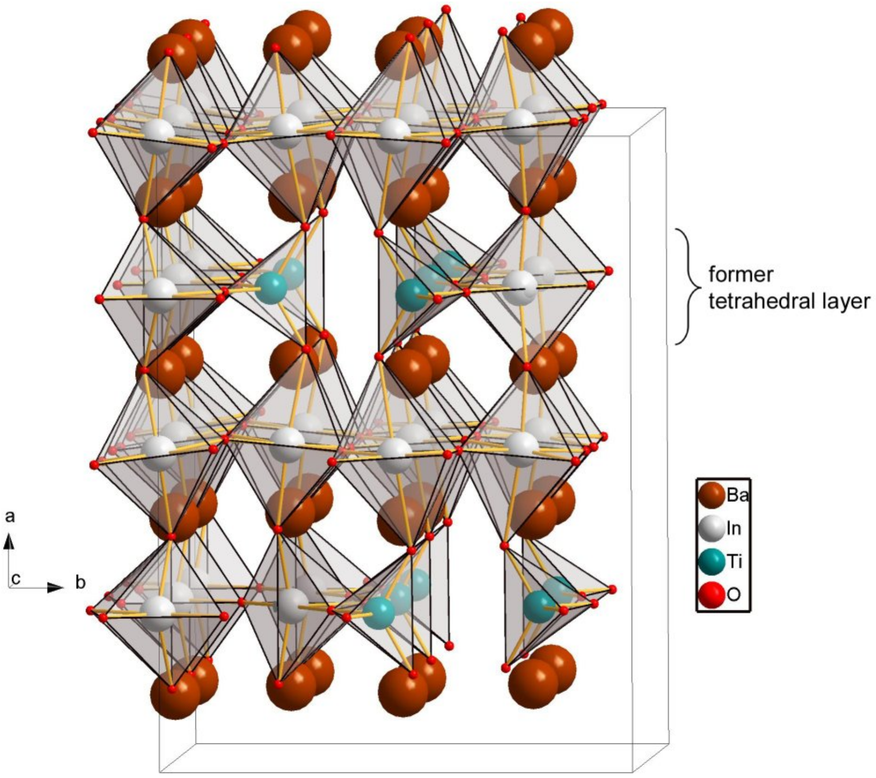

Figure 3.7: Simulation cell of an energetically very favourable crystallographic structure of BIT25 based on the Brownmillerite structure having all Ti-ions inside oxygen tetrahedra linked to In-pyramids within the former tetrahedral layers of the Brownmillerite structure.

A particular structure of BIT25, which is geometrically not possible to construct in a 37-atom cell but with a 184-atom one is presented in figure 3.7. Supposedly it may be regarded as (one of) the most stable *and ordered* configurations of this compound; its total energy (simply divided by four) is given as index 12 in the energy-overview of figure 3.6. To call this structure the "most stable one" is rather tentative for this structure simultaneously resembles a maximum the Brownmillerite structure and additionally accommodates Ti exclusively in very regular tetrahedra (identified as being energetically favourable). Those are located in the former tetrahedral Brownmillerite layer. Now this layer contains a very regular sequence of titanium tetrahedra but also indium pyramids due to the supplementary oxygen that is introduced by the Ti^{IV}. This illustrates the particularity of Ti^{IV} that despite it requires the integration of additional oxygen ions on stoichiometric grounds it just does not associates with them.

3.3.2 Local structures: molecular dynamics results

The following results concern the estimation of the local structures as obtained by molecular dynamics simulations. The approach pursued is to keep track of the number of all six coordination "species" that occur, which are tetrahedra, pyramids and octahedra for both of the two B-site cations. It might be remarked that during the molecular dynamics runs no other (e.g. square planar) coordination configuration could be observed. A simple counting algorithm was employed which at every timestep of the MD-trajectory evaluates all B-site-oxygen distances that exist in the simulation cell. The routine (based on the pair-correlation function routine) then simply counts the numbers of B-site cations that have four, five or six oxygen neighbours within a cutoff certain range. This cutoff range is chosen to be at a distance of the first minimum of the corresponding cation-oxygen PCF, i.e. considerably above the average bond-length. This ensures, that only true tetrahedra and pyramids are counted and that no temporary large cation-oxygen distance is mistaken as a vacancy.

What will be given in the following is an account on the actually observed fractions of each of these polyhedra in order to obtain an idea, which one will be predominantly present at a given temperature. It has to be stressed, that in the general case the initial structural configurations are "guessed". That means the distribution of the oxygen vacancies is often roughly performed according to the preliminary static calculations (i.e. Ti-tetrahedra, Zr-octahedra).

For an illustration of the time behaviour of the number figure 3.8 shows this aspect for the case of BIZ25 at three temperatures. This compound consists of 24 indium and 8 zirconium ions and it is the absolute number of each type of coordination polyhedron which is traced in the figure. Each depicted data point is an average over 400 fs which is the reason for fractional absolute numbers. The three temperatures show some basic characteristics concerning the equilibration behaviour. 800°C is the lowest temperature considered for the study of the dry compounds. As is clearly visible the kinetics w.r.t the oxygen redistribution is still very

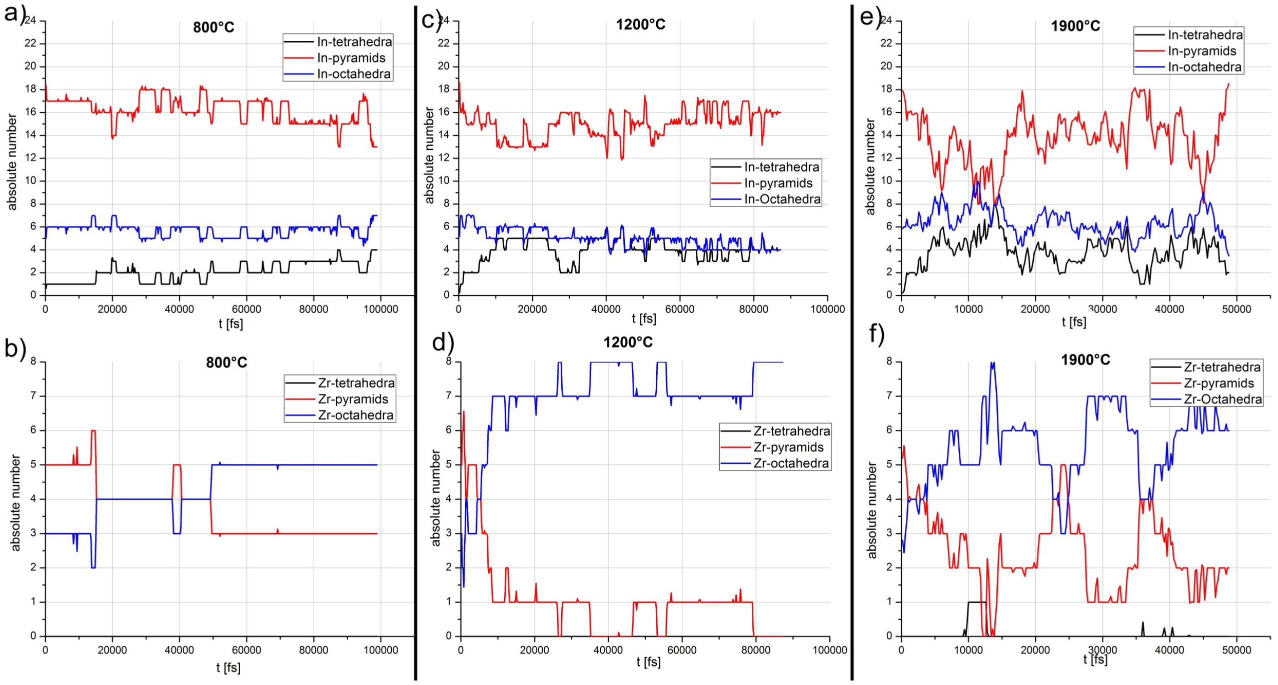

Figure 3.8: Time evolution of the counted absolute number of the six different coordination polyhedra in BIZ25 at three temperatures (800°C, 1200°C and 1900°C) observed by MD-simulations of 184 atoms system (including 24 In^{III} and 8 Zr^{IV}). a),c),e) are for the In-polyhedra, b),d),f) describe the Zr-polyhedra

hindered (as will also be noticeable for the diffusivity in section 3.6). In this particular case we see only a couple of actual changes of coordination which are characterized by a gradual change from three to five Zr-octahedra for example (subfigure b)). This behaviour hints to the fact that the structural equilibration concerning the oxygen-vacancies will not be very trustworthy at this temperature.

The behaviour at the intermediate temperature 1200°C is significantly more convincing for what the equilibration is concerned. Here within 30 ps we see a complete and reasonable equilibration towards zero Zr-tetrahedra, less than one Zr-pyramid and the seven to eight Zr-octahedra, reflecting immediately the major energetical preference of Zr for the octahedral coordination. Still at 1200°C, by consequence almost every vacancy is located not only next to In-polyhedra but exclusively between *two* of them. One missing oxygen (one vacancy) between two different cations would give rise to two pyramids, i.e. one In and one Zr one.

At 1900°C the kinetics is even less of a problem whereas however the fluctuation in structural properties become more and more pronounced. However concerning the real error of this kind of property a similar argument as for the pure recorded internal energies holds. This aspect was introduced in "Methods" section 2.5. The real error therefore is of the form $\Delta A \propto \frac{s}{\sqrt{N}}$

with A being the observed property, s the simple measurable standard deviation of it and N the number of *uncorrelated* data points. So when comparing 1200°C and 1900°C we can notice considerable increase in s, however two data points separated by a given time-lag will be less correlated at high temperature than at low temperatures. This latter affirmation will thus lead to an increase in N and might (over?)-compensate the increase in s.

Figure 3.9 and 3.10 gives the averaged numbercounts of the tetra/pyra/octa-fractions for all compounds investigated as a function of temperature. The fractions are given with respect to the number of the considered B-site cation: a fraction of 0.4 pyramids for In meaning that 40% of the indium ions are 5-fold coordinated.

For all compounds the indicated total vacancy content c(v) has to be taken into account. They are indicated for each composition as vacancies per B-site cation therefore ranging from 16/32=0.5 for BaInO down to 4/32=0.125 for BIT75.

The maximum number of tetrahedra and pyramids has to be seen within the limits of available oxygen vacancies. So with increasing Ti^{IV} or Zr^{IV} content this maximum number obviously decreases.

The values for T=800°C are given for the sake of completeness, despite their limited trustworthiness as mentioned before. Indeed as can be seen at many instances the polyhedron fraction at 800°C is deviating from what for all the higher temperatures can be called a regular behaviour (i.e. a decrease or increase with temperature). Examples are BIT50 or BIZ25. The following paragraph will give a more detailed account on the observations that can be made.

Two main aspects are important for the evaluation of these results: the overall level of any polyhedron fraction and its temperature evolution:

The overall level of the fraction of any coordination structure is already a first indicator of any preference. Within generalized reasoning however it cannot necessarily be related to a energetic preference because (as always) it is a free energy difference which gives rise to differences in observable concentrations of species. Let for example two polyhedra (i.e. energy levels) have a ΔE of exactly zero, then by virtue of an entropy difference (i.e. one type of polyhedron has more possible permutations than the other) we would nevertheless observe different concentrations.

In case entropy differences were small the temperature evolution of a concentration directly reflects the energetic aspects. When for increasing temperature a rising number of polyhedron

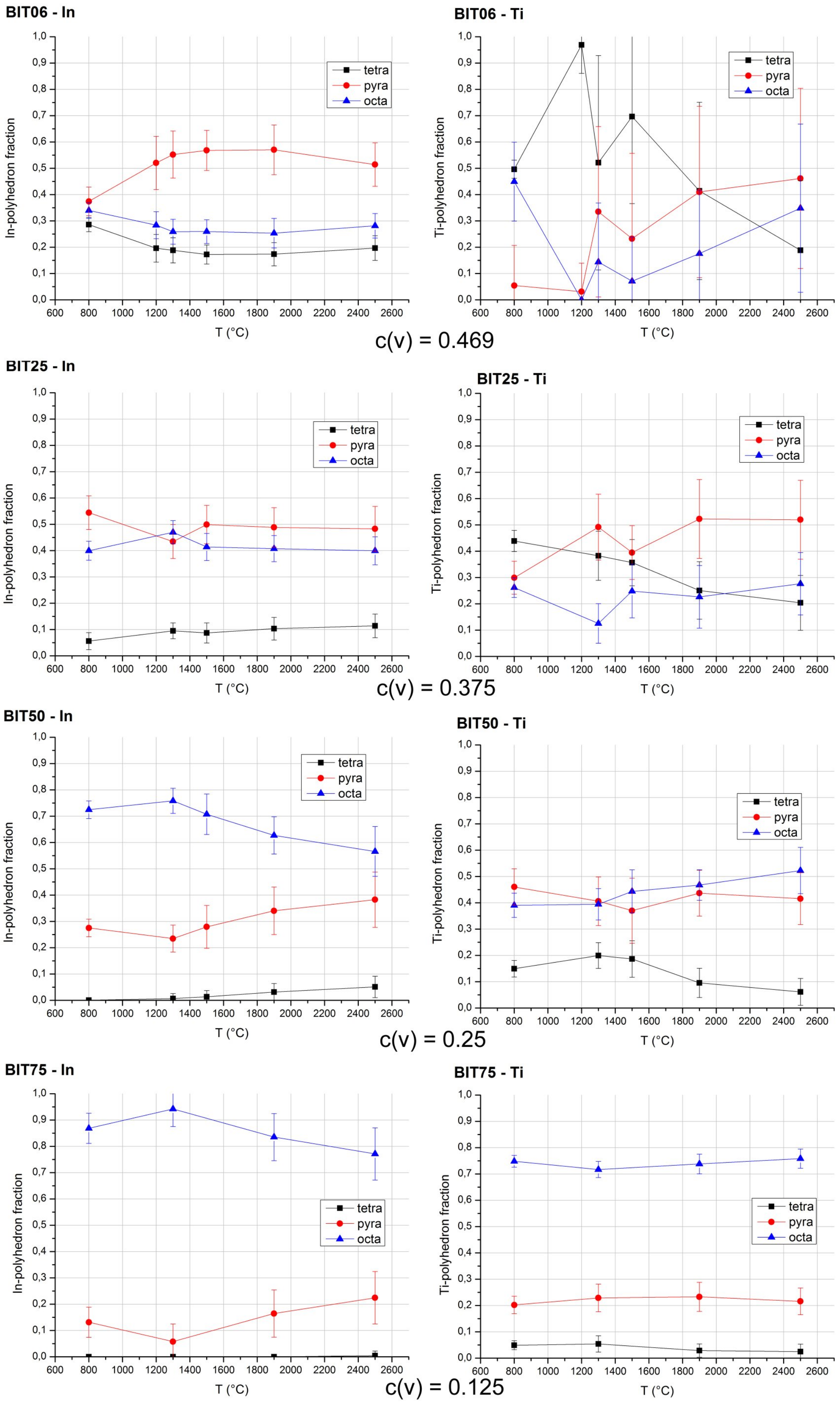

Figure 3.9: Averaged fractions of the three dominant coordination polyhedra for BITx (6.25, 25, 50 and 75%) compounds. Left coloumn: In-polyhedra, right coloumn: Ti-polyhedra. The c(v) value given is the total vacancy concentration per general B-site cation.

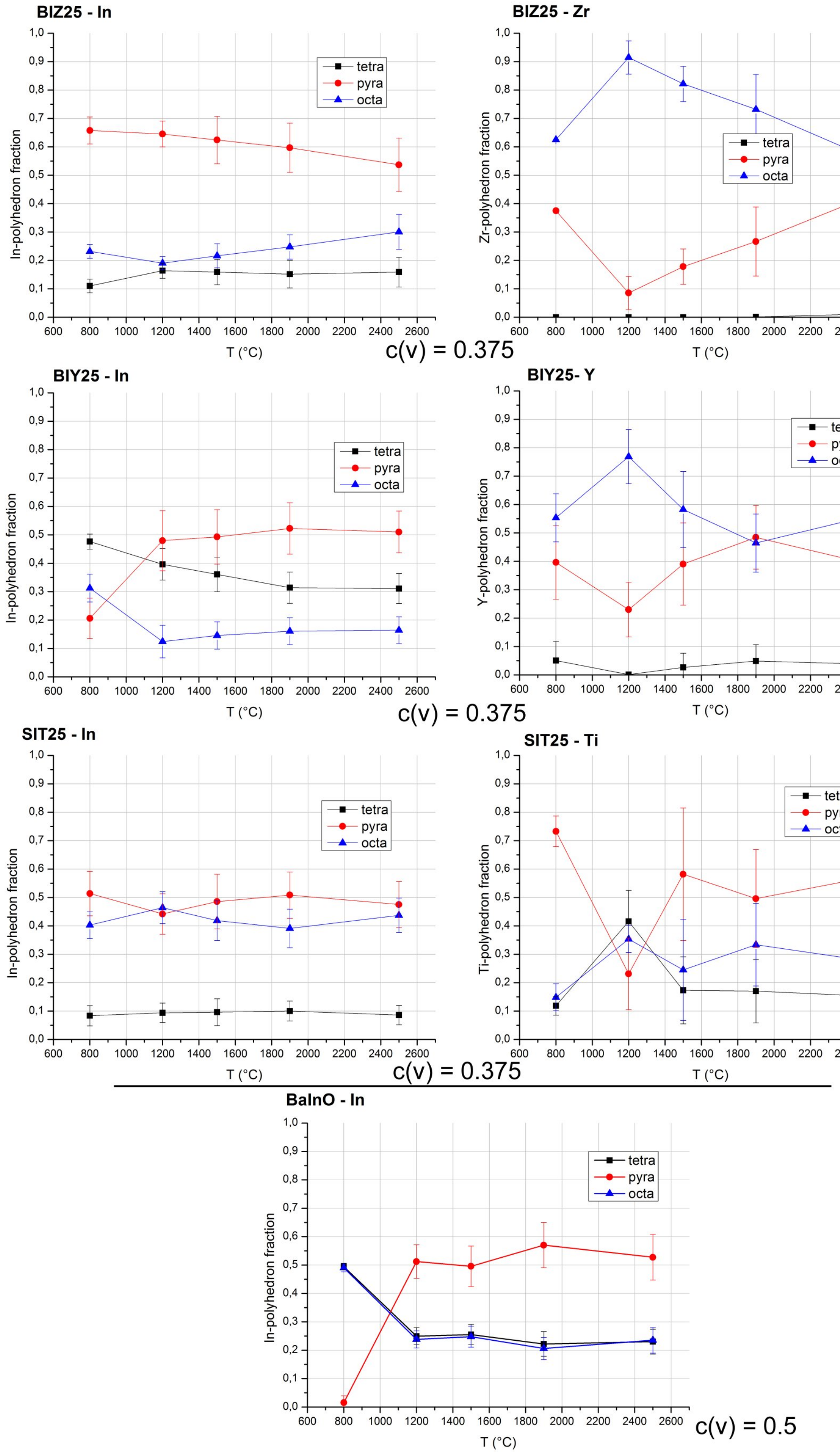

Figure 3.10: Fractions of coordination polyhedra for 25% substituted compounds (SIT25, BIZ25, BIY25), In-polyhedra to the left, substituent's polyhedra to the right. In-coordination polyhedra for BaInO are given at the bottom for comparison. The c(v) value given is the total vacancy concentration per general B-site cation.

type A and a decreasing number of polyhedron type B can be observed this translates into a more favourable energy for type B which is nothing but the acting of a Boltzmann statistics.

In the normalization chosen here (polyhedron of type x per cation type y) an identical value for Indium and the substituent at a given temperature would therefore mean that there is no *free energy* difference between those two. Free energy in this case includes both vibrational and configurational entropy as this is what is sampled during the MD-simulation. Here we encounter a serious drawback of the MD-treatment which because of kinetic reasons has to be conducted at somewhat unphysically high temperatures of T>1200°C. We are very likely confronted with a range polyhedra fractions which is not actually the one that can be expected in equilibrium at ”normal” temperatures. Therefore we are more going to be interested in the temperature *evolution* for the temperatures investigated. The following listing summarizes some key tendencies and results which are going to be presented and discussed:

Ti-tetra always favoured over In-tetrahedra in BITx

This fact can be observed by comparing any value for the tetrahedra fraction of Ti and In in figure 3.9. At no instant (composition and temperature-wise) do In-tetrahedra outnumber Ti-tetrahedra. Due to the decreasing oxygen-vacancy content with increasing Ti-content and the increasing Ti-content itself the value of the Ti-tetrahedra *fraction* of course drops from (very tentatively) 50-100% for BIT06 to 5 to 20% for BIT75. This is interesting noting that the initial reference structure of BaInO is composed of 50% In-tetrahedra and 50% In-octahedra.

Ti-tetrahedra are not systematically more frequent than Ti-pyramids

This is a manifestation of the issues mentioned above concerning the very high temperatures and the entropies. In the section on the static trial configuration (table 3.I) an approximate energy difference of 0.3 eV was given between Ti-tetrahedra and Ti-pyramids. Thus despite this fact, the MD-runs show how at high temperatures this energy delta does not lead to a very pronounced preference. Especially for the important cases of BIT25 and BIT50 (as well as BIT75) higher pyramid-fractions than tetrahedra-fractions can be observed.

6.25% Ti are sufficient to destabilize BaInO at 800°C

This result concerns the direct comparison between the pure BaInO compound with its 6.25% Ti-substituted counterpart. The interesting aspect here is that the Ti although only rather diluted (2 Ti to 30 In) has an significant effect onto the behaviour of the In. As an exception this observation is based on the simulations at 800°C. This shall be considered safe for this case as we are not interested in quantitive thermodynamically equilibrated fractions but in a qualitative impact. The key observation is the pronounced stability of BaInO at 800°C in terms of keeping its 50/50 distribution of tetrahedra and octahedra with the exception of occasional tetrahedra rotations (which give rise to the temporary transformation of octahedra to pyramids; an issue already discussed in section 3.2). As the obsveration shows the 2 Ti cations are capable of perturbing the Brownmillerite structure sufficiently that already at 800°C there is an equilibrium fraction of about 40% indium pyramids.

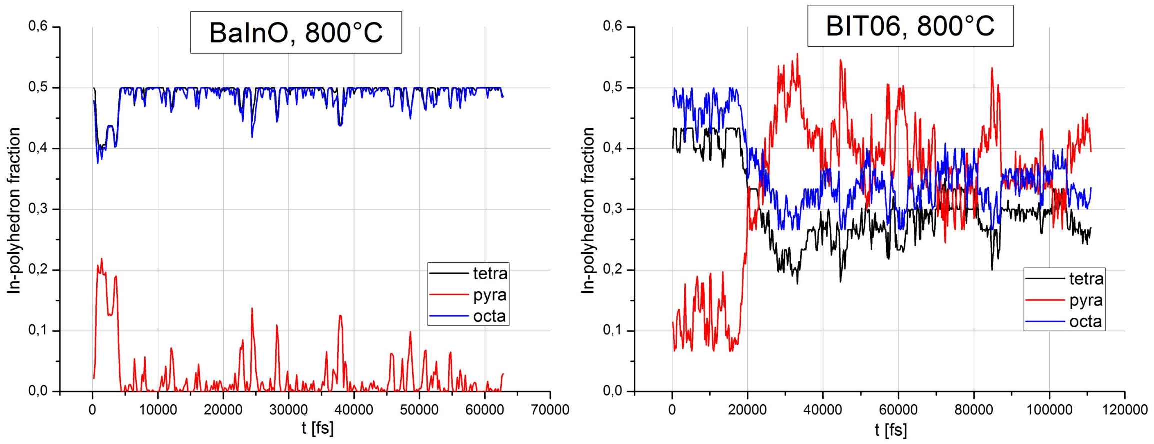

Figure 3.11: Comparison of the In-polyhedron fractions over time for BaInO (left) and BIT06 (6.25% Ti) (right) at 800°C.

This is illustrated more in detail in figure 3.11 where the time evolutions of the In-polyhedra fractions are shown. It has to be noted that one of the two Ti-cations was put into the octahedral layer, the other one into the tetrahedral layer of the "almost perfect" Brownmillerite structure; the (one) supplementary stoichiometry-required oxygen ion, too.

For what the Ti cations themselves are concerned in BIT06, the statistics of those merely two Ti ions is not sufficient to conclude quantitatively for 800°C. Indeed the Ti-cation in the tetrahedral layer remains that way throughout the run, whereas the Ti located in the octahedral layer switches between octahedron and pyramid. To summarize this simulation shows directly the well established fact of how substituents "stabilize" disordered phases at lower temperatures which is not less than the main objective of substitution in general; the concept that was outlined in the general presentation of the Brownmillerite structures section 1.1 in figure 1.2.

In BITx the octahedron is the most stable configuration for indium

Comparing BIT25, BIT50 and BIT75 for temperatures from 1200°C upwards we see a diminishing trend for the octahedra-fraction for all the compounds. At the same time either one or two of the vacancy-related coordination fractions rise. As stated before a decrease of concentration with temperature is a very strong indication of a favourable energy level of the associated species.

Zr and Y as substituents behave inversely to Ti

The observations presented in the BIZ25 and BIY25 panels of figure 3.10 immediately make clear the complete reversal of coordination preference compared to Ti. Zr and Y have very high octahedra fractions throughout (which moreover decrease with temperature looking at the behaviour $T \geq 1200$°C). Their corresponding pyramid fractions increase with temperature and show however on a rather low level. Tetrahedra of Zr and Y are absent at all but the highest temperatures. The indium is forced to associate with the oxygen vacancies that exist in the systems. These very pronounced preferences of Zr and Y highlight the somewhat special behaviour of indium to easily adapt its coordination in a mixed compound depending on the preferences of the other cations present.

For the particular case of BIZ25 there exists a direct experimental X-ray absorption spectroscopy confirmation at room temperature. It comes from Giannici and co-workers [62] and is based on the comparison of pure $BaZrO_3$ and BIZ25. The Zr K-edge XANES region for those two turn out to be more or less identical which unambiguously allows to conclude on an octahedral coordination for Zr. They underpin this finding with theoretical calculations based on the multi-scattering approach FEFF which match the experimental spectrum when performed for an ideal octahedral environment for Zr. (A XANES confirmation for the Ti-case will be presented in the following section).

25% Yttrium have an equal/smaller effect on BaInO destabilization than 6.25% Ti

Concerning this aspect we revisit the aspect of how substituents perturb the Brownmillerite structure. Naturally Y^{III} is an interesting candidate as its isovalency to In^{III} requires no additional oxygen and therefore would potentially enable a mixed-B-site-cation Brownmillerite. However an assumed *random* distribution on the B-site lattice of BaInO in addition to a strong preference of Y for the octahedral coordination necessarily destabilize the Brownmillerite structure.

An in-depth study of this aspect was not performed within the scope of this work. However it can be stated that experimentally (X-ray diffraction) the 25% Y substitution argueably does not lead to an overall cubic structure as in the case of Ti and Zr, but only to a tetragonal one [1]. What can be concluded by comparison of the BIT06 and BIY25 panels in figures 3.9 and 3.10 is that the impact on the In-polyhedra distribution of merely 6.25% Ti does seem to be *stronger* (or at least comparable to) than that of 25% Y. The main sign of this affirmation is the MD-simulation at 800°C which shows a bigger overall stability for a Brownmillerite structure for BIY25 than for BIT06, but in any case than for BIT25. The fraction of In-pyramids (as a measure for Brownmillerite instability) in BIY25 is observed to remain smaller (fraction 0.2) than for BIT06 (fraction 0.4).

3.3.3 The XANES experiment to confirm the predictions for BITx

The X-ray absorptions spectroscopy (XAS) experiment was carried out in order to experimentally confirm (or falsify) the somewhat unusual tetrahedral coordination preference of Ti^{IV} in the BITx compounds evidenced by the DFT-based calculations. To this end it was decided to perform measurements of the near-edge region (giving the acronym XANES for X-ray absorption near edge spectroscopy). This mode of experiment is often used more in a fingerprint-like fashion what will be done here, too.

The titanium K-edge was probed for a couple of BITx dehydrated compounds (6.25, 12.5, 25 and 50%) as well as three reference compounds $BaTiO_3$, $PbTiO_3$ and Ba_2TiO_4. Those latter three were chosen to represent Ti^{IV} in differently disturbed octahedral environments or a tetrahedral environment (for Ba_2TiO_4). $BaTiO_3$ serves as moderately distorted reference which in its room temperature tetragonal structure modification has Ti-O bond lengths of 1×1.83, 4×2.00 and 1×2.2 Åwhereas $PbTiO_3$ has 1×1.63, 4×1.98 and 1×2.50 Å which makes the Ti-ion be bonded much stronger to 5 out of its 6 coordination oxygen ions. Ba_2TiO_4 is experimentally found to exhibit a not perovskite related orthorhombic (spacegroup: P 2_1 n b - no. 33) or monoclinic structure (spacegroup: P 2_1/n - no. 14) ([63] or [64], respectively). The differences between those two crystallographic interpretations of diffraction data concern only details and

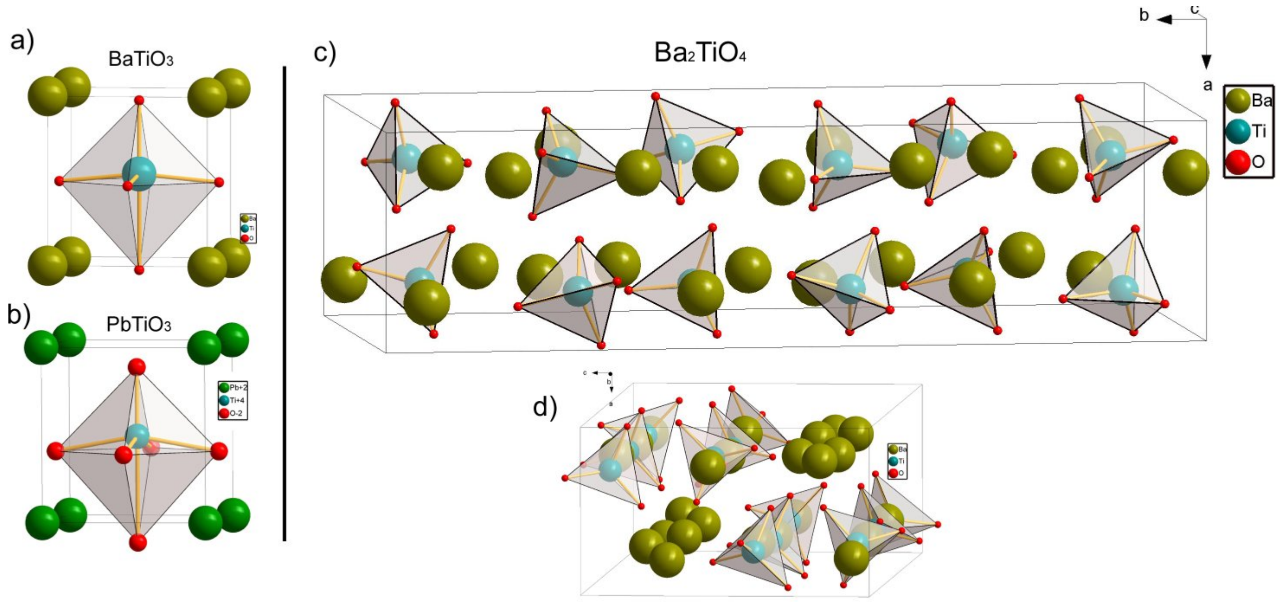

Figure 3.12: crystal structures of the three reference compounds: a) $BaTiO_3$, b) $PbTiO_3$ and especially Ba_2TiO_4 (c) side view and d) top view of the orthorhombic cell, SG 33).

especially do have no influence on the local Ti-structure. All Ti ions are inside regular tetrahedra with a Ti-O bond length from 1.80 to 1.83 Å according to XRD data in [63].

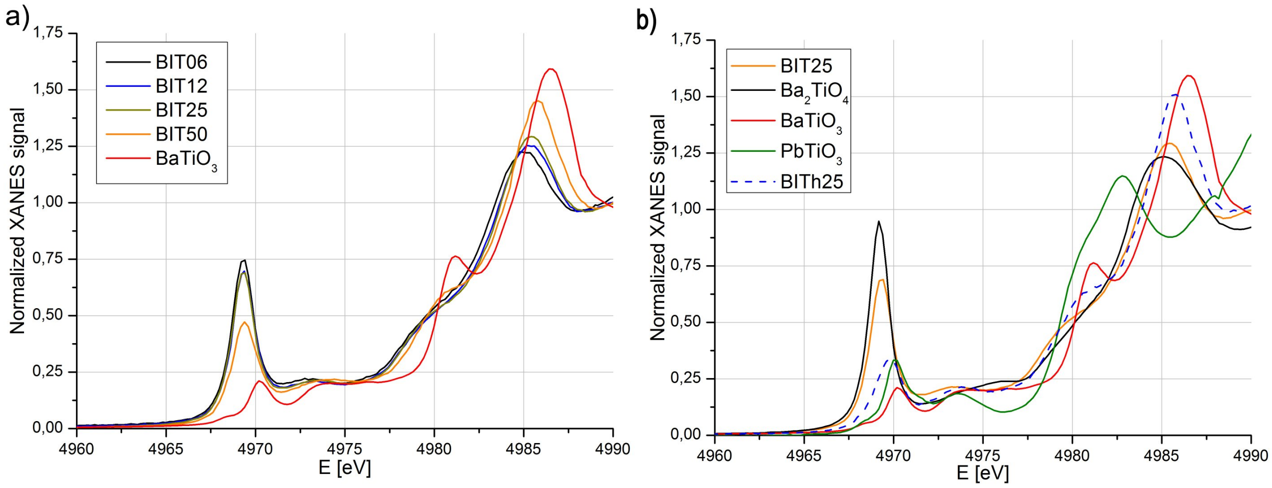

Figure 3.13: a) XANES spectrum of the Ti K-edge in several BITx compounds (6.25, 12.5, 25 and 50% b) the BIT25 compound compared to the references $BaTiO_3$, $PbTiO_3$ and Ba_2TiO_4; the fully hydrated BITh25 is given for later reference

The XANES experiments were carried out at the SAMBA beamline of the SOLEIL synchrotron facility at Gif-sur-Yvette near Paris. For studying the dehydrated samples all measurements were carried out at room temperature in fluorescence mode mostly in order to be coherent with later in situ measurements which were made inside a heatable sample recipient which (due to its window geometry) does not allow for the transmission mode. All spectra were recorded three times to improve the statistical weight with a measuring duration of ≈20 minutes each. The data treatment consisted of standard routines for normalization, fluorescence correction and self-absorption correction using the *ATHENA* software package [65].

The major outcome of this experiment is summarized in figure 3.13 where in a) the near edge regions of BITx are shown for 6.25%, 12.5%, 25%, 50% (and 100%) and in b) BIT25 is compared to all three references that were introduced above. Already at this stage, the calculated prediction of the Ti-tetrahedral preference is confirmed by simple comparison of the general character of the 6.25, 12.5 and 25% BITx compounds. Both their pre-peak features (height and position) as well as the entire remaining absorption edge resembles the Ba_2TiO_4 compound to a very large extent. This therefore can be considered the direct experimental confirmation of what the calculations predicted. Naturally the BIT50 composition cannot resemble the lower Ti-concentration samples as the supplementary oxygen ions reduce the maximum possible number of tetrahedra and impose the presence of more 6-fold coordinated Ti (with the extreme case of $BaTiO_3$ of course).

The most pronounced feature of the spectra are the differing intensities of the so called pre-peak at approximately 4969 eV which has a considerable information content for the description of Ti-containing oxide compounds [66, 67]. The key feature is that its intensity is directly linked to the deviation from the local centro-symmetry the titanium is located in. By crystal field symmetry considerations the mixing of the 4p-orbitals (Ti) with the 3d-orbitals (Ti) is suppressed in an ideal octahedral symmetry. By consequence the transition 1s(Ti)→ 4p(Ti) will have no intensity into the ”Ti-3d” band. This latter transition is responsible for the pre-edge intensity in an distorted/non-centrosymmetric environment. Therefore the more centro-symmetrical the Ti cation is coordinated the less this pre-peak is present (w.r.t. its intensity) and the more it is shifted to higher energies.

For the vast majority of Ti-containing oxide compounds Ti^{IV} is located in either of the three configurations tetrahedron, square-based pyramid or octahedron as observed for the BIT compounds in sections 3.3.1 and 3.3.2. In a very broad comparative study Farges and co-workers [66] establish a clear cut relation between the integrated height and the absolute position of the pre-peak. For compounds with only one single Ti-coordination this relation can be visualized by the grey areas in figure 3.14 b) labeled IV, V and VI. Subfigure a) shows the detailed pre-peak region of the own XANES measurements this time accentuating the evolution with increasing Ti-content. The subfigure b) is taken from [66] and shows the evolution pre-peak height and

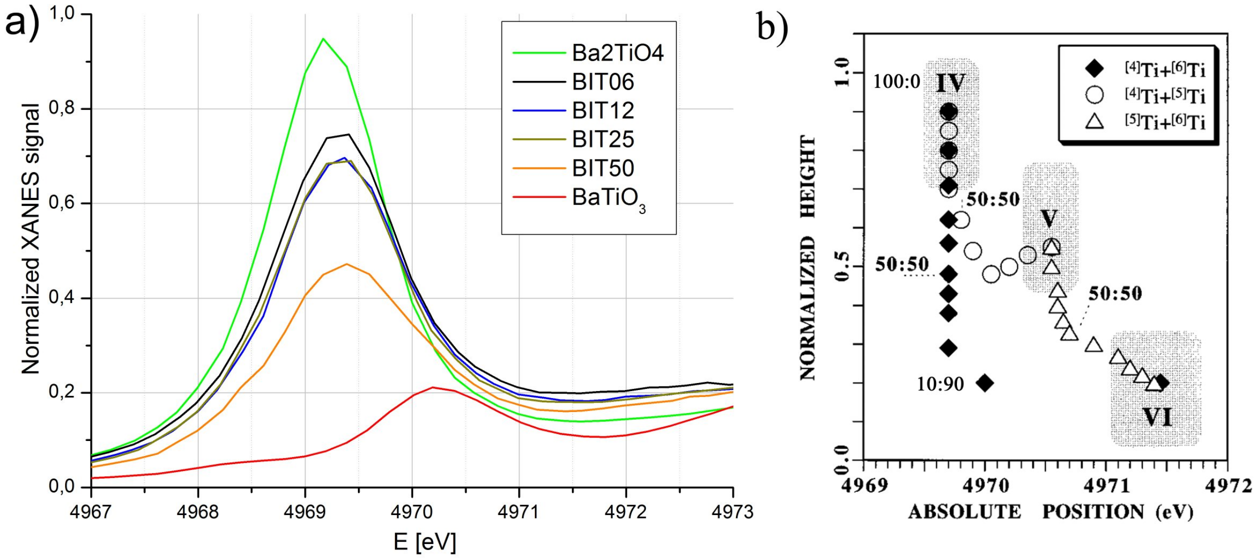

Figure 3.14: a) Detailed pre-peak region of the tetrahedral model compound Ba_2TiO_4, several BITx and $BaTiO_3$ showing the evolution of the pre-peak with Ti-content. b) Summary of an extensive mapping of mixtures of reference compounds having well identified 4- ,5- or 6-fold coordination showing the evolution of the pre-peak parameters position and intensity (taken from [66]).

position for binary compound mixtures having Ti in two different coordination states[3] (octahedral).

As it is obvious by comparing Ba_2TiO_4 and BITx (6, 12 and 25%) the latter ones contain a mixture of different polyhedra as the peak heights of BIT are significantly lower than for the reference compound. It is however safe to say that the vast majority of coordination polyhedra is tetrahedral (with a tentative even somewhat higher tetra-fraction for BIT06). Taking the results of FARGES as an aid, we can also conclude that the second coordination species in BIT (6, 12 and 25%) is more likely pyramidal than octahedral. This can be justified by noting the slight but notable shift to higher energies of the BIT compounds compared to Ba_2TiO_4. This is in agreement with the summary of figure b) which presents such a shift only in the case of a tetrahedral/pyramidal mixture.

Of course also a small amount of octahedra may still be present in the BITx (6, 12 and 25%) but due to the small intensity of a corresponding peak (comparable to $BaTiO_3$) they would not be observable.

To summarize, the XANES experiment on BIT could not only confirm the general tendency

---

[3] the binary mixtures are based on: $Ni_{2.6}Ti_{0.7}O_4$ (tetrahedral), $Ba_2TiGe_2O_8$ (pyramidal) and $CaTiSiO_5$

for the tetrahedral coordination of Ti^{IV} but also the very big likelihood for the presence of pyramids as the second most frequent polyhedron in complete agreement with the molecular dynamics based study presented in the previous section 3.3.2.

3.3.4 Discussion of the coordination preference

In order to rationalize the somewhat unusual behaviour of Ti with respect to its tetrahedral coordination preference it is fruitful to examine some ionic size matters a bit more in detail. First of all one could state that the total energy calculations performed by DFT stand as (experimentally confirmed) result of its own. Given the correctness of these results one can search for some solid state chemistry arguments that underpin these results.

By classic solid state chemistry arguments, ionic radius ratios predominantly determine the expected coordination of a cation. The corresponding ratio for Ti^{IV} in combination with O^{-II} is 0.428. So already with this simple geometrical and empirical argument Ti is situated rather close to the demarcation line between an expected octa- and tetrahedral coordination for which the critical radius ratio goes from 0.414 down to 0.225. However the background of these kind of estimation is important too. Whereas the ratio-limits between oxygen and cation radii are determined solely on geometric grounds (the packing of hard spheres) the tabulated ionic radii are taken from known substances which in their majority accommodate Ti^{IV} in an octahedral environment.

One very relevant substance that accommodates Ti^{IV} exclusively in very regular tetrahedra is $\mathrm{Ba_2TiO_4}$ which was already presented in the previous XANES section and used there as the tetrahedrally-coordinated reference compound. The experimental Ti-O bond lengths are considerably shorter than tabulated in the standard works of e.g. Shannon and Prewitt [68] which however are based mostly on 6-fold coordinated Ti. It is intriguing and noteworthy that the equivalent Sr-compound $\mathrm{Sr_2TiO_4}$ does crystallize in a Ruddlesden-Popper phase, which is actually the expected behaviour for the $\mathrm{A_2BO_4}$ stoichiometry within the classification of perovskite structures. Within the Ruddlesden-Popper phase, B-site cations remain inside regular octahedra as they are in the corresponding perovskites. Test calculations were made in order to compare the Ba- and Sr- based phases with respect to their total energies in the orthorhombic (tetragonally coordinating) phase and the Ruddlesden-Popper phase (VASP, PAW-PBE potentials, 600 eV cutoff, the same parameters as for all other static calculations). Not going into

Table 3.II: oxygen-oxygen distance range (in Å) for various coordination polyhedra in BIT25, BIZ25, BIY25, BISc50 obtained by static, fully relaxed DFT calculations

dist_{O-O}	Tetrahedron	Pyramid	Octahedron
Ti	3.00	2.7-2.8	2.75-2.9
Zr	3.2	2.9-3.1	2.95-3.05
Sc	3.2-3.5	-	3.05
Y	3.45-3.9	-	3.2-3.3
In	3.3-3.8	3.05-3.4	3.0-3.3

the details they yield an energetic advantage for the tetragonally coordinated phase for *both* substances. However (and in a good sense for the experimental evidence) the Sr-based phase only shows a difference of ≈0.03 eV per formula unit against the favour of the experimentally stable Ruddlesden-Popper phase. The (hypothetical) Ruddlesden-Popper phase of Ba_2TiO_4 is worse by 0.4 eV compared to the experimentally observed tetrahedral-coordinated phase. This hints to a decisive influence of the Ba ion.

The existence of Ba_2TiO_4 may in that sense already be considered an important argument for the plausibility of the Ti-behaviour in BIT. For what the BIT case is concerned it is possible to argue with the help of a simple ionic-bond relation: Given the small size (in relation to Ba, In, Zr, Y), and the high formal charge of 4+ and an incomplete valence shell (diminishing the shielding of the effective positive ionic charge) the ion can be considered very polarizing (which is a statement according to ”Fajan’s Rules” of classic solid state chemistry). These characteristics enable it to create rather short bonds with oxygen, which as a very polarizing counterion would empirically lead to a pronounced covalent character of this bond.

Thus on simple chemical grounds very short Ti-O bonds will be expected to be energetically preferable. With the help of DFT-calculations (those that were used to determine the simple tendencies concerning the local structures) Ti can be put into arbitrary configurations. By comparing fully relaxed local structures Ti octahedra were found to end up with the shortest O-O distances of all polyhedra investigated (with minimum values of about 2.75 Å). The corresponding values are reported in table 3.II. As can be seen O-O distances of Ti-tetrahedra are considerably longer which render this O-O repulsion aspect a very likely structural contribution to the tetrahedral preference of Ti in system where ”there is the choice”. Yet another favourable contribution to the overall balance is that any oxygen located at a tetrahedron has only three next-nearest oxygen neighbours on the same tetrahedron compared to four neighbours in the case of an octahedron.

To summarize, tetrahedra (and to a lesser extent also pyramids) enable the Ti-cation to establish favourably short Ti-O bonds of about 1.8 Å but minimize O-O repulsion by the geometrically relatively long O-O distances of a tetrahedron.

3.4 Bader-charge distribution

Bader charges are a useful measure to attribute physically meaningful charges to ions in a crystallographic structure. They were introduced in the "Methods" chapter in section 2.1.1. The method here shall serve as an aid to determining the extent of ionic bonding in a system, however a rigorous analysis on theoretical-chemical grounds is outside the scope of this work. In any case backed by an agreement with an electronegativity reasoning the Bader analysis can shed some light onto tendencies concerning the hydration energies.

In the following the dehydrated compounds are analyzed with respect to their Bader charge distribution.

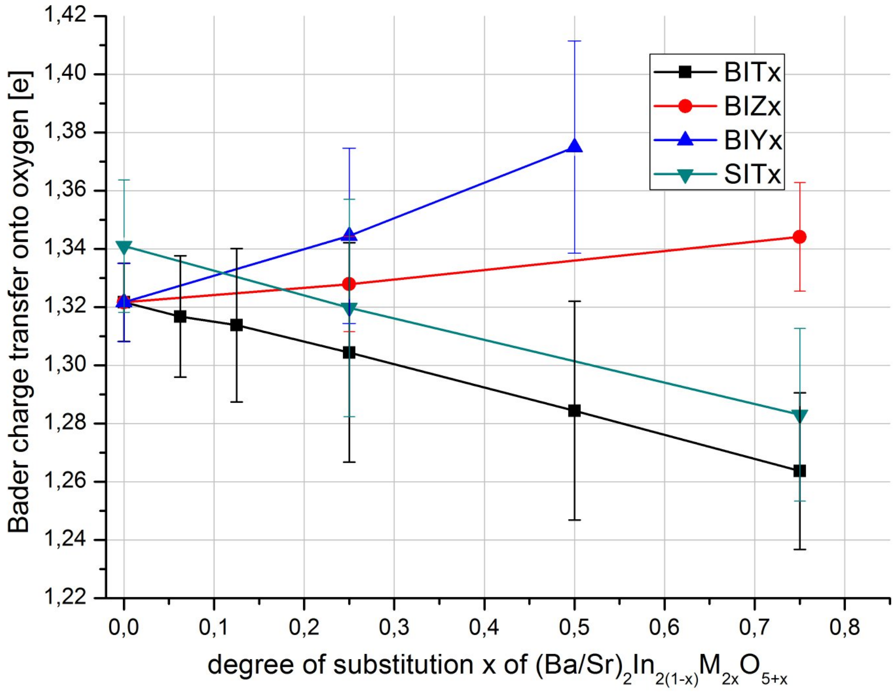

Figure 3.15: Average negative charge transfer onto all oxygen ions of different compounds as a function of their "degree of substitution". Uncertainties arise due to the averaging over relatively large numbers of simulation cells with a variety of local structures. Lines are guide to the eye.

Figure 3.15 assembles in a very summarizing manner the effective charge properties of all compounds that were investigated by static DFT calculations. The measure that was chosen to be presented is the number of additional elementary charges per oxygen ion, i.e. an effective degree of oxidation. That is the total value of ”Bader charge” minus the 6 valence electrons that are explicitly introduced in the system with every oxygen atom by the PAW pseudo-potential. The absolute maximum of this value would equal 2 corresponding to the degree of oxidation, given a correct chemical outcome of the DFT calculation. In the Bader framework this will almost never actually be the case as a complete, spatial charge transfer according to the formal charge is physically not the case. As an example, a DFT test calculation on NaCl (one prototypical ionic compound) shows a charge transfer of 0.87 electrons for a formal charge transfer of 1.00.

The averages were taken from a number of dehydrated structures which were generated by cooling and subsequent relaxation of some corresponding MD-runs at 500°C as well as reasonable ad hoc imposed structures (however assuring oxygen-vacancy distributions in general according to their preferences as described in section 3.3.1 and 3.3.2). As can be seen it turns out that the differences between different degrees of substitution or substituents are reasonably significant compared to the spread within the oxygen ions of one compound. This spread stems from the variation of all oxygen sites in any considered configuration (simulation cell) the like of which 5 to 20 different ones were used for generating figure 3.15. The evolution over the substituents content x in general is quite linearly in agreement with what would be expected.

Here we tentatively interpret the extent of average charge transfer onto the oxygen ions as a measure for the average degree ionic interaction in a compound. The higher the effective charge on the oxygens the more pronounced the ionic character of the chemical bonds is considered in the given compound.

According to basic chemical principles the ionicity of the chemical bonding in a compound can be described in terms of electronegativities. Even less than the effective physical charge on an ion, this property is not uniquely defined. The most widespread scale is the Pauling Scale dating back to 1932 which is based on differences in elementary dissociation energies. The Pauling values for the ions relevant here are given in table 3.III. As widely known however, the definition and properties of several EN-scales vary considerably. Most striking are cases where ”higher-as/lower-as” relations are reversed when different scales are consulted. This is indeed the case for the couple In/(Ti,Zr,Y,Sc) where for the widely used classic Pauling and Allen

Table 3.III: Pauling and Zhang electronegativities [69] for relevant ions

	O^{2-}	Ba^{II}	Sr^{II}	In^{III}	Ti^{IV}	Zr^{IV}	Y^{III}
Pauling scale	3.44	0.89	0.95	1.78	1.54	1.33	1.22
Zhang Scale	2.22	1.005	1.004	1.445	1.577	1.467	1.209

scales indium is ascribed a significantly higher EN-value than the other four (1.78 compared to $\approx$ 1.2-1.5). Alternative scales such as the Mulliken or Zhang scale [69] (as given in the table too) reverse the relation and attribute an electronegativity to indium now within the range of those four transition metals. Notably the In/Ti relation is now reversed with Ti^{IV} being the more electronegative ion.

Looking at the evolution of the oxygen charge transfer of figure 3.15 this now is in rough agreement with what is observed. A decreasing averaged charge transfer with increasing is in-line less ionic character of the Ti-rich compounds compared to the In-rich ones. Moreover it can be observed that the other two substituents (Zr and Y) both render the compounds more ionic with increasing amount of them. So based on this behaviour the following qualitative "ionicity"/electronegativity sequence for barium-based substituted Brownmillerite may be established: Y>Zr>In>Ti which very qualitatively is in agreement with the proposed Zhang scale except for the fact of Zr and In being almost identical in this scale. The comparison between SITx and BITx however shows another severe drawback concerning the usability of the Zhang scale, according to which the exchange of Ba and Sr in a compound would not alter the EN-properties much (comparing the corresponding values 1.005 and 1.004 in the table). However the application of simple EN-rules already for ternary compounds is more than speculative. A supplementary investigation of $Sr_2In_2O_5$ and $Ba_2In_2O_5$ shows that the larger charge transfer onto the oxygen for $Sr_2In_2O_5$ originates from Sr^{II} and In^{III} to equal parts.

Being interested in the properties of hydration of the compound the related concept of "basicity" is often employed to characterize one major contribution to the hydration energy. The concept states, that by tendency a higher effective charge density on a given oxygen ion will lead to a stronger potential O-H bond when protons are introduced into the structure. It can be concluded that the the Bader charge concept enables to have direct access to this very information and that it will prove useful in interpreting the hydration energy tendencies later on.

3.5 Vibrational properties

This section shall present the results that can be obtained concerning the vibrational properties of the dehydrated compounds both by normal mode analysis (NMA) and the Fourier transform of the velocity autocorrelation function (VAF). As technically introduced in section 2.2.4.3 the first approach is based on a static, fully relaxed configuration of the given compound whereas the second approach uses information of an entire MD-simulation run in order to extract a vibrational spectrum.

By definition this kind of vibrational information can be brought into contact with experimentally obtained IR or Raman spectra. However, for the calculation approach used in this work only the actual vibrational density of states is accessible. We obtain an information about ”how many” vibrational modes do occur within a given frequency range. In turn we do not calculate the corresponding IR-intensities, which are related to the actual *charge* displacement which is associated to each vibrational mode. Also all symmetry constraints which render certain modes IR/Raman active/inactive are not being considered.
Thus the merit of this analysis is the clarification of a couple of structural relations and nevertheless a quite matching confrontation to experimentally obtained IR-spectra for BIZx.

The two comparative main figures of this section present an overview over the vibrational aspects of all the dehydrated compounds investigated. Figure 3.16 compares the entire BITx compositional range from $Ba_2In_2O_5$ to $BaTiO_3$ whereas figure 3.17 shows several 25% substituted compounds (BIT25, BIY25, BIZ25 and SIT25) on the one hand side to track the influence of the degree of (Ti)-substitution and on the other hand side to elucidate qualitative differences between several subsituents.

The figures contain the ion-species resolved Fourier transforms of the VAF and histograms of all frequencies obtained by the normal mode analysis of representative static configurations of the compound.

The genuinely dynamical vibrational DOS are calculated from the VAFs of well equilibrated MD-runs at 800°C using only the last 25-40% of a given run in order to come as close as possible to the structural equilibrium. The DOS are given in a non-normalized manner, i.e. the (integrated) intensities do not depend on the fraction of the given cation in the structure. This is to ensure a good comparability of the qualitative vibrational features. In turn, when certain oxygen modes are directly related to one of the two B-site cations (e.g. the high frequency Ti-O modes), then their intensity will depend on the Ti-content. Especially for BIT06 (2 Ti for 30 In) this is observable.

As a general result one can state that the species resolved Fourier-transform VAF yields very reasonable frequency domains characteristic for the vibrating motions of each species. Described in a perovskite framework three major frequency regions can be expected and are evidenced by the spectra [70, 71]:

(I) A low frequency region around 100 cm^{-1} which is characterized by collective vibrations of the A-site cation against an entire B-site cation polyhedron. As can be seen this region is most distinctively separated by the others for the actual perovskite $BaTiO_3$ in 3.16 f). This is furthermore the only frequency region which is accessible for the A-site cations Ba^{II} and Sr^{II} that is why almost all their spectral intensity is concentrated there.

(II) An intermediate region between around 300 - 500 cm^{-1} that is mostly characterized by a broad mixture of mostly bending modes that very much depending on the structure involve (B-site)-O-(B-site) bending vibrations or O-O wagging modes. In any case given the disordered structure of the compounds of interest an unambiguous mode designation in that region is not fruitful.

(III) The highest frequency region which will in all cases contain (B-site cation)-O stretching modes which may be symmetric (in the spirit of an octahedral breathing mode, without the displacement of the cation) or asymmetric. The latter cases then involves the vibration of the B-site cation against only some (or even just one) of the oxygen ions that make up its coordination polyhedron.

It is this last region (III) which shows one of the more interesting evolutions with respect to the Ti substitution. Beginning with BaInO the highest frequency region are breathing mode like vibrations of the oxygen ions against the indium ions more or less regardless whether being coordinated tetrahedrally or octahedrally. The drastic change is observed for the BIT06, 6.25% Ti compound which is most interesting due to the Ti-vibrations (figure 3.16 b). Here two of the most important features of the Ti-substitution are mirrored in the Ti's vibrational DOS:

First, its pronounced iono-covalent character (as discussed in 3.4) which is reflected by a very short bond length and a high bond stiffness. This directly manifests itself in the rather high frequency region of between 700 and 800 cm^{-1}. The other key feature is its preference for

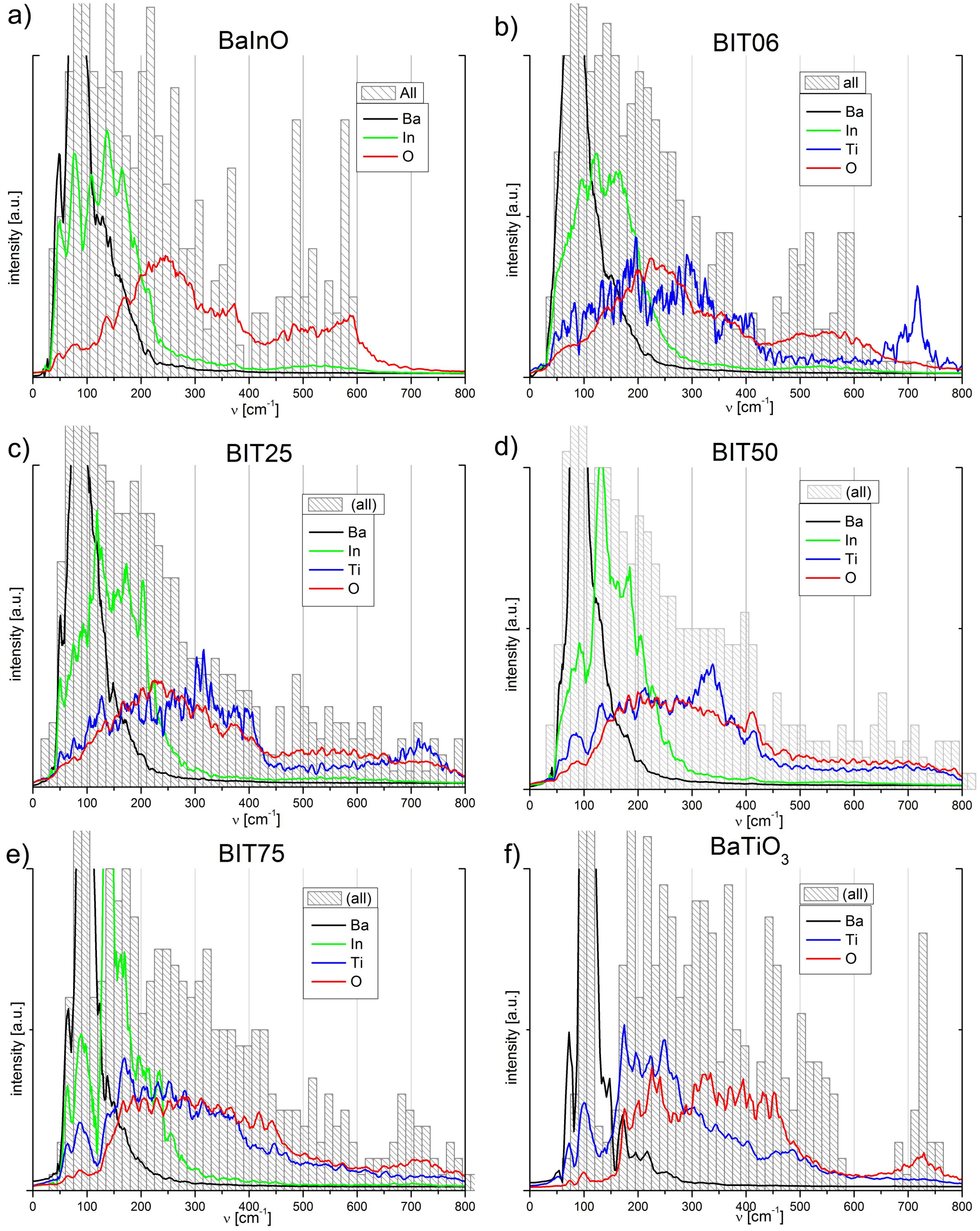

Figure 3.16: Overview over the vibrational DOS obtained for BITx (0≤x≤<1) by MD-simulations at 800°C as well as the NMA frequency histograms for all ions present in the simulation cell.

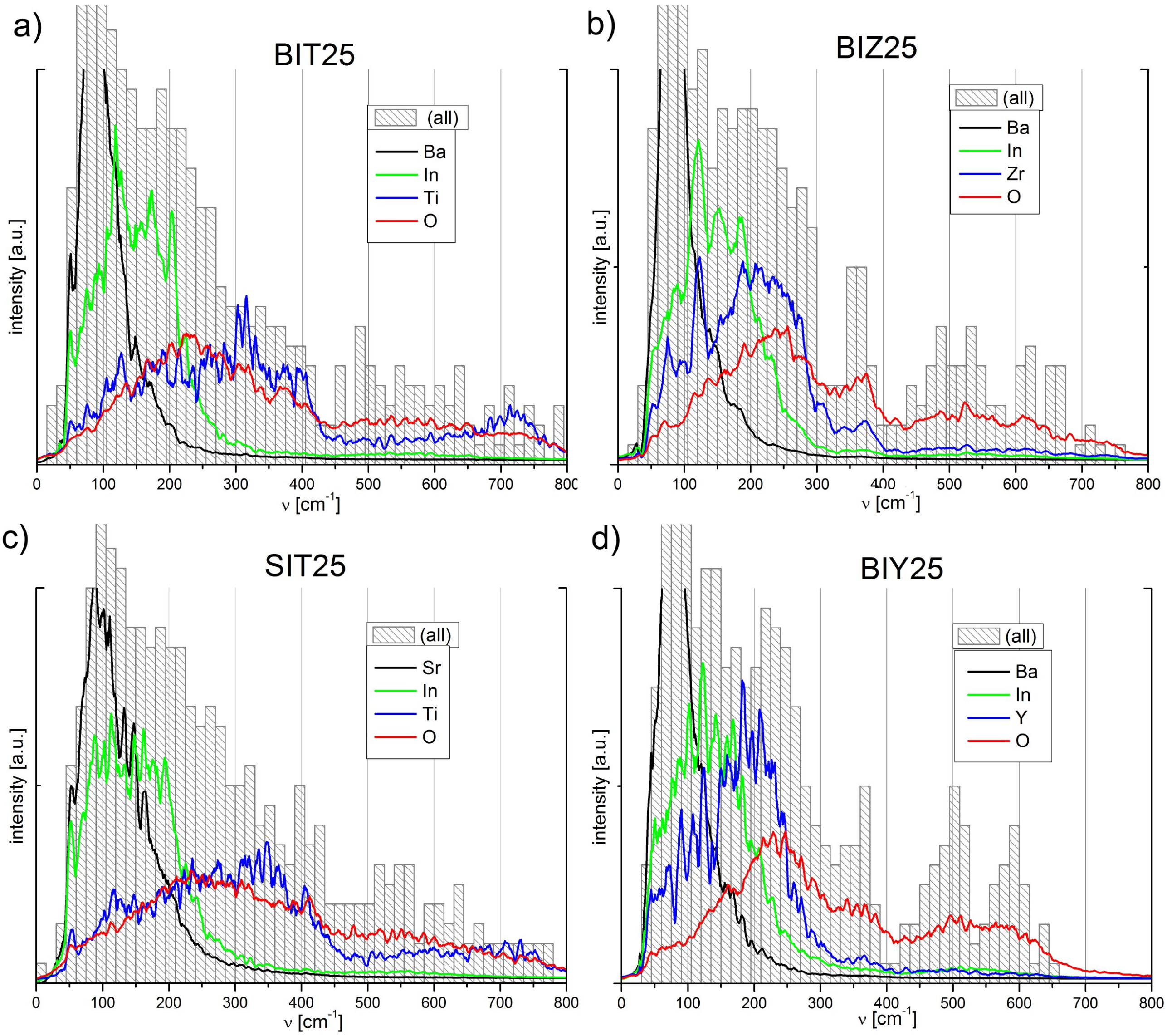

Figure 3.17: Vibrational DOS and NMA of four different 25%-substituted compounds.

the tetrahedral coordination. An optical inspection of the highest frequency modes of BIT06 show that these are made up of highly asymmetrical modes of the Ti-tetrahedron in which the Ti-cation vibrates against one of the four oxygen ions and leaving the remaining three oxygens rather uninvolved. The corresponding eigen-vectors of Ti and O point towards one another and have *both* considerable norms, i.e. amplitudes. That explains the very high intensity of this Ti-tetrahedron-mode in the vibrational DOS.

With increasing Ti-content along the BITx composition the intensity of this Ti mode decreases due to the fact that less and less Ti-tetrahedra are possible to be created due to the decreasing overall content of oxygen vacancies. Logically the extreme case $BaTiO_3$ contains neither tetrahedra nor pyramids. However octahedra do not anymore allow for the kind of asymmetric Ti-O mode observed for tetrahedra because of the higher number of Ti-O bonds symmetrically arranged around the Ti-cation. Nevertheless high frequency modes performed by the Ti-bonded oxygen ions are still observable. Again for the extreme case of $BaTiO_3$ these modes are now a couple of centrosymmetric bond-elongation modes of the Ti-octahedra.

On a more general note the entire set of vibrational DOS very nicely shows the particularity of Ti compared to all other B-site cations: it is sufficiently lightweight to couple very intensively to a large domain of oxygen modes. Especially compared to what can be observed for indium in the BITx compounds where it is almost entirely active in a region only about 50-100 cm^{-1} above barium.

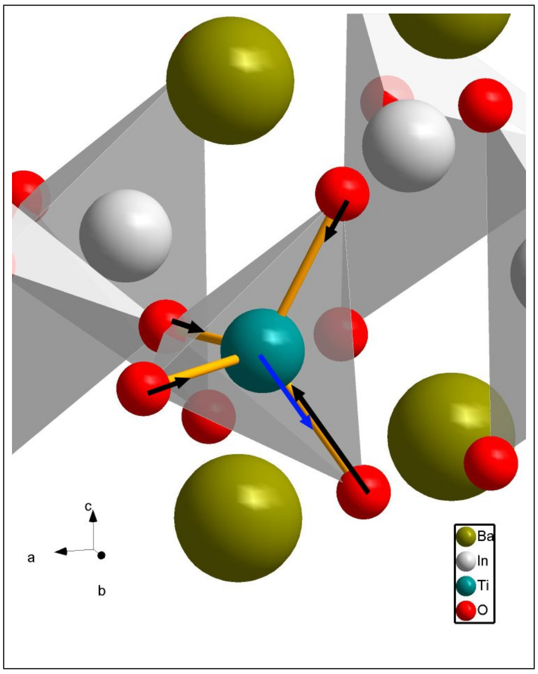

Figure 3.18: Visualization of the high frequency Ti-O vibration mode in Ti-tetrahedra as observed in BITx compounds. The arrow lengths approximately represent the vibr. amplitude.

The SIT25 compound whose vibrational DOS is presented in figure 3.17 c) does not show really drastic deviations from its homologue BIT25 right above. However it is noteworthy how the considerably lighter-than-Ba cation Sr^{II} displays only a minor shift towards higher frequencies in its vibrational DOS compared to Ba in the BITx compounds. Noting that strontium also is significantly more lightweight than indium, and indium nevertheless occupies a higher frequency region, one nicely sees that the frequency domain is much more determined by the chemical bonding environment than the atomic mass.

3.6 Oxygen diffusion

Although not being of primary interest for this work, the molecular dynamics simulation on the dehydrated compounds allow to directly deduce diffusion coefficients by the analysis of the mean-square-displacement (technique described in the chapter "Methods", section 2.2.4.2). The investigated temperatures range from 800°C up to 2500°C and comprise three intermediate temperatures (most often 1200°C, 1500°C, 1900°C).

The raw mean square displacements are obtained by and averaged over the totality of the oxygen ions. Thus in order to ensure a comparability between compounds with different numbers of oxygen ions (depending on the degree of substitution) the raw coefficients can be multiplied by the simple ratio of $\frac{N_O}{N_V} = \frac{96-N_V}{N_V}$, which is the number of considered oxygen ions divided by the number of oxygen voids. This number of oxygen vacancies decreases from 16 for BaInO to 4 for BIT75 with respect to the constant total of 96 oxygen sites in the perovskite structure framework.

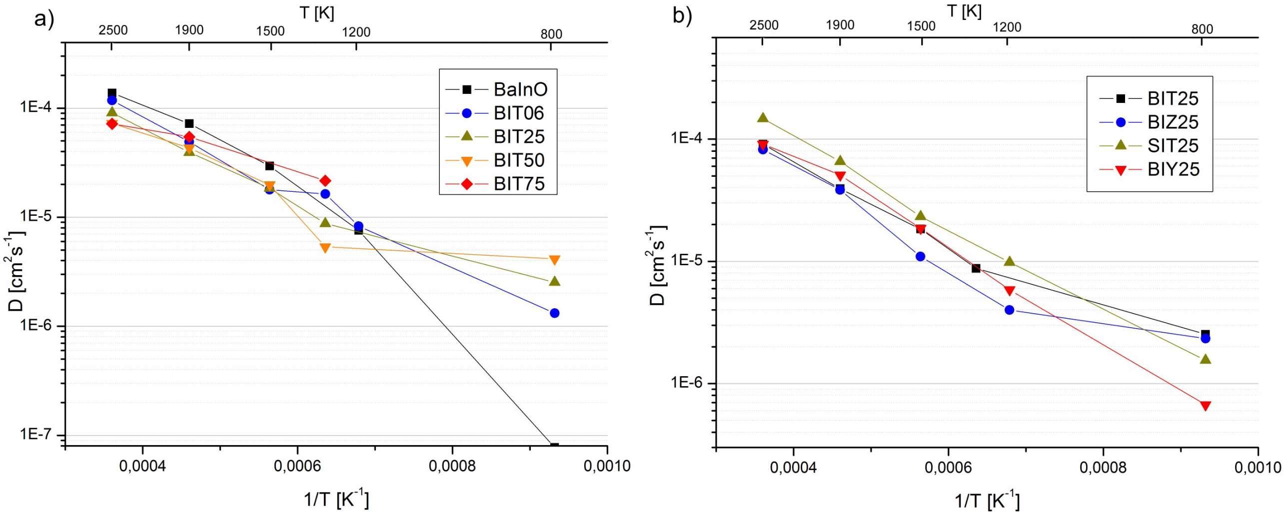

Figure 3.19: a) "vacancy" diffusion coefficients as obtained by MSD-analysis of the dry compounds. Lines are guide to the eyes

In practice the values are obtained from runs of 60 to 90 ps length. For what the sampling weight is concerned, the lowest temperature (800°C) can often not be considered sufficient for a MSD-analysis. Taking the difficult case of BIT50 (i.e. only 8 vacancies for 96 oxygen sites) only around 10 out of the 88 oxygen ions perform one to two elementary jumps throughout the entire run. Therefore the error to be assumed on the those low temperatures is rather big. From 1200°C on upwards and especially between 1500°C and 2500°C the statistics improve considerably, with e.g. again for BIT50 having now every oxygen ion (!) jumping one up to three times and more. As can be seen in the graph, however also in the high temperature region of somewhat sufficient statistical confidence, the mutual differences are rather negligible.

By employing the standard description of thermally activated diffusion processes, it may be tried to approximately evaluate them in terms of a single Arrhenius expression including one prefactor and an activation energy exponential:

Table 3.IV: Fitted activation energies and prefactors of the oxygen diffusion coefficients. "Errors" in the prefactors are well in the range of 50%, activation energies are about ± 0.3 eV

	E_{act} [eV]	prefactor [$1{\cdot}10^{-3}$ cm^{2}s-1]
BaInO	0.63	1.98
BIT06	0.77	2.92
BIT25	0.72	1.71
BIT50	0.68	1.60
BIZ25	0.74	1.84
BIY25	0.64	1.60
SIT25	0.73	3.16

$$D = A \cdot \exp\left(\frac{-E_a}{kT}\right) \tag{3.5}$$

The fitted results as presented in table 3.IV yield reasonable values for the activation energies and prefactors (given the rather big tolerances).

It is noted that in contrast to the protonic diffusion no systematic error-estimation was made with the help of the Monte Carlo algorithm. However great care has to be taken in reading this kind of fitted activation energies. As will be explained in detail in section 5 (and backed by Monte Carlo case studies) thermally activated processes are not at all necessarily describable by a single activation energy when they take place in energetically disordered systems. As presented before the here considered compounds indeed display a great number of locally different energetical states (i.e. oxygen vacancy arrangements). Hence, for studies like in our case that cover a very large temperature range (greatly exceeding what is experimentally accessible) only one set of Arrhenius parameters might not be appropriate.

Taking for example a closer look on the black line of BaInO in figure 3.19 a) a distinct curvature may be recognized. If, on a *very* hypothetical basis the diffusion coefficients for BaInO were considered error-less then the activation energies between 1200°C, 1500°C, 1900°C and 2500°C successively would read: 0.88 eV, 0.65 eV and 0.56 eV which represents a downwards curved Arrhenius representation. This argumentation shall illustrate that the meaning of the word error in relation to single-Arrhenius terms may at times be misleading, as no single term can be expected when such a large temperature region is considered. A more detailed account on this field of problems is given in the framework of the Monte Carlo chapter which deals with diffusion on disordered lattices in general.

Compared to typical experimental values the obtained migration activation energies are (on an average) 0.2 to 0.3 eV lower than the average of a number of experimental values given in [21]. This latter study by KREUER and co-workers provides data of vacancy-diffusion activation energies and prefactors of around 20 different acceptor doped perovskite type zirconates and titanates. The doping/substitution level ranged up to 25% (i.e. the equivalent to what would be 75% in our case). The majority of activation energies that are given situated around 0.9 eV to 1.0 eV with an absolute minimum value of 0.67 eV for 5% scandium-doped strontium titanate. The prefactors are confined between $8 \cdot 10^{-4}$ and $2 \cdot 10^{-2}$ cm^2s^{-1} and in turn compare very well to the MD-obtained equivalents. In the aforementioned Monte Carlo chapter it is going to be discussed, under which conditions the temperature region in which an Arrhenius plot is created might influence the parameters that are deduced from it.

One clear standing observable fact, is the influence of already the smallest degree of Ti-substitution (6.25 % being equal to 2 Ti mixed with 30 In) on the properties of the material. This is a direct reflection of what was found by the exploitation of the MD data concerning the local structures in section 3.3.2: at 800°C already 2 Ti for 30 In lead to a notable destabilization of the Brownmillerite structure and gives rise to the formation (more precisely a dynamical equilibrium) of many indium pyramids in the former tetrahedral and octahedral sheets. Naturally this "activity" is directly mirrored by the averaged mean square displacements of oxygen ions. The diffusion coefficient of BaInO at 800°C has no proper meaning as the only oxygen displacements are temporary tetrahedra-rotations which by far does not correspond to a long range diffusion.

3.7 Chapter's conclusion

This chapter dealt with the structural, vibrational and diffusive properties of a number of completely dehydrated Brownmillerite-based compounds. The performed investigations were conducted by static DFT calculations as well as DFT-based molecular dynamics. They allowed to gain access to an unambiguous determination of the local coordination structures of Ti, Zr and Y substituted $Ba_2In_2O_5$. It was found that in Brownmillerite/perovskite-related materials containing indium on their B-site it is this indium which adapts its coordination structure according to the needs of the other B-site occupant. Ti is enabled to become 4-fold coordinated, whereas Zr and Y show a strong preference for the 6-fold coordination. By own XANES measurements the experimental confirmation of the calculated prediction could be successfully brought about for the case of the BITx compounds. XANES measures from GIANNICI [62] did (coincidentally) also confirm the corresponding coordination preference for the BIZx compounds which leaves us with a rather large confidence on the reliability of the structural DFT calculations.

An experimentally very important concept has also been successfully reproduced: the stabilization of disordered structures at lower temperatures in the case of cation-substitution: direct molecular dynamics evidence was given of how already very low Ti-concentrations (6.25%) give rise to structural instabilities at temperatures (800°C) where pure barium indate still remains ”perfectly” Brownmillerite (see 3.3.2).

The pure Brownmillerite BaInO was put under scrutiny, too. Being free of the cation-mixture complex of problems it served as a reference, additionally showing an order-disorder phase transition. The here employed molecular dynamics approach manages to locate the transition temperature between 800°C and 1200°C (experimental: 930°C). This very reasonable reproduction of a well defined structure-dynamical feature again speaks for the validity of the DFT-based molecular dynamics approach for the description of structural solid state chemistry problems.

Bader-charge analysis was identified to supply a consistent view of the average charge transfer cation→oxygen as a function of composition. Given the multitude of definitions of the ”electronegativity” however, one cannot speak of a clear correspondence between the two concepts. As will be discussed for the hydration energies in the upcoming section 4.4 the actual Bader charge provides a more consistent means for the discussion of properties which are influenced by the charge distribution. This will be the case for the mentioned hydration energy.

Concerning the diffusional properties of oxygen in these compounds we can state that the obtained values (activation energies and diffusional prefactors) are located in the correct order of magnitude. However mutual differences are supposedly too small to be accurately reproduced by a direct DFT-based molecular dynamics method.

Chapter 4

Structure and energetics of the fully hydrated compounds

4.1 Introduction

This chapter shall deal with the Brownmillerite based compounds in their hydrated form from a structural and energetic point of view. It is clear that general structure, local structure and also the overall hydration energy may later be mirrored by the diffusivity or at least will influence it. So in order to better understand and interpret the actual diffusivity experiments (computational, though) this chapter will in detail deal with the structural particularities that characterize the fully hydrated state of the compounds in question. It begins with an overview over the general as well as vibrational properties of all hydrated compounds in section 4.2 and section 4.2.1.

Afterwards the rather complicated proton arrangements are studied with respect to the reference compound $Ba_2In_2O_4(OH)_2$ which already shows some interesting features (two distinct types of proton sites in an layered arrangement, a characteristic proton blocking layer). This situation becomes even more complicated with the cation-substitution which introduces a very important new aspect to consider: the trapping or obstacle concept according to which protons associate more or less with one or the other cation-polyhedron. These effects are going to be investigated by molecular dynamics in sections 4.3.1, 4.3.3 and 4.3.2.

Beginning with section 4.4 the chapter will focus on the hydration energies i.e. the extent to which a hydrated compound is energetically more favourable than the dry compound plus water in the gaseous state. Although no direct access is possible to genuine *free* hydration energies, the MD-simulations yield valuable (because thermodynamically justified) hydration energies. Corresponding results are presented in section 4.4. These results are then brought into contact with some neighbouring aspects which are the Bader charges presented in the ”Dry”-chapter and some proton-structural arguments.

In contrast to much previous work, the notion of complete hydration is of importance, as the concentration of protons in these states is *not dilute*. Therefore, many very well established considerations in dealing with protons in oxide materials can not be applied by implication because they rely on the defect nature of the proton in an otherwise unperturbed environment. In the case of the Brownmillerite based compounds treated in this work however, we are confronted with two paramount modifications:

Firstly, the high proton concentration leads to average structures that are in part *created* by the proton's presence. This is especially true for the case of the crystallographically well defined layers of extra-octahedrally bound protons. Those layers exhibit a pronounced tilt of the concerned octahedra giving rise to rhombus-shaped inter-octahedral spaces that harbour a very stable (hydrogen bonded) proton along the short oxygen-oxygen distance.

On the other hand side, the most interesting compounds have a substantial fraction of their B-sites occupied by a cation other than indium. In general the concentrations considered in the following range from 6.25% to 75% of substituded indium by titanium. Zirconium and yttrium as alternative substituents are studied only in the case of a 25% substitution. The number of protons in completely hydrated compounds is determined stoichiometrically by the indium-to-substituent ratio in case of aliovalent substituents Ti and Zr:

$$Ba_2In_{2(1-x)}(Ti/Zr)_{2x}O_{4+2x}(OH)_{2(1-x)}. \tag{4.1}$$

For Yttrium, isovalent to Indium, in turn the number of protons is equal as in the pure In-compound. It is given by: $\mathrm{Ba_2In_{2(1-x)}Y_{2x}O_4(OH)_2}$ as two protons per formula unit. Strontium, as A-site cation isovalent to barium does not alter the proton content.

The proton number is equal to the number of In-cations in the structure and therefore decreases with increasing aliovalent substituent content. This fact will be important for the interpretation of the relation between proton-concentration, trapping-site concentration and generally-available site concentration, discussed later in this chapter. The cations are always assumed in their standard degree of oxidation (4+ for Ti and Zr, 3+ for In and Y).

As in the chapter on the dehydrated compounds before, the different compounds will be designated with the three-letter acronym indicating the A-site cation (B or S), Indium (I), the substituent, the letter "h" for "hydrated" and the percent fraction of substituent in that order. SITh25 e.g. meaning completely hydrated $\mathrm{Sr_2In_{1.5}Ti_{0.5}O_{4.5}(OH)_{1.5}}$[1].

---

[1] the complete set of hydrated compounds being BaInOH, BITh06, BITh25, BITh50, BITh75, BIZh25, BIZh50, BIYh25 and SITh25

Concerning the determination of properties by calculation the issue is more or less identical to the identification of plausible vacancy structures in the dry state: in order to properly mimic a cationically disordered compound, the minimal cell size we deemed trustworthy contains 32 A and 32 B sites, along with 96 oxygens and 32 to 16 protons (going from $Ba_2In_2O_4(OH)_2$ to BITh50 or BIZh50. Each cell has 96 oxygen ions which exhibit up to 8 different proton sites, one site per edge. An important condition that is always assumed for the molecular dynamic runs is the absence of any particular cationic order for the mixed B-sites. Making reference to section 3.3.1 where it was shown that in any case the thermodynamically most stable cationic distributions are of an ordered nature, we take for granted that disordered structures can experimentally always be created. So for all 7 substituted compounds cationic disorder of the simulation cells is created ”by hand”.

4.2 General structure of the fully hydrated compounds

As does $Ba_2In_2O_5$, on a general basis the substituted compounds treated in the scope of this work undergo a complete hydration reaction at temperatures below 500°C in humid atmosphere (e.g. [72, 73] for Ti, Y and Sc or [72, 71, 62, 8] for Zr). The reaction consists of the filling of the oxygen voids as well as the distribution of the protons on the oxygen lattice. Once incorporated there does not remain any particular association between the oxygen coming from the water molecule and the protons.

A general rule from diffraction experiments from the just mentioned papers is that crystal structures of many Brownmillerite-related *fully hydrated* compounds tend to show tetragonal symmetry up to relatively high degrees of substitution of around 20-40% at room temperature. However, while the reference compound (introduced in section 1.1) $Ba_2In_2O_5$ is orthorhombic in its dry state, the substitutional compounds are disordered cubic when dry. Nonetheless, both become tetragonal during the hydration (up to cation-depending maximum degrees of substitution) [1, 73]. Inferring from the fact, that for the dry BIYx, BITx and BIZx no cation ordering has been evidenced [2, 72, 62, 74] we can conclude, that the tetragonality *is* induced by the protonic structure. It is reasonable to assume, that those high concentrations of protons can trigger structural particularities like the tetragonal phase in this case.

Moreover by analogy to fully hydrated $Ba_2In_2O_4(OH)_2$ (introduced in section 1.1) it is

Table 4.I: Cell parameters and volume of the fully hydrated (left columns) and dry (right columns) simulation cells used in the MD simulations

hydrated	a [Å]	b [Å]	c [Å]	V [Å^3]	dry	a [Å]	b [Å]	c [Å]	V [Å^3]
BaInOh	12.0759	12.1063	18.1993	2660.41	BaInO	12.4783	12.1219	16.8753	2552.56
BITh06	12.0861	12.0232	18.1153	2631.57	BIT06	12.4221	12.1178	16.8329	2533.83
BITh25	11.8581	11.8788	17.9419	2527.16	BIT25	12.0014	12.0653	16.8892	2445.46
BITh50	11.8323	11.9559	17.0788	2415.04	BIT50	11.8809	11.8547	16.7443	2358.05
BITh75	11.7368	11.7592	16.6953	2303.78	BIT75	11.7000	11.7270	16.5424	2269.66
BIZh25	12.0575	12.0308	17.9085	2597.48	BIZ25	12.1369	12.1436	16.9468	2497.67
BIZh50	12.1490	12.1324	17.3575	2558.20	BIZ50	12.0941	12.0875	17.0913	2498.51
BIYh25	12.1270	12.1022	18.4232	2702.81	BIY25	12.5157	12.2467	16.9916	2604.26
SITh25	11.5760	11.5921	17.4156	2336.72	SIT25	11.6338	11.6571	16.3325	2214.81

evident that the tetragonal character manifests itself by the presence of layers containing an ordered arrangement of extra-octahedral protons which was illustrated in figure 1.3 on page 14. This affirmation is consistent with all upcoming DFT-calculation results which find this kind of hydrated structure to be the energetically favourable ones. So up to considerable substitution degrees the hydrated compounds resemble the hydrated Barium-indate structure. It will be subject to section 4.3.1 to elucidate the stability of these extra octahedral layers with varying degree of substitution and temperature.

As was already stated for the dry phases, an in-depth analysis of the relaxed cell volumes or lattice parameters was not conducted due to the large variation of this property depending of what particular local structure is realized in a given simulation cell. The table 4.I will therefore only assemble the cell parameters and the volume of the simulation cells that were used for the molecular dynamics simulations. For a quick comparison the equivalent completely proton-less dry cells are given as well. As a remark, all lattice constants systematically are too large by 0.5 to 1.5% compared to experimental values which is within the range of expectation for the PBE-GGA correlation exchange potential used for the calculations [75].

Figure 4.2 recalls the structural difference between the two classes of protons which are encountered with a distribution of slightly differing binding angles and bond-lengths in the pure and substituted compounds (up to 25% substitution). One immediatetely visible consequence of the two proton sites are their rather distinguishable O-H and H$\cdots$O bonding lengths as well

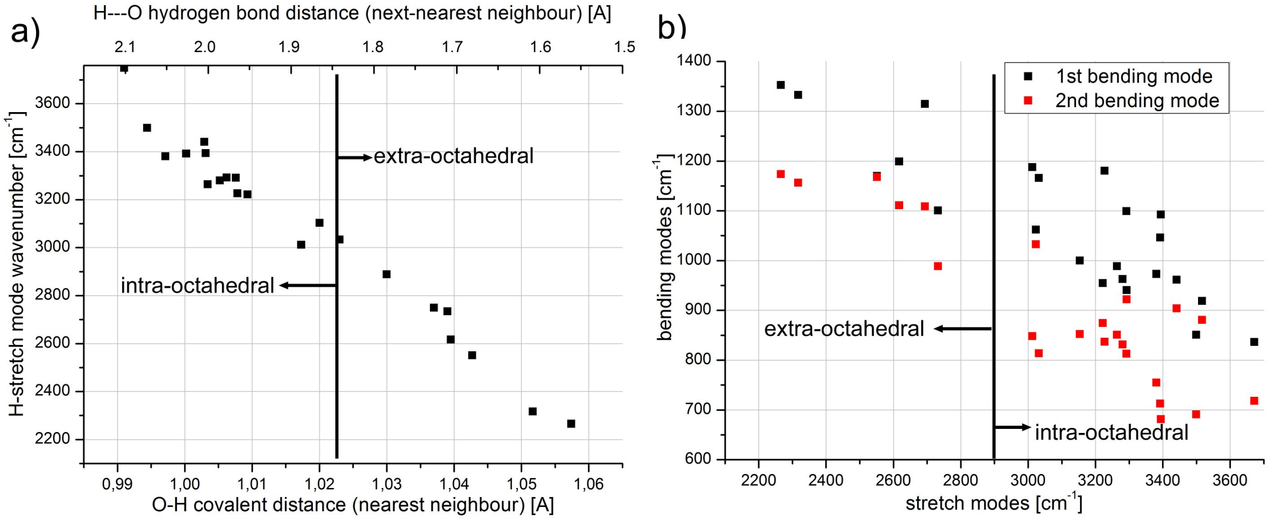

Figure 4.1: Tendencies of protonic vibrational modes: a) Correlation between nearest proton-oxygen distances and corresponding stretch mode frequencies for a selection of relaxed protons from several compounds; b) Correlation of the two bending modes per proton with its stretch modes. Sampling of points stems from various compounds both pure and cation-substituted. The regions of predominantly intra- and extra-octahedral protons are marked by the division line.

as their vibrational differences as shown in figure 4.2. It is the degree of hydrogen bonding to a next-nearest oxygen neighbour which determines the two proton-oxygen distances and by consequence their typical vibrational frequencies.

The stronger the hydrogen bond, the softer the stretch-frequency and the longer the covalent O-H bond. This is shown in figure 4.1 a) which is an assembly of well correlated O-H (lower X-scale) and H$\cdots$O (upper X-scale) distances and the corresponding stretch mode frequencies of protons in a variety of different compounds here all mixed together. Not surprisingly this expresses a sort of universality of these local proton properties where the exact cationic environment does not have a direct influence.

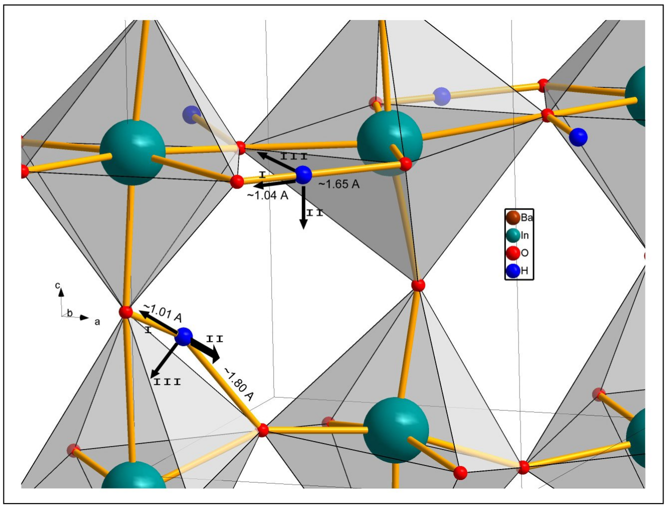

Figure 4.2: Typical local structures of intra- and extra-octahedral protons. I, II and III designate the stretch- and the two bending modes, values in Å are typical O-H or H$\cdots$O distances

However, the extent and number of hydrogen-bonded protons *does* differ depending on cation substitution.

Figure 4.1 b) establishes the correlation of the aforementioned stretch modes and the two remaining bending-modes. The stiffer the stretch modes, the softer these bending modes become as they are bound in a less tighter manner to the next nearest oxygen neighbour via the hydrogen bond.

As will be seen, the relatively high number of protons (large simulation cells) used for the MD-runs gives rise to a rather large systematic spread of this kind of property due to a pronounced (protonic) disorder, already for the unsubstituted compound.

4.2.1 Vibrational properties

The analysis of the occurring nuclear vibration spectra is a very helpful tool to characterize the fully hydrated structures. MD-simulations permit to do so in a very elegant way which is the Fourier-transformation of the velocity autocorrelation function (VAF) of a given ionic species. As was the case for the dehydrated compounds in section (dry-vibration) the normal mode analysis is of interest too, in order to better assign the frequency domains to particular modes. The general character of this investigation is similar to what was presented in section 3.5 on the dry structure's vibrational properties. In the case of the fully hydrated compounds it is the protons that are of biggest interest as they exhibit structural degrees of freedom connected to different vibrational signatures.

Beyond the intrinsic interest in the vibrational properties, their knowledge is essential in order to assess the quantum-effect corrections to the hydration energies (see upcoming section 4.4.5) as well as to the thermally activated protonic displacement modes (see section 6.4.3). Moreover the so-obtained frequencies can be brought into relation with the pre-factors of these displacement modes.

Figures 4.3 a) through f) present an overview of the entire vibrational spectrum of all ionic species that are present in the particular compounds. 4.3 a),b) and c) show the evolution from BaInOH with increasing degree of Ti-substitution up to 50%. b), d), e) and f) compare four different compounds with 25% Ti, Zr or Y substitution, respectively. In all figures two different results are presented: the solid lines represent the fast fourier transform of the VAF of the indicated ionic species which has been smoothed for clarity whereas the gray histograms show

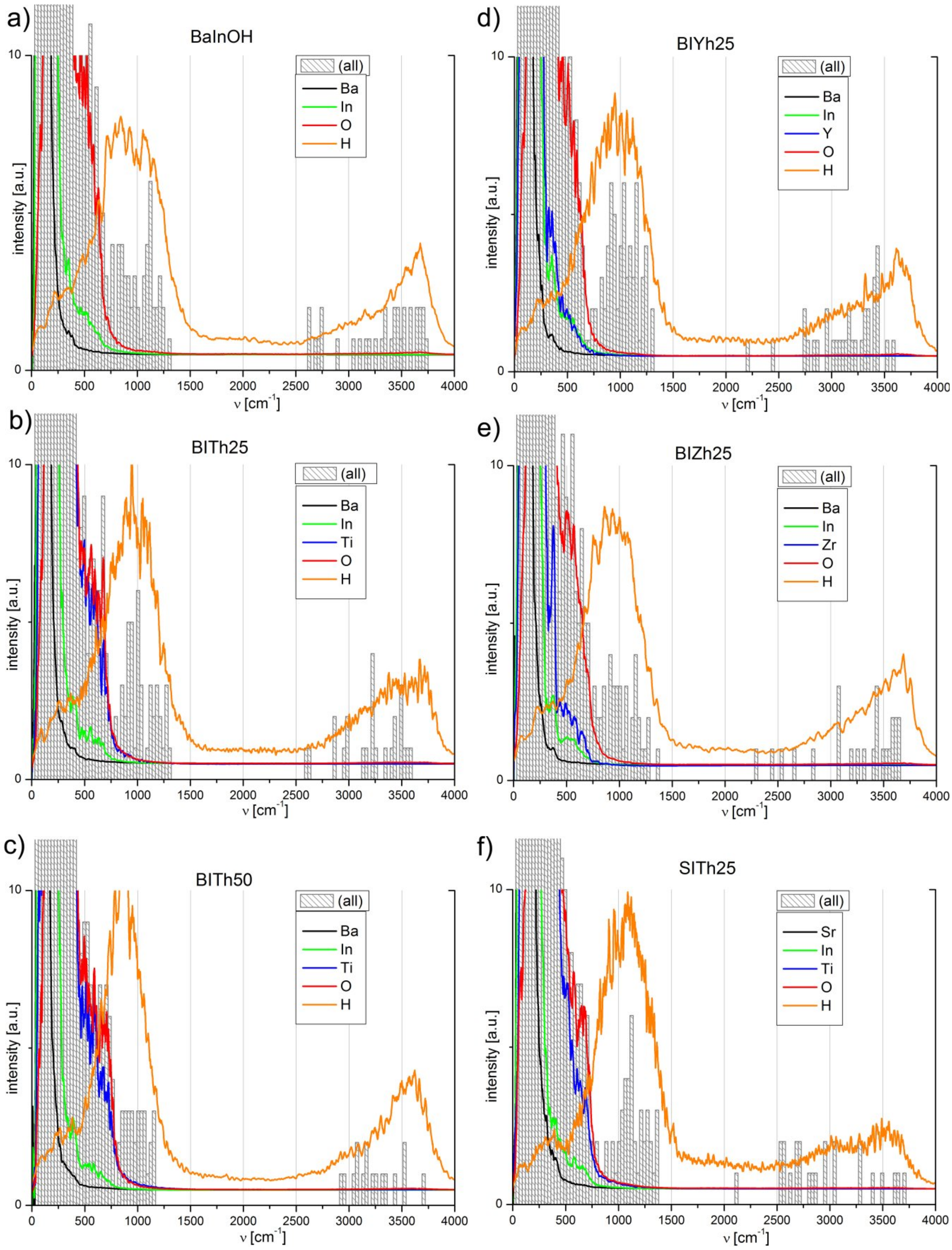

Figure 4.3: Complete Vibrational DOS obtained by an FFT of the VAF at 500°C (lines) and an NMA for corresponding relaxed static structures. a), b) and c) show the evolution with increasing Ti-content from 0 over 25 to 50%; b), d), e) and f) compare several 25% substituted compounds.

the frequency distribution as calculated by the normal mode analysis (NMA) on fully relaxed structures for the entire set of ions present.

Firstly, the overall behaviour of the protons is well explained as being separated into two major frequency domains, one around 1000 cm^{-1} consisting of the two protonic bending-modes and the other in the region of from 2500 to 3500 cm^{-1} corresponding to the stretch-mode. This is an expression of the way protons are incorporated in the oxide structure as being covalently bonded to one oxygen and *more or less* hydrogen bonded to another oxygen. Importantly the relaxed configurations that are the basis of the NMA histograms are created by relaxing an instantaneous configuration during an MD-run at 500°C in order to account for proton positions being distributed more "naturally" than in the guessed initial configurations which are more ordered. Anyway a rather large spread of the protonic frequency domains can be observed already in the histograms where this can be observed in the high-frequency region which strictly contains only O-H stretch modes. Even for the unsubstituted BaInOH compound the stretch-modes are comprised in a range between ≈2500 cm^{-1} and 3750 cm^{-1}. The further separation of modes well below and well above 3000 cm^{-1} is primarily due to the different characteristics of the intra- and extra-octahedral protons which are present in a 50/50 fraction.

The completely strontium based compound (figure 4.3 f)) shows a systematic protonic frequency shift to higher values for the bending-mode region and to lower values for the stretching-mode region. This is one direct and confirmed consequence of the smaller general lattice constant due to the considerably smaller Sr cations compared to Ba. The smaller distances give rise to a bigger likelihood for strong hydrogen bonds to be created, also for intra-octahedral protons, which in turn directly leads to the observed behaviour, particularly in agreement with the general correlation shown in figure 4.1.

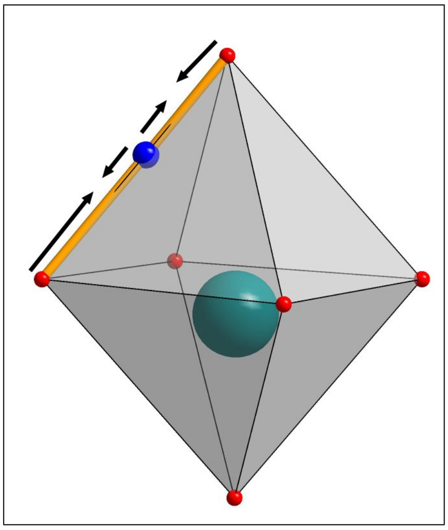

Figure 4.4: Transient unfavourable linear O-H-O configuration giving rise to particularly high O-H stretch frequencies.

As it could already be established earlier for the vibrational spectra of the dry compounds (in section 3.5) the vibrational association of oxygen ions with Ti is much stronger than with any other B-site cation (In, Zr, Y). Again this is visible in any Ti-containing spectrum by comparing the red oxygen and blue titanium lines which show Ti in the rather high frequency oxygen domain well above 500 and up to 750 cm^{-1}.

A recurring difference between the NMA-histograms and the corresponding VAF-based spectra is the systematically higher maximum stretch-frequencies for the protons. Optical inspection of several of the corresponding MD-runs do hint to a genuine dynamic effect which may arise during the MD-runs. This effect are transient, particularly intimate intra-octahedral O-H-O arrangements which structurally are very far off the relaxed configurations the NMA is based on. In those relaxed structures the NMA yields the highest possible stretch frequencies for protons with a rather distant next-nearest oxygen, i.e. not being strongly hydrogen-bonded. This vibrational stiffness is characteristic for rather independent internal O-H groups. The closer a next-nearest oxygen is located the softer the corresponding stretch frequency gets. These facts were already shown in figure 4.1 for an arbitrary selection a number of protons and their stretch modes as a function of the respective distance to their two oxygen neighbours.

During the MD-runs however local amplitudes of oxygen and proton modes may become considerable and give rise to transient configurations as shown in figure 4.4. A proton may bend in between a short O-O couple which leads to the situation that it may effectuate particularly high frequency vibrations until the O-O distance grows considerably or the proton bends out again. These high-frequency vibrations thus are not due to some bond stiffness but are caused by the strong repulsive force of the temporarily too closely spaced oxygens.

4.3 Structural properties investigated by Molecular Dynamics

4.3.1 Dynamic equilibrium between Intra- and Extra-octahedral sites

Motivation

This section is going to investigate the role of the structural extra-octahedral protons that exist in fully hydrated Brownmillerite based compounds. Undoubtedly they are one of the major distinctions to protonated perovskites. First, those structural extra-octahedral protons are statically stable in contrast to transient extra-octahedral positions which are only produced temporarily by particular instantaneous configurations. Nevertheless transient extra-octahedral may of course also be present in the substances here considered.

As it turns out the extra-octahedral protons are constitutive for the general structure also of the substituted compounds, which is true for the degrees of substitution of 6.25% and 25%. The 50/50 compounds (BITh50 and BIZh50) do not show this feature anymore.

Being interested in the diffusivity of the protons, the extra-octahedral proton-layer is interesting in several ways: Mostly of course, there is the question of how stable extra-octahedral protons are, and to what extent they will contribute to the overall diffusivity or whether they may be considered a trapped proton-concentration. Remembering that for $Ba_2In_2O_4(OH)_2$ 50% of the proton content is extra-octahedral this is obviously an important issue. On the other hand side, that kind of structure could possibly constitute a blocking barrier for the remaining protons that diffuse between different intra-octahedral sites.

Structurally the extra-octahedral layers are interesting objects, as the cation-oxygen polyhedra collectively adopt a particularly tilted structure apparently only because of the presence of the high number of protons, which profit from these tilts by establishing strong hydrogen bonds. The rhombus-shaped interstices between octahedra do accommodate 1 proton each along the very short inter-octahedral O-O distance. Thus the standard simulation cells used have two layers with eight octahedra positions available giving 16 extra-octahedral sites per simulation cell.

Molecular dynamics naturally are a very convenient way to observe the thermodynamical stability of this kind of structure. In the framework of the elementary-displacements counting algorithm (introduced in section 2.2.4.4) it is possible to keep track of the number of intra- and extra-protons at any moment. However no distinction between the structure-relevant extra-octahedral protons and also possible transient extra-protons was made.

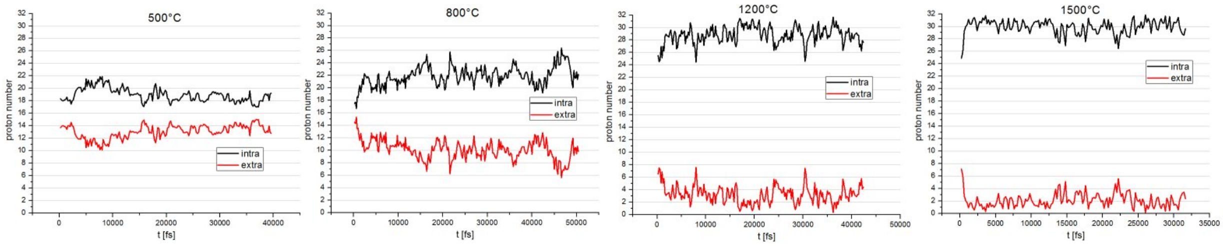

Figure 4.5: Time evolution of the number of intra- and extra-octahedral protons in $Ba_2In_2O_4(OH)_2$ at four temperatures (500°C, 800°C, 1200°C and 1500°C)

Figure 4.5 shows a typical evolution of the raw-numbers for $Ba_2In_2O_4(OH)_2$. Stability was considered to be reached at least during the second half of each run, and the simple average up to the end of the run was taken as measure for the concentration with respect to the 16 sites available per simulation cell. As it is observed (for all other structures alike) even at the lowest temperature simulations were run at, an equilibrium is well achieved within MD-simulation time.

In the following it will be presented, how the stability of the extra-octahedral position can be modeled based on the averaged-equilibrium concentration and how it depends on cation-substitution indicating to what extent the degree and type of substitution influences on the stability of the extra-octahedral layer.

The theoretical description of the intra-extra ratio can be successfully based on a two-level Fermi-statistics model, e.g. often used for hydrogen in metals as well as *ad-hoc* postulated different site energies of protons in oxides. Literature sources for the hydrogen in metal case are very widespread. The reason to use a Fermi-statistics treatment is the site-constraint which arises when a certain number of particles has to be distributed on a lattice whose sites attract these particles to a different extent. When the concentration of particles is in the same region as the concentration of the trapping site, and additionally one trapping site cannot be occupied by more than one particle[2], Fermi-Dirac statistics have to be applied.

The issue of the hydrogen concentration at particular sites for example dislocations is addressed e.g. in [76, 77, 78] where a Fermi-Dirac statistical model is employed. In the same spirit HEMPELMANN and co-workers apply a similar two-site trap model to the interpretation of hydration curves of perovskite related oxides as $Ba_3(Ca/Nb)_3O_{9-\delta}$ [79] or $BaZr_{0.85}Y_{0.15}O_{2.925}$ [80]. They assume (at least) two distinct binding sites of protons inside the oxide. Fitting experimental proton content data (obtained by nuclear resonance reaction analysis) in the BZY case for example they determine a site fraction of $2.5\,mol\%$ of protons being trapped at sites which lie 0.3 eV lower than the regular hydration energy here in excellent agreement with an average oxygen-fraction being bound to two Y cations which are therefore identified as trapping sites.

---

[2] which is the analogue to the Pauli-principle for electron statistics

Concept of the description

Here the two-site Fermi-model will be applied to protons being located in intra- or extra-octahedral sites in considerable fractions as obtained by the MD-simulations. The basic approach is characterized by the statement of an equation-of-state for the protons in the system that takes into account the two sorts of protons (intra- and extra-octahedral), their delta in site-free-energy (ΔG) and the two concentrations c_P and c_T for the overall proton-concentration and the "trap" (or extra-site) concentration. These two concentrations will remain fixed throughout the treatment. The "trap" concentration is (the trap concentration is defined with respect to the total number of proton sites, i.e. intra- and extra-sites).

$$c_P = \frac{c_T}{1 + exp\left(\frac{\Delta G - \mu}{kT}\right)} + \frac{(1 - c_T)}{1 + exp\left(\frac{-\mu}{kT}\right)} \tag{4.2}$$

The two concentrations are constant in our case, as the proton concentration for our system is kept constant (complete hydration at all temperatures). The trap concentration c_T will later be a structural parameter defined by the rhombus shaped interstices in the fully hydrated compounds in relation to all other potential proton sites from which there exist 8 per oxygen ion. Equation (4.2) determines the chemical potential of the protons in this two level system which by re-arrangement reads:

$$\mu = kT \ln \left\{ \left[((xc_T + xc_P - x - c_T + c_P)^2 - 4x(c_P - 1)c_P)^{1/2} - xc_T - xc_P + x + c_T - c_P \right] / (2(c_P - 1)) \right\} \tag{4.3}$$

with $x = \exp\left(\frac{\Delta G}{kT}\right)$.

Now this expression for $\mu(T, c_T, c_P)$ is inserted in the common Fermi type occupation number equation to express the fraction of protons in extra- or intra-sites as a function of temperature:

$$c_{extra} = \frac{c_T}{1 + \exp\left(\frac{\Delta G - \mu(T, c_T, c_P)}{kT}\right)} \tag{4.4}$$

This equation can now be fitted to the concentration c_{extra} observed during the MD-runs. As the number of extra-octahedral protons does rapidly decrease with temperature ΔG is necessarily negative, i.e. (structural) extra-octahedral protons may considered to be a lower lying energetical level which is less and less populated for increasing temperature.

Consideration of vibrational entropy for ΔG

A refinement of the treatment lies in the consideration of the ΔG being composed of a true energy-delta and an entropic term as $\Delta G = \Delta E - T\Delta S$. Given the approach so far, this entropy difference exclusively consists of vibrational contributions as the configurational entropy is taken care of by the concentration expressions c_P and c_T within the Fermi-expressions. So to obtain an estimate of the entropy difference between the two proton types the standard thermodynamics definition of the entropy

$$S_i = -\frac{\partial G_i}{\partial T} = \frac{\partial (kT_B \ln q_i)}{\partial T} \tag{4.5}$$

is used, with q_i being the complete vibrational partition function of the proton in the given crystallographic site. Since the two states compared both have 3 vibrational degrees of freedom, the entropy difference (using classical partition functions) is temperature independent which is illustrated in figure 4.6. It can be easily calculated in a similar manner as presented for the elementary displacement steps (section 6.4) using $q_{cl} = \prod_i^3 \frac{h\nu_i}{kT}$ and the last equation (4.5). As also can be observed in the figure the entropy difference does not significantly change when applying the quantum-mechanical vibrational partition function (see section 6.4.3 for a more detailed discussion of quantum corrections). The so obtained approximate value of ΔS will be used in the forthcoming fitting procedure.

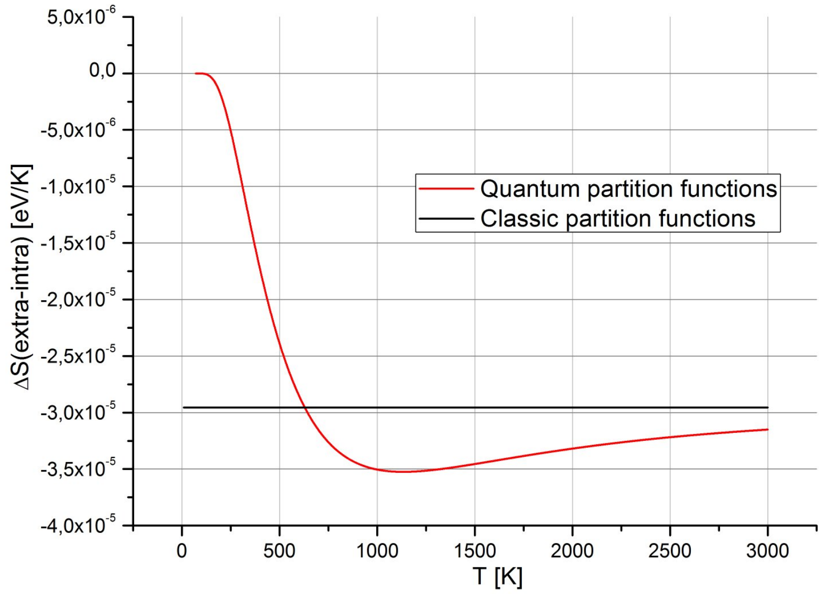

Figure 4.6: Difference of vibrational entropy between extra- and intra-octahedral protons with the extra-octahedral site has the higher absolute entropy. The used normal mode frequencies are examples from figure 4.1: 3500, 880 and 850 cm^{-1} for intra- and 2900, 1200 and 1060 cm^{-1} for extra-octahedral.

The fitting procedure

A further observation which enters into the quantitative description is the fact that the number of extra-octahedral protons obtained by the counting algorithm does not drop to zero even at the highest temperature of 1500°C and on the contrary may even be higher than at 1200°C (as observed for BIYh25). However, structural arguments as they are e.g. supplied by corresponding pair-correlation functions (or simple optical inspection of the trajectories) clearly state the *absence* of the structural extra-octahedral layer at these temperatures.
Thus this behaviour expresses an increasing number of ”transient” extra-octahedral protons, i.e. protons that are only locally hydrogen bonded to another oxygen of an adjacent polyhedron due to a particular instantaneous local configuration. As these proton sites are not present at all in the relaxed structures (i.e. at low temperatures) they may safely be associated with a higher energy level than the regular intra-octahedral proton sites.

This argumentation of two different kinds of extra-octahedral protons is used for the fit of the number of extra-octahedral protons over the entire temperature range from 500°C to 1500°C that was studied by MD-simulations. The fit to the number of counted extra-octahedral protons over temperature is therefore taken to be composed of two contributions coming from the two kinds of extra-types. This is done by establishing a sum of two terms of equation (4.4) with a negative and a positive ΔE for the structural and the transient extra-protons, respectively. Moreover these two terms are weighted by a smoothed step-function over temperature, which assures an exclusive contribution of the structural extra-protons at low temperatures and of the transient extra-protons at high temperatures.

Two simple Fermi-functions were chosen as step-like functions that switch the temperature regions of the two contributions being the structural (low temperature) and transient (high temperature) extra-octahedral protons (given in figure 4.7 b)).

The complete term to fit the number n of extra-octahedral protons thus becomes:

$$n = \left(\frac{1}{1+\exp\left(\frac{T-t}{w}\right)}\right)\cdot\frac{c_s}{1+\exp\left(\frac{(\Delta E_s - T\Delta S)-\mu_s}{kT}\right)} + \left(1-\frac{1}{1+\exp\left(\frac{T-t}{w}\right)}\right)\cdot\frac{c_t}{1+\exp\left(\frac{(\Delta E_t - T\Delta S)-\mu_T}{kT}\right)} \tag{4.6}$$

This equation now includes two sets of site-concentrations which are c_s for structural extra-site and c_t for transient extra-sites both explicitly and included in the corresponding chemical potentials μ_s and μ_t, respectively. The constant values for them are based on geometric con-

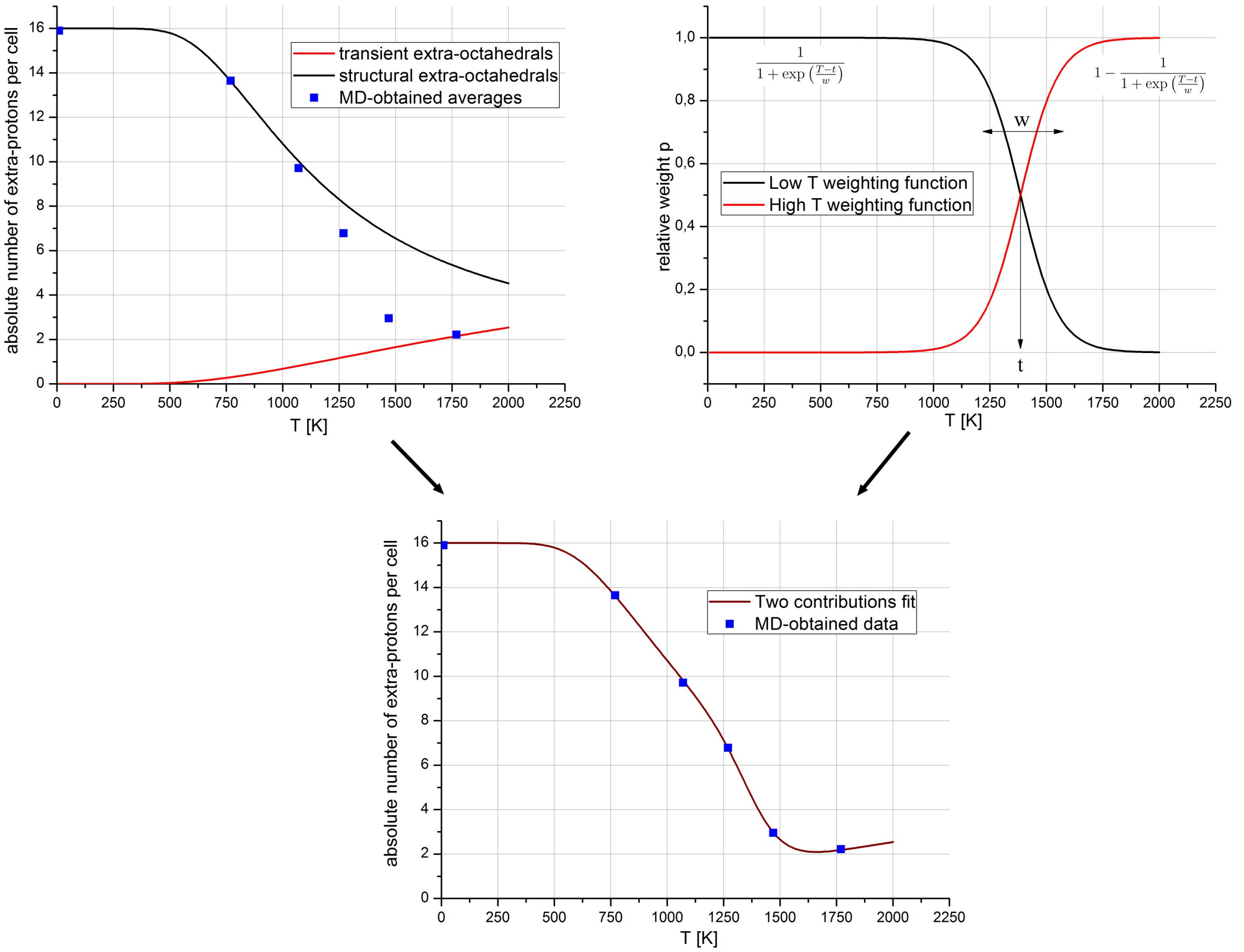

Figure 4.7: Fitting procedure on the basis of BaInOH at 5 different temperatures. The two postulated extra-octahedral species (upper left) are weighted with their corresponding Fermi-type functions (upper right) to give the complete fit (bottom).

siderations with respect to the simulation cell. Each of the 96 oxygen ions is taken to have 8 distinguishable proton sites, which is identical to the number of nearest oxygen neighbours. As already the number of structural extra-octahedral sites is 16 per cell; 8 sites located in two different layers. Due to the potential very large fraction of structural extra-octahedra protons, the number of remaining intra-octahedral sites has to be reduced from its ideal value being 8 times the oxygen number (96) per cell. Oxygens that form the extra-octahedral layer will not accommodate intra-octahedral protons due to steric hindrance. The number of intra-octahedral sites used was 389.

The concentration c_t of the transient extra-sites is determined by $\frac{1}{2}(4 \cdot 96) = 192$ the number of possible extra-octahedral sites for the four directions a proton can form a hydrogen bond to an oxygen belonging to a neighbouring polyhedron. 96 is the number of oxygen ions in the cell and the factor 0.5 prevents double counting. The number of ”regular” i.e. intra-octahedral here is taken as the optimum value of $8 \cdot 96 = 768$ as unlike for the structural extra-sites their degree of occupation is not very high.

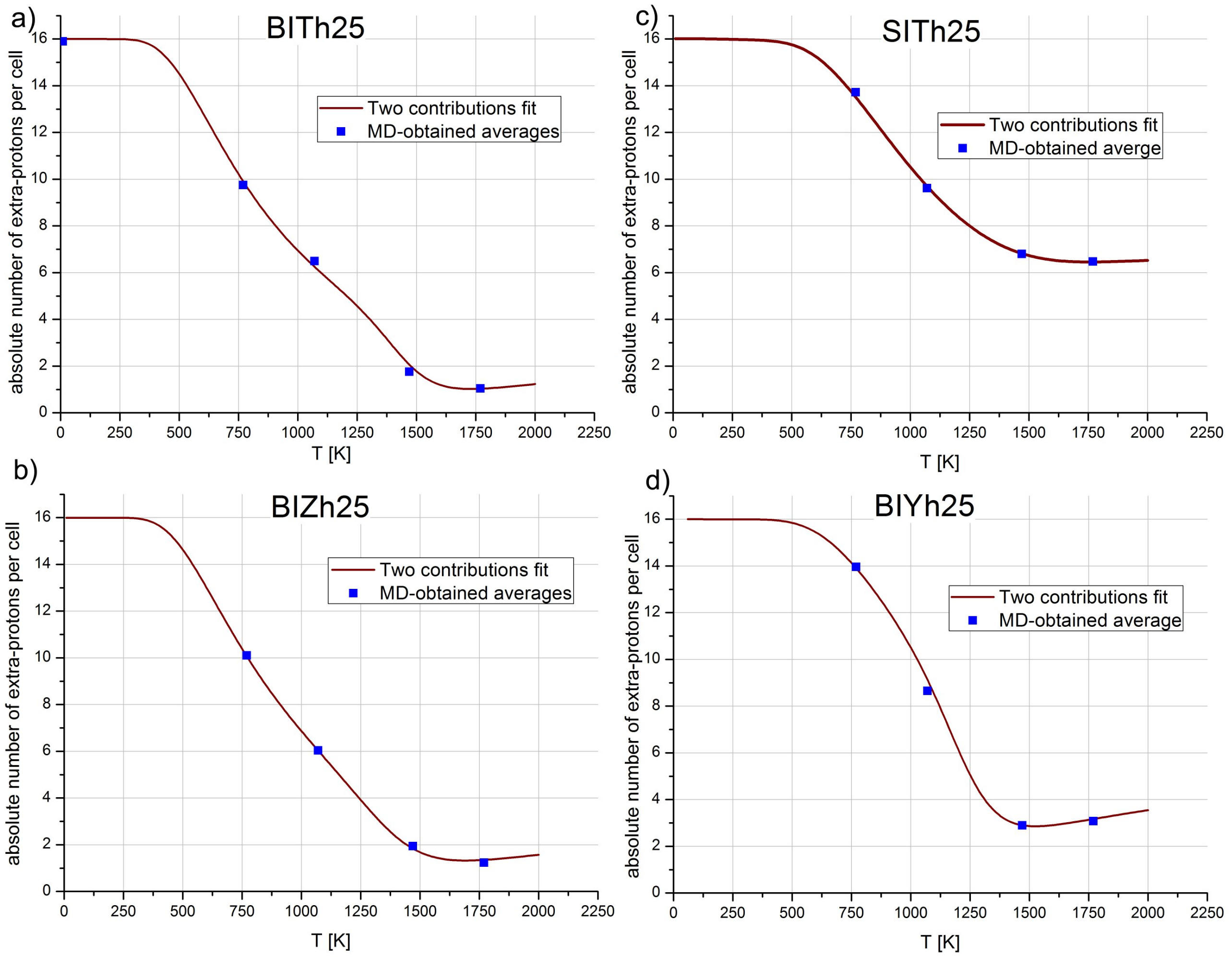

Figure 4.8: Number of extra-octahedral protons for 25% substituded compounds along with the fitted evolution. MD runs for all compounds were run at 500, 800, 1200 and 1500°C

Figure 4.7 provides an illustration of the fitting procedure for BaInOH based on MD runs at 500°C, 800°C, 1000°C, 1200°C and 1500°C. All graphs presented in the figures are scaled back to the absolute extra-number 16 to be compared with the actual MD numbers per simulation cell. ΔE_s is < 0 (energetically more favourable than the intra-position) whereas ΔE_t is > 0 indicating a less favourable energy than intra-octahedral protons. The ΔS term is taken to be identical for the two species. The two values that enter the weighting (Fermi) function are a ”transition temperature” t and a corresponding transition width w. The choice of this Fermi function does not have any particular physical meaning though. This procedure is plausible noting that particularly letting fade out the existence of the structural extra-octahedral protons

Table 4.II: Fitted energy and weighting parameters for the extra-octahedral proton content in 25% substituted compounds and BaInOH

	ΔE_s [eV]	ΔE_t [eV]	t [K]	w [K]
BaInHO	-0.335	+0.24	1350	120
BITh25	-0.270	+0.32	1440	90
BIZh25	-0.275	+0.275	1361	119
BIYh25	-0.350	+0.175	1230	95
SITh25	-0.38	-0.03	1580	236

may be justified by its cooperative character, i.e. the disappearing of the well defined layers containing the rhombus-shaped sites that accommodate the extra-octahedral protons. Put otherwise we deal with potential energy landscape which itself is temperature dependent and in this model is thought to segue smoothly from one state to the other.

Results for different compounds

The results for all 25% substituted compounds along with BaInOH are presented in figure 4.8 and table 4.II which contains the fitted energy differences and the two parameters of the weighting function. The latter ones will not be strictly interpreted, as they cannot be directly associated with an actual physical concept. The most important result are the differences in ΔE_s which directly reflect the stability of the structural extra-octahedral layers for the differently substituted compounds. Given the framework of the fitting procedure this energy delta may be identified with a gain in energy a single proton has by occupying a formerly empty structural extra-octahedral site. One obvious contribution to this gain is the stronger hydrogen bond that, on an average, is formed for structural extra-octahedral protons in comparison to regular intra-octahedral protons (see figure 4.1 in section 4.2 for example).

For what the comparative aspect is concerned we can clearly state that the stability of the low-temperature extra-octahedral structure is significantly influenced by the cationic substitution. The entirely Sr-substituted compound (SITh25) shows the most drastic deviation in having a considerably more stable extra-site (-0.38 eV per proton) both compared to its homologue BITh25 but also to all the other compounds. This is obviously due to the overall smaller lattice constant (and by consequence smaller O-O distances), which enables the formation of hydrogen bonds to a higher degree. This is true for the structural extra-octahedral layer but also with respect to the high temperature extra-octahedral protons SITh25 shows a particularity. It is the only compound to have a negative energy delta also for the transient extra-octahedral protons (which is plausible by noting the high number of extra-octahedral protons still at 1500°C). Figure 4.9 illustrates how small O-O distances do occur not only in the in-plane tilted extra-octahedral layer but also in other lattice planes. It is this structural feature that stabilizes the large number of extra-octahedral protons both at low and high temperatures. From a dynamical viewpoint this will also lead to an elevated rate of extra-octahedral proton transfer, what will be discussed in the section on the displacement rates 6.4.2.2.

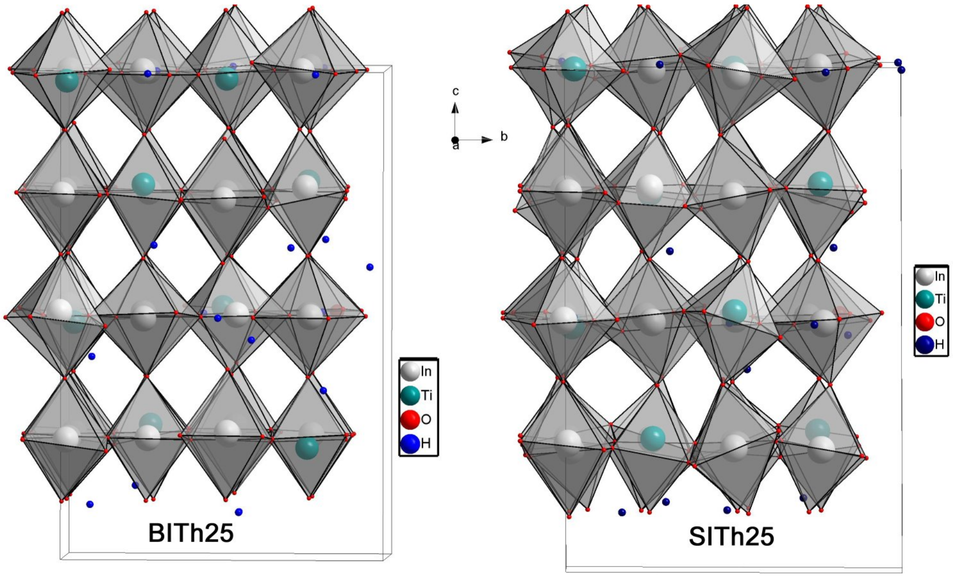

Figure 4.9: Front views of relaxed snapshots of BITh25 (left) and SITh25 (right) compounds indicating the pronounced octahedral tilt of the Sr-based compound.

Compared to the reference compound BaInOH, the expectation that an introduced cationic disorder destabilize the well ordered extra-octahedral layer is met by Ti and Zr. For both compounds energy deltas are considerably smaller than for BaInOH (-0.275 eV compared to -0.335 eV) indicating that at any temperature the extra-octahedral will be less perfect than for the pure compound. Put otherwise one could also speak of ”protonic vacancies” in the otherwise well defined extra-octahedral layer. This is one aspect to keep in mind for the assessment of the contributions to the general proton diffusivity.

The behaviour of BIYh25 is found to be particular as by virtue of the fitted parameter the low-temperature extra-octahedral proton stability appears at least unaffected (or even improved) by the substitution although the general structural framework remains similar to

BaInOH (in contrast to the SITh25 case where the entire structure is profoundly modified). A partial explanation could perhaps be given by the vibrational densities of state for the hydrated phases obtained by the MD-runs as presented in section 4.2.1. A closer investigation of the six presented figures there shows that no other substituent than Y does resemble the majority cation indium so closely with respect to its vibrational spectrum. So with respect to the extra-octahedral structure yttrium is the least influential cation-substituent which at least is an argument supporting the affirmation that Y does not *de*stabilize the extra-octahedral layer.

This big stability of the extra-octahedral layer in BIYh25 will also contribute to the remarkably favourable hydration energy that was obtained by the MD-simulations given in section 4.4.4. BIYh25 turned out to be the only compound to have a higher hydration energy than unsubstituted BaInOH. Furthermore this was found to be in agreement with the electronegativity tendencies (negative charge on the oxygen ions). However also the pronounced stability of the extra-octahedral protons found here necessarily does contribute to this favourable hydration energy.

Indirect experimental evidence from the thesis of S. Noirault [1] also does support the here found trend of extra-layer stability. In section 4.2 it was stated that up to a certain degree of substitution BIZh, BITh and BIYh exhibit a tetragonal crystal structure. Furthermore it can be safely assumed that a tetragonal structure is the manifestation of a protonic-layered structure. It turns out that the maximum degree of substitution with Y, Ti or Zr agrees with the finding of a significantly more stable extra-layer in BIY25. For this compound the tetragonal structure is stable at room temperature for x>0.35 (i.e. 35%, which was the maximum content studied). BIZh and BITh both crystallize tetragonally only up to between 20% Zr- or 25% Ti-content, respectively.

4.3.2 Trapping behaviour of different substituents

After having presented the differences that arise with respect to the structural extra-octahedral proton layer it is logic to ask how, on a local scale, the protons react to the presence of the different substituents. The key question is whether a given substituent acts as a trap or as an obstacle to the protonic motion, compared to the majority B-site cation being the indium. This will have implications on the expected diffusivity behaviour as e.g. proton trapping will (in a simplified view) decrease an effective diffusivity whereas an "obstacle"-effect supposedly would be less detrimental.

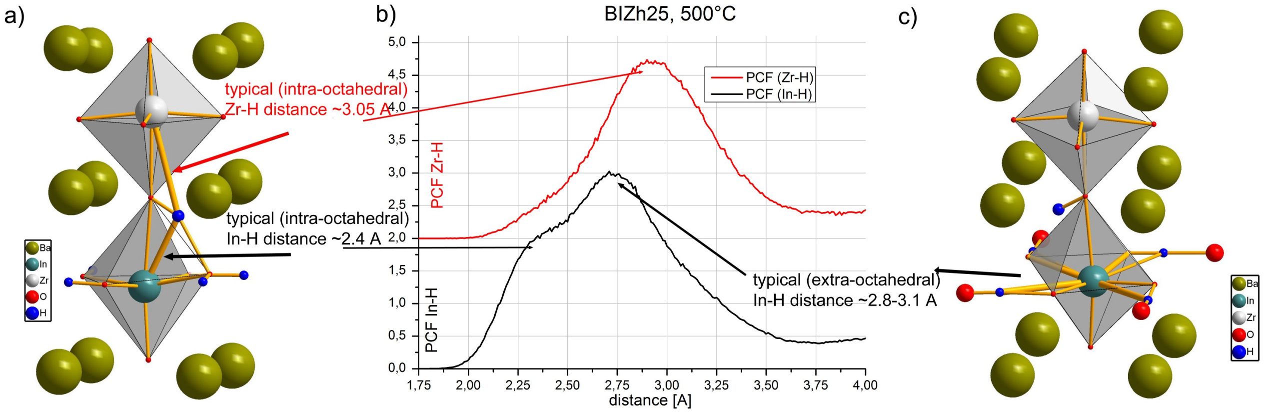

Figure 4.10: Illustration of the characteristic cation-proton lengths arising in BIZh25 (as example for all 25% substituted compounds): a) and c) show local structural situations and their manifestation in the PCF in b).

The means to do so based on the molecular dynamics simulations are the pair-correlation functions (PCF). By simply recording the corresponding cation-proton PCFs an idea of how attracted protons are to one or the other substituents compared to indium. More precisely one should speak of protons bound to oxygen that belong to oxygen ions that in turn belong to one of the three possible couples: Zr-O-Zr, In-O-In or mixed Zr-O-In (for the case of Zr as substituent). However, especially for the compounds with a low proton content (16 protons for BITh50 or BIZh50, 8 protons BITh75) the resulting statistical weight did not justify to categorize the proton association into these three classes. Moreover, for all compositions substituted to 25% the choice was made not to have two substituent-cations next to one another, which translates in the absence of any Zr-O-Zr constellations; an aspect which shall mimic a good mixing behaviour of the B-site cation couple In/Zr, In/Ti and In/Y.

The figures 4.10 a) and c) refer to a typical Zr-O-In situation with an intra-octahedral proton being covalently bonded to the bridging oxygen as well as four extra-octahedral protons. As indicated at 500°C the local structure is still relatively detailed. In subfigure b) we observe a superposition of several characteristic In/Zr-H distances. Concerning the intra-octahedral protons (case a)) the distinction is rather clear of having the proton being oriented away from a Zr-polyhedron as shown. For what the extra-octahedral protons are concerned the distinction between In and Zr is less evident as all distances Zr-H (intra- and extra-protons alike) lie all in the same range. For In (as is also shown for the pure BaInOH compound on the next figure 4.11) there is a clear separation between long distances for extra-octahedral protons and short distances intra-octahedral protons.

Figure 4.11 assembles in a comparative manner all B-site-proton PCFs for all investigated compounds at four temperatures from 500°C to 1500°C.

The reference compound BaInOH figures on top as of course only having the In-H PCF couple. A feature consistent with what was observed concerning the intra- and extra-octahedral protons is seen here by a shift of the coordination peak towards lower lengths for increasing temperatures. As already stated, short distances here are associated with intra-octahedral protons, whereas the peak at larger separations stems from extra-octahedral ones. The temperature evolution of these two kinds of proton sites was explained in the previous section and is consistently reflected in the PCFs, too. By 1200°C the characteristic double peak signature has completely vanished. This is an effect observable for the entire set of presented compounds. The merit of this comparison lies in the now visible qualitative differences between Ti, Zr and Y as substituents, with protons being effectively attracted by Ti whereas they are repelled by Zr and Y, all compared to indium.

Before coming to the further interpretation of the so obtained results, a more quantitative measure of the trapping/obstacle behaviour can be introduced. Therefore we define an (imaginary) cutoff radius r_{max} at which we determine the integrated value of the two PCFs In-H and S-H (for substituent). The cutoff value r_{max} is determined by the plausible requirement for the value of the sum of those two integrated PCFs to equal the number of protons present in the structure N$_H$:

$$N_H = N_{In} \underbrace{\int_0^{r_{max}} \frac{\langle n_{In}(r, r + \Delta r)\rangle}{N_{In}\Delta r} dr}_{P(In)} + N_S \underbrace{\int_0^{r_{max}} \frac{\langle n_S(r, r + \Delta r)\rangle}{N_S\Delta r} dr}_{P(S)} \tag{4.7}$$

This is an application of equation (2.2) from the "Methods" section giving an expression of the kind "number of particles B per particle A". N_{In} and N_S are the numbers of indium or substituent ions in the cell and N$_H$ is the corresponding total proton number for this compound. After having determined the r_{max} radius we obtain an idea of "how many protons are associated to one indium ion (or one substituent ion) by simply taking the single integrals (labeled P(In) and P(S) beneath the equation) at the cutoff radius. Having now an expression of the type "protons per cation", a convenient measure for the preferences can be given by dividing this ratio by another ratio which is a constant for a given compound: "total number of protons" by

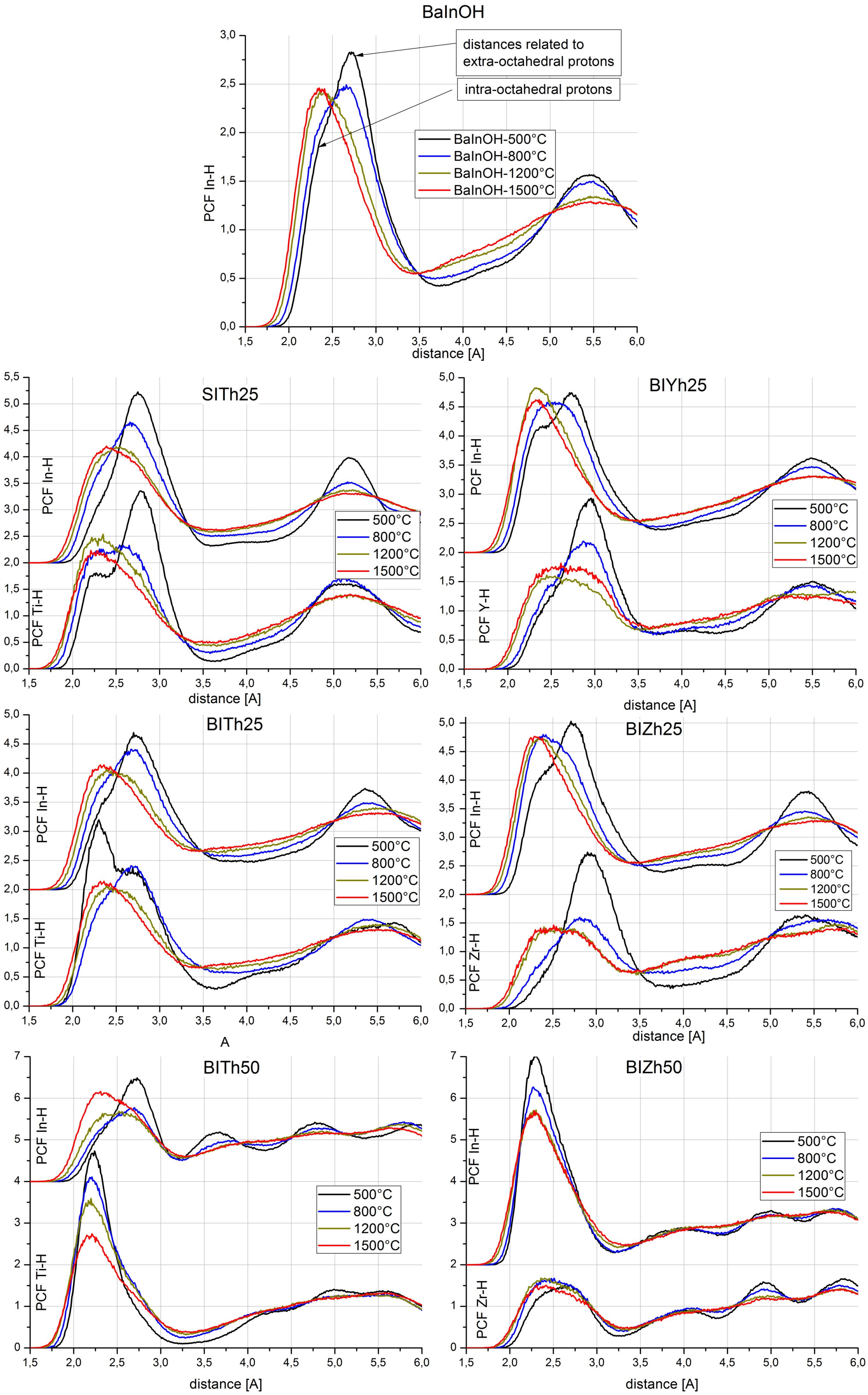

Figure 4.11: PCF of the couple B-site cation (In or substituent) and proton for all investigated compounds at four temperatures.

Table 4.III: Relative strength of proton association P'(In) and P'(S) in several substituted compounds

	500°C		800°C		1200°C		1500°C	
	In-H	S-H	In-H	S-H	In-H	S-H	In-H	S-H
BITh25	0.87	1.40	0.91	1.26	0.88	1.33	0.90	1.27
BITh50	0.44	1.56	0.55	1.46	0.59	1.40	0.85	1.13
BIZh25	1.17	0.43	1.19	0.41	1.16	0.51	1.15	0.55
BIZh50	1.60	0.38	1.46	0.536	1.39	0.59	1.42	0.58
BIYh25	1.15	0.58	1.15	0.57	1.14	0.58	1.11	0.67
SITh25	0.94	1.20	0.95	1.19	0.92	1.23	0.97	1.10

"total number of B-site cations".

$$P'(In) = \frac{P(In)}{N_H/(N_{In}+N_S)};\ , P'(S) = \frac{P(S)}{N_H/(N_{In}+N_S)}; \tag{4.8}$$

This takes into account the dependency between the proton number N_H and the number of alio-valent substituents[3]. A value of 1 for the two PCF couples therefore equals the case of a uniform distribution of the protons over the both cation species. Table 4.III gives the values of P'(In) and P'(S) for S = Ti, Zr, Y. To summarize, this property indicates the factor by which the proton association is higher or lower compared to the case of a pure random distribution of protons next to both of the present B-site cations.

In a very clear manner the results show significant tendencies. Firstly, for all compounds investigated we can state a clear preference for one or the other B-site cation. A closer inspection shows the special role of titanium, which in contrast to Zr and Y "attracts" protons considerably more than the indium cations present at the same time. Both for BITh25 and BITh50 for example we have a preference of Ti-H association by 40 or 56% at 500°C, respectively. Moreover the definition of P' allows a direct comparison between compounds with differing Ti and proton content and states that the preference for Ti in BITh50 is even stronger than in BITh25. Also in the Ti-substituted SITh25 compound, Ti is preferred but to a lesser extent than in the barium-based ones. On the contrary Zr and Y always exhibit values well below 1 indicating a distinct preference for the In in the corresponding compounds, i.e. they may be considered obstacles to the proton movement. Here again, closer inspection of the values shows

---

[3] For the simulation cells treated here, the B-site number always is 32 whereas the proton number falls between 32 and 16

a more pronounced separation for the BIZh50 compound (0.38 at 500°C) than for the BIZh25 compound (0.43 at 500°C). Also Y displays an obstacle effect, albeit to a lesser degree (0.58 at 500°C) than Zr again indicating the most pronounced similarity to In among the substituents. This fact is inline with the aforementioned aspect of Y, not to alter too much the intra/extra behaviour compared to pure BaInOH, as well as having very similar vibrational properties to In; all that in stark contrast to Zr and Ti as substituent.

The evolution with increasing temperature brings to light the very persistent character of almost all preferences as even at 1500°C (!) several preferences (BIZh50, BITh50 especially) are still very pronounced. This hints to the reasonable estimation of the energy differences to be in the range of several tenths of an eV. Unfortunately the exact behaviour with increasing temperature is somewhat ambiguous for no clear *trend* can be identified for all compounds. A reason for that may lie in the interference with the intra- and extra-octahedral behaviour, which contributes a supplementary interdependence (i.e. the question whether an intra/extra-octahedral proton is associated with an In- or Ti-octahedron). Due to the absence of the intra/extra aspect for the compounds substituted to 50% it is only there we can state the expected behaviour of the extent of the preference becoming smaller with increasing temperature[4] and supposedly be completely disappeared at still higher temperatures.

4.3.3 Blocking layer

As already mentioned in the introductory section of the hydrated reference material BaInOH, it displays a striking particularity compared to say proton-acceptor doped perovskites. This particularity is a crystallographically well defined oxygen site of the Brownmillerite structure that can be excluded to bind to protons. This has already been put forth by Jayaraman and co-workers [11] by considering bond-valence sums. Fernandez and co-workers confirmed this point of view by static structural DFT calculations of BaInOH and found a significant unfavourable energetic situation for protons attached to this O-site deliberately. Anticipating the results of the MD-simulations these particular oxygens indeed do constitute a genuine blocking barrier concerning the proton diffusion. A way to conveniently investigate this matter are atom-resolved pair correlation functions (PCF) i.e. to perform a local pair-distribution

---

[4] An exact treatment would neccessite an approach similar to the one used for the intra/extra aspect: a site counting concept (accounting for the configurational entropy) and a Fermi-like occupation statistic.

analysis. This is simply to achieve by the calculation of one PCF of the oxygen-proton couple for every single oxygen present in the structure the like of which there are 96 per simulation cell. This approach allows to check which oxygen sites were being bonded or not to any protons throughout the run time of the simulation.

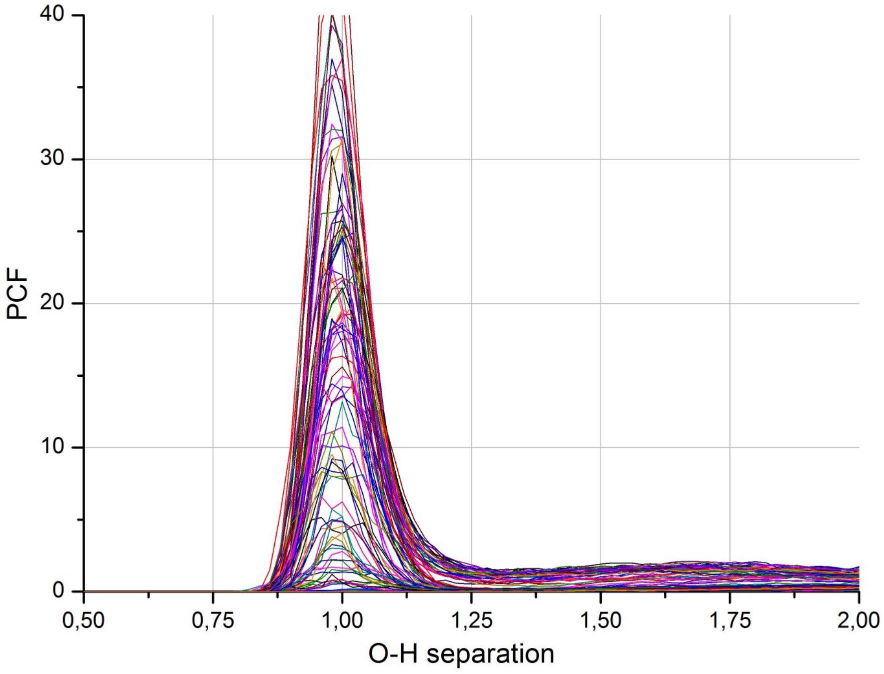

Figure 4.12: O-H PCF resolved for all 96 oxygen ions present in BaInOH at 500°C.

Important to notice here is the question, whether the statistical weight of the simulation is sufficient to do this kind of analysis. The parameters that enter are (for the BaInOH case as an example) 32 protons to potentially be distributed on 96 oxygen ions. Based on the investigation of the jumping and rotation rates (in forthcoming section 6.4) it can be deduced, that the slowest process is the stretch-activated hop of a proton which involves the breaking and reforming of its covalent O-H bond. At 500°C (i.e. the lowest temperature considered) the rate is about 0.33 per proton and ps which amounts to around 500 jump events for the 32 protons during a typical run time of 50 ps. This value compared to the oxygen number of 96 shows that we cannot actually speak of a sufficient sampling as despite the 500 jumps, many of them will be back-and-forth jumps which do not ”explore” new oxygens. More so, when the unvisited oxygen would energetically be less favourable, which however is the point to be proven. So no further quantitative conclusions (as for example averaged energy differences of different proton sites) will be drawn based on these considerations. However tendencies are unambiguously interpretable.

The oxygen-resolved PCFs quickly reveal an inequivalence of the oxygen ions in the structure for what their proton-acceptance is concerned. Figure 4.12 as an example presents the 96 overlaid single O-H PCFs for BaInOH (no substitution) at 800°C (a 65 ps run with 32 protons). The wide spread in the (integrated) heights at the covalent bonding distance of 1 Å indeed represents how inequivalent the oxygen ions are concerning proton association even in the non-substituted compound. Naturally the oxygen ions having the most intense contact to protons are the ones in the extra-octahedral layer (which still is structurally present at 800°C).

Singling out the oxygens with the smallest integrated PCF-intensities around 1 Å very straightforwardly identifies them as (predominantly) the oxygen ions being located in the plane which does not accommodate the extra-octahedral protons as is indicated in figure 4.13. The oxygen with no single proton contact (i.e. a PCF-value of zero) are marked in green whereas all others keep their standard color red. An equivalent analysis at 800°C (not shown) obviously smooths the situation somewhat, but also there the oxygen ions belonging to In(1) polyhedra remain almost proton-less.

What is shown in this figure can indeed be generalized to all the compounds with 25% substitution, too. BIZh25, BIYh25 and BITh25 all show an identical behaviour within the rather large tolerance of this approach. Hence this indicates not an immense impact of the substituent on this aspect. At 800°C the situation smooths out and about half of the formerly not accessible oxygen sites in the ”blocking layer” see at least some proton binding during the MD-simulation, however this does not yet guarantee that these protons may be transfered to the other side of the layer in a diffusive sense. This change at higher temperatures of course is reasonable by noting that the existence of the particularly proton-phobic oxygens in the In(1) layer is linked to the global structure also characterized by the intra/extra-octahedral layers, the stability of which was observed to decline considerably above 500°C in the previous section. It is left to note, that the underlying reason for the particularity of these sites is related to the binding lengths with the two B-site cations the oxygen is always connected with. By structural coincidence the blocking layer is therefore directly linked to the presence or absence of the extra-octahedral layer because they both are an expression of the overall layered character of the hydrated Brownmillerite structures.

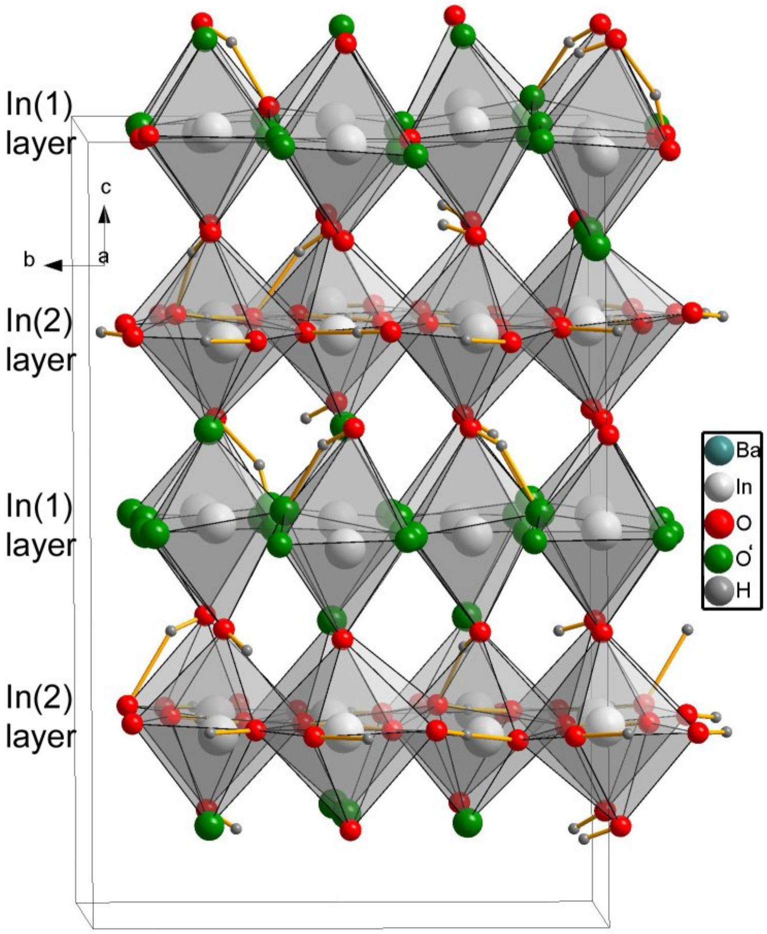

Figure 4.13: BaInOH structure: oxygen ions marked in green (O') have had no proton contact whatsoever during an entire run at 500°C. The two oxygen planes of the In(1) position are particularly affected.

4.3.4 Discussion of the structural properties of the hydrated compounds

General structural features of fully hydrated Brownmillerite-related compounds

This discussion section shall illuminate certain aspects of the last three sections which deal with local structural aspects. As presented, the three main topics that characterize the local structures of the hydrated Brownmillerite related phases is the presence of the intra- and extra-octahedral proton sites, the local trapping (or obstacle) behaviour of substituents and the existence of particular oxygen sites, that do not bind to protons and constitute a genuine proton-blocking layer.

Generally it can be stated, that the presence of protons elongates average cation-oxygen bonds when the unit cell is considered in a general view (as observed in the cell-volume increase upon hydration, see table 4.I). For the case of BaInOH (which does not mean a loss of generality

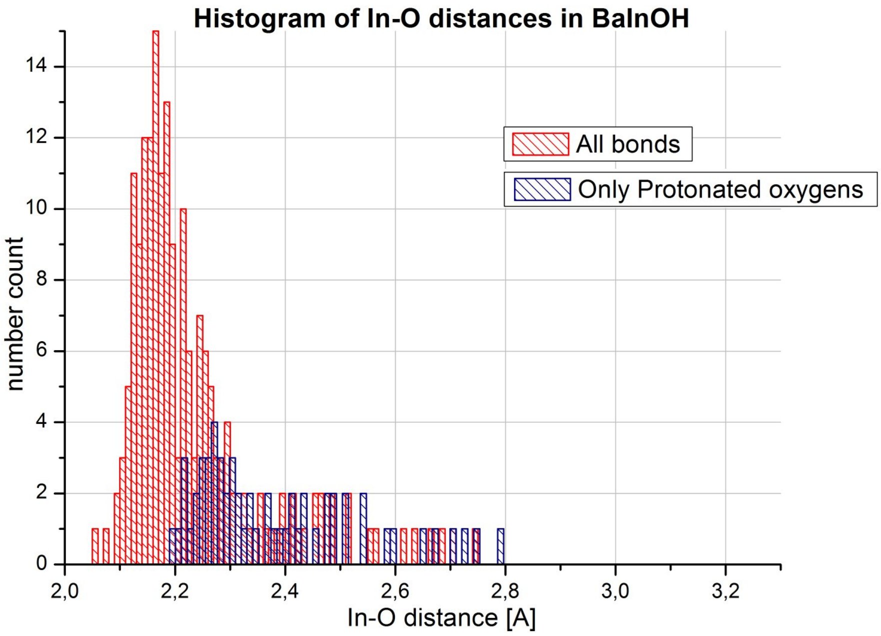

Figure 4.14: Histogram view of the In-O distance distribution in BaInOH. The structure is taken as a "snapshot" from 40 ps into a 500°C MD-simulation and afterwards fully relaxed. The entire set of the occurring In-O distances are given in red, the blue subgroup are the In-O distances of oxygens that are covalently bonded to a proton

concerning the substituted compounds, for that matter) a corresponding more accurate account is given in figure 4.14 in terms of actual In-O bond lengths. Clearly proton-associated oxygen show elongated bond lengths towards their two principal indium ionic bonding partners. This of course is easily to be interpreted by a reduced effective net negative charge of the internal O-H group, where formally the In^{III} does not anymore interact with an O^{-II} but an OH^{-}. In other words, to a certain extent the proton is capable of detaching the corresponding oxygen from its former structural location determined by the B-site cation.

Locally a closer inspection of a hydrated BaInOH cell shows that In-O distances are between 2.25 and 2.45 Å for oxygen ions that are bond to a proton compared to 2.05 to 2.15 Å for oxygen ions *without* a proton. This characteristics is regardless of the extra/intra-octahedral issue.

This means that the proton presence weakens the ionic cation-oxygen bond (in the case that ionic bond lengths may be taken as measure for that). So necessarily the situation is characterized by a local energy balance for the association of a proton:

(I) Loss of ionic bond energy (cation-oxygen bond elongation)

(II) The gaining back of possible strain energy which may have been present before the proton association (w.r.t. the oxygen-cation environment, or induced by the presence of a nearby proton)

(III) Gain of more hydrogen-bond energy than the proton was responsible for on its previous site (i.e. having the next-nearest oxygen now closer to the proton than in the proton's previous position)

(IV) Loss of strain energy *due* to this hydrogen bond (as e.g. seen for the oxygen marked with a green ”x” in figure 4.15, which is obviously torn out of its plane due to the hydrogen-bond with an intra-octahedral proton above it)

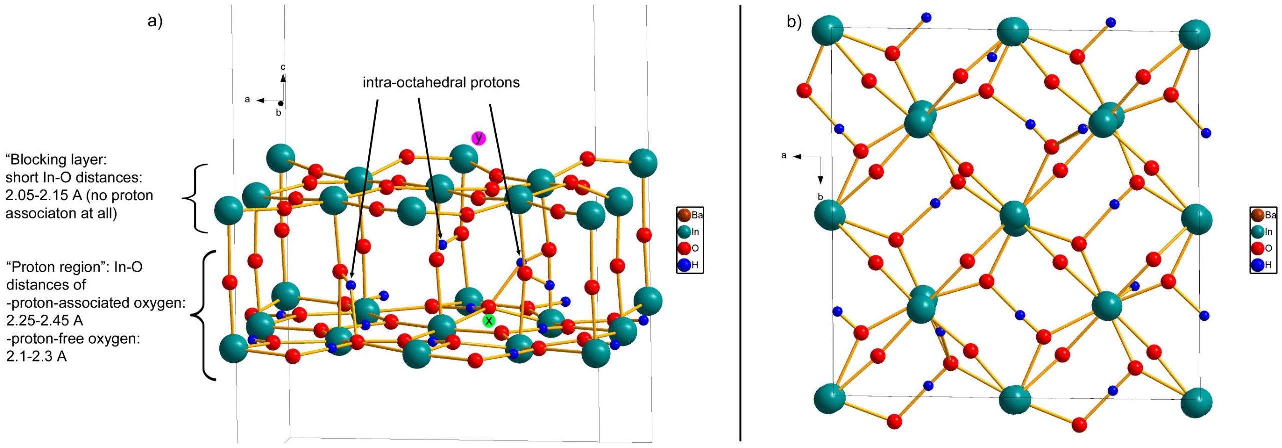

Figure 4.15: Alternative representation of a fully relaxed BaInOH cell (taken from a 500°C MD-run): a) side view, b) top view. The main interest is on the layers. The blocking layer (on top in a)) and the fully occupied extra octahedral layer (at the bottom in b)).

The existence of the distinctive structure of the hydrated Brownmillerite may be rationalized by a complex interplay between those aspects. Obviously the best energetical compromise is indeed to form two rather antagonistic local (but layer-wise extended, so perhaps rather 2-dimensional) structures being the extra-layer and the blocking layer, respectively. The great energetical advantage of the extra-octahedral layer is the very ordered and long ranged hydrogen-bond formation (i.e. maximum distances to a proton's next nearest oxygen neighbour of 1.7 A) which puts every proton in a very favourable position. By the energetical analysis presented in section 4.3.1 the order of magnitude of effective energy gain per proton could be estimated to be 0.3 eV. However inferred from the structural aspects (rather long In-O bond lengths) this situation surely decreases ionic bond energy between In and O.

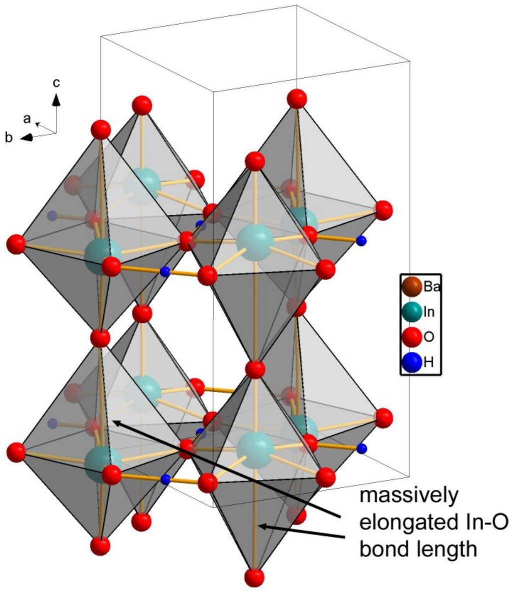

Figure 4.16: Hypothetical BaInOH structure comprised of two identical extra-octahedral layers. The overall structure is significantly less favourable than the real one.

Now although the proton content would allow the formation of a second extra-octahedral layer this apparently does not happen. A simple test-calculation of said structure indeed yields a stress free and consistent double-extra-layer for the entire structure. However this relaxed double layer structure leads to a very strong tetragonal elongation of the cell, effectively rendering the In-polyhedra extremely distorted (largest In-O distance 3.3 Å). Due to the collective character of the layering all indium ions are concerned with this large In-O distance thus decreasing massively one ionic bond per Indium which after all keeps this hypothetical structure hypothetical. Figure 4.16 gives an impression of that.

So the character of the second structural layer, the blocking layer is determined by a rather tight arrangement of a short distance indium-oxygen network that may not easily be penetrated by a single proton as this would cause considerable local strains. This layer is therefore maximizing the ionic-bond strength (i.e. the ionic bond energy content) in contrast to the extra-layer. As a compromise the remaining 50% of the protons (in BaInOH; less in the substituted compounds) are present as intra-octahedral protons (as marked in figure 4.15). By their presence they as well force the associated oxygen to ”lose” ionic bond energy (to elongate In-O distances), but this strain may rather easily be diverted by a slight out-of-plane shift of the In-ion in question (marked with a violet ”y” in figure 4.15). The momentarily proton-free oxygen ions inversely can tear their In-neighbours a bit closer and therefore create relatively strong ionic-bonds.

The substituent's impact

Concerning the behaviour of the different substituents studied here for the fully hydrated state some important similarities with their properties in the dry state can be established. The most pronounced effect associated with the substituents is their distinct trap or obstacle behaviour, i.e. the question whether or not protons are likely to be found next to a given B-site cation as observed by the PCF study in section 4.3.2. The crucial analogy between the hydrated and the dry state is the equivalence between the preference of a given coordination polyhedron in the dry state (section 3.3) and the proton trapping/blocking behaviour.

Remembering the basic chemical fact discussed above that oxygen ions that are covalently bonded to a proton lose ionic bond strength with their B-site cations with their respective bond-length becoming larger. Put otherwise protons are capable to so to speak ”detach” oxygen ions from their cation polyhedron. This is the only argument necessary to rationalize the preference of proton association at Ti-octahedra: by this detaching mechanism protons can enable the Ti-cation to adopt a very distorted local structure that will resemble more a pyramid (one proton attached) or a tetrahedron (two protons attached).

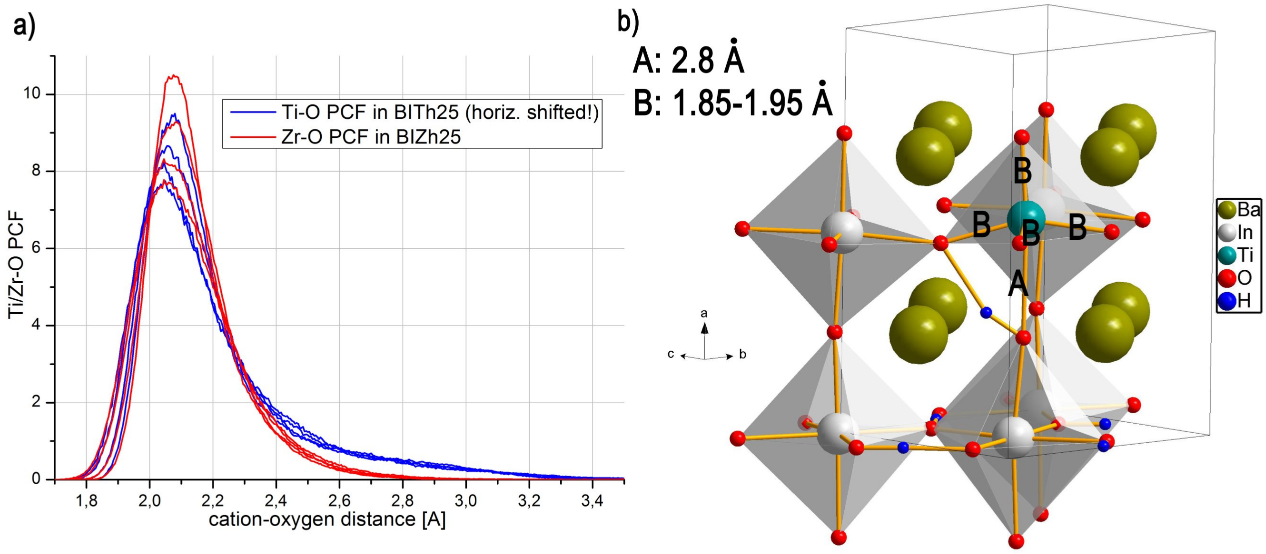

Figure 4.17: a) Ti-O and Zr-O PCF in BITh25 and BIZh25 (all temperatures are superposed); the Ti-O PCF has been shifted horizontally by 0.18 Å to better illustrate the relative behaviour b)

Vice versa the same is true for BIZhx and BIYhx: their pronounced dry state preferences for being octahedrally coordinated have exactly the logical consequence to *not* associate to protons. This enables them again on a local scale to maintain their preferred coordination.

Figure 4.17 a) illustrates this aspect by the representation of the Ti-O and Zr-O pair correlation functions in BITh25 and BIZh25, respectively. One has to note that the Ti-O PCF has been horizontally displaced by 0.18 Å for illustrative purposes. Not shown is the Y-O equivalent PCF from BIYh25, which however qualitatively matches the BIZh25 one. The aspect of interest here is the long-tail behaviour of the Ti-O graph which shows a very pronounced intensity at very large Ti-O distances for this however formally 6-fold coordinated fully hydrated structure. The oxygen ions which can be found at such large distances from Ti can unambiguously identified with oxygen ions associated with a proton. It can be noted that the Ti-O PCF is similar for all Ti-concentrations which were studied (6.25, 25, 50 and 75%) which of course is consistent with the Ti-H preferences given in table 4.III. Picture b) to the right hand side shows a structural example of a situation in which one intra-octahedral proton being associated to a Ti-polyhedron gives rise to an immense elongation of one out of the six Ti-O bonds of the formal octahedron. Noting the indicated gap in bond lengths of 5× ≈1.9 Å to 1×2.8 Å the "chemical" coordination of the Ti-cation in this case can rather be called a pyramid than an octahedron. Still in close analogy to the dry state it is the indium, which serves as very flexible buffer that allows other B-site cations present to realize their energetical optima be it tetrahedra or proton association for Ti, or octahedra and proton absence for Zr and Y.

To conclude, making reference to the XANES experiment presented in section 3.3.3 it is clearly following that the coordination of Ti in the hydrated state compound BITh25 still displays a remarkable pre-peak as was shown in figure 3.13 on page 63. By comparison the although formally 6-fold coordinated Ti is still significantly differing from the local structure in $BaTiO_3$ for what the pre-peak height and position, i.e. its distortion is concerned.

4.4 Hydration energetics in equilibrium

4.4.1 Introduction

This section shall present which kind of information on the energetic aspects of hydration can be obtained by static DFT-energy calculations as well as full molecular dynamics runs. It will be seen to what extent actual values may be confronted to experimental tendencies as well as inherently chemical properties.

Experimentally the de/hydration process can be evidenced by a number of different approaches. The most useful one is thermo-gravimetric analysis which directly allows to determine the two major thermodynamic parameters that characterize this chemical reaction: the energy/enthalpy and entropy of hydration E_h and S_h.

Another approach to the (de)-hydration process is possible by the *in situ* XANES experiment at the Ti K-edge that was conducted in the framework of the characterization of the titanium local structure as presented in section 3.3.3. By use of a temperature controlled sample chamber the dehydration process of a fully hydrated BITh25 sample was followed *in situ* from room temperature up to 850°C.

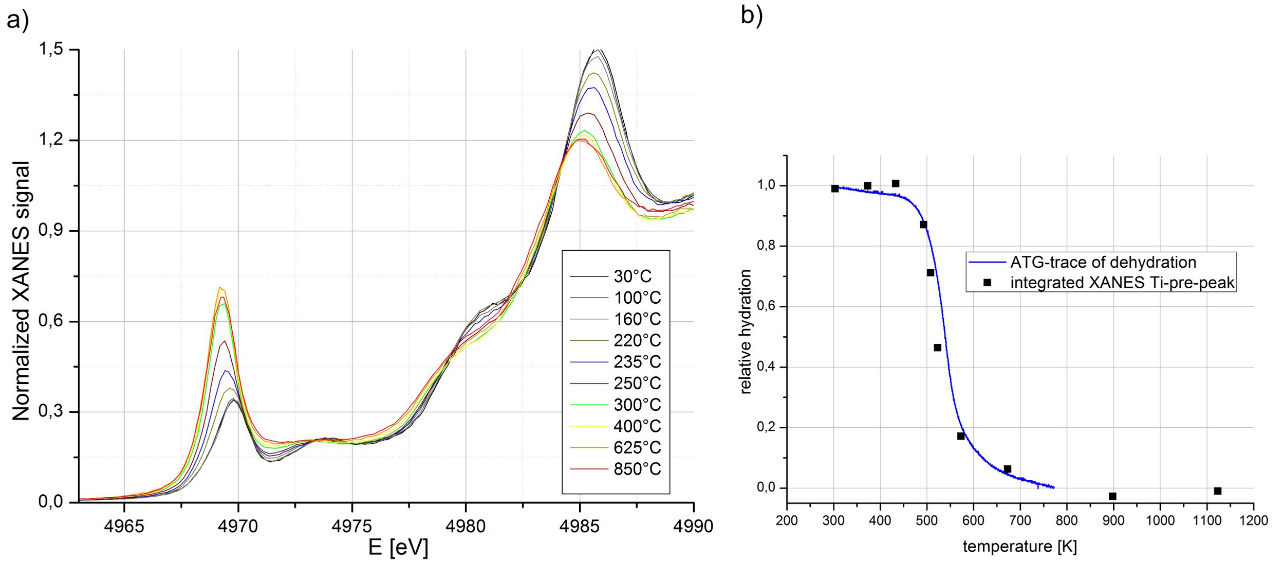

Figure 4.18: a) Series of *in situ* XANES spectra (Ti K-edge) following the dehydration reaction of BITh25 from room temperature to 850°C. b) The same reaction observed by a TGA experiment and as the relative change of the pre-peak area going from hydrated to dehydrated.

In figure 4.18 the two mentioned methods are presented to illustrate the dehydration process. The left hand side shows the overlaid XANES spectra of BITh25 from room temperature up to 850°C. The sample with the composition $Ba_2In_{1.5}Ti_{0.5}O_{4.5}(OH)_{1.5}$ becomes $Ba_2In_{1.5}Ti_{0.5}O_{5.25}$ and loses 0.75 H_2O molecules per formula unit and now contains stoichiometrically required oxygen vacancies. The structural change that gives rise to the XANES evolution is the change of coordination of the Ti^{IV} cation from distorted octahedral in the hydrated state to basically tetrahedral in the dry state for temperatures above 300° due to its preference for this coordination.

On the right hand side of the figure a TGA trace of an identical process is shown in blue. The scale is renormalized to 1 to become a relative degree of hydration. A tentative integral measure of the very distinct pre-peak of Ti is presented as well and shows good agreement to reproduce the process of de/hydration[5]. Within the accuracy the relative change of area of the pre-peak is therefore a measure of the degree of (de)-hydration.

---

[5] The ATG measure is courtesy of S. Noirault and E. Quarez of the IMN

Mostly it is from thermogravimetric data as shown in figure 4.18 b), that hydration energetics are obtained by fitting the temperature dependent proton-content with the equilibrium constant K of the hydration reaction $H_2O(g) + O_o + V_o^{\bullet\bullet} \rightarrow 2OH^{\bullet}$. When the de/hydration reaction is the only process taking place the mass loss can be directly converted to the current degree of hydration when the material was initially fully hydrated. The equation for the equilibrium constant reads [81]:

$$K = \frac{[H]^2}{[H_2O] \cdot [V_O] \cdot [O]} = \frac{4[H]^2}{p_{H2O}(c - [H])(6 - c - [H])} \tag{4.9}$$

where c is the fraction of (III)-valent cation on the B-site. By the further identity

$$K = \exp\left(\frac{-(\Delta H_h - T\Delta S_h)}{kT}\right) \tag{4.10}$$

the two relevant properties enthalpy and entropy of hydration ΔH_h and ΔS_h can be determined.

Many hydrated perovskite or Brownmillerite materials show hydration enthalpies comprised between -0.4 eV and -1.0 eV as well as corresponding entropies of $80\frac{J}{mol \cdot K}$ and $200\frac{J}{mol \cdot K}$, leading to substantial degrees of hydration for temperatures up to the region of 300°C to 500°C. By experimental tendency, ΔH and ΔS are rather proportional to one another. A handwaving interpretation is that the more energetically stable sites exist in a material, the smaller their concentration seems to be. I.e. the fewer permutations exist for a given proton to occupy one of them. This lowers the configurational entropy of protons in the material and therefore increases the entropy difference to the gaseous water molecule.

Concerning the total balance of the hydration reaction we can note, that the net number of covalent O-H bonds remains constant as they are just transferred from the water molecule to the interior of an oxide but there is a net gain of two ionic bonds inside the oxide for every water molecule incorporated, namely the bonds of the newly arrived oxygen to its two B-site cation neighbours.

The principal energetic contributions for the hydration energetics may be grouped into these three categories:

(I) A regain of a more or less large amount of oxygen-vacancy enthalpy of formation (or

equivalently, the creation of new ionic (rather iono-covalent) cation-oxygen bonds)
(II) A *difference* in the covalent O-H bond strength within the hydrated material compared to the water-molecule
(III) Formation of hydrogen-bonds O-H...O inside the compound for compounds with sufficiently small lattice constant (which is the case for almost all compounds studied here).

One can note that points (I) and (III) are in favour of the oxide hydration, whereas point (II) globally favours the existence of the water molecule what can be rationalized by noting that the "basicity" of a free, gaseous/aqueous OH^- will always outdo an oxide-internal oxygen. However there will be differences and tendencies between different compounds which are related to their electronegativity. Points (I) and (II) have been discussed since the 1990s (e.g. in review articles by Kreuer [81, 20], Norby and Larring [82]) to be the determining factors for differences in proton incorporation into binary oxides and acceptor-doped perovskites. However no conclusive all-explaining description can be given as there is a complex interplay between purely chemical aspects (basicity, electronegativity - point (II)) and more structural aspects like vacancy accommodation in the dry state, relaxation effects around these vacancies and relaxations around the actual doping/substitutive cations.

Having completely hydrated Brownmillerite compounds as a reference, point number (III) can be introduced as a criterion in its own right, as already pure $Ba_2In_2O_4(OH)_2$ accommodates 50% percent of its protons in very short length hydrogen-bond brigdes (as extra-octahedral protons). It will be seen, that the energetical contribution to the overall hydration energy is considerable and therefore the hydrogen-bonds are treated here as an additional main contribution.

Unfortunately the treatment of Brownmillerite-based compounds is not as straightforward as it is for acceptor doped perovskites. For the simplest case of having the perovskite as the frame of reference, a dilute cationic substituent/dopant and its charge-compensating oxygen vacancy can simply be treated as a perturbation being linked to a rather well defined energetic deviation. This energy would be called vacancy formation enthalpy. It takes into account the local deviation in chemical bonding situation ("two dangling ionic bonds") and associated crystallographic strain energies which however are very localized around the defect and therefore would increase rather linearly with the degree of perovskite-substitution. In perovskite oxides this kind of situation can always be considered energetically unfavourable. Therefore, as a result of hydration this energy may be accounted for as "regained", when filling up the vacancies and thus more or less recreating the initial perovskite. By calculation for instance one can rather successfully introduce a corresponding bookkeeping scheme that disentangles the contributions.

For $Ba_2In_2O_5$ based compounds there is no actual perovskite reference so that a "vacancy formation enthalpy" is rather hard to define (and to calculate). Nevertheless the creation of two new ionic In-O bonds per water molecule is still a fact which by definition has to contribute to the stability of the hydrated structure. In contrast the definition of a lattice strain of the Brownmillerite structure with respect to a hypothetical perovskite is not applicable and will therefore be implicitly included in the hydration energies that will be reported in later section. For what their actual total values are concerned however, hydration energies for Brownmillerite based as well as perovskite based compounds are not very different.

4.4.2 Experimental tendencies

The following table presents experimental hydration enthalpies and entropies for BaInOH, BIT, BIZ and BIY, the main compounds studied by the MD treatment later on as well as some acceptor-doped perovskite values.

Table 4.IV: Experimentally obtained hydration enthalpies and entropies. Indeces for ΔE_h and ΔS_h 1 and 2 signify either high- or low temperature regions (HT and LT) or hydration energies for regular-site/trap-site models. TGA-K fits refer to results according to equation (4.9)

	ΔE_h [eV](1)	ΔS_h (1) $[\frac{J}{mol \cdot K}]$	ΔE_h [eV](2)	ΔS_h (2) $[\frac{J}{mol \cdot K}]$	Reference
BaInOH	-0.3 (regular site)	-74	-0.76 (trap)	-74	2-level model in [83]
BaInOH	-0.90	-122	-	-	TGA-K fit[84]
BaInOH	-0.90	-	-	-	Zhang-Smith Model [85]
BITh20	-1.33 (LT)	-211 (LT)	-0.74 (HT)	-112 (HT)	TGA K-fit [73]
BITh40	-1.07 (LT)	-187 (LT)	-0.90 (HT)	-157 (HT)	TGA K-fit [73]
BITh60	-1.02	-189	-	-	TGA K-fit [73]
BIZh25	-1.12 (LT)	-160 (LT)	-0.77 (HT)	-109 (HT)	TGA K-fit [62]
BIZh50	-1.03 (LT)	-152 (LT)	-0.62 (HT)	-95 (HT)	TGA K-fit [62]
Y10%:$BaZrO_3$	-0.82	-88.9	-	-	TGA K-fit[81]
Y15%:$BaZrO_3$	-0.98	-83	-1.26 (trap)	-83	2-level model in [80]
Sc02%$SrTiO_3$	-0.22	-97.5	-	-	TGA K-fit[81]
Ba(Y/Sn)O_3	-0.83	-108.8	-	-	TGA K-fit[81]

As indicated in table 4.IV a unique enthalpy of hydration is very often not well defined.

Especially for compounds on the Brownmillerite side of composition where a high proton-concentration encounters a complex energy landscape, several temperature regions associated to different hydration energies seem to be more the rule than an exception. Notably for indium rich BIT and BIZ this is clearly evidenced: Giannici and co-workers [62] find two very well distinguishable regions of hydration energies for both BIZh25 and BIZh50, whereas BITh25 even exhibits a phase transformation as pointed out above again associated with different hydration energies. In both cases the more negative hydration enthalpy is associated with the low temperature behaviour and it decreases with increasing Ti or Zr content. Interestingly enough, the behaviour of BITh and BIZh may be seen as qualitatively similar, as the fitted hydration energies at low temperatures systematically seem to be larger than the hydration energies for the higher temperature regime. This behaviour might tentatively be rationalized by remembering the high proton concentration for the fully hydrated structures. Due to this high concentration protons act as constitutive elements of the structure and it is reasonable to rather consider the lack of one proton a defect, than their presence. Structurally this is the exact equivalent of what is generally observed for e.g. aliovalent perovskite-doping (introducing vacancies into the perovskite structure [81]). The higher the *defect* concentration the more the lattice may collectively relax or perform even some sort of defect ordering. These latter mechanisms in turn *decrease* the specific defect-formation enthalpy at high concentrations of the defect (which according to this argumentation would be the lack of protons). Concluding, this concept might be described as the first defect (proton-extraction in this case) being the hardest one to achieve.

Section 4.3.1 on the properties of the two distinct proton types intra- and extra-octahedral will support this concept of a collective stabilization of the protonic structure at high proton concentrations.

4.4.3 Hydration energies by static DFT calculations

When it comes to the determination of hydration enthalpies (or -energies in our case) by calculation this principally can be accomplished in a rather simple manner. DFT calculations permit to directly compare total energies of any given compound. The corresponding expression is

$$\Delta E_h = E_{hydra} - E_{dry} - n \cdot E_{H2O} \tag{4.11}$$

where the total electronic-ionic DFT energy of a completely dry compound and n times the energy of a single water molecule is subtracted from the total energy of a fully hydrated simulation cell. n is the number of water molecules that the hydrated cell has incorporated and ranges from 16 (BaInO to BaInOH) to 8 (for BIT50 to BITh50). The main problem however to assess properties of the hydrated state is its disordered character, i.e. the multitude of permutations of the protons in the simulation cell. This is true concerning the crystallographical sites and the immense number of permutations given the high proton content. Already for a rather small 24 atom cell of pure BaInOH, the number of crystallographically inequivalent proton configurations is around 100 [12], let alone the added complexity introduced by cationic substitution in an eight times larger cell. Moreover the uncertainty of the dry state's disordered structure with which the hydrated state is compared, enters to the same extent.

So as a first approach, a number of reasonably structured hydrated cells were investigated statically and the hydration energy was taken with respect to the *most favourable dry equivalent* which were presented in section 3.3.1. These most favourable dry configurations basically take the preference of coordination structure in consideration. Although with the pursued calculations we cannot be entirely sure, whether the dry or hydrated states are really the most favourable ones, the systematic comparison of a given hydrated structure to its most favourable dry counterpart sets some frame of reference. For what the actual hydrated structures are concerned, all simulation cells had the same cation distribution as the dry equivalent. Concerning the distribution of the protons, the BaInOH hydrated structure was taken as a reference and protons were removed accordingly in case of alio-valent substituents. Despite the evident shortcomings in terms of completeness of this kind of approach it nevertheless does show pretty well the basic principles of which kind of proton structure is likely to be realized. More detailed, figure 4.19 indicates the energetically most favourable hydrated compounds (related to the most favourable dry configurations) with the red symbols.

As can be seen, the numerical values of the hydration energies are in any case in the reasonable range of hydration energies obtained experimentally as presented in table 4.IV. For the Ti-compounds with 6.25, 12.5 and 25% the most negative hydration energy obtained stays about equal and decreases from 50% on rather harshly down to -0.4 eV for the 93.75% composition (which corresponds to 6.25% In-doped $BaTiO_3$). A clear trend for SITh25 as well as BIZh25 cannot readily established, albeit both values seem somewhat more negative. A significant result however might be the most negative hydration energy of -1.08 eV for BIYh50. Here and for BISc50 the protonic structure identically resembles the BaInOH reference for Y

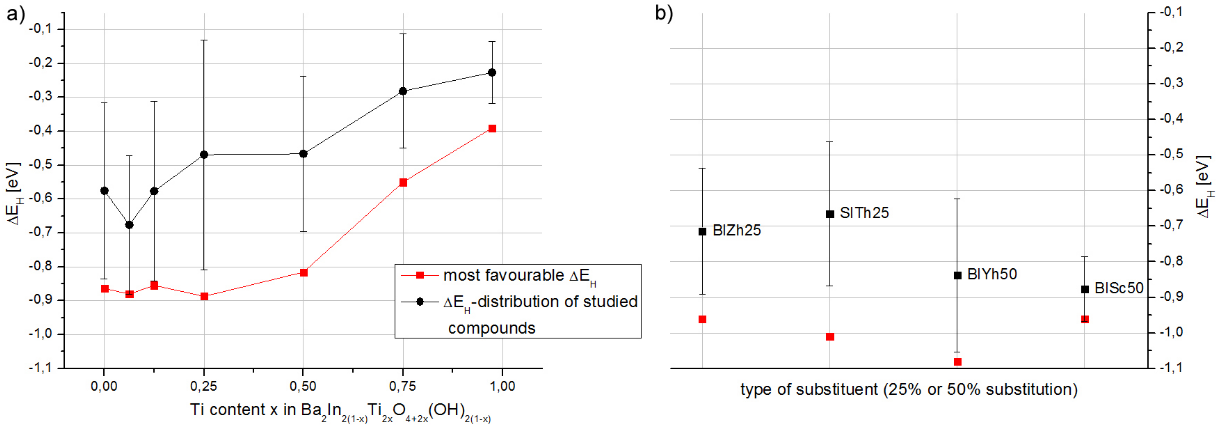

Figure 4.19: a) Set of statically obtained hydration energies along with the most favourable value as calculated by equation (4.11) for BITx compounds and b) for several 25% and 50% substituted compounds. The distribution of hydration energies (black line) has no significative character as it shall only give an idea of the energy range of structures tested. Their values are depending on the arbitrarily chosen test-structures. The "error" is the standard deviation of the set

and Sc are isovalent to In. Therefore the BIY50 and BISc50 values may immediately be compared to BaInOH, noting this significant increase for BIY50. The corresponding dry structure in this case is a perfectly ordered BIY50-Brownmillerite which respects the Y's preference for the octahedral coordination. Therefore the structural uncertainty of the BIY50 dry state is not very large, as very likely there is no better hypothetical arrangement for BIY50 within the Brownmillerite framework than having all Y inside the octahedral sheet and keeping the Brownmillerite overall structure.

This renders the static BIYh50 hydration energy value less ambiguous and hints toward an explanation on purely chemical grounds via the electronegativity/Bader charge concept as discussed in upcoming section 4.4.7. This is to be seen in contrast to the Ti or Zr substituted compounds, which have structures not being identical to the pure Brownmillerite due to the difference in oxygen vacancy content (dry state, w.r.t. BaInO) or proton number (hydrated state, w.r.t. BaInOH).

One of the most obvious tendencies, which the energetically most stable hydrated structures have in common is the persistence of the strongly hydrogen bonded structural extra-octahedral layer for degrees of substitution (0), 6.25, 12.5 and 25% which is equally the case for BIT, BIZ, BIY, BISc and SIT. This indicates the importance of the hydrogen-bond aspect in these highly protonated compounds.

4.4.4 Hydration energies and specific heats by molecular dynamics

As was stated in the previous section, the wealth of different oxygen vacancy or proton configurations for the dry or hydrated state, is a conceptual problem of disordered systems. The molecular dynamics simulation of sufficiently large disordered cells therefore have the potential to supply an accurately averaged idea of possible configurations. They open up the possibility to compare actual internal energies of both states and to obtain a thermodynamically more correct hydration energy than is possible with the ”guessed” static configurations that yielded the hydration energies in the previous section. A drawback of the approach lies in the elevated calculation cost which permits only a rather small number of runs at only some temperatures. The main problem is, that reliable internal energies are only available for rather high temperatures as it is essential, that the corresponding MD-runs have reached the ”true” structural distribution of oxygen vacancies (dry state) or protons (hydrated state). In the framework of this study, this is taken to be the case for temperature regions $\geq$ 1200°C for the dry structures in which the oxygen-ion (vacancies, respectively) need to equilibrate with respect to their thermodynamical equilibrium positions next to either B-site cation.

For the hydrated structures mostly only the three highest temperatures (800°C, 1200°C and 1500°C) are considered as all those temperatures yield substantial proton displacements to ensure a reasonable sampling of the potential energy landscape. One very serious implication of this approach is the smearing out of energetical particularities which have only small energy-differences. Therefore all phenomena that are related to energy differences of around 0.1 eV and smaller will essentially be absent. One aspect possibly affected by this issue are the collective extra-octahedral proton structures, which show a stability only up to around 800-1000°C. Thus the hydration energies calculated with MD-data will not be capable of exactly reproducing the direct experiment values as the latter include low temperature/low energy configurations as weak hydrogen bonds etc.

Equivalent to the simple equation for the static case (T=0 K) the hydration energy obtained by MD E_H at any given temperature is calculated by the same elements, now being thermodynamic averages

$$E_H(T) = \langle U_{hydr}(T) \rangle - \langle U_{dry}(T) \rangle - U_{H2O}(T) \tag{4.12}$$

with U being the internal energies of the fully hydrated or dry cell as well as the water molecule. U_{hydr} and U_{dry} are determined by the sum of the ”ionic-electronic” DFT total energy as supplied by VASP as well as the corresponding total kinetic energy of all ions present. The averages are the arithmetical means over the number of steps made during the MD-run which lie in the range of several 10.000 steps where the first ≈20% of the run were simply omitted to ensure thermalization. The internal energy of the water molecule is determined by the sum of its total DFT energy and the temperature dependent contributions of its translation, vibrations and rotations. These are given by the molar specific heat of the molecule defined by $c_v = \frac{f}{2} \cdot k_B$ with f being the degrees of freedom. For the water molecule we have 3 translational, 3 rotational and 3 vibrational degrees of freedom. These three vibrational degrees split up into a potential energy part and a kinetic energy part giving 6 total degrees of freedom linked to the vibration which gives f the value 12 and fixes c_v to yield

$$U_{H2O} = E_{H2O-DFT} + c_v \cdot T = E_{H2O-DFT} + 6 \cdot k_B T. \tag{4.13}$$

Very importantly, as the VASP-based molecular dynamics routine is entirely classic, important quantum effects are not included in the direct simulation. This concerns predominantly the discrete character of the energy levels of atomic vibration, which gives rise to the low-temperature Debye-like behaviour of the specific heats as well as the zero-point vibrational energy (which will be discussed in section 4.4.5). Therefore in the MD framework the internal energy of the studied compounds increases strictly linearly with increasing temperature (i.e. has a constant c_v down to zero-temperature).

Figure 4.20 a) exemplifies this fact for BIT25 and BITh25, respectively, showing the evolution of their internal total energies. The error bars on the energies are of the order of the line width in this representation according to what was stated in section 2.5.

Also the method of how the hydration energies are obtained is indicated. Each internal energy evolution is fitted linearly with the resulting linear functions $U_{dry}(T)$ or $U_{hydr}(T)$ being inserted into equation (4.12). The corresponding results for all compounds are shown in subfigure b) and c) along with the fitted parameters which are the MD-obtained hydration energy E_H (which corresponds to the intersection with the energy axis) and a Δc_v (corresponding to the slope). For all substituted compounds the MD simulation yielded a very linear behaviour what also can be seen in figure Figure 4.20 a).

The hydration energies in the inset table are very clearly indicating the influence of the choice and quantity of substituent for indium. Concerning this high-temperature hydration energy an increasing Ti-content clearly decreases significantly the favourability of hydration as seen in the values from BaInOH up to BITh75. Also the values for the two Zr-substituted

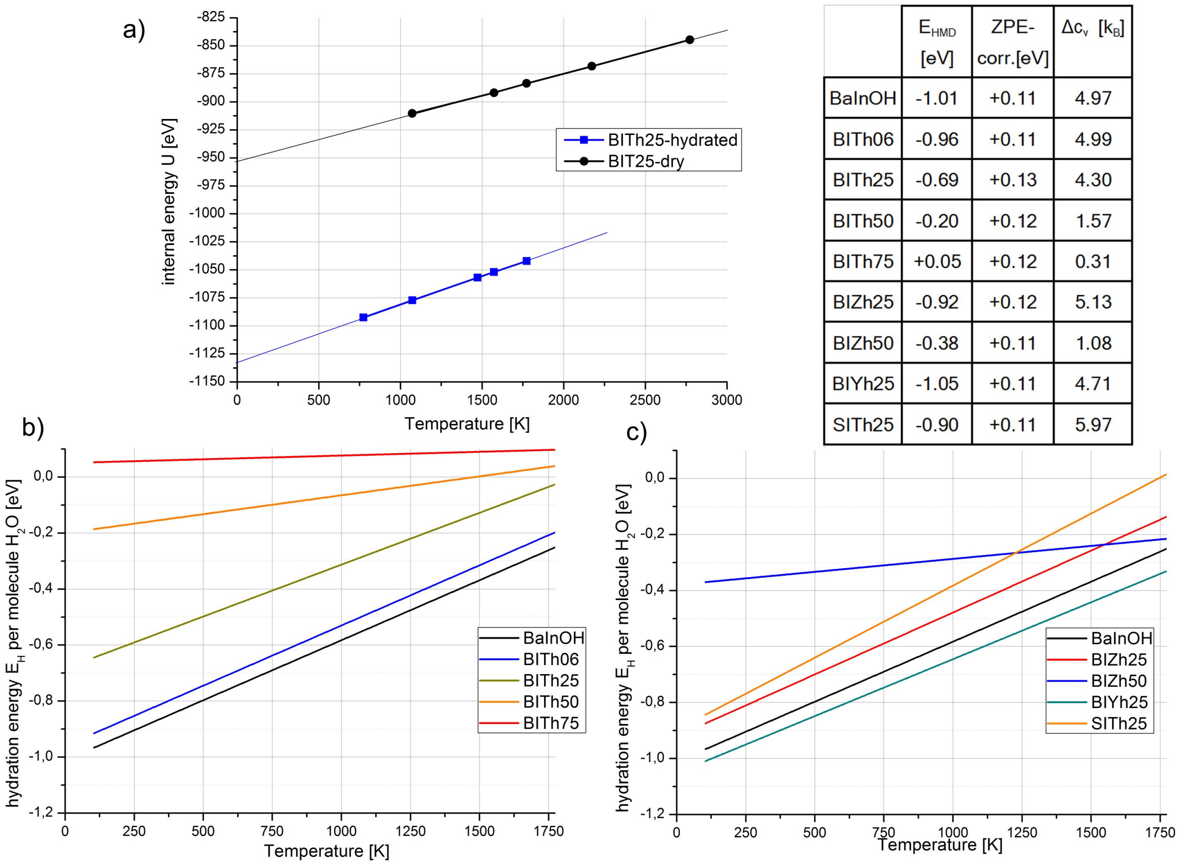

	E_{HMD} [eV]	ZPE-corr.[eV]	Δc_v [k_B]
BaInOH	-1.01	+0.11	4.97
BITh06	-0.96	+0.11	4.99
BITh25	-0.69	+0.13	4.30
BITh50	-0.20	+0.12	1.57
BITh75	+0.05	+0.12	0.31
BIZh25	-0.92	+0.12	5.13
BIZh50	-0.38	+0.11	1.08
BIYh25	-1.05	+0.11	4.71
SITh25	-0.90	+0.11	5.97

Figure 4.20: a) Example of linear internal energy evolution with temperature for BIT(h)25; hydration energies obtained via equation (4.12) by DFT-MD for b) increasing Ti-content and c) alternative Zr,Y or Sr substituted compounds. The table presents the actual hydration energies E_h per water molecule, the order of magnitude of the quantum correction and the Δc_v which equals the slopes in b) and c)

compounds (BIZh25 and BIZh50) show a decrease of hydration energy, although not as severe as for Ti. Clearly one observes an important contrast to the statically obtained hydration energies in section 4.4.3 which were based on ”plausible” hydrated and dry structures representing the energetically most favourable cases for these two classes. From these static calculations especially *no* evolution with the Ti-content from BaInOH up to BITh50 was observed with the best hydration energy remaining at about -0.95 eV as presented in figure 4.19.

The obvious presence of a temperature dependence of the hydration energies stems from the fact, that the hydrated and dry phases exhibit different specific heat capacities (even when the specific heat of the water molecules is added to the dry case). Given the constant volume MD simulation, these are specific heat coefficients at constant volume, c_v. These Δ c_v take the role of a difference in heat capacity between a gaseous water molecule and its former constituents inside the material (i.e. one oxygen and two protons). This difference indicates that the latter ones show a larger specific heat capacity than the gas molecule. This may be rationalized by noting, that a total number of 12 degrees of freedom (6 vibrational, 3 rotational, 3 translational) for the water molecule are traded in for 18 internal vibrational degrees of freedom inside the material. This equals the 3 vibrations for each of the 3 ions multiplied by two to account for the kinetic and potential energy character of their vibrations.

The following three sections will be dedicated to the more detailed study and discussion of the three aspects given in the table in figure 4.20: the zero point energy correction (section 4.4.5), the specific heat coefficients (section 4.4.6) and finally the actual hydration energies (4.4.7).

4.4.5 Zero point energy (ZPE) correction

In order to approach further the real experimental values it is necessary to apply a quantum correction to the hydration energies. This quantum effect which is not included in any of the DFT-calculations directly manifests itself as an increase in energy compared to the ground state electronic/ionic energy which can be determined by DFT at T=0 K. This holds for any quantum particle which is located at the minimum of a concave potential. For the special case of the harmonic potential (being a reasonable approximation for all chemical bonds in a solid at low temperatures) quantum mechanics (in agreement with the Heisenberg uncertainty principle) states an energy offset of $\frac{1}{2}\hbar\nu$. Thus when it comes to energetically compare two systems with different vibrational properties differences in the total ZPE can arise because of the dependence on the frequency (the wavenumber ν).

Especially given the fact that we deal with the comparison of H_2O as a gas and with one O and two H "inside" a material notable zero-point vibrational energy differences are likely to occur. As was the case for the increased specific heat for the hydrated material compared to the dry ones (plus the water molecule), it is the increased number of high-frequency vibrational modes that makes the difference. These arise due to the two now independent protons inside the compound (having a total of six vibrational modes) compared to the water molecule having only three vibrational modes of the same order of magnitude.
Thanks to the availability of the vibrational spectra of either type of cell the absolute vibrational zero-point energy for a given simulation cell can be obtained via

$$E_{ZP} = \frac{1}{2}\int^{\infty} \hbar\nu g(\nu) d\nu \tag{4.14}$$

which is the absolute energy of the first occupied vibrational level of any mode which occurs in every compound. g(ν) is the vibrational density of state as presented in the sections on the vibrational properties. So the correction is then given by

$$\Delta E_{hZP} = E_{ZP}(hydrated) - (E_{ZP}(dry) + E_{ZP}(H_2O)) \tag{4.15}$$

with the ZPE of the gaseous water molecule taken as $E_{ZP}(H_2O) = \frac{1}{2}\sum_i^3 \hbar\nu_i$ for the three molecular vibrational modes.

As this correction concerns the actual low temperature properties, the used DOSs should be the ones obtained at the lowest temperature. Equivalently also the frequency spectrum obtained by the lattice-dynamics harmonic approach can be used. Either spectrum has to be normalized to the number of vibrational degrees of freedom per cell to yield a comparability to the total energy of the cell.

The calculation of the ZPE correction yields values that render the hydration energies less favourable hydration energies of 0.1 to 0.13 eV for all investigated compounds (BaInOH, BITh06, BITh25, BITh50, BITh75, BIZh25, BIZh50, SITh25, BIYh25) with no particular dependency observable. The corresponding detailed values are given along with the hydration energies in figure 4.20.

To conclude we note, that what is obtained by the Fourier-transform of the velocity autocorrelation function of an MD-run as well as by the solution of the dynamic matrix, does not strictly represent the entire range of the requested density-of-states g(ν). In fact, a small portion in the low-k value/long wave-length part of the spectrum is lacking due to the finite cell-size, which excludes collective vibration modes of larger wave length than the cell dimensions. However the change of the DOS due to these contributions should be small because the cell size is nevertheless considerable.

4.4.6 Specific heats as obtained by molecular dynamics

Specific heats of hydrated and dry compounds

The table 4.V gathers the specific heats c_v for the high temperature region of the single compounds (dry and hydrated) in units of k_B which are the absolute specific heat capacities of the materials. Columns I and II are given normalized to the variable particle number according to the degree of substitution (varying oxygen number for the dry compounds, varying proton numbers for the hydrated compounds). For a better comparison column III and IV also give the absolute values per simulation cell and including, in the case of the dry compounds, the contribution of the appropriate number of gaseous water molecules (i.e. $n \cdot 6k_B$). Thus the aforementioned Δc_v are represented by the higher values in column IV compared to column III which compare systems (dry+water $\Leftrightarrow$ hydrated) with identical particle-content.

In addition to the systematically higher c_v for the hydrated structures (for a fixed cation situation) we can also state significant differences within the sets of hydrated and dry compounds especially depending on the degree of substitution. These are appropriately represented in columns I and II, given per particle. Within the set of dry compounds, structures with a higher content of oxygen vacancies give rise to a larger specific heat. Equally within the set of hydrated compounds those with the highest proton content show the highest specific heat coefficients. This is observable for the compounds with increasing Ti-content from BaInO(H) to BIT(h)75 with the number of oxygen vacancies and protons decreasing, respectively, for increasing Ti-content. Comparing BaInO(H) with BIZ(h)25 and BIZ(h)50 yields the same tendency.

c_v $[k_B]$	I dry (per particle)	II hydrated (per particle)	III dry+$H_2O(g)$ (cell)	IV hydrated (cell)
BaInO	3.20	3.31	557	637
BIT06	3.18	3.30	551	627
BIT25	3.08	3.15	527	579
BIT50	3.08	3.01	517	530
BIT75	2.97	2.91	488	489
$BaTiO_3$	2.87	-	539	-
BIZ25	3.12	3.23	534	595
BIZ50	3.02	2.93	508	516
BIY25	3.13	3.44	535	634
SIT25	3.15	3.32	539	610

Table 4.V: Specific heat capacities given in units of k_B. Columns I and II are given per particle in the corresponding simulation cell. Columns III and IV are given per entire simulation cell. Col III is the sum of the dry simulation cell and the c_v of the corresponding number of gaseous water molecules ($6\,k_B$ per molecule) that the corresponding hydrated structure contains.

One major point of interest here is the extent to which the value of a given compound deviates from the value 3 k_B, which (in a purely classic framework as the VASP-MD) is *the* specific heat coefficient per particle of an ideal solid which consists exclusively of harmonically oscillating ions corresponding to the Dulong-Petit law (or better the high-temperature limit of the Debye-approximation).

Concerning this ideal vibrational behaviour however it is difficult to ultimately decide whether the value 3 k_B is actually supposed to be valid for the VASP-molecular dynamics routine, employing the Nosé thermostat. Hoover [86] was the first to show, that for the special case of an imposed pure harmonic potential, the Nosé thermostat leads to a non-ergodic behaviour, i.e. does not sample the phase space of the harmonic oscillator properly. Nevertheless the following discussion part will show that the relative differences between the compounds do have significance.

Discussion of the specific heats

Vibrational contribution

A comprehensive explanation of the detailed behaviour of the specific heat coefficients is outside the scope of the work, as very subtle effects are known to govern what might generally be called anharmonicity, i.e. any deviation from the Dulong-Petit high temperature behaviour. Nevertheless a qualitative account shall be given in the following.

Generally the main factors which influence the non-harmonicity of specific heats, can be divided into vibrational and structural effects. The truly vibrational effects in turn may be treated as a superposition of the so called quasi-harmonic treatment (as e.g. described in [87]) and a genuine anharmonicity of a given vibrational mode. Here the quasi-harmonic treatment does not substantially differ from the purely harmonic one, except in allowing for a certain variability with respect to some parameter of any given mode $\omega(X)$, which however rests a purely harmonic vibration.

The quasi-harmonic approximation is conveniently characterized by a free-vibrational energy of a solid given for example as

$$F_{qh}(T) = \sum^{N} \left\{ \frac{\hbar\omega(X)}{2} + kT \cdot ln \left[1 - \exp\left(\frac{\hbar\omega(X)}{kT} \right) \right] \right\} \tag{4.16}$$

with $\omega(X)$ depending on a structural variable as the volume or bond-lengths etc. The specific heat follows by double differentiation with respect to the temperature:

$$c_v = -T \cdot \frac{\partial^2 F_{qh}(T)}{\partial T^2} \tag{4.17}$$

A simple numerical study shows that given the variability of ω this approach already yields specific heats, that exceed the $3k_B$-value at high temperatures at the condition that the vibrational frequencies *decrease* with increasing temperature/bond length/volume (which is considered the largely predominant case). In this picture, longer bond lengths lead to an increase of specific heat due to the softening of vibrational modes. A very thoroughly conducted DFT investigation on the specific heat of pure metallic aluminium by GRABOWSKI and co-workers [88], very illustratively puts this approach into comparison with a genuine anharmonicity, i.e. a deviation from the parabolic shape of the effective interaction potential. By comparing complete DFT-molecular dynamics runs (which include every contribution) with a set of bond-length (i.e. volume-) dependent normal-mode-analysis calculations they manage to ascribe only a very small contribution to the excess-specific heat to this "genuine" anharmonicity. This anharmonicity is taken as the difference between "measured" total c_vs by molecular dynamics runs and calculated c_vs by the quasi-harmonic approach.

This anharmonicity turns out to have a *diminishing* effect on the total specific heat, which very often is assumed to be the opposite (as discussed in [58]). Their observed total increase of specific heat with temperature is caused by the quasiharmonic implicit T-dependence of the harmonic vibration modes modified by a small reduction due to the "real" anharmonicity.

An (experimental) study on $BaTiO_3$ [89] identifies this compound as rather likely to exhibit a low-temperature anharmonicity for the cubic-phase (i.e. above 120°C) which is due to the "frustrated" potential of the Ti(IV)-ion inside the too large oxygen octahedra.

Concerning the current study it has to be remembered however, that all MD-runs were strictly made at a constant volume of the simulation cell. Therefore no actual volume-expansion effect on the potentials may be expected, which normally accounts for the variability of $\omega(X)$ within the quasi-harmonic approach. Nevertheless vibrational spectra of the Brownmillerite based compounds at different temperatures show a slight temperature dependence (lower frequencies for higher temperatures). The evolution is not striking but a small positive contribution to the excess of specific heat might be attributed to it due to the quasi-harmonic effect.

The genuine anharmonicity is not easily identifiable. However it can be estimated based on what was presented in section 3.2 for $Ba_2In_2O_5$ and $BaTiO_3$. There the two reference compounds $Ba_2In_2O_5$ and $BaTiO_3$ were examined at a low temperature (500°C) with respect to their vibrational potential supplied by their pair correlation functions. $Ba_2In_2O_5$ was identified having a rather harmonic vibrational potential in contrast to $BaTiO_3$ which shows a pronounced shoulder (which only vanishes above 800°C - not shown). The corresponding low temperature specific heat coefficients presented in this section showed that for a material having rather harmonic potentials (as was shown for barium-indate) and no activated structural degrees of freedom the value for c_v can be expected to be around 3 k_B. By comparison with barium-titanate with its specific heat of 2.87 k_B it becomes evident that kind of genuine anharmonicity has a tendency to lower the specific heat coefficient. However the case of $BaTiO_3$ can be regarded as special as was presented in section 3.3 where in the vast majority the pair correlation functions of the substituted dry compounds as BIT06, BIT25 or BIZ25 etc. do not show such strong anharmonicities in their free energy profiles of any of the PCF couples (Ba-O, Ti-O, Zr-O etc.).

Structural contribution

A yet to show more important aspect of the c_v-differences again is the disordered character of both the dry and hydrated compounds, with their oxygen-vacancy or proton disorder, respectively. They give rise to a number of differing internal energy levels (i.e. the distribution of the oxygen vacancies next to Ti/In or the multitude of protonic sites being not equal in energy). In case those different energy levels inside the material are thermally accessible at a given temperature, these act as structural degrees of freedom and may contribute considerably to the specific heat of the compound as a structural specific heat.
In order to estimate this contribution two model systems may be taken as examples. These examples will again be employed in the framework of the kinetic Monte Carlo studies presented in section 5.2.1.

One of them is the so called random-trap (RT) potential energy landscape, which will be introduced more in detail in section 5.2.1 however focusing on its diffusive properties. Concerning this model we deal with an (in principal) smooth uniform distribution of site-energies within a range from 0 to E_{max}. Analytical determination of the average energy of one particle in such a potential yields a constant structural c_v of practically $1k_B$ up to a temperature which depends on the width of random energy distribution on this lattice e.g. being of the order of 1000 K for a uniform distribution $0 \ldots 0.4$ eV.

The other analytically solvable model is a two-level system characterized by two kinds of sites for particles to reside on separated by a single ΔE. This kind of approach was already employed in section 4.3.1 for describing the intra- and extra-octahedral energetics. The occupation statistics of this kind of system is described by an analytical Fermi-statistics expression (see equation (4.2) on page 92). Thus in this system the internal energy is simply given by the product of the concentration of particles that occupy the high-energy levels ($\bar{n}$) times ΔE (defining the lower level as energy-zero). The corresponding heat capacity may then easily be calculated as

$$c_v = \frac{\partial E}{\partial T} \text{ with } E = \bar{n}\Delta E \tag{4.18}$$

Analytical results are shown in figure 4.21 where the contribution to c_v due to this two-energy level system is given for several sets of parameters.

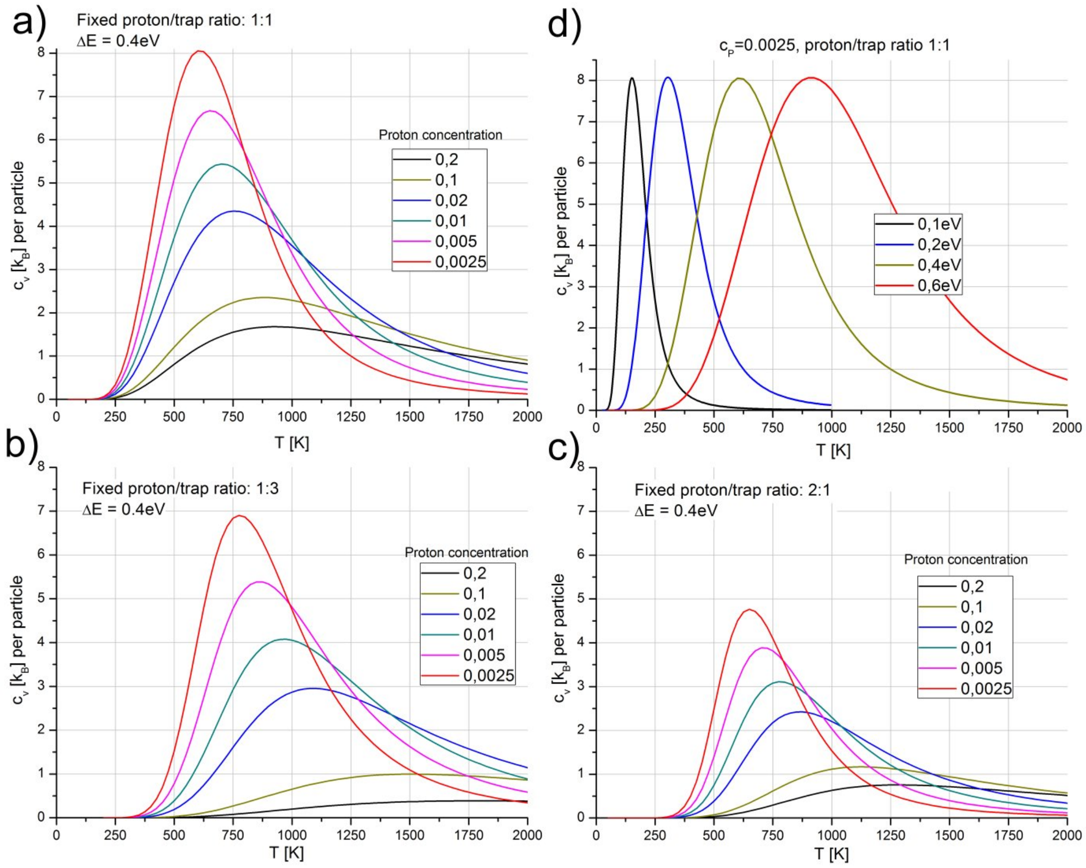

Figure 4.21: Structural specific heats c_v of two-energy-level systems over temperature. a), b) and c) differ in the ratio of particle over low-energy sites 1:3, 1:1 and 2:1. The parameter within each graph is the absolute proton concentration c_P w.r.t all sites ranging from 0.2 to 0.0025. d) shows the influence of the energy difference for fixed concentrations.

The most important outcome here is that (though very much depending on the details) such a disordered potential energy landscape can give rise to c_v-values of even significantly more than k_B per particle which is exposed to this landscape. Applied to the systems under investigation here the number of particles that are concerned by this occupation statistics is of the order of the number of the vacancy or proton number in the dry or hydrated structures, respectively. This aspect has to be compared to the value of $3k_B$ which are contributed by *all* of the ions present due to their oscillator character.

As can be seen in the figure, the depth (or height) of the energy difference has no influence on the attainable maximum value but does instead enlarge the maximum region up to higher temperatures. It is the relation between the proton concentration with respect to the two kinds of lattice sites that determines the structural specific heat within this two level model (this is plausible given the thermodynamic relation of the specific heat to an entropy change $c_v = T/N\frac{\partial S}{\partial T}$) A large specific heat (normalized per particle) is observed (I) For small overall concentrations of the particles w.r.t. all lattice sites and (II) the closer the particle-concentration is to the concentration of the low-energy sites (traps).

This reasoning can therefore relatively effortlessly explain a behaviour as observed in column I of table 4.V where the high-temperature c_v-value decreases for the BIT-structures with decreasing vacancy content (=increasing Ti content). Thus given the structural degrees of freedom due to the high oxygen vacancy- or proton-concentration these will non negligibly contribute to the specific heat coefficient obtained by the molecular dynamics runs at temperatures which allow for these structural degrees of freedom to be activated (i.e. >1200°C for the dry structures with the corresponding oxygen-vacancies and >800°C for the hydrated structures and their different protonic energy levels).

4.4.7 Discussion of the energies of hydration

4.4.7.1 General remarks on the comparability of theory and experimental values

It is important to notice, that all hydration energies obtained by calculation and that were presented in the previous sections (static and by MD) strictly refer to completely hydrated compounds which are compared to completely dry structures. This represents a considerable simplification to the energetics that can be obtained by experiment. Computed hydration energies are a comparison between two drastically different systems, completely hydrated and dehydrated, respectively. Due to the enormous number of possible proton distributions already the fully hydrated state itself is very complex. The true state of the fully protonated compound is an average of all the possible proton energy levels. Whereas for slightly protonated perovskites all sites can more or less be considered chemically and structurally equal [81], the heavy cationic and structural disorder will give rise to a multitude of protonic site energies[6]. An account by molecular dynamics on this site behaviour of the protons is given in sections 4.3.1 for the intra/extra-case and in section 4.3.2 for the B-site trapping aspect.

---

[6] The most visible one being the intra- and extra-octahedral protons as presented in section 4.3.1 as well as energetic preferences of particular B-site ion octahedra

The presence of various energy levels however automatically entails, that even at constant proton concentration the hydration energy will be temperature dependent, as lower lying levels (e.g. the extra octahedral sites) will be less and less occupied for increasing temperature. This is consistently confirmed by the direct result of the MD-treatment as presented in section 4.4.4 where by pure energetical data a difference in the specific heats of the dry and the hydrated phase result in a temperature dependence of the hydration energy. This has to be kept in mind when comparing things with the experimental values, as they (being a single number) are obtained by thermogravimetric data.

Additionally for compounds with a large water uptake, the *degree of hydration* influences the general structure which can for example be directly experimentally observed by the phase transformation of BITh25 when going from the hydrated to the dry state. Thus what fitted TGA-experiments usually provide are concentration dependent hydration energies (i.e. $E_H(c)$) which for BIT25 and BIZ25 happen to coincide with a low and a high hydrated phase as given in in table 4.IV. However what is calculated by equation (4.11) represents a total hydration energy. The calculation of differential hydration which would correspond to the TGA-energies would require to compare a fully hydrated simulation cell with a slightly less hydrated simulation cell etc. down to only a slightly hydrated simulation cell. Even more so intermediate hydration states include the presence of cation disorder, oxygen vacancies and protons at the same time being all interdependent.

4.4.7.2 Hydration energies and electronegativities

In the introduction in section 4.4.1 three main contributions to the hydration energy were given: (I) a structural part consisting of the filling of oxygen vacancies (new ionic bonds) and lattice strain parts, (II) the covalent O-H bond strength and (III) the hydrogen bond strength.

The electronegativity (of the host lattice) is the key property that determines point (II) - the bond-strength of the internal O-H groups in a hydrated oxide. The crucial claim is that the more negative charge is located on the oxygen ions of an oxide the better this oxide will hydrate. This concept reflects the chemical notion of basicity which relates a strong proton attraction for negatively charged ions. A very convenient comparative tool we have at hand is the Bader charge analysis that was presented for the dehydrated compounds in section 3.4.

There very clear results about the average negative charge on the oxygen ions in all considered compounds were obtained and were related to an electronegativity scale.

In the following the MD-obtained hydration energies which were presented in figure 4.20 are put into relation with the effective Bader charges of the host materials (discussed in section 3.4). (The charge-distributions come from calculations for the dehydrated state.) This is done for each group BIThx, BIZhx, BIYhx and SIThx. Unfortunately BIYhx consists only of two single points being BaInOH and BIYh25. SITh25 which does not at all belong to a compositional group (as no MD-simulations for $Sr_2In_2O_4(OH)_2$ were undertaken) is therefore represented only as one data point.

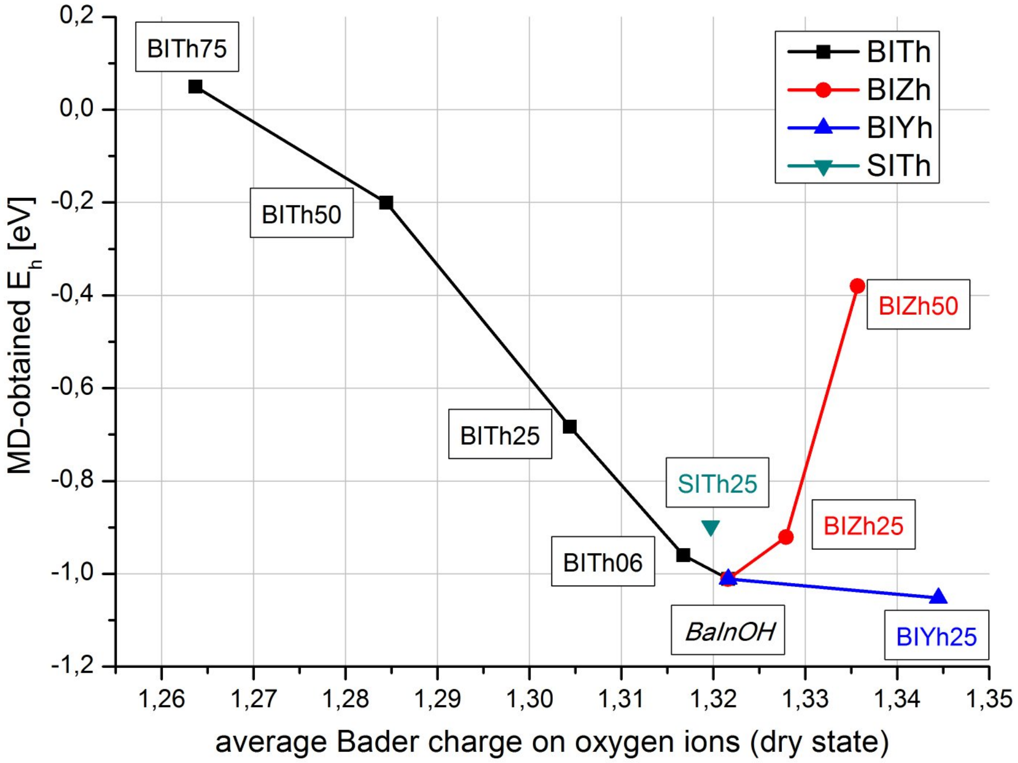

Figure 4.22: Correlation between average Bader charges on oxygen ions (average basicity) in dehydrated compounds and the MD-obtained hydration energy for all compounds studied.

Figure 4.22 contains several interesting aspects. It has to be remembered that a high negative charge on oxygen ions is related to a large basicity which means that in this light the expected behaviour is more negative hydration energies with increasing oxygen charge. However this expectation concerns only energetic aspect number (II) mentioned above, the covalent O-H bond strength.

BIThx

It can be seen on the figure that for BIThx this expectation is rather satisfactorily met. Starting from the relatively large oxygen charge of 1.32 e for BaInOH there is a distinct decrease (towards less favourable values) of hydration energy for decreasing oxygen charge along with the increase of Ti-content. The highest Ti-concentration of 75% even displays a slightly positive hydration energy.

As said before this evolution correlates with the increase of average absolute electronegativity (according to the Zhang scale [69]) with respect to the cations (going from In-rich to Ti-rich). Moreover there is agreement with generally available tendencies of experimental hydration energies which are rather low for perovskite titanates (e.g. -0.2 eV for Sc:$SrTiO_3$ as given in table 4.IV and even lower (though not fitted) for Sc:$BaTiO_3$ [19]). Important to notice is that for these particular cases of Sc-doped $SrTiO_3$ and $BaTiO_3$ the hydration energy is obtained by TGA for degrees of hydration that are far from being complete. Complete in this sense means that all oxygen vacancies that were brought into the material by the dopant be filled in the hydrated state. In these cases only 10-20% of the maximum hydration is attained. This said, we one might recall what was stated in the previous discussion section about the different character of hydration energies obtained by calculation and on real materials. Taking the case of the positive E_h for BITh75 it is very likely that a hydration degree of merely 20% might yield a *more favourable* hydration energy per water molecule than the one that was determined by MD for the case of complete hydration.

BIYh25 and SITh25

Due to the lack of a sufficient number of data points those two compounds are somewhat more difficult to discuss. As does BIThx the case of BIYh25 meets the expectation concerning the correlation of oxygen charge and hydration energy: a higher oxygen charge (a more ionic cation-oxygen bond character in BIY25 than in BaInO) leads to a more negative hydration energy, although only to a lesser extent than for BIThx. The BIYh25 compound is hence the compound with the highest hydration energy altogether, which is even in agreement with the static trial compounds whose hydration energies were presented in figure 4.19. Tentatively one might also conclude that the overall high level of hydration energy observed by calculation is in agreement with other yttrium-containing materials (see table 4.IV) or the rather high dehydration temperature for BIYhx in [72], where unfortunately an energy fit to the TGA data is not easily possible due to a superposing phase transformation upon heating.

For what SITh25 is concerned there is no direct comparison with other degrees of Ti-substitution possible. However we can compare it with the other 25% Ti containing compound BITh25. As can be seen in the figure we again observe a correlation as expected having a more negative E_h for SITh25 which is associated to a higher oxygen charge of 1.320 compared to 1.305 for BITh25. In this case the relation to tabulated electronegativities is less evident given the only minimal difference between Sr and Ba in for example the Pauling and Zhang scale. However there exist other scales for example introduced by ALLEN [90], where Sr is even more different from Ba than Ti from Zr. In this light, no systematic investigation of the relation between hydration energies and tabulated electronegativities is sought to be performed here.

BIZhx

The Zr-substituted compounds stand for an exception concerning their oxygen charge - hydration energy behaviour: the sequence BaInOH-BIZh25-BIZh50 shows an evolution towards less favourable hydration energies although (in agreement with EN-relations between Zr and In) the average oxygen charge increases with increasing Zr-content. So on first sight, we are confronted with smaller hydration energies *although* the average lattice is more "basic"/has a higher negative charge density on the oxygens. A very likely explanation of this apparent contradiction might be supplied by taking into consideration structural aspects that were treated earlier.

This makes direct reference to 4.3.2 where the differences in proton-association between the substituents were presented. The MD-simulations showed that protons are very much more likely found to be associated to Ti-polyhedra in BIThx than to Zr-polyhedra in BIZhx. For BIZhx this means protons are predominantly associated to *indium*-polyhedra. The effect is very significant in extent and furthermore prevails up to very high temperatures. Hence the explanatory argument is, that although the average oxygen charge in BIZ rises with increasing Zr content, the protons are not actually located on the sites that *locally carry* this charge but remain associated to indium. The contrary is true for BITh (and SITh) where protons *are* associated next to the cation that on an average carries less charge than indium and therefore the effect is reversed and the overall hydration energy does not correlate with the *average* basicity.

For what the comparison of BIZh and BITh is concerned, we can state that for the two degrees of substitution 25% and 50% the Zr-compound shows the more favourable hydration energy for an equal degree of substitution in each case. This can be rationalized firstly by the basicity aspect: Protons inside BIZhx located next to In-ions (as observed) compared to protons inside BIThx next to Ti-ions (as observed) will be exposed to a ”more basic” environment.

However also an entirely different structural aspect goes in this direction. As mentioned in the section’s introduction 4.4.1 one part of the total hydration energy must come from the re-creation of ionic bonds cation-O upon the refilling of the oxygen vacancies. Recalling the results from the study of local structures in the dehydrated phase we immediately see that this energy regain will be *less big* for BITx than for BIZx (or BIYx). The reason is the pronounced structural preference of Ti to associate to oxygen vacancies compared to Zr and Y. But again, recalling yet another structural argument mentioned in the discussion section of the ”Protonic structures” section 4.3.4, O-H belonging to Ti-polyhedra elongate the corresponding Ti-O distance such that chemically Ti almost lose this oxygen (figure 4.17).

Conclusion

Within the system of the here obtained ideal hydration energies (i.e. based on a comparison of the *completely* dry and the *completely* hydrated state the tendencies concerning the chemical composition can be rationalized. There are two main points that characterize the findings:

(I) The Bader charge located on oxygens in the dry phases provides a very reasonable measure of correlation to the hydration energies. This is a contrast to tabulated electronegativity values that differ *qualitatively* from one definition to the next. The more effective Bader charge an average oxygen ion has in the dry state the higher the overall hydration energy of the corresponding compound can be expected to be. This is the very effect of basicity which finds an expression by charge analyis.

(II) However, and this is a severe implication, structural contributions can override this tendency! The BIZhx case supplies a coherent example for such an interpretation. In its case a structural property (of course also linked to an energetical preference) leads to a decrease of the overall hydration energy although the averaged oxygen charge/basicity increases.

4.5 Chapter's conclusion

This chapter dealt with the structural properties of completely hydrated compounds as well as their hydration energies. The study was predominantly conducted by DFT-based molecular dynamics applied to simulations cells of considerable size that allow to represent both a B-site cation disorder (by having 32 B-sites in total) and of course a protonic disorder (by distributing 8 to 32 protons on several hundreds of possible sites). The outcome of the structural investigations highlights three distinct concepts that characterize the proton arrangements in the Brownmillerite based compounds:

(I) The distinct proton sites labeled intra- and extra-octahedra which give rise to a layered proton structure. As extracted out of the MD-treatment the extra-octahedral proton site stabilizes the protons that occupy it. The observed concentrations of extra-octahedral protons could successfully be modeled by a Fermi-statistics approach which yielded an energetic stabilization of -0.2 to -0.3 eV, depending on the cationic substitution.

(II) The trapping or obstacle effect of the various B-site cations concerning the preferred proton arrangement. The particular preference of tetrahedral coordination of Ti in the dry state could be related to the role of the Ti as a trap in the case of the hydrated materials. Accordingly the other substituents Zr and Y with a pronounced preference for the octahedral coordination in the dry state are found to act as proton obstacles.

(III) The known issue of a particular proton-avoiding oxygen site in the hydrated Brownmillerite structure could be identified to constitute a genuine blocking layer concerning the proton diffusion. The effect is evidenced for temperatures as high as 500°C for $Ba_2In_2O_4(OH)_2$ as well as for all cation-substituted compounds up to degree of substitution of 25%.

The section on the hydration energies examined the differences of general affinity towards being hydrated as a function of chemical composition. Also conducted in the molecular dynamics framework the obtained energies satisfactorily match their experimental counterparts in order of magnitude and reproduce several experimentally observed trends (e.g. higher values for yttrium compounds, lower values for titanates etc.). A coherent correlation could be established between the effective Bader charge transfer (presented in the chapter on the "Dehydrated compounds") and the evolution of obtained hydration energies over chemical composition. However an important contribution of structural aspects was evidenced, too. Given the fully dynamical character of the approach, these hydration energy values can be considered to be statistically meaningful in a sens that static DFT calculations cannot provide. Related to the hydration energies also the specific heat coefficients were discussed concerning their distinct behaviour for dry and hydrated states. It was elucidated which factors gouvern the value of the specific heat in the case of the investigated systems.

Chapter 5

Monte Carlo studies on diffusion-properties

5.1 Introduction

This chapter can be considered a bit apart from the others, as it has a rather general character dealing with the problem of diffusion on lattices similar to the perovskite-proton system. It was decided to put it before the actual ”Proton transport” chapter in order to already hint to the difficulties that arise for the interpretation and the assessment of the study of such kind of transport in disordered media. However the reader may as well skip this Monte Carlo chapter for the moment and continue with chapter 6 instead, to see the results of the actual MD proton diffusivity study first.

The basic layout of the repetitive structure of the used MC-lattice is presented in figure 5.1. As stated already in the introductory section (2.3) the used lattice is composed of a 3-dimensional network of octahedra with 24 possible proton sites each. The aspect of the particular intra- or extra-octahedral structure was neglected. Hence the lattice represents a perovskite-type lattice and will be called ”protonated perovskite lattice” in the following. In most cases (especially those with a distribution of site or barrier energies) the kMC simulations were run on lattices with 6×6×6 polyhedra containing 5184 sites in total which allows for a sufficient ”randomness” of site and barrier energies.

In analogy with the analysis of the molecular dynamics results in the upcoming MD-treatment two properties will be of importance: the overall diffusion (expressed by the diffusion coefficient) as well as the rates (i.e. jump-events per time) of the elementary displacement steps. Due to the neglect of the extra-octahedral aspect, the protonated perovskite lattice is characterized by three of them: the stretch-jump (covalent bond breaking and creation), the rotation and the flip (both reorientation) are illustrated in figure 5.1.

The key aspects which characterize the problem is the disordered character of the lattice both with respect to site energies as well as barrier energies. This kind of diffusional situation leads to non-Arrhenian behaviour of the diffusion constant or the elementary rates. Literature sources on this field have succeeded in describing the problem on general grounds (see for ex-

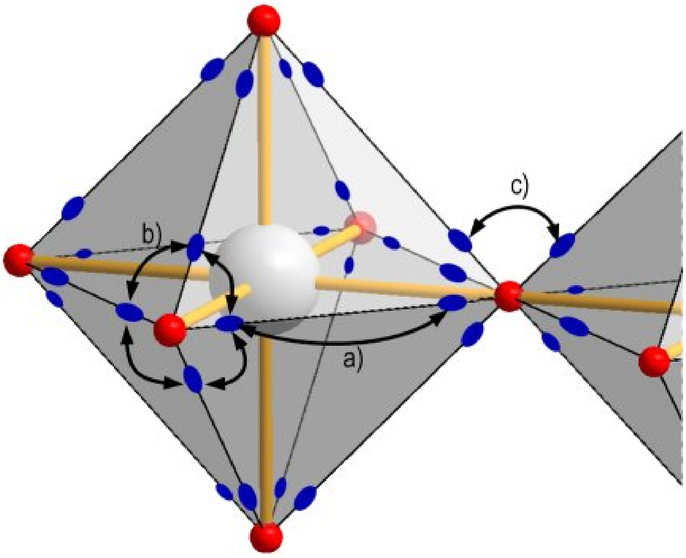

Figure 5.1: The 24 total proton sites at each octahedra which are linked by (a) stretch-hops (along the edges), rotations (b) (around the summits) and flips (c) (changing the octahedron). Each proton site therefore is 4-fold coordinated (1 stretch, 1 flip, 2 rotations) (repetition from page 33

ample [91, 14, 15]).

The presentation of the MC calculations is organized in the following way: In the following section 5.2 a general account is given on how diffusion is supposed to behave in a random barrier (RB) or random trap (RT) environment. Those two cases serve as model systems and are well established in the literature.

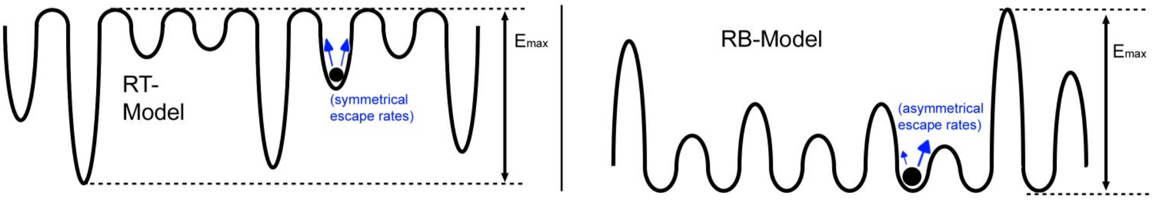

Figure 5.2: random-trap model (left) and random-barrier model (right)

After that, the consideration is enlarged to the three distinct barrier types (stretch, rotation, flip) occurring in protonated perovskite. Finally more or less random traps are incorporated in the lattice in order to qualitatively simulate and shed light on the particular case of the behaviour BITh50/BIZh50 which will be presented in section 6.3 on the effective protonic diffusion coefficients. The influence of the multi-particle aspect (i.e. the ratio of traps per proton) and the trap-depth are investigated. In the last section, the MC allows to deal with some particular situations as for example the cases of (non)-percolating low-energy basins (as it is suspected to be relevant for the BITh50 and BIZh50 compounds), or the effect of a diffusional blocking layer the like of which was evidenced in section 4.3.3 for $Ba_2In_2O_4(OH)_2$ and the 25% substituted compounds.

5.2 Random barrier and random trap models for single-particle diffusion

The random-barrier (RB) and random-trap (RT) models are extremely useful in understanding the disorder concept with respect to diffusion. They shall be defined to be discrete lattices that are characterized by a distribution of either uniformly and randomly distributed traps at each site, or uniformly and randomly distributed barriers between those sites. Also other than uniform distributions are possible (e.g. gaussian, exponential) which however will not be explored here (see [92, 93, 94] for examples).

Being well defined particular cases, it is possible to derive analytical expressions for many cases. A one-dimensional sketch was shown in figure 5.2 indicating the two concepts. The crucial difference between them is the symmetry consideration, that in the RT model, the escape rates from a given site (trap) are necessarily the same in all directions as for one site the energetical barrier to overcome is of equal height in all directions. This is equivalent to saying that each hop is entirely uncorrelated to the previous one. The RB-model in contrast allows for different hopping rates in different directions, because barriers may have different heights. This topology can give rise to temporal correlation. This means, that after having surpassed a rather low barrier, the probability of a re-passing it will be (much) bigger than a forward hop over an adjacent higher barrier.

One of the most interesting aspects of those models, is that they show opposite tendencies in their temperature behaviour. The RB model *in general* shows a convex (upward) curvature of the $ln\,(D)$ over $1/T$ (Arrhenius)-graph whereas it is concavely (downward) curved in the RT model. With rising temperatures the apparent activation energies increase for the RB model and decrease for the RT model.

A very important implication of possibly curved Arrhenius representations is that the usually given parameters "activation energy" and "prefactor" are not uniquely meaningful but describe only the temperature region which is accessible to experiment or which was simulated (with molecular dynamics in our case). Especially care will have to be taken for the comparison of experimental diffusion data (coming from the temperature range from 200°C to 500°C) with the results of the MD simulations of this work. They range from 500°C to 1500°C for the proton conduction and therefore probe a larger and different region of the potential energy surface.

5.2.1 Random trap model

Starting with the simpler RT-case for one particle and following Kehr and co-workers ([15]) the illustrative explanation of the temperature dependence is the thermodynamic occupation of sites with different energy according to a Boltzmann statistics distribution[1]. With increasing temperatures sites with higher and higher energy will be occupied. The escape-barriers associated to those site thus are lower and lower which leads to the decrease of apparent activation energy for the overall diffusion. It can be shown, that in all dimensions, for all site-connectivities and coordination numbers > 2 the effective diffusional rate is given by a reciprocally averaged expression over all rates Γ_i present (i.e. the rate expression which contain the single trap depths E_i)

$$\Gamma = \left\{ \frac{1}{\Gamma_i} \right\}^{-1} \tag{5.1}$$

with $\Gamma_i = \nu \exp\left(\frac{-E_i}{kT}\right)$.

Equation 5.1 essentially is the expression for a series of conductances in an electrical circuit. At low temperatures the smallest rate (with the highest activation barrier) determines the system's general behaviour. Rising temperatures however will modify it and the influence of the lower barriers will increase lowering the effective overall barrier (i.e. apparent activation energy).

An example is given in figure 5.3, showing values obtained by the MC-routine on the protonated-perovskite lattice. Shown are Arrhenius plots of the diffusion coefficient D (a) and one of the three rates (b) as well as their apparent-activation energies over temperature. The simulation lattice has of a pure random trap character with traps being distributed from 0 to -E$_{max}$ (0.2, 0.4, 0.6 and 0.8 eV). The activation energies are obtained by a numerical deriva-

---

[1] More precisely multi energy level systems, with a constraint concerning the occupancies, obey a Fermi-type of statistics as seen for the intra- and extra-octahedral proton sites.

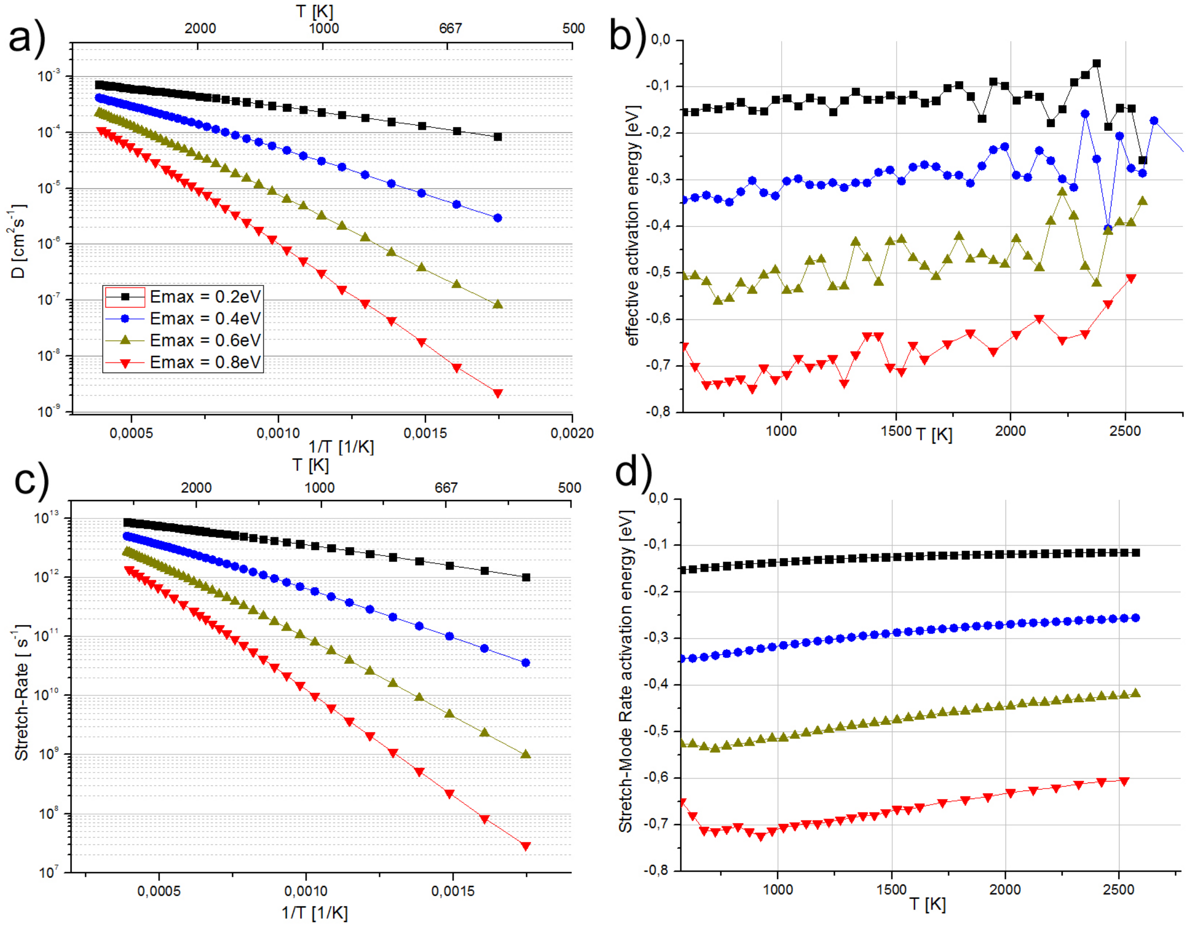

Figure 5.3: a) diffusion coefficient of a RT-PES and b) the corresponding activation energies. c) Stretch-Rates obtained from the same simulation with d) their respective activation energies

tive of the $ln(D)$ over $1/T$ expression[2]. Given the choice of the MC-prefactors as well as the energy parameters the values of D and the rate are in the region of what will be observed in the molecular dynamics simulations.

From figure 5.3 it is obvious that for the pure RT-case the diffusion coefficient and the rates of (one of) the displacement modes behave exactly equal. Both their respective activation energies are identical in value and tendency and clearly show the curved non-Arrhenian behaviour with decreasing activation energies over temperature, i.e. a convex-curvature of the corresponding plot.

---

[2] For the sake of easy comparability all MC or analytical examples are given in units of Kelvin, eV and the values (as for example the trap depths etc.) are chosen to match the order of magnitude for proton diffusion.

5.2.2 Random barrier model

This random barrier model has a more complicated character. Most of all in contrast to the random trap model, its behaviour is closely linked to the *topology* of the underlying lattice which is characterized by the dimensionality, the connectivity and the local coordination number. It shall be repeated here that the protonated-perovskite lattice which is modeled by the MC-routine is 3-dimensional and that each lattice site is 4-fold coordinated.

It turns out, that the percolation concept is very useful in interpreting the diffusion in such a RB-PES. For simple special cases however there exist instructive solutions, whose character is however not supposed to change drastically for more complex lattices.

To begin with, there is an analytical result for the one-dimensional infinite chain having randomly distributed barriers. The diffusional rate in this case is identical with the result obtained from the RT model in all dimensions [95] (being the serial-circuit of conductances) equation 5.1. Notably here we are of course not concerned with any percolative character which will enter at higher dimensions.

An approach, called critical path approach [93] explains the diffusional behaviour in terms of bond percolation phenomena for higher dimensional lattices. Taking the case of a completely random uniform distribution of barriers ranging from 0 to E_{max} it states, that the effective activation energy can be *estimated* by $E_{eff}=p_c \cdot E_{max}$ with p_c being the percolation threshold fraction which is topological property of any given lattice. This translates into the fact, that there exists at least one "easy path" in the system that is (I) entirely percolating and (II) is made up of barriers strictly not higher than p_c E_{max}.

Being *the* easiest path of the lattice, at temperatures $T \rightarrow 0$ it will be the only one contributing to long-range diffusion. In this low temperature limit this situation equals a one-dimensional case mentioned before. Its temperature behaviour is given by $\Gamma = \left\{\frac{1}{\Gamma_i}\right\}$ with the average now being taken over all barriers present along the easy percolation path (and not over the entire lattice as in the case of the RT-model described above).

As this is valid for low temperatures, this latter expression corresponds to the thermal behaviour of a single (the highest) activation energy (see the low T limit for the effective activation energy, equation 5.6), the bond-percolation estimate can therefore be considered exact for $T = 0$ and therefore gives the intersection with the X-axis of the $E_{act-eff} - T$ plot. Hence the (important) low temperature activation energy of diffusion on a uniform random barrier lattice is determined (or, at T=0, equals) p_c E_{max}.

A special case concerning a random barrier PES is the four-fold coordinated two-dimensional square lattice. Having an exact bond-percolation value of $p_c = 0.5$ the effective activation energy for $T = 0$ (being $E_{eff} = p_c \cdot E_{max}$) coincides with the high temperature limit which has the same value for a uniform barrier-height distribution. Therefore for this geometrical case there exists no temperature dependence and the effective activation energy is exactly $0.5 \cdot E_{max}$ for all temperatures. This is in agreement with a treatment by the effective medium approximation (EMA) [14] which features a T-dependence expression vanishing for $Z = 4$. However any considerations of dimensionality and connectivity are not included in this approach. Therefore leading to the conflict, that lattices with a fourfold coordination but no percolation threshold of 0.5 are likely to have a T-dependence. Indeed approximate values of p_c for the $Z = 4$ diamond lattice are around 0.39 [96]. However, the percolation threshold of the protonated-pervoskite lattice (with Z=4) as used here is not known as its connectivity is not equal to neither the square lattice nor the diamond one. In order to interpret the behaviour of this lattice, the results shown in figure 5.4 indicate that the bond-percolation is situated *slightly* below 0.5 as towards low temperatures a curvature of the effective activation energies for the diffusion can be observed (see figure 5.4 c)). Although the low temperature results (for E_{max}=0.4 eV and 0.2 eV) are taken from very-long lasting runs, it can however not be excluded that the curvature is due to not sufficient statistics given the exponential decrease of absolute diffusivity which implies an equal increase of simulation time necessary in this direct MC-approach.

For the general case of a pure RB-PES in three dimensions an upward (concave) Arrhenius behaviour is observed, which goes with an increasing effective activation energy with increasing temperature. This is a plausible behaviour for a RB situation, where with rising temperature more and more high-barrier paths are free to contribute to the overall diffusion. This can be seen as an important contrast to the RT-case, where also at low temperatures *all* paths do contribute as a random walker will at some point always end up in a deep trap, while for the RB-case, it is not forced to cross any high barrier.

A merit of the RB-model is the very effortless interpretation of discrepancies between the behaviour of the diffusion and the event-counting rates that will actually be encountered for the MD-simulations of proton conduction in the next chapter: in the case of a barrier disorder

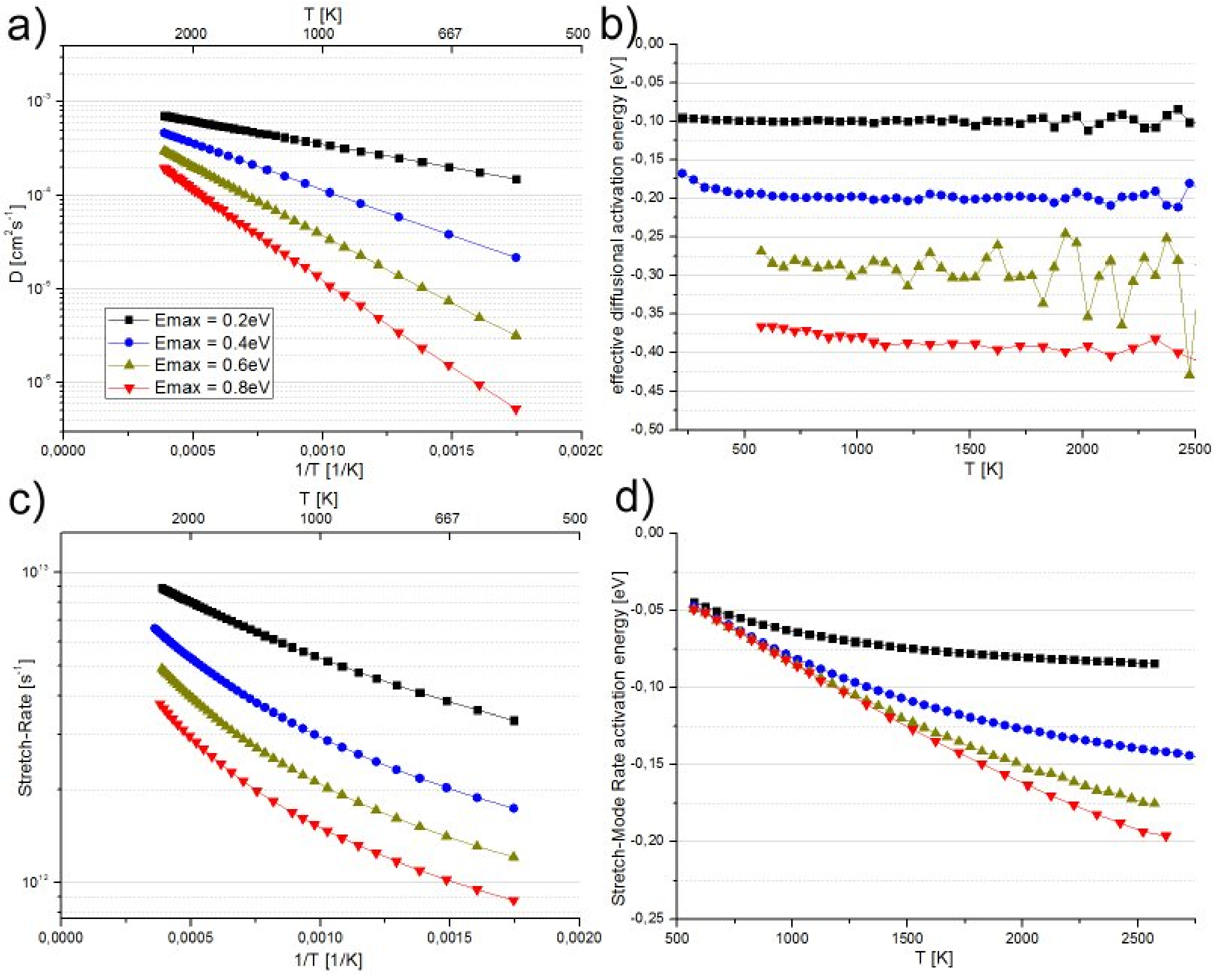

Figure 5.4: a) diffusion coefficient of a RB-PES and b) the corresponding activation energies. c) Stretch-Rates obtained from the same simulation with d) their respective activation energies

(in contrast to pure site disorder) the activation energies of the net-diffusion and the activation energy of the countable elementary steps are not directly related, but the latter ones will *always* be underestimated.

This is nicely illustrated in the diffusion and rate activation energies of figure 5.4 b) and d): over the entire temperature range, the effective rate-counting activation energy rests lower than the corresponding diffusion E_a. Moreover the temperature evolution of the hopping-rates towards low temperatures shows how only lower and lower barriers are crossed. This leads to generally very large hopping rates[3]. In our particular case of a uniform barrier distribution from 0 to E_{max} eV the activation energy tends to this zero-value. Microscopically this behaviour corresponds to situations where the particle is located in regions of easy barriers, performing a large number of "wasted" jumps over these low barriers, but *does not contribute* to the long range diffusion.

---

[3] Observable by comparing the y-scales of 5.4 c) and 5.3 c)

Hence the method of event-counting does not yield a valid information in a sense of a rate-determining step for the diffusion, given the discrepancy of the diffusional activation energy and the highest activation energy for any of the single elementary steps.

Having two effects with opposed tendencies (convex or concave curvature of the Arrhenius plot), the question arises about the properties of diffusion on lattices with both trap- and barrier-disorder. Exhaustively analyzed by MUSSAWISADE and co-workers ([94]) the answer is not a general one. To summarize, a cancellation of the two tendencies is possible however only for a limited temperature region and for certain conditions concerning the barrier and the trap distribution.

In the remainder of this section, the analytical expressions for effective rates and activation energies will be given for the reciprocal exponential average (RT case) and the direct exponential average (RB-case).

- Direct exponential average (directly valid for random-barrier hopping rates)

  The direct exponential average holds for a situation where an effective rate is determined by elementary rates, that all have the possibility to be active but are not necessarily doing so. This case is important for the description of the diffusion in a pure barrier determined PES. An analogon to this situation would be a parallel circuit of conductances with the overall conductance being predominantly determined by the largest conductance (i.e. the highest elementary rate - the easiest diffusional path). The effective rate Γ is given by

  $$\Gamma = \{\Gamma_i\} = \frac{1}{N}\sum_i^N \left(\alpha_i \cdot exp\left(-\frac{a_i}{kT}\right)\right) \tag{5.2}$$

  Introducing α_i and a_i which designate the prefactors and the barrier energies, respectively. In the (very) high temperature limit the rate becomes therefore a simple arithmetical average of the prefactors $alpha_i$. The effective activation energy follows by logarithmic differentiation with respect to (1/T) and reads:

  $$E_a = \frac{d\ \ln(\Gamma)}{d(1/T)} = \frac{-\sum_i^N a_i\alpha_i \exp(-\frac{a_i}{kT})}{\sum_i^N \alpha_i \exp(-\frac{a_i}{kT})} \tag{5.3}$$

  Thus for low temperatures the effective activation energy tends to the single lowest barrier value that constitutes the system (as can be seen in figure 5.4 d) with a_0 in 5.4a being the smallest barrier in the system as all other exponentials with bigger barriers become negligibly small compared to the one containing the smallest barrier for $T \to 0$.

In the high temperature limit (5.4b) yields a prefactor modified mean value.

$$\begin{aligned} E_{act-app}(T \to 0) &= -\frac{\alpha_0 a_0 exp(-\frac{a_0}{kT})}{\alpha_0 exp(-\frac{a_0}{kT})} = -a_0 && (5.4a) \\ E_{act-app}(T \to \infty) &= -\frac{\sum_i^N \alpha_i a_i}{\sum_i^N \alpha_i}. && (5.4b) \end{aligned}$$

- Reciprocal exponential averages (valid for random-trap diffusion and hopping rates)

The reciprocal averaging describes situations comparable to a series-arrangement of conductances thus yielding effective rates controlled by the smallest rate/conductance. Concerning diffusion problems, this situation is encountered in a pure (random)-trap PES with respect to the diffusion and the event elementary step rates. The effective rate is given by

$$\Gamma = \left\{\frac{1}{\Gamma_i}\right\}^{-1} = \left(\frac{1}{N} \cdot \sum^N \frac{1}{\alpha_i \exp\left(\frac{-a_i}{kT}\right)}\right)^{-1} = \frac{N}{\sum^N \frac{exp(\frac{a_i}{kT})}{\alpha_i}} \tag{5.5}$$

which for high temperatures yields a reciprocal average of all occurring prefactors.

The T-dependent activation energy is supplied by the logarithmic derivative with respect to (1/T) reading

$$E_a = \frac{d\ln(\Gamma)}{d(1/T)} = \frac{\sum_i^N a_i \prod_{j\neq i} \alpha_j \exp\left(\frac{a_i}{kT}\right)}{\sum_i^N \prod_{j\neq i} \alpha_j \exp\left(\frac{a_i}{kT}\right)} \tag{5.6}$$

So in this case the effective activation low-T limit is uniquely determined by the highest occurring barrier. For high temperatures the exponentials in equation 5.6 become unity and the activation energy tends towards the arithmetical mean of all activation energies modified by all prefactors.

5.3 Case of three distinct displacement modes

Fixed barrier height

Up to now all presented MC-simulations treated the three displacement modes equal. That means that for example in the case of the random barrier distribution the barriers were assigned their value regardless of their character. In order to get a better idea of the proton diffusion the three barriers (stretch-hop, rotation and flip) are distinguished by their value domains.

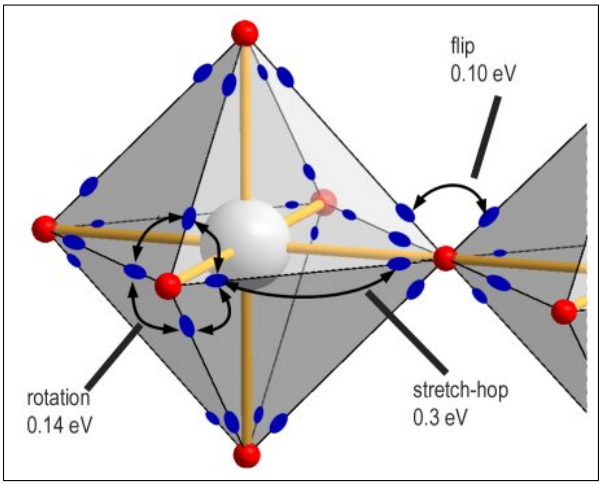

Figure 5.5: Assignment of the three different displacement modes. All 24 sites per polyhedron remain trapless.

The energy barriers that are chosen for those three modes correspond to what is very common in proton conducting perovskites as well as Brownmillerite compounds. The stretch-hop involves the breaking and re-forming of the covalent O-H bond and thus will be the highest barrier set to a value of 0.3 eV. The two other re-orientation modes are usually a lot easier. Here, in agreement with the observations made in the MD-simulations presented in the upcoming section 6.4 we assign them with the prototype value of 0.14 eV for the rotation and 0.10 for the flip motion.

As is easily imaginable already this situation gives rise to a non-constant activation energy of the overall diffusion process because the three different modes are involved. It turns out, that this situation is exactly comparable with a distribution of three kinds of trap sites and can be described by the *reciprocal* average of the three rates (equation 5.1). Therefore the ln D over $1/T$ plot exhibits a convex curvature. This behaviour can be understood by noting, that for long-range diffusion obviously all three modes have to be equally active as is the case for the (random or not) trap distribution, where in a statistical sense all traps are necessarily being explored during a long-range diffusion. Using equation 5.5 the rate can analytically be described as

$$\Gamma = \frac{3 \cdot \alpha \cdot 2\beta \cdot \gamma}{2\beta\gamma \exp\left(\frac{a}{kT}\right) + \alpha\gamma \exp\left(\frac{b}{kT}\right) + \alpha 2\beta \exp\left(\frac{c}{kT}\right)} \tag{5.7}$$

Here α, β and γ stand for the prefactors of each of the three modes. The number 2 is due to the fact that the rotational displacement mode may be active in two directions from any proton site. a, b and c (>0) are the activation-barriers.

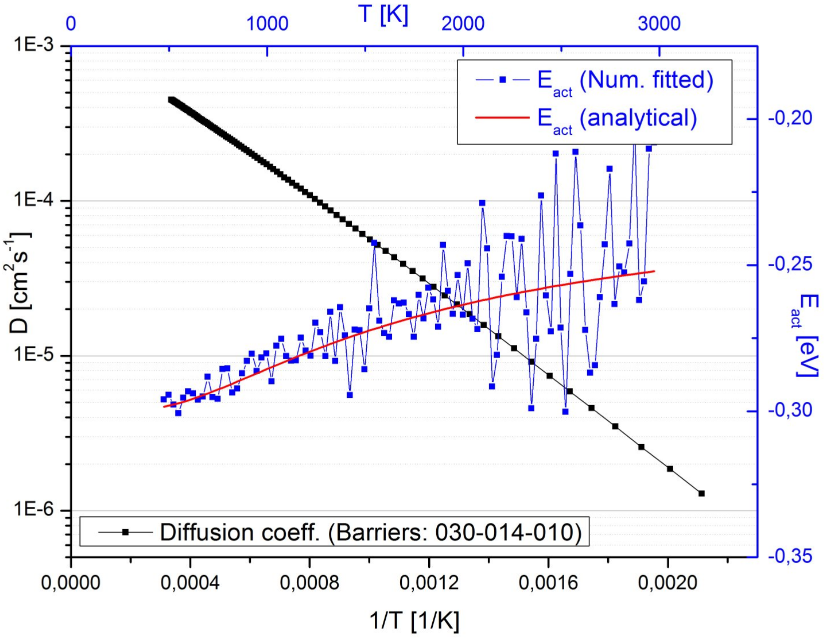

Figure 5.6: Diffusion coefficient as obtained by MC-simulations for a trap-free protonated-perovskite lattice. Stretch-hop, rotation and flip are activated by 0.3, 0.14 and 0.10 eV, respectively. The effective activation energy is derived numerically (in blue) as well as calculated by equation 5.6. Mind the different scales of the two temperature axes.

Figure 5.6 gives an idea of the behaviour of this lattice. As presented, the choice of barrier energies does not lead to a substantial curvature. The low temperature behaviour is clearly dominated by the 0.3 eV stretch-mode. The presence of the two easier modes becomes noticeable only well above 1000 K and does not decrease the effective activation energy substantially. The evolution of the numerical derivative $\frac{d\ln(D)}{1/T}$ compared to the exact result nicely illustrates the reasonable behaviour of the MC-code.

Random barrier height

The situation changes when the three barriers are made randomly distributed from 0 to a given maximum value. The behaviour will be found to differ from the case of the general random barrier case in which the modes were treated equal. Here also the diffusion coefficient shows an upward curvature i.e. low activation energies at low temperatures, high ones at high temperatures. As an example the three barriers were now assigned a uniform distribution of energies: stretch-hop (0...0.3 eV), rotation (0...0.14 eV) and flip (0...0.10 eV). Figure 5.7 presents the proton diffusion on this PES.

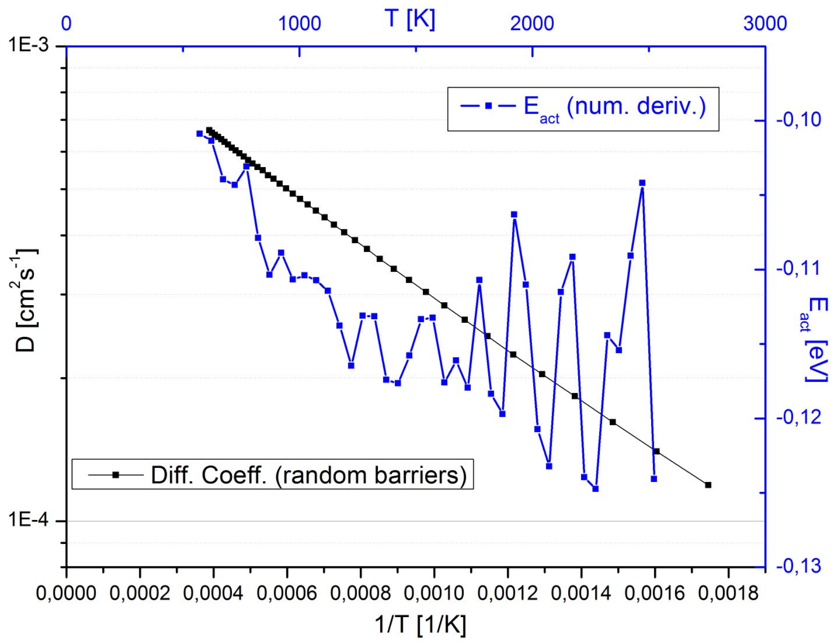

Figure 5.7: Diffusion coefficient and apparent activation energy from a MC-simulation on a random barrier height protonated-perovskite lattice.

The key point is that now the actual diffusion activation energy increases from around 0.10 eV at 770 K up to about 0.125 eV at 2700 K which leads only to a slight curvature in the diffusion coefficient. Also we have to note, that there is no more analytical expression which would describe the evolution because the diffusion on a barrier-disordered lattice depends on the connectivity, dimensionality and the site coordination number of the latter.

5.4 Multi particle diffusion

For the many particle case, in general the treatment is not trivial, except for some well defined cases. One big exception is a pure random barrier situation, where theoretically ([97]) there is strictly no difference in diffusivity except for the pure site blocking effect that can be expressed by a constant factor at all temperatures. MC-runs on various barrier disordered lattices indeed merely show a constant (negative) offset of the diffusion coefficient. In the case of energy landscapes that contain traps however the effect of the particle concentration becomes extremely important. Obviously one of the most important figures is the ratio between trap and particle concentration. When the particle concentration is higher than the trap concentration all traps become occupied and every supplementary particle may move in a more or less smooth energy landscape. This effect is called trap saturation and will also be an element in the discussion of proton diffusivity in BITh or BIZh.

In the following some of those aspects shall be highlighted which illustrate the complexity of diffusivity related to trap-containing potential energy landscapes.

5.4.1 The random trap distribution for many particles

For the first example of multi particle effects the pure random trap PES is revisited. As it was the case in section 5.2.1 the displacement modes are not distinguished and each site is assigned a trap depth ranging from 0 to -0.4 eV. Again, the allocation of the depths among the sites is uniform. Figure 5.8 summarizes the effect of many protons for this lattice. The property which is given in the graph is the ratio between the collective diffusion coefficient (for any proton concentration) and the single-proton diffusivity.

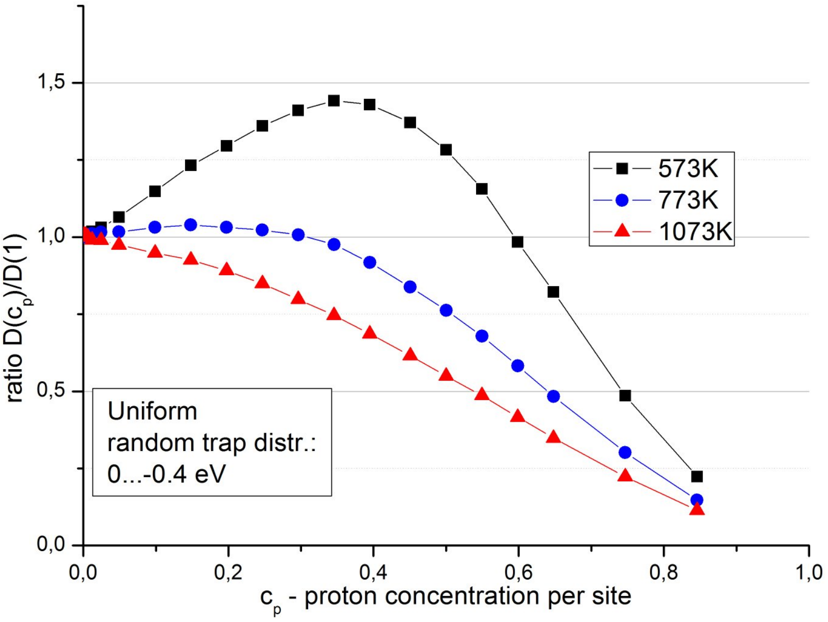

Figure 5.8: Diffusion coefficient of many protons on the random-trap PES with energies depths 0…-0.4 eV. The ratio is w.r.t. the diffusion coefficient of a single proton on the same PES.

The proton concentration refers to the total site number, expresses the proton fraction on the lattice. The general tendency for all temperatures is a decrease of average diffusivity with proton content, simply due to the normal site blocking effect. However depending on the temperature (or rather the ratio of temperature and maximum trap depth) a significant but not drastic increase in diffusivity is observed. At 573 K the diffusivity is increased by about 50%

compared to a single proton which indicates a trap saturation effect. This effect becomes smaller and smaller with increasing temperature. Furthermore it shifts the maximum improvement to smaller concentrations (see 773 K). For still higher temperatures the improvement is suppressed completely and the site-blocking effect dominates for any concentration.

From the viewpoint of the temperature dependence the particle number also has a notable influence onto the diffusion properties, changing them in a qualitative manner. To illustrate this the diffusion coefficient as well as the stretch-hop rates are shown together with their activation energies in figure 5.9. In contrast to the figures displayed in the random trap section 5.2.1 only one uniform trap distribution 0…-0.4 eV is considered. The parameter under scrutiny here is the proton concentration per site. 5184 sites are considered and the MC-simulations were run with 1, 432, 1296, 2592 and 3888 particles corresponding to the fractions given in the figure's legend.

The key statement this simulation runs provide is that with increasing particle density the random-trap behaviour smoothly segues into an effective random-barrier behaviour albeit the underlaying random-trap energy landscape of course remains unchanged. Concerning the diffusion coefficient one can observe a downward curvature for the dilute (1 particle) case which was already presented before. The effective activation energies therefore decrease with increasing temperature. Comparing this to the most dense lattice which was studied (c_p=0.75) one can observe the disappearance of this curvature, at least within the limits of the accuracy of the MC-simulations. The effective diffusional activation energy is more or less constant at a value of 0.25 eV. We note, that this value has no particular significance with respect to the trap-distribution from 0 to 0.4 eV. It is the result of the non-trivial combination of the random-trap PES with the presence of a large number of particles. The evolution is yet more pronounced for what stretch-hop rates are concerned. For high particle concentrations they show the distinct behaviour of a random barrier lattice which is characterized by increasing activation energies (see the red line in 5.9 d). This leads to the peculiar fact that now also on the random trap PES we observe a large discrepancy between the activation energies of the diffusion (around 0.25 eV for the highest concentration) and the activation energy for the elementary step rate (0.13 eV at low temperatures). Likewise the comparison of subfigures a) and c) shows how at low temperatures the highest concentration has the lowest diffusivity however the largest "jump activity". Microscopically this is equivalent to the random-barrier case: indeed by occupying the deepest traps it is the particles themselves which create some sort of random-barrier energy landscape for the "non trapped" remaining particles. This is

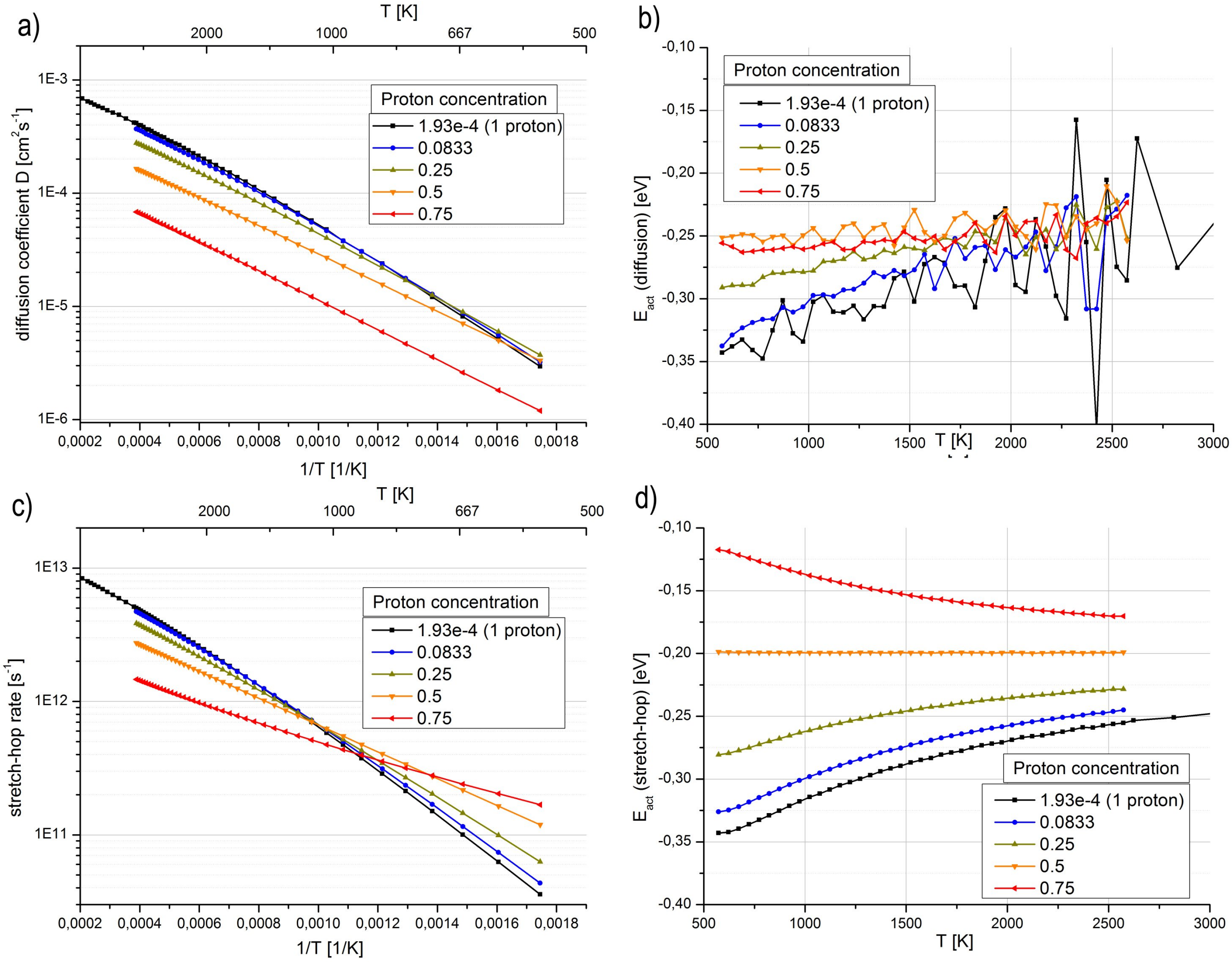

Figure 5.9: Overview of the temperature evolution of diffusion and stretch-hop rates for a 0…-0.4 eV random trap PES as a function of particle concentration. a) diffusion coefficient b) numerically derived diffusion activation energy, c) stretch-hop rates and d) numerical stretch-hop activation energies

equivalent to saying that temperature dependent number of un-trapped particles move on a temperature dependent energy landscape.

5.4.2 Fixed trap depths for some geometrical arrangements

In contrast to the previous cases in the following we shall consider no smooth distribution of trap depths (which after all is more appropriate for the modeling of really amorphous compounds) but only traps with a single trap depth. From the energetical viewpoint the lattices represent two-level systems. This concept has already been used in section 4.4.6 concerning the structural specific heat coefficients on page 124. The description of the occupancies of either level over temperature is easily possible within a Fermi-statistics expression which takes into account the numbers of the two kinds of sites and of the particles like it was demonstrated for the occupation of the intra- and extra-octahedral proton sites in section 4.3.1.

However no straight-forward analytical access is possible to the diffusion properties of such systems because the spatial distribution of the traps will influence the displacement.

Scattered versus grouped-traps

This section is going to consider two extreme cases of how traps can be grouped on a lattice. The two model systems that are considered are relatively simple in consisting only of two kinds of sites (traps or not) at a site concentration of 50% and *no* supplementary barriers. This model therefore might be considered a prototype for a 50/50 cation-substituted proton conductor for which one of the cations acts as a proton-trap. For the scattered trap system (a 1-dimensional sketch is given below figure 5.10 a) the traps of depth -0.3 eV are randomly distributed. The other system has the traps grouped together in cubic regions of 4·4·4 polyhedra which consist of 24 single proton sites each. The non-trap sites are arranged around the low-level basins as sketched below subfigure b).

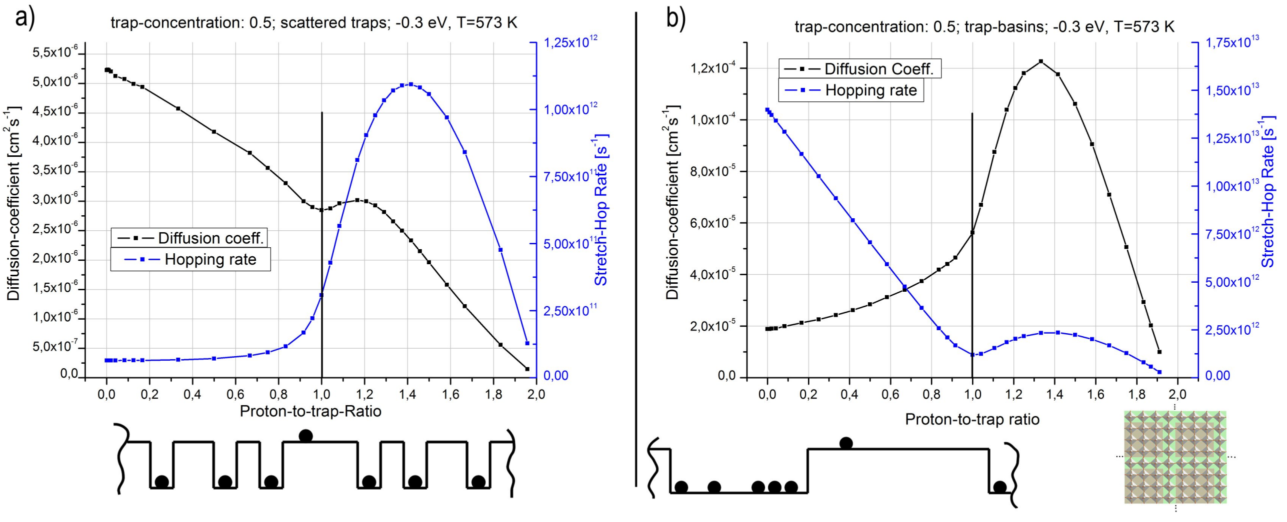

Figure 5.10: Comparison of a pure trap PES (no additional barriers) with fixed depth -0.3 eV at 573 K. 50% of all proton sites are traps. a) randomly scattered over all sites, b) traps are grouped in large "trap-basins" containing 1500 trap sites. The basin-concept is shown in the small sketch on the bottom right. They are *non-percolating* unlike the surrounding regions marked in light green.

The calculations were done an arbitrary and fixed temperature and focused on the evolution of the diffusivity with the proton concentration. Along with the diffusion coefficient the rate of the hopping-events are given as well in blue linked to the scale on the right hand side. As a general tendency both properties tend to decrease with increasing particle concentration due to simple site blocking; the rising probability of an adjacent site to be occupied for a given particle. The calculations however reveal several significant differences. For case a), the scattered trap-landscape, one can observe a continuous drop of diffusivity up to the proton/trap ratio 1 which is due to the site blocking effect mentioned before. This happens in contrast to the random-trap situation where *every* site is associated to a randomly deep trap and for which at 573 K figure 5.9 showed an increase in diffusivity of about 50%. At a particle/trap ratio of 1 however we now can observe a small increase which rests rather small though. At the same time the hopping-rate rises steeply just for the concentration where the trap-saturation is reached as seen in a). Given this behaviour one can conclude that for ratios>1 once more an effective random-barrier environment has been created by the blocked traps. Although every supplementary particle now more or less moves on a trap-less energy landscape, the blocked sites are too concentrated and give rise to many local dead ends where many hops are possible but the long-range diffusion is blocked. This situation correspondingly would change for lower trap concentrations.

The picture is literally reversed for the case of the constructed basin-trap energy landscape whose results are shown in figure 5.10 b). Here it is the diffusivity which increases up-to *and beyond* the particle-trap-equality and it is the hopping rate which decreases. Especially the diffusivity increase below for values up to 1 is not trivial on first sight given the fact that by thermal equilibrium considerations 99% of the particles reside in the low-energy basins[4]. Also here a general tendency of normal site blocking would hinder the displacement, however more or less *inside* the basin. A consequence of this is simply that with ever increasing concentration of particles in the basin more and more particles are permanently along the edges of it. This increase the probability that some of them eventully thermally overcome the basin-wall and afterwards diffuse freely (as no actual site-to-site barriers are used in this particular system). Conversely to the scatterd trap system it is only the hopping rate which suffers from the massive site blocking inside the basins. After crossing the particle/trap equi-concentration an easy to understand steep increase in diffusivity occurs which also is accompandied by a temporary rise in the hopping rates: now really all basin-sites are occupied and the additional particles are exclusively diffusing on the percolating part of the lattice (indicated in light green below subfigure b).

---

[4] A calculation that can easily be performed with the help of the Fermi-statistics equation 4.4 on page 92 introduced to describe the intra/extra-octahedral two-level system

Effect of a blocking layer on particle diffusivity

Here we are going to quickly assess an aspect which was found to be of importance for the fully hydrated compounds up to a degree of substitution of 25%. As presented in section 4.3.3 at temperatures of at least 500°C (to lesser extent even 800°C) the fully hydrated compounds contain a layer of oxygen sites that do rarely or not at all bind to protons throughout the entire MD-simulation. This implies that under real conditions i.e. at lower temperatures, where the materials still are fully hydrated this will be even more the case.

MC-simulations were carried out that resemble more or less the ones from the previous section on the basin-traps. The difference in the lattice topology now is to have a structure of low- and high-energy layers. These MC-simulations foremost served the purpose to assess the (necessarily negative) contribution of such a blocking layer on the overall diffusion coefficient. The Arrhenius-plot of three related MC-simulations are drawn in figure 5.11 next to a 2-dimensional illustration of the topology.

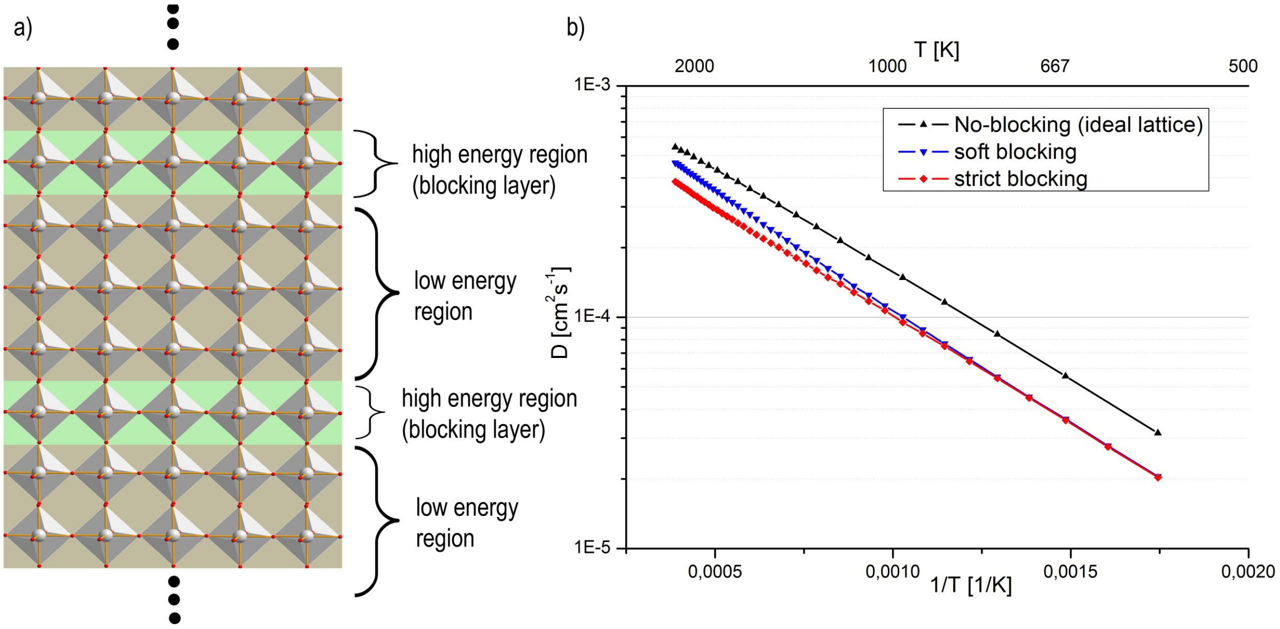

Figure 5.11: a) 2-dimensional illustration of the blocking-layer topology. b) Arrhenius plot of single-proton MC-runs on lattices without and including high-energy regions. Strict blocking: ΔE=0.65 eV, soft blocking: ΔE=0.25 eV

In contrast to the basin/trap approach of the previous section for the blocking layer study explicit barriers were used. That means that withing the grey or green regions stretch-hop, rotation and flip are associated with barriers 0.2 eV, 0.14 eV and 0.10 eV respectively in order mimic an approximate proton conduction behaviour. The simulation labeled ”no blocking” was run on the pure barrier equipped lattice and serves as standard for comparison. The other two simulations now move the "low energy region" down by 0.25 eV (soft blocking) or 0.65 eV (strict blocking). Most importantly we notice the extent to which the blocking layer decreases the diffusion coefficient which is by 30-35%. The larger differences are observed for lower temperatures.

Of course these values will still depend on details for example how far the blocking layers are spaced apart, the relation of the energy difference to the remaining relevant energies in the system, the size of the blocking layer etc. However one can conclude that the blocking barrier is not a major problem for the diffusivity as such.

Issues that are not addressed here are however related to the effect that a *multi grain* arrangement might bring about. Considerations on this scale do require more knowledge of the structural features of grain boundaries which the diffusing particle/proton encounters.

5.5 Chapter's conclusion

This chapter served as a very general view onto the diffusion properties of lattices with different kinds of disorder. This was done by means of a standard kinetic Monte Carlo algorithm which allows to observe diffusivities for significantly enhanced statistical certainty than for the VASP-based molecular dynamics simulations that are going to be topic of the following chapter. The MC approach is based on model lattices, which are more or less characterized by arbitrary parameters are intentioned to only roughly represent the proton diffusion in perovskite type materials.

It is shown how complex the interplay between those parameters barriers, traps and particle number can become. Most importantly we learn that the notion of a single set of Arrhenius parameters for diffusion on disordered lattices is only a very limited approximation for a small temperature interval. In general (but heavily depending on the actual situation) Arrhenius representations will be curved depending on the type and extent of disorder. This is exemplified for the pure random-barrier or random-trap situations which in general either yield a upward or downward curvature (as shown in section 5.2).

Moreover multi-particle effects may alter this behaviour substantially, with the most important case being the trap-saturation effect where some particles occupy traps and leave a smoother potential energy landscape for the remaining ones (see section 5.4.1). This is very likely to be of importance for the fully hydrated compounds which are characterized by a "trap concentration" of the same order as the concentration of diffusing protons.

Finally also the relation between the elementary rates and the net-diffusion can conveniently be rationalized by the MC-simulations. Again depending on the type of disorder, a counting approach which keeps track of the performed elementary displacement steps will very often not yield valid information on a rate-determining step. This will be applied to the MD-simulations of the real proton diffusion in section 6.4. There indeed activation energies of any elementary step will be found to be lower than the activation energy of the net-diffusion which in turn is a clear indication of a disordered energy landscape of proton diffusion.

Chapter 6

Proton transport

6.1 Proton diffusion in heavily inhomogeneous environments

As already formulated before, the main goal of this thesis, is to contribute to the understanding of proton-diffusion in Brownmillerite based materials by means of molecular dynamics simulations. Having at this point investigated a broad range of structural properties of the completely hydrated state as well as having presented a supplementary Monte Carlo study on diffusion processes in general, the following sections are going to deal with the actual diffusivity and its elements. Taking a look back on previous simulation work on perovskite materials (notably by KREUER, MÜNCH, GOMEZ, BJÖRKETUN, SUNDELL and coworkers), we are left with a rather complete description of how protons are supposed to diffuse in them. An overview of their work was given in the literature section 1.3. Protons, covalently bonded to a lattice oxygen change their site by a combination a hopping mode (the reaction-coordinate being the O-H stretch frequency) and a reorientation (reaction-coordinate being the two O-H bending modes) so that these three modes have to be thermally active at the considered temperature. In the simple case of a slightly protonated perovskite with a rather large lattice constant, the diffusion is determined by the hopping motion and very easy to almost barrier-less reorientations (modes 1, 3 and 4 in figure 6.4 section 6.4) with the hopping motion clearly being the essentially limiting step.

In contrast to the just mentioned simple perovskite, for the case of largely hydrated *Brownmillerite based* and cation-substituted compounds, we face several very serious complications in describing the diffusivity which can be summarized by the following key-phrases:

(I) The re-orientation movements are not necessarily barrierless anymore. Long range diffusion requires three elementary displacement steps linked to differing activation energies and prefactors. This may already be the case for small cell-constant perovskites, where protons may form hydrogen bonds O-H...O and therefore the re-orientation modes may become harder to overcome.

(II) There is proton-proton interaction due to the high concentration, most simply leading to pure site-blocking but also by modifying the PES. By consequence one cannot properly define of diffusion paths, because seen from a given proton, the PES is not static due to the mere presence or induced structural changes by the other protons.

(III) Two entirely different protonic sites, being the intra- and extra-octahedral ones, representing two distinct energy levels under the constraint of the number of available extra- or intra-sites.

(IV) The presence of distinct protonic sites (i.e. oxygen ions which differ substantially in their effective basicity) other than the intra/extra-sites mentioned before. This is already the case in the reference compound $Ba_2In_2O_4(OH)_2$ (structural trapping or -blocking).

(V) The presence of particular site energies due to the cation-substitution (substituent trapping or -blocking at the substituent).

(VI) An inequivalence of barrier heights within one out of the three elementary displacement steps induced either by structural disorder (as present in the pure In-compound) or (superimposed to that) cationic disorder in the substituted compounds.

Concerning the thesis' objective, i.e. to elucidate the relation between degree of substitution (mostly of the In/Ti-couple) and the protonic diffusivity, we can safely say, that *all* points mentioned above are affected by the concentration of the substituent. Moreover, even by mere qualitative consideration the effects are not at all uni-directional i.e. they partially counteract each other. So, with respect to the expected impact on the diffusivity the following statements can be made:

(I) Due to several reasons the re-orientation modes may not be neglected (w.r.t. their activation energy) in Brownmillerite based compounds and *are* influenced by the degree of substitution via the average lattice constant variation

(II) Proton concentration decreases with increasing Ti-content by stoichiometry, leading to less proton-proton site blocking (positive) but also to less and less trap-saturation (negative)

(III) the overall stability of the extra-octahedral proton site will be affected by increasing Ti-content (as was found in section 4.3.1: the more Ti, the less stable the extra-octahedral position becomes)

(IV) The presence of high-energy, very unfavourable proton sites in pure $Ba_2In_2O_4(OH)_2$ is modified by Ti-cation presence (This is true for the O(2) oxygen sites as discussed in section 4.3.3). By tendency this *decreases* blocking effects, i.e. rendering sites and paths available for the proton to access, that were not before.

(V) The higher the Ti-concentration, the higher the concentration of proton-traps. This has clearly been evidenced in section 4.3.2 to be opposed to the case of Zr which associates much less with protons. This trapping behaviour of Ti in BIThx therefore counteracts the previous point (IV).

(VI) Cationic substitution equally increases disorder in the barrier distribution. The impact of a barrier disorder was shown in the Monte Carlo chapter to be a possible curvature of the Arrhenius representation of the diffusion coefficient.

The following sections therefore try to bring into relation the structural aspects with the actual diffusivity behaviour as it can be observed directly in MD-simulations.

The comparative aspect is realized from different viewing angles: Firstly, taking BaInOH as a reference point the set of Ti-substituted compounds looks at the influence of the degree of Ti-substitution of 6.25, 25 and 50%. Secondly, other substituents than Ti are probed for the compounds BIZx (x is 25% and 50% Zr) and BIY25 (25% Y). Thirdly the SIT25 (25% Ti and A-site barium completely replaced by strontium) serves as model compound with a significantly smaller general lattice constant but comparable chemistry to BIT25.

6.2 Literature data from experiment and simulation

In order to relate the diffusion coefficients that were obtained by the MD-simulations here to other computational as well as experimental studies this section gathers some of the available information on them.

The vast majority of experimental literature data on protonic conductivity is inferred from electrochemical impedance spectroscopy (EIS). Using the Nernst-Einstein relationship (given in section 6.3) it is possible to furthermore deduce the protonic mobility or diffusivity under the condition that the proton concentration is known. A critical point has to be made concerning the type of perovskite-*related* compound whose proton conductivity is given. Most of the data found in the literature (especially in the numerous experimental papers of KREUER and co-workers) deal with slightly protonated, acceptor doped perovskites. Usually the dopant concentrations do not exceed 20%, most of the time being 2-10%[1].

Table 6.I: Typical single parameter fits of proton diffusion in perovskite type or Brownmillerite based compounds. Numbers in brackets are equivalent experimental values given in the same literature source.

	E_{act} [eV]	D_0 [cm^2s^{-1}]	method
$BaCeO_3$	0.49 ± 0.09 (0.48)	$6\cdot10^{-4}$	tight binding DFT, direct MD [23]
$BaZrO_3$	0.83 ± 0.63 (0.42)	$8\cdot10^{-4}$	–”– [23]
$SrTiO_3$	0.50 ± 0.22 (0.41)	$2\cdot10^{-3}$	–”– [23]
$CaTiO_3$	0.42 ± 0.3	$2\cdot10^{-3}$	–”– [23]
In:$CaTiO_3$	0.66	$2.2\cdot10^{-2}$	kin. MC; input from DFT-obtained PES [33]
1.6Ga:$BaZrO_3$	0.59	$31\cdot10^{-2}$	kin. MC; [36]
3.7Ga:$BaZrO_3$	0.59	$9.7\cdot10^{-2}$	–”– [36]
12.5Ga:$BaZrO_3$	0.62 (0.78)	$2.2\cdot10^{-2}$	–”– [36]
1.6In:$BaZrO_3$	0.31	$3.6\cdot10^{-2}$	kin. MC; [36]
12.5In:$BaZrO_3$	0.36 (0.48)	$1.5\cdot10^{-2}$ ($2\cdot10^{-4}$)	–”– [36]
BIZh25	0.40	$0.9\cdot10^{-4}$	impedance measures on fully hydrated samples [62]
BIZh50	0.62	$1.1\cdot10^{-4}$	–”– [62]
BIZh50	0.75±0.23	($2\cdot10^{-4}$-100)*	neutron spin-echo spectr. [98]
BaInOH	0.77	-	imped. measures, fully hydrated samples [85]
BaInOH	0.63 ± 0.025	$1.5\cdot10^{-5}$	imped. measures, fully hydrated samples (≈ 180°C) [11]
BITh25	0.67 ± 0.025	$6.5\cdot10^{-4}$	–”– [11]
BITh50	0.54 ± 0.025	$5.0\cdot10^{-6}$	–”– [11]

---

[1] This would correspond to a BIT80 or BIT90 compound in this work which were explicitly not taken into consideration.

6.2.1 Computational studies

Table 6.I gives an non-exhaustive overview over the range of diffusion coefficients obtained by computer simulation and experiment. All mentioned simulation studies focus on the doped-perovskite case and deal with dilute proton concentrations in a pure or doped oxide matrix. The first three entries present the work of Münch and co-workers [26, 25, 24, 23] for pure perovskites by direct DFT-based MD-simulations. Their activation energies compare more or less well to the experimental counterparts, however ”only” within the statistical error which is rather big. As for all computational studies presented in the table, the set of Arrhenius parameters is always determined by exact two temperature points. This of course prevents any consideration of a possibly curved Arrhenius representation of the diffusion coefficient.

The other computational studies (by the group of Björketun and Bilic/Gale, respectively) are based on an analysis of the potential energy surface by means of a number of static DFT calculations for all proton sites as well as all the barriers. Furthermore they model the diffusion in a similar manner as was shown for the kinetic Monte Carlo scheme in this thesis. The prefactors of the single MC-displacement steps on their protonated lattice were modeled as the frequency ratio obtained by a normal mode analysis of protonic equilibrium and corresponding transition states (this formalism is presented in more detail in section 6.4.1).

Of particular interest here are the results of Björketun [36] which may be interpreted in a somewhat new light here especially the behaviour concerning the pre-factors. The table gives values for two groups of dopants for $BaZrO_3$ with the major difference that Ga acts as a (very) deep trap for the protons (≈ -0.5 eV) whereas In associates only weakly (≈ -0.15 eV) with the proton: its trapping effect is therefore much weaker. These findings were obtained by static analysis of the corresponding doped structures with respect to protonic site and barrier energies.

Now there is the question about the actual meaning of the prefactors and how their behaviour may be rationalized. Given the fact that we still deal with a rather simple system it is quite instructive to run some equivalent Monte Carlo simulations on a lattice that qualitatively equals the one used in [36]. This was done here for a PES characterized by some fixed, small barriers (0.1, 0.08, 0.06 eV for stretch-hop, rotation and flip, respectively) and a small concentration of 0.3 eV deep and randomly distributed traps. The values do not have a particular meaning. There is one proton diffusing on this lattice so that the parametric situation is comparable to the one in [36]. Figure 6.1 a) shows the log of the diffusion coefficients of this system over inverse temperature and for several trap-concentrations.

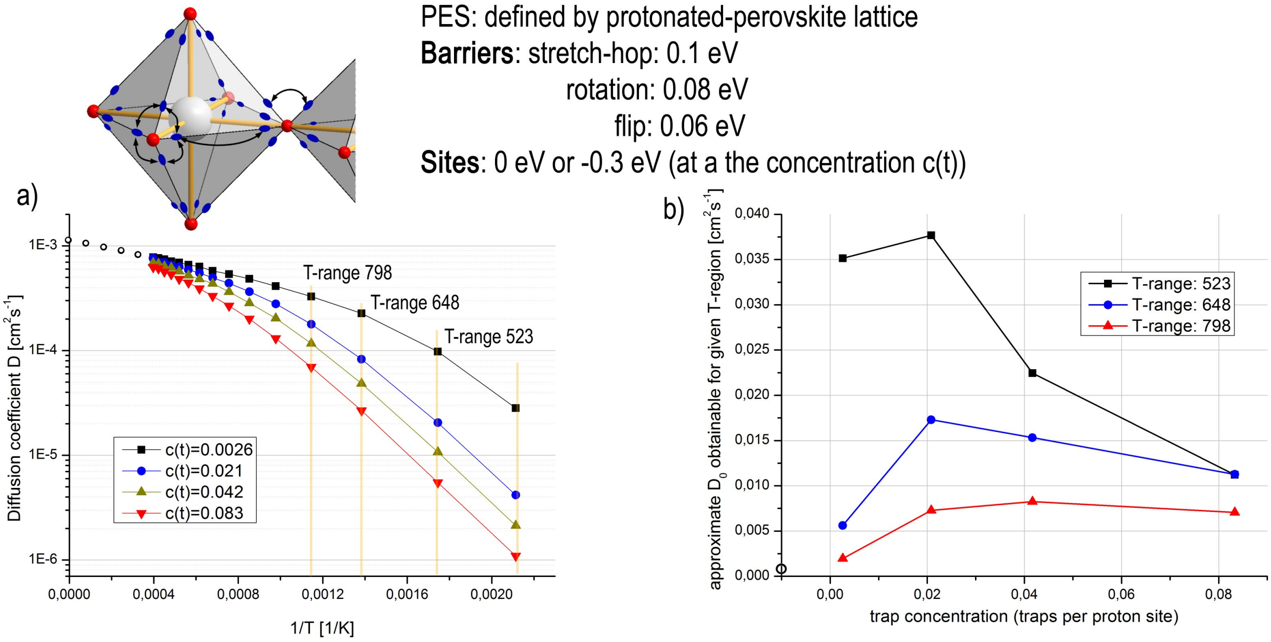

Figure 6.1: a) Arrhenius representation of the single-proton diffusion coefficient for a simple trap-decorated PES. b) Illustration of the behaviour of a fitted diffusional prefactor D_0 as a function of trap-concentration and the temperature region from which the data was fitted.

As it was explained in detail for the random-trap model (and average rates in general) the plot shows a distinct convex curvature which is characteristic for every PES containing trapping sites (and not too strong barrier disorder). It has to be stressed that this diffusion behaviour is a lattice property and does not suffer from any measuring flaw or difficulty whatsoever. All diffusion coefficients presented are equilibrium values based on MC-runs of 20^5 steps (around 2 ns) and averaged displacement of at least ≈100 Å for the lowest temperatures.

A first implication is that it is *not sufficient* to characterize such a system by only two points and to infer a set of one prefactor and one activation energy. The extractable values do significantly depend on the temperature region in which the fit is performed (and its relation to the lattice energies). Figure 6.1 illustrates this by giving the "effective" diffusional prefactors when a linear fit was performed only in the given temperature regions. The D_0 coefficients are given in a sequence making reference to the values for Ga:BaZrO$_3$ in table 6.I, i.e. by increasing dopant/trap concentration.

This illustration states that the actual evolution of the so obtained prefactors does not have an immediate signification at all when dealing with disordered systems:

(I) All prefactors overestimate the "correct" one, i.e. the real high temperature limit of D. Its location is indicated in figure 6.1 a) (extrapolated points) and in b) as a single point at around $1.3 \cdot 10^{-3}$ cm^2s^{-1}. It is this value which corresponds to the D_0 associated with the prefactors of the elementary steps that are inserted into the MC-routine (see section 2.3). This is a well defined property of trap-decorated lattices.

(II) Relations such as "which trap-concentration has a larger prefactor than another one" *change* when considering a different temperature interval.

Both in [36] and [33] the temperature range was only 300 K large and consisted only of two points. Hence although for the own MD-results single prefactors and activation energies will be given they should never be regarded as well defined system properties. A measured prefactor is therefore not only representing vibrational properties of the migrating species but carries not easily identifiable information on the energetic landscape, too.

It is left to note that the considerations made here are also applicable to the experimental situation. The difference mainly being that for the conductivity experiment on proton conductors the accessible temperature range is always rather small and lies in the same region of about 200°C to 500°C. Put otherwise this ensures a comparability among materials. Furthermore very often the measures are blurred by the dehydration process which may entail a substantial change of the PES.

6.2.2 Experimental studies

For the experimental examples, the most relevant ones for this work were chosen in table 6.I: fully hydrated, heavily disordered and rather Brownmillerite than perovskite BIZh and BITh compounds. These are actually the most intensively studied compounds in the following. As can be seen by the values their low-temperature obtained Arrhenius parameters are not substantially different from their perovskite related counterparts. As already stated in the introduction their potential interest rather lies in the high proton concentrations that they can integrate. As is easily seen from the table, at least for the compounds currently under scrutiny no drastic improvements of the mobility can be expected. It is unlikely that Brownmillerite related compounds mobilities can exceed those of perovskite-based compounds by orders of magnitude. However the Brownmillerites' merit is to display similar mobilities with a significantly increased proton *content* though. This is obvious by remembering that we might consider a say BITh25 compound as a 75% acceptor doped perovskite.

Nonetheless it is crucial to maximize the corresponding Brownmillerite-compound's mobility. Comparing the experimental values of BaInOH with the Ti-substituted compounds then shows that substitution indeed brings about *significant* improvements of the diffusivity level (albeit with a higher activation energy, the prefactor plays the decisive role here). It has to be noted, that the pre-factors for the BIThx compounds that are given are based on only one conductivity value combined with the corresponding activation energies. Given their experimental errors (which are relatively small though) the uncertainty for the prefactor will nevertheless be rather large because of the very small temperature region that is examinable (ranging from room temperature to 180°C).

All experimental values were obtained by the Arrhenius-fit of measured diffusion coefficients D_σ from impedance spectra and the knowledge of the proton content. The only exception is the neutron spin-echo experiment of KARLSSON and co-workers [98]. This method allows to probe proton relaxation times on the ps-scale. However the low-temperature diffusivity contains an uncertainty which leads to the huge error for the activation energy and even more so for the prefactor (whose value is actually not given in the paper). There is also an actual signification for the large errors, which is a very broad distribution of protonic relaxation times on a very local scale, which can be identified with a rather uneven energy landscape.

6.3 Effective diffusion coefficients by MD simulation

6.3.1 General remarks and results

The determination of effective diffusion coefficients of protons in the different compounds can be considered one of the principal outcomes of this study for it is this measure that determines the proton mobility as a factor of the conductivity.

To record the mean-square displacement (MSD) of the ensemble of particles (protons here) in an MD simulation in principle easily allows for obtaining the diffusion coefficient. The technical approach was explained in section 2.2.4.2 as well as the expected statistical error in section 2.4. The MSD was extracted out of the MD simulations at four temperatures (500°C, 800°C, 1200°C and 1500°C) for all chemical compositions investigated (except BITh75). All calculations were performed for initially fully relaxed atomic configurations both with respect to the cell size and atomic positions. These starting configurations are based on appropriately modified versions of the pure BaInOH system for what their proton distribution is concerned.

Identical starting configurations were used for all temperatures.

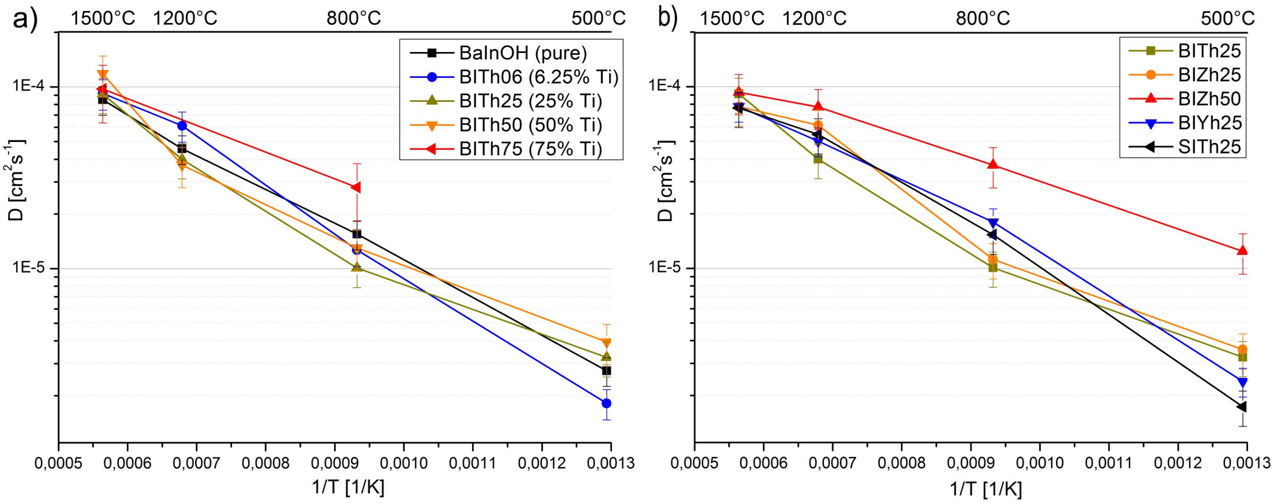

Figure 6.2: Proton self-diffusion coefficients as obtained by MSD-analysis at several temperatures for a) fully hydrated BIThx compounds ranging from pure BaInOH to 75% Ti and b) several 25% substituted compounds (the lines are guide to the eye)

Figure 6.2 gives an overview over all completely hydrated compounds investigated in the study. Subfigure a) presents the BIThx sequence of compounds from BaInOH up to BITh75 whereas in b) the remaining compounds including BIZh25, BIZh50, BIYh25 and SITh25 are compared to BITh25.

As can be observed the overall diffusivity level is reasonably well located compared to experimental and other computational studies. To further elucidate this, table 6.II presents the associated fitted sets of single-Arrhenius parameters (activation energy E_a and prefactor A) obtained by a direct exponential fit to $D = A \cdot \exp\left(\frac{-E_a}{kT}\right)$, or a linear fit to $\ln(D) = ln(A) + \frac{-E_a}{kT}$, respectively. These two fits shall serve as an indicator of the coherence of the fit to only two parameters. The larger the discrepancy between the two sets of values so obtained, the larger the non-Arrhenian behaviour (i.e. curvature)[2]. The two different ways of fitting do not treat equal the four points so that one method will often better match the low temperature points, whereas the other matches the high temperature ones more closely.

By having only 4 temperature points available for exploitation of course we are far away from actually being able to assess a curvature as unambiguously as it was possible in the Monte Carlo studies in the previous chapter. Therefore the discussion with respect to that has to remain rather qualitative. Moreover the actual error-(bar) on the diffusion coefficient is not taken into consideration explicitly and therefore extends the actual E_a region even further.

---

[2] Of course the non-Arrhenian behaviour in that sense could also be purely error-related.

Table 6.II: Arrhenius parameters for the effective diffusion coefficients obtained by MD. The values of E_a and A are given obtained by two ways of fitting along with their standard deviations of the respective fit.

	E_a (exp.fit)[eV]	E_a (lin.ln-fit)[eV]	A (exp. fit) [$1\cdot10^{-3}$cm^{2}s^{-1}]	A (lin. ln-fit) [$1\cdot10^{-3}$cm^{2}s^{-1}]
BaInOH	0.39 ± 0.035	0.40 ± 0.01	1.05 ± 0.27	1.17 ± 0.13
BITh06	0.39 ± 0.06	0.47 ± 0.02	1.24 ± 0.5	2.25 ± 0.48
BITh25	0.61 ± 0.06	0.40 ± 0.05	5.42 ± 2	1.1 ± 0.5
BITh50	0.81 ± 0.15	0.38 ± 0.06	23.2 ± 22	0.98 ± 0.83
BITh75	-	0.30	-	0.66
BIZh25	0.34 ± 0.1	0.39 ± 0.04	0.77 ± 0.5	1.08± 0.59
BIZh50	0.22 ± 0.03	0.24 ± 0.01	0.4 ± 0.075	0.49± 0.066
BIYh25	0.22 ± 0.005	0.41 ± 0.03	0.43 ± 0.015	1.28± 0.4
SITh25	0.34 ± 0.05	0.46 ± 0.03	0.74 ± 0.26	1.78± 0.67

The proton-diffusivity in BITh75 was only evaluated at two temperatures and therefore by definition is ”perfectly arrhenian” due to this fact the compound will not explicitly be included in the discussion.

Most of the values presented here correspond rather well to the direct MD-simulations by MÜNCH and co-workers albeit on much simpler pure perovskite systems. However it can be noted by comparison to the first four values of table 6.I on page 164 that the prefactors lie in the same region of $1\cdot10^{-3}$ which is in contrast to the largely over-estimated prefactors of BJÖRKETUN. The latter are based on the eigen-frequencies of the protons in their ground- and transition-states which were analysed by normal mode analysis of each individual position. This is very likely a manifestation of the more exact implicit treatment of the transition process within the molecular dynamics routine than by a determination of the prefactors by a vibrational analysis of the ground- and transition states alone. For example direct MD fully considers the contribution of the oxygen lattice vibrations to the proton transfer steps.

The reference compound BaInOH behaves remarkably regular, i.e. is very linear in the Arrhenius representation which is also reflected in the small difference between the two fitting methods. An activation energy of 0.4 eV is found in both cases coupled to prefactors of around $1.1\cdot10^{-3}$ cm^{2}s^{-1}. It turns out that a direct comparison to the experimental values is not straight forward. Compared to the experimental evidence on BaInOH in table 6.I the activation energy seems underestimated whereas the prefactor is overestimated in the MD-simulations. Both aspects are therefore in favour of a higher diffusivity in the simulation. However care has to be taken with respect to which effects are supposed to be included in the simulation:

(I) The MD-simulation is performed in a perfect mono-crystal environment, naturally excluding *any* deviation in the diffusion properties brought about by grain boundaries. An estimation of how important this aspect may be is unfortunately not possible given the complexity of a microscopical treatment of grain boundaries.

(II) The problems associated with the definition of *the* activation energy or *the* prefactor itself: As was laid out in section 6.2.1 the relation between temperature interval and the characteristic energies of the system under scrutiny determine to a large extent the value of the prefactor (and the activation energy) that would be extracted. This is the case for any effective process that is based on more than one distinguishable elementary process as was elucidated by the Monte Carlo simulations. Indeed the temperature regions of the experiment (below 200°C) and of the MD-simulation (500° to 1500°C) are largely different and it was shown that already BaInOH stands for a highly inhomogeneous potential energy surface (see the sections on the Blocking layer, the intra- and extra-octahedral proton sites as well as the upcoming study on the elementary jump-rates - sections 4.3.3, 4.3.1 and 6.4, respectively)

(III) An issue which in a systematic manner may lead to too small activation energies is the 500°C temperature point of the MD-simulation. Arguably the runs at 500°C *overestimate* the diffusivity and therefore entail smaller slopes. This overestimation may be caused by the fact that observed proton displacements partially are ”only” due to the establishment of the structural equilibrium concerning the proton positions. Despite the fact that the mean square displacement is not used during the initial part of the MD-run (see section 2.2.4.2), 500°C probably do not supply a sufficient statistical weight for a direct diffusion analysis.

6.3.2 The influence of the cation substitution up to 25%

As it may be expected from the experimental evidence the cation substitution does not cause ”miraculous” improvements of the overall diffusivity. So the interpretation of its impact always has to seen in the frame of the overall confidence one can have on the MD-obtained diffusion coefficients.

For the case of the BIThx compounds (up to 25% substitution) we can observe an increase in averaged activation energy obtained by two fitting methods alike for 6.25% and 25% (BITh06 and BITh25). This is in agreement with the expectation that diffusional activation energies increase by the presence of trapping sites in a lattice. Given the evidence from section 4.3.2 this is more and more the case in BIThx with increasing Ti-content because Ti-polyhedra act as proton-traps. Additionally we can note, that an E_a-increase for BITh25 compared to BaInOH is at least not contradictory to the experimental data in table 6.I.

This tendency can further be discussed by considering the other 25%-substituted compounds BIZh25 and BIYh25. For both of them the activation energies using both fitting methods are below (or equal) to the ones of BaInOH and BITh25. The section on the proton trapping clearly showed that Zr- and Y-polyhedra do not readily associate with protons but merely consitute obstacles for proton motion. Hence for Zr and Y concentrations of 25% this merely corresponds to a blocking effect of *some* diffusional pathways which has no tremendous effects on the diffusion coefficient as the indium-polyhedron lattice is largely percolating the entire structure. A presumed actual decrease of activation energy for Zr- and Y- might furthermore be related to an overall destabilization of the parent structure of BaInOH with respect to its intra/extra-octahedral proton layer (which was clearly evidenced for BIZh25, section 4.3.1). The tendency to have lower activation energies for BIZh25 than for BITh25 is qualitatively confirmed by the experimental data in table 6.I.

Thus in very simplified picture one should attribute a negative impact to the substitution with Ti as it creates genuine traps for proton diffusion. The activation energy tendency is in agreement with the experimental values in table 6.I with 0.4 eV for BIZh25 and 0.67 eV for BITh25. Important however is, that the proton concentration exceeds the trap concentration so that the non-trapped portion of protons may diffuse unhindered. Furthermore the prefactors of BITh25 and BIZh25 differ by a factor $\approx$6 both in experiment and in the simulations in favour of BITh25. (However having one order of magnitude offset, overestimating the computational prefactor).

6.3.3 The 50/50 cation substituted compounds

The 50/50 Ti/Zr compositions probably show the most distinct (and also statistically safe) differences. Two major issues are worth a somewhat deeper investigation. (I) the particular behaviour of BITh50 to show a rather regular behaviour between 500°C and 1200°C but a considerable gain in diffusivity for 1500°C and (II) the pronounced difference between BITh50 and BIZh50 except at 1500°C. Especially BITh50's diffusion coefficient is somewhat peculiar what already could be observed in table 6.II: the direct exponential fit (which basically fits the steep increase between 1200°C and 1500°C) gave an abnormally high activation energy of 0.81 eV associated to a very high prefactor compared to all other prefactors obtained. The corresponding diffusion curves are shown in figure 6.3.

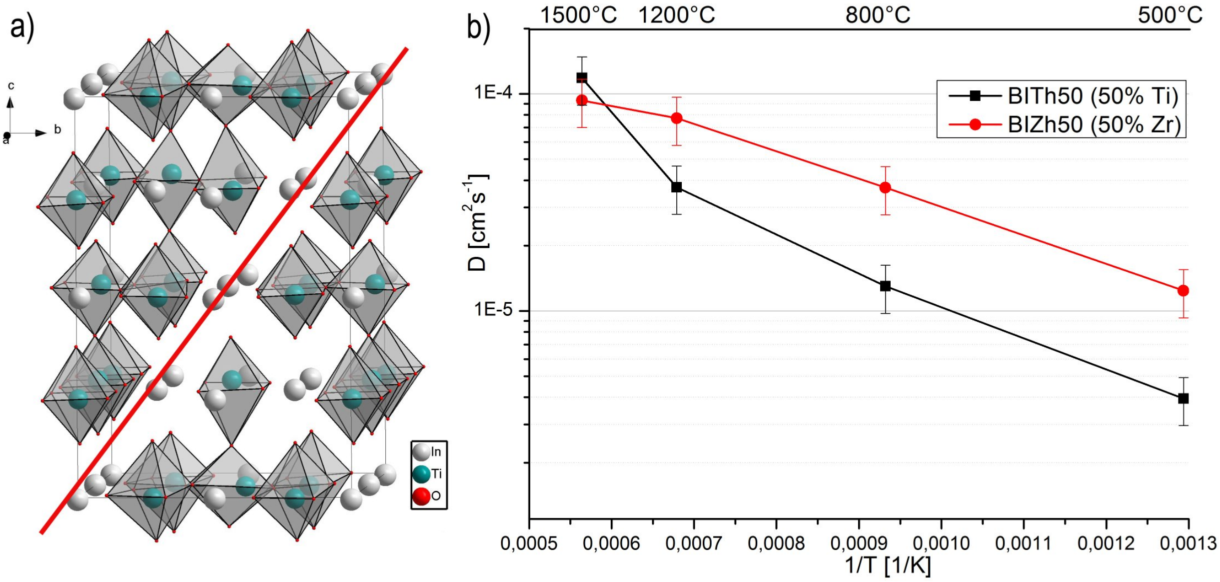

Figure 6.3: a) Representation of the non-percolative character of the Ti-polyhedra in the simulation cell of fully hydrated BITh50, b) Comparison of the temperature evolution of the proton diffusivity of BITh50 and BIZh50. The activation energy for BITh50 when omitting 1500°C is ≈0.30 eV as opposed to the values given in table 6.II

It is possible to unambiguously state that the diffusion coefficient of BITh50 is underestimated by a particularity of the 50/50 mixture. The simulation cells used for the MD-simulations are, as said in the technical introduction, created to represent a disordered cationic structure. However the 50/50 case represents a very delicate situation with respect to the generation of a really disordered lattice. Although the simulation cells are relatively large having 32 B-site cations one is not safe to generate particular ("pathological") configurations. Relatively late in the course of the work it turned out that the Ti-polyhedron sub-lattice is not percolative. This means that there is no closed pathway from one simulation cell to its repetition in the three dimensions that consists only of Ti-polyhedra. It has to be stressed that this is the property of the here-chosen simulation cell. In the general case (i.e. for a very large number of polyhedra) there necessarily *is* a percolation path. This affirmation can be rationalized by the two following facts:

(I) A perovskite like lattice, where we take the polyhedra as lattice points is of the simple-cubic structure.

(II) The (here relevant) site-percolation threshold for the simple cubic lattice is around 0.31 (e.g. [96]).

This means that in the real compound a percolation in the sense defined here is guaranteed already from a degree of substitution 31% upwards. Thus for the 50% we are concerned with here one can be sure to have many percolation paths in a real material. The simulation cell of the MD-simulation is therefore rather a special case than a proper representation of BITh50.

Several things can be learned however from this MD-simulation. Regarding the jump in diffusivity at a temperature as high as 1500°C indicates some drastic change at this point. Indeed a comparison with table 4.III on page 103 helps to clarify this effect. The property which was given in this table is the factor by which proton association is more or less pronounced next to either Ti or In. Comparing the values for BITh50 for rising temperatures reveals a drastic drop of this preference between 1200°C and 1500°C. This is in contrast to any other compounds for which the evolution over temperature is much smoother. Hence the jump in conductivity is concomitant with a drastic increase in indium proton association.

Given the structural argument of the non-percolation this leads to the conclusion, that only at this high temperature, protons massively escape the trapping effect of the Ti-polyhedra. In our particular case these Ti-polyhedra may be considered basins in the same sense as used before for the Monte Carlo simulations.

To repeat and summarize this issue: the behaviour of the MD-simulation for BITh50 is very likely related to the particular choice of a simulation cell with no Ti-percolation. As a consequence the diffusing protons are forced to remain within the basins of Ti-polyhedra and do not extend to the indium polyhedra up to 1500°C. This geometrical constraint hinders the long-range diffusion. Thus, calculations with percolating Ti-configurations should be able to yield a systematically higher diffusivity: it may be suspected that the overall diffusivity should be similar to BIZh50. An argument for this will be presented in the next section dealing with the elementary displacement steps, which are more or less equal or even easier for BITh50.

In contrast to the 25% compositions we cannot state an agreement with the experimental tendencies. Both BITh50 and BIZh50 show higher experimental activation energies than BaInOH of 0.54 eV and 0.6-0.7 eV, respectively. The MD-simulations however indicate *the lowest* values for BIZh50 and BITh50 (the latter one only without the particular point at 1500°C). This is especially true for BIZh50 with its regular behaviour and the activation energy of 0.22 eV.

Except of structural reasons for this deviation from experiment (like grain boundaries etc.) one possible argument might be the disordered character and the fact that the temperature region used in the simulation (500°C to 1500°C) is much higher than for any experiment (up to ≈300°C for fully hydrated samples). Following what was presented in the previous section 6.2.1, the MD-simulation would unfortunately just see another part of the possibly curved Arrhenius representation and therefore yield different parameters.

6.4 Modes of proton displacement

6.4.1 Formalism

As stated in the previous section on the effective diffusion coefficients, only a limited significance can be attributed to the mere comparison of their pure values. Therefore it is necessary to study the underlying diffusion mechanisms in more detail, which are the proton displacement modes. This section gives a detailed account on which of these modes are occurring to what extent in the fully protonated compounds.

For this treatment of MD-data, a proton's position is taken to always be defined by the association with its *two* nearest oxygen neighbours. These are the nearest neighbour (NN) to which it is covalently bonded and the next-nearest neighbour (NNN) which is the oxygen to which it is hydrogen-bridge-bonded to. This concept uniquely determines the site character of any proton at any moment throughout the MD-run of being intra- or extra-octahedral depending on whether the NNN belongs to the same B-site octahedra as the NN or not.

Note that this definition somewhat arbitrarily also categorizes more or less "freely rotating" protons as being one of the two kinds; a situation which may arise for a covalently bonded proton having its NNN in more than about 2 Å distance which can be regarded as an upper limit to an actual hydrogen-bond.

In classing the protons into intra- and extra-octahedra however the counting routine does not distinguish between extra-octahedral protons that are part of a corresponding structure-defining extra-layer (present for the Brownmillerite structured compounds) or extra-octahedral protons having a transient character; a concept that was introduced in the section 4.3.1 on the intra- and extra-octahedral proton sites. The first ones were referred to as structural because they are constitutive to the crystallographic structure of the hydrated Brownmillerite based compounds. The second category of extra-octahedral proton assume an extra-octahedral character only during transfer events, which turn out to be not characteristic for the compounds studied with the exception of the SITh25 compound. Given the smaller overall cell parameter due to the smaller Sr ion on the A-site, this is plausible and was also described in the intra/extra-section. Also some doped orthorhombic perovskite proton conductors such as $CaTiO_3$ or $SrTiO_3$ do show a substantial amount of extra-octahedral proton transfer[23].

This strict categorization of protons allows to distinguish between the six elementary displacement modes that were identified. An illustration of them is given in figure 6.4. It has to be noted that at no temperature as high as 1500°C any other elementary step was observed in any of the structures. Any observed change in proton-oxygen association falls into one of the six categories presented here. Modes labeled 1, 3 and 4 are the three constitutive modes that exist in any protonated perovskite structure. Mode number 1 is linked to the O-H stretching-vibration mode and involves the breaking of the covalent O-H bond and therefore is supposed to be rather difficult to perform. The actual process is however heavily influenced by the transient shortening of the corresponding O-O distance.

Modes 3 and 4 are two modes activated by the two bending vibrations of a proton. Commonly they are referred to as ”re-orientation” modes lumped together as one single process. Indeed the possibility to distinguish between them is only due to the fact, that the protons are always considered to be hydrogen-bonded to their next-nearest oxygen neighbour. By definition both modes involve the breaking of that very hydrogen-bond which is supposed to be easier than the covalent bond-breaking. However things depend on the particular compound and mostly their O-O distances. The smaller these distances the more pronounced the hydrogen bonds and the weaker the O-H bonds. Moreover, due to the disordered nature of the compounds there are a few protonic sites, which do not permit the creation of a hydrogen bond, so that protons in those site may be considered more or less freely bending. This latter aspect will contribute to the rather small effective activation barriers observed for these modes.

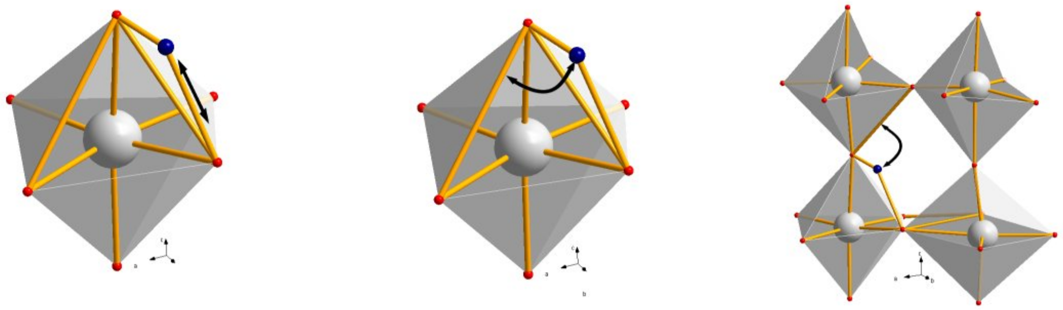

Mode 1: intra-octahedral stretch   Mode 3: intra-octahedral rotation   Mode 4: intra-octahedral flip

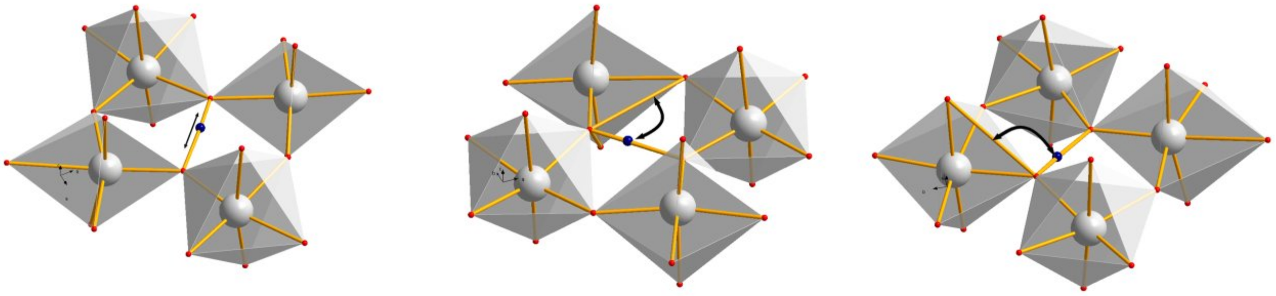

Mode 2: extra-octahedral stretch   Mode 5: extra/intra-octahedral in-plane bend   Mode 6: extra/intra-octahedral out-of-plane bend

Figure 6.4: The six elementary proton displacement modes. The upper three modes (numbers 1, 3 and 4) are common to all protonated perovskite materials. Modes 2, 5 and 6 are unique to extra-octahedral protons with 5 and 6 being the intra/extra-producing/annihilating modes.

The last two modes 5 and 6 can be seen as creation/annihilation modes for the two proton classes intra-octahedral and extra-octahedral. Similar to modes 3 and 4 they are activated by bending vibration modes.

Differently than in protonated perovskites, a 3-dimensional long range diffusion in Brownmillerite based compounds has to be effectuated by *all* of the identified modes. Modes 1, 3 and 4 alone would ensure a long range diffusion alone, but only in a 2-dimensional way in between the extra-octahedral layers (in case they were considered blocking, which they are not as we will see).

In order to characterize each of the single displacement modes, a counting algorithm was employed on the MD runs which distinguishes all six different proton changes possible (4 modes that leave the proton type unchanged and 2 modes corresponding to the switching between an intra and extra-octahedral proton). Given the fact that we deal with thermally activated processes, (convential) transition state theory is used to extract thermodynamical parameters out

of the raw counting rates. These parameters are a prefactor and the associated activation energy.
Important here is, that the MD-runs strictly obey classical behaviour with respect to their vibrational properties. Thus, to characterize the MD-results, exclusively classical partition functions shall be used. The influence of quantum effects (most importantly zero-point energy) will be discussed in section 6.4.3. The description is based on the following equations (following [99] for example):

The rate of any given displacement step is determined by the choice of a reaction coordinate (here a vibration ν_R) and the corresponding partition functions:

$$r = \nu_R \cdot \frac{q^{*'}}{q} exp\left(-\frac{E_a}{kT}\right) = \nu_R \cdot q_{\nu_R} \cdot \frac{q^*}{q} exp\left(-\frac{E_a}{kT}\right) \tag{6.1}$$

The equations's right hand side indicates the possibility to separate out the reaction-coordinate's partition function which will be taken as the classical expression for a vibration $q_\nu = \frac{kT}{h\nu_R}$ giving

$$r = \frac{kT}{h} \cdot \frac{q^*}{q} exp\left(-\frac{E_a}{kT}\right) \tag{6.2}$$

which allows to drop the actual reaction-coordinate. Taking the classical vibrational partition function here is however still strictly correct, as it concerns the vibrational frequency/reaction-coordinate *at* the transition state, where by definition it approaches zero and therefore even the quantum mechanical vibrational partition function becomes identical to the classical expression.

In the following the actual form of the q-ratio is going to be discussed. It is the ratio between the vibrational partition functions in the ground state and the transition state. For all of the six displacement modes, we can state that the proton is characterized by three vibrational frequencies in the ground state and two frequencies in the corresponding transition state, where basically the reaction-coordinate vibration is missing (or imaginary). It is now, that we consciously use classical partition functions, for the five frequencies concerned. The entire classical prefactor becomes:

$$\frac{kT}{h} \cdot \frac{q^*}{q} = \frac{kT}{h} \cdot \frac{\frac{kT}{h\nu_{TS1}} \cdot \frac{kT}{h\nu_{TS2}}}{\frac{kT}{h\nu_{GS1}} \cdot \frac{kT}{h\nu_{GS2}} \cdot \frac{kT}{h\nu_{GS3}}} \tag{6.3}$$

Where subscripts GS1,2,3 stand for the three ground-state frequencies and TS1,2 for the two transition-state frequencies, respectively.

All k_B, T and h cancel so this simplifies to the very instructive form of a temperature-independent prefactor for a diffusional elementary step, giving the rate as

$$r = \frac{\nu_{GS1} \cdot \nu_{GS2} \cdot \nu_{GS3}}{\nu_{TS1} \cdot \nu_{TS2}} \cdot \exp\left(-\frac{E_a}{kT}\right) \tag{6.4}$$

when the real-valued normal mode frequencies in the ground- and transition state are known. By comparison of equations (6.4) and (6.2) we learn that the q-ratio for this case becomes temperature dependent. Equating the q-ratio with the entropy-difference exponential $\exp(-\frac{\Delta S(T)}{k})$ we can write the rate equation in the form:

$$r = \frac{kT}{h} \exp\left(\frac{\Delta S(T)}{k}\right) \exp\left(-\frac{E_a}{kT}\right) = \frac{kT}{h} \exp\left(-\frac{\Delta G}{kT}\right) \tag{6.5}$$

Finally we note that the temperature dependency of $\Delta S(T)$, which is due to the unequal numbers of vibrational modes in the ground- and transition-state, has the form $\propto \frac{1}{T}$. It simply is obtained by dividing the T-independent prefactor by $\frac{kT}{h}$. This prefactor is supposed to equal the ratio of the occurring frequencies as in equation (6.4).

Technically this expression can of course be fitted from the MD-data, however it cannot necessarily be directly related to the ratio of the corresponding vibration frequencies. The reason for this lies in the potentially barrier-disorder that may be associated to a given displacement mode. As it was discussed in the Monte Carlo chapter (section 5.2.2) the extrapolation of a single prefactor for a curved Arrhenius representation is of course questionable.

6.4.2 Proton displacement rates by MD-simulations

6.4.2.1 Intra-octahedral displacement modes

First, only the modes 1, 3 and 4 are going to be studied, because all of them leave the proton-type unchanged intra-octahedral. Moreover those modes are the modes occurring in protonated perovskites.

The graphs of figure 6.5 show the absolute rates in units of $events \cdot s^{-1}$ which are normalized to the averaged number of intra-octahedral protons. The same is done for rates concerning the extra-octahedral protons later on.

For a better discussion table 6.III assembles the Arrhenius fitted activation energies and prefactors for each mode. The prefactors are given in actual rate units as well as cm^{-1} in the sense of equation (6.4).

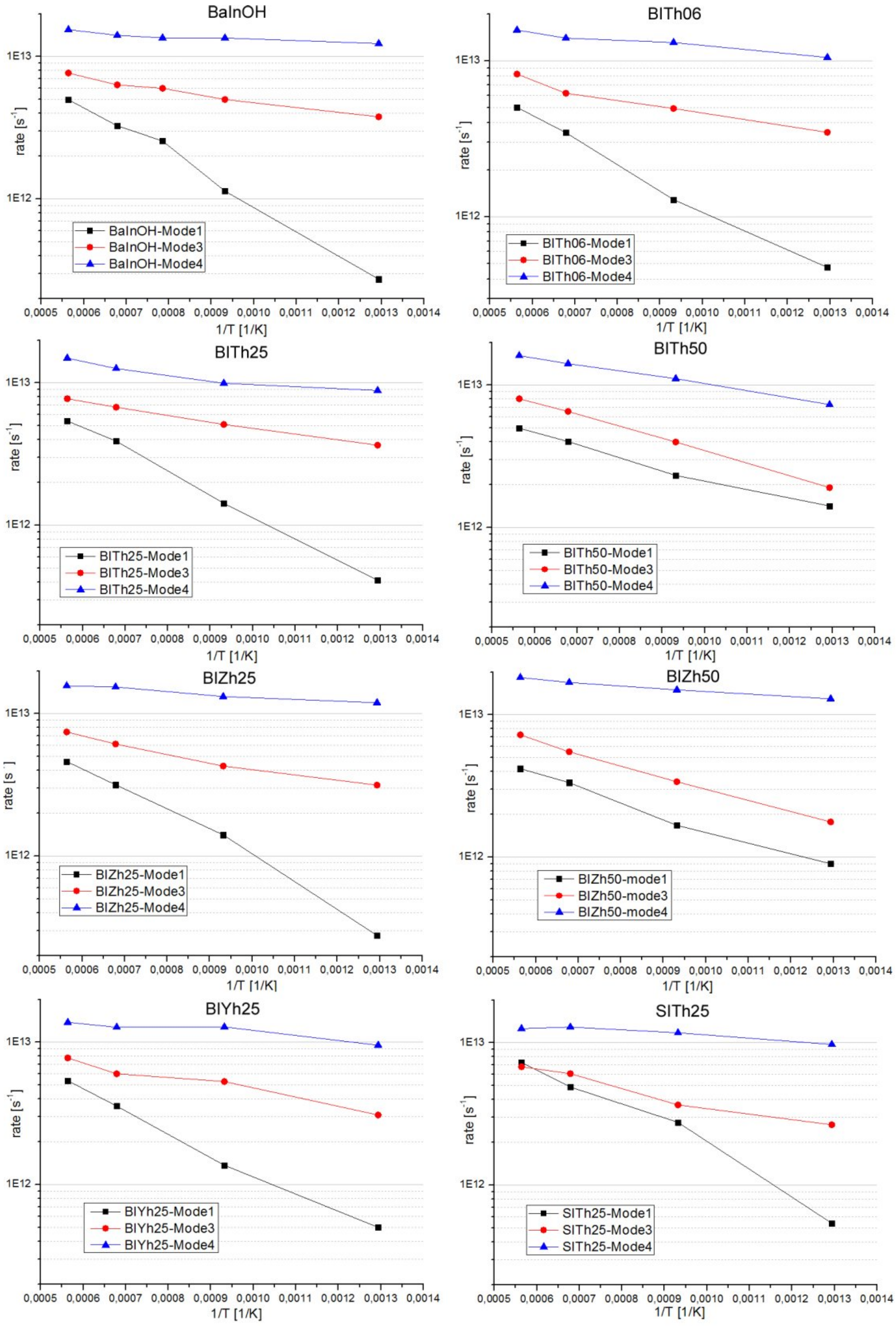

Figure 6.5: Rates of the three protonic displacement modes stretch-hop (1), rotation (3) and flip (4) obtained by an event-counting algorithm from the MD simulations.

Table 6.III: Activation energy (in eV) and prefactor (in $1 \cdot 10^{13} s^{-1}$ and in equivalent cm^{-1} in parentheses) of the three purely intra-octahedral elementary rates fitted to equation (6.5) for all compounds including four temperatures: 500°C, 800°C, 1200°C and 1500°C

	Mode 1		**Mode 3**		**Mode 4**	
	E_{act}	prefactor	E_{act}	prefactor	E_{act}	prefactor
BaInOH	0.31	3.80 (1270)	0.085	1.30 (434)	0.024	1.75 (584)
BITh06	0.30	3.65 (1218)	0.10	1.53 (510)	0.044	2.06 (687)
BITh25	0.28	3.42 (1141)	0.10	1.48 (494)	0.070	2.32 (774)
BITh50	0.16	1.43 (477)	0.17	2.41 (804)	0.092	2.94 (981)
BIZh50	0.20	1.53 (510)	0.17	2.20 (740)	0.041	2.35 (784)
BIZh25	0.29	3.07 (1024)	0.11	1.48 (493)	0.035	1.99 (664)
BIYh25	0.24	2.42 (807)	0.10	1.44 (480)	0.034	1.78 (594)
SITh25	0.26	3.83 (1277)	0.12	1.53 (510)	0.040	1.78 (594)

The results obtained by the rate-counting approach in general are rather instructive. They show clearly that for all compounds and temperature the intra-octahedral stretch mode will remain the most difficult one to perform. In the MD-simulations in this work it is characterized by effective activation energies of 0.15 eV to 0.3 eV. The rotation mode already is much easier having activation energies of 0.1 eV to 0.17 eV. The flip mode turns out to be almost un-activated with a very small temperature dependence resulting in activation energies in the region well below 0.1 eV. However it becomes clear that the separation of the reorientation motion is useful as it yields well distinguishable processes.

Right in the beginning one should recall one of the most fundamental results that was presented in the Monte Carlo chapter, which is the discrepancy between countable elementary displacement steps and the true long range diffusion. In the general case (and foremost for any form of barrier disorder) a counting rate approach will not supply an information on the ”rate limiting step”. Rather rates will have tendency to be correlated and thus be *overestimated* compared to the long-range displacement due to ”wasted” hopping events inside some basin regions, associated traps or the like.

In a first general comparison it becomes clear that for all compounds except BIZh50, none of the here presented elementary steps reaches activation energies that compare with the activation energy obtained for the net-diffusion (table 6.II on page 170). All counted modes seem too easy compared with the observed diffusion coefficient. An explanation of this effect may at least be two-fold:

- For compounds that contain an extra-octahedral layer of protons (all but BITh50 and BIZh50) the rates associated to the escape of this layer will be included in the net-observed diffusivity. As will be evidenced in the upcoming section 6.4.2.3 those modes are likely to have activation energies of up to 0.5 eV which might contribute to the net-diffusion activation energy.
- At the same time (and especially for BITh50, which does not contain extra-octahedral sites) the disorder concept mentioned above may come into play. This would account for easy back-and-forth hops that lead to high elementary step rates but do not contribute to the long range diffusion.

The comparative aspect between the compounds has several axes: there seemingly are systematic evolutions for BaInOH through BITh50 in the BIThx series as well as a very distinct behaviour of the two 50% substituted compounds compared to all others. Concerning the first aspect, on an average the stretch-mode obviously becomes easier in compounds with increasing Ti-content. The inverse tendency holds for the rotation and flip modes, which increase along with the Ti-content. This can very likely be the expression of an increase in average hydrogen-bond strength or number. Strong hydrogen bonds are equivalent with relatively short O-O distances between the oxygen ions to which the proton is associated. By approaching the two oxygens the corresponding stretch activated hop becomes easier. In turn the displacements related to bending vibrational modes become more difficult as the proton is more and more tightly bound on two sides.

An indicator of this property is supplied by the pair correlation functions which are given for BaInOH, BITh25 and BITh50 in figure 6.6. A surplus in hydrogen bonding can safely be identified for the Ti-containing compounds. For BITh50 in particular the extent of H-bonding is remarkable given the absence of the extra-octahedral proton layer, which by definition is characterized by very strong H-bonds and is present for BaInOH and BITh25.

It can be concluded that Ti-substitution gives rise to a more pronounced hydrogen-bond structure, which essentially concerns two oxygens that are part of a Ti-polyhedron (see Ti-trapping effect section 4.3.2). From the transport point of view this leads to a decrease of stretch-barrier height but an increase in rotation and flip-barrier height up to a point in which (for BITh50) the rotation and the stretch hop have *identical* activation energies of 0.16 eV. Moreover this indirectly allows the affirmation that we deal with a massively barrier disordered

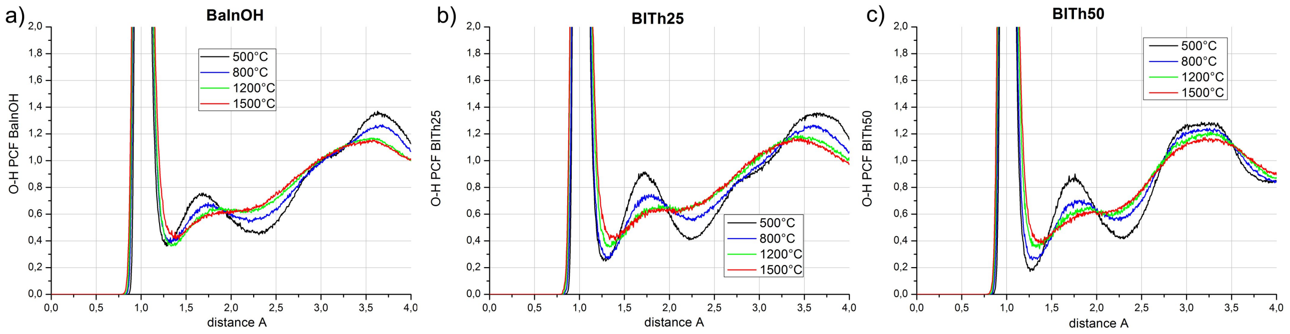

Figure 6.6: PCF of the O-H bond in a) BaInHO, b) BITh25 and c) BITh50 showing the extent of hydrogen bonding by the (integrated) intensity of the 2nd peak at ≈1.75 Å

system because of the discrepancy of those highest activation barriers and the observed diffusion activation energy.

In view of section 6.3.3 on the particular difference in diffusivity between BITh50 and BIZh50 the analysis of the relevant displacement rates reveals that the bad-performing BITh50 actually has a smaller "largest" activation energy (i.e. 0.17 eV for the stretch hop compared to 0.20 eV in BIZh50), so that the pure elementary steps cannot clarify the large diffusivity offset. That behaviour is indeed very likely related to the geometrical explanation given in this section.

(800°C)	In-polyhedron			Ti/Zr-polyhedron		
	O-H	H-O	O-O	O-H	H-O	O-O
BITh50	1,243	1,281	2,469	🟩 1,226	🟩 1,263	🟩 2,421
BIZh50	🟩 1,234	🟩 1,271	🟩 2,452	1,242	1,278	2,451

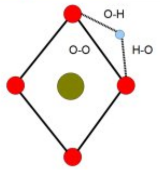

Figure 6.7: Geometrical properties of the stretch-hop transition state in BITh50 and BIZh50 at 800°C. The dominant process is green-shaded.

Still on the comparison between BITh50 and BIZh50 one observes some similarities but also slight differences. In general both compounds show the evidenced reinforced hydrogen bond presence. The highest activated rate for BIZh50, according to the fits, remains the intra-octahedral stretch mode with an activation energy of 0.2 eV which is higher than BITh50 but lower than any other stretch mode (especially BIZh25). Additionally it is known that in BIZh50 the protons bind very preferably to In-polyhedra. It is possible to rationalize this slightly higher activation energy for BIZh50 by a quick analysis of the MD-averaged transition state geometry of the stretch mode. Figure 6.7 gives the geometrical parameters of this mode for the two compounds at 800°C. The values are averages over a couple of thousand recorded stretch hops distinguished according to the polyhedron around which the hop took place. The green-shaded boxes indicate the majority-process for the two compounds (BITh50: 10% at

In-polyhedra, 90% at Ti-polyhedra; BIZh50: 80% at In-polyhedra, 20% at Zr-polyhedra). One sees that for the dominant process in BITh50 the O-O distance (2.42 Å) is smaller than for the dominant process in BIZh50 (stretch-hop at In-polyhedra, 2.45 Å). This higher proximity will facilitate the intra-octahedral proton transfer and will therefore be the reason for the even lower activation energy in BITh50. Furthermore this is in agreement with the understanding of having lesser negative net charge on oxygens that border Ti-polyhedra than those that border In-polyhedra (this was shown in the section on the Bader charges 3.4). Consequently lesser charged oxygens around Ti cations are likely to be less repulsed from one another than for more ionic situations as it is the case around In.

6.4.2.2 The extra-octahedral stretch mode

The assessment of this mode (mode number 2 in fig. 6.4 on page 177) is complicated by the aforementioned fact that actually two distinct extra-octahedral modes are counted as one: at low temperatures (predominantly) the back and forth hop inside a rhombus-shaped interstice and at high temperatures the transient extra-octahedral transfer. Following statements can be made:

- The mode has no importance whatsoever for the two 50% BITh50 and BIZh50 compounds as structural extra-octahedral proton do not exist and, as an observation, transient extra-octahedral transfers are negligible compared to intra-octahedral transfer

- The compounds that at 500°C and 800°C contain an extra-octahedral layer (BaInOH, BITh06 and all Ba-based 25% substituted ones) show rather high rates of this mode. The entire number of counted extra-octahedral hops is associated to protons located in the extra-octahedral layer. For 500°C and 800°C the rates are confined to the range of $3{\cdot}10^{12}\text{s}^{-1}$ and $8{\cdot}10^{12}\text{s}^{-1}$ per extra-octahedral proton for all compounds. This is comparable to the intra-octahedral rotational mode and will therefore lie in the same activation energy range of around 0.1 eV.

- For all Ba-based compounds the extra-octahedral aspects loses its signification for temperatures >800°C due to small concentrations of extra-protons

- SITh25 contains significantly more extra-octahedral protons and shows an elevated extra-stretch rate as well.

This last point deserves a bit more detailed account as it highlights the particularity of the Sr-based compound. Its most important impact is the smaller ionic radius of Sr compared to Ba. This entails a generally denser lattice (see table 4.I on page 84) as well as a much more pronounced tilt of the In/Ti-polyhedra as it was shown in figure 4.9 on page 98. In the framework of the energetical analysis of the intra- and extra-octahedral protons in section 4.3.1 it was found that SITh25 provides a substantially higher stability for extra-octahedral protons both at low temperatures (structural) and high temperatures (transient). For what the transfer rates are concerned the event-counting here gives values that are comparable to the flip mode for SITh25. The actual values range from $10{\cdot}10^{12}\text{s}^{-1}$ and $13{\cdot}10^{12}\text{s}^{-1}$ and the activation energy is therefore also supposed to resemble the ones given in table 6.III for the flip modes.

6.4.2.3 The intra/extra- producing/annihilating modes

This final section on the rates will focus on the modes labeled 5 and 6, ”in-plane” bending and ”out-of-plane” bending. As for the extra-octahedral stretch mode, only BaInOH, BITh06 and the 25% substituted compounds are concerned because for higher degrees of substitution the extra-octahedral proton layer does not exist anymore. Especially for the low temperature phases, i.e. when the extra-octahedral layer is still intact, it is important to know how activated these modes are. The question here is to what extent the extra-octahedral protons impede the proton diffusion in the fully hydrated materials. This concerns the extra-protons themselves and the question whether they basically remain completely in their extra-octahedral sites and therefore reduce (by 50 or more %) the diffusing proton concentration. An important information concerning the issue has already been given in section 4.3.1: strutural extra-octahedral protons represent a proton-trap ranging from -0.38 eV (BIYh25) to -0.25 eV (BITh25, BIZh25) and BaInOH in between (-0.33 eV).

From a kinetic point of view this would therefore be the lowest possible activation energy for the escape from an extra site. The event-counting algorithm now shall clarify whether there is an additional barrier to this process. Recalling the chapter on the Monte Carlo simulations this activation energy would then be integrated into the effective activation energy, in addition to the obvious activation energies of mode 1, 3 and 4. But as was seen in subsection 6.4.2.1 none of the activation energies of those modes was as high as the effective activation energy of the diffusion.

A problem encountered during the analysis of mode number 5 was its strongly correlated character for the direction of ”production” of an intra-octahedral proton: the vast majority of times the corresponding event was counted the extra-octahedral proton was only switching back and forth inside its rhombus-shaped interstice. The resulting rates were not usable. Therefore the counting algorithm was adjusted in order to count exclusively those events that were followed by a intra-octahedral rotation (mode 3) which means that the proton had left the plane of the extra-layer.

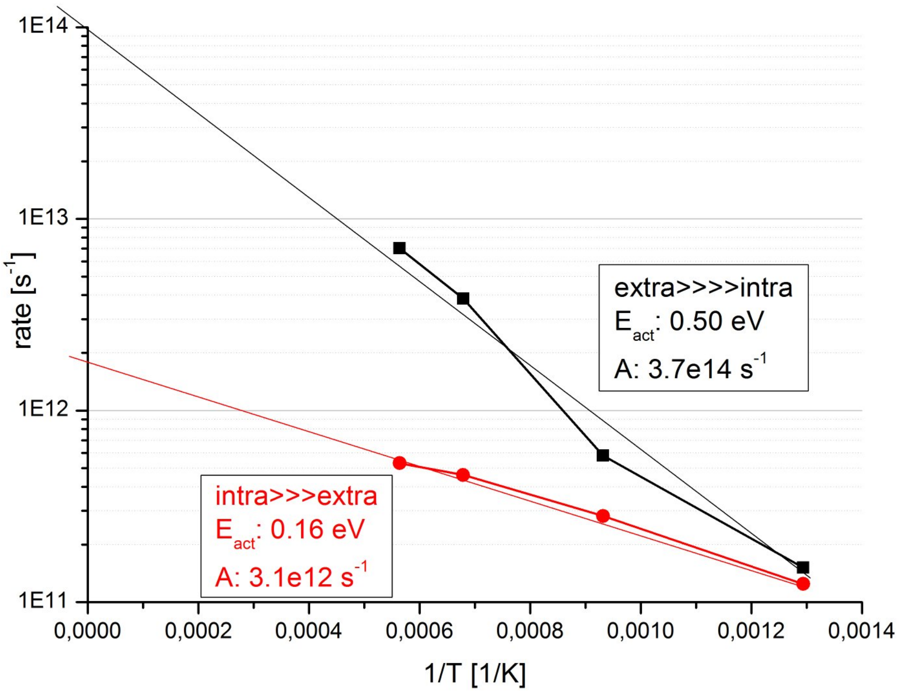

Figure 6.9: Arrhenius representation of the intra/extra production/annihilation process. The modes are a combination of no. 5 and 6.

This analysis was performed only for the case of BaInOH in order to assess an approximate value characteristic for this kind of extra-octahedral layer. The results are given in figure 6.9 together with the obtained activation energies and prefactors. As expected the intra-producing rate has a higher activation energy than the extra-producing one with the difference being the energetic stabilization of the extra-octahedral proton site. The 0.16 eV for that matter would correspond to the "additional barrier" indicated in the sketch 6.8 whereas the 0.5 eV are the trap depth plus this additional barrier. In this simple view we end up with a trap depth (0.5-0.16)eV = 0.34 eV which compares very well with the 0.335 eV given for the energy difference intra/extra for

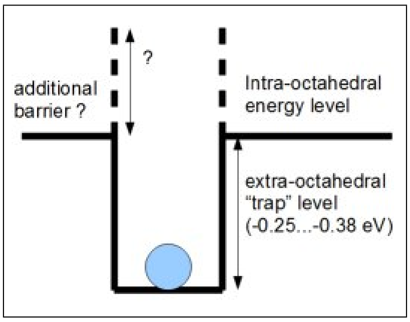

Figure 6.8: Intra/Extra-energy levels

BaInOH in table 4.II on page 97 however obtained by a different approach.

The important outcome here is that concerning diffusion processes the ”escape” from the extra-octahedral layer has to happen over a larger barrier than the highest regular barrier (the intra-octahedral stretch mode) in the system. Therefore this displacement mode will have its contribution to the overall diffusivity which helps to rationalize the 0.4 eV barrier found for proton diffusion in BaInOH.

6.4.3 Quantum corrections to the modes of transport

An important question which arises in the context of treating the diffusion of protons inside a host material is to what extent their behaviour is subject to (dynamic) quantum effects which by definition are not considered by the DFT based molecular dynamics scheme. Despite the fact that the electronic part of the system is quantum mechanically ”correctly” described at any time step, the description of the nuclei (including the protons) rests entirely classical as positively charged point masses. Thus also their temperature-imposed motion is purely classical. In the special case of protons their small mass gives rise to sometimes experimentally accessible quantum effects. Namely these are their ability to be transported by tunneling and their Zero-Point-Energy (ZPE) vibrations. Neither of them is included in the DFT-MD simulations but they both affect the transport properties for real materials. It is though not a serious drawback of the work for the neglect of those quantum effects may also be interpreted as an aid to disentangle different contributions.

The tunneling effect has an enhancing influence onto the real diffusivity because, illustratively speaking, simply a further mode of transport is made available for the proton besides the thermally activated ones studied in the previous section. However for proton-conducting oxides as they are investigated here the tunnel effect is known to be of importance only at rather low temperatures as the thermally activated modes of displacement quickly outweigh it at temperatures above room temperature. Nowick and co-workers conclude that based on experimental evidence (pure Arrhenian behaviour over the entire temperature range studied) proton tunneling can be ruled out as a noticeable effect in acceptor doped $KTaO_3$ and $SrCeO_3$ [100]. Matsushita [101] give an estimation based on a simulation study of $SrTiO_3$ stating that a tunneling rate along the stretch-mode coordinate be larger than the thermally activated rate only up to temperatures of about 20 K (!). Similar considerations in [102] lead to a "safe disregard of tunneling in proton conducting oxides above 500 K". More in detail ZHANG,WAHNSTRÖM and coworkers [38] perform a true path-integral molecular dynamics simulation for the protonated perovskite $BaZrO_3$; a calculation method which by definition includes both of the aforementioned quantum effects explicitly. They very convincingly ascribe an immense relative importance of the tunneling mechanism to the overall proton diffusivity for temperatures below 600 K. According to this study at low temperatures the diffusivity is limited by the reorientation modes (modes 3 and 4 in figure 6.4) which are less affected by the tunneling mode than the stretch-hop mode. This in sharp contrast to comparative simulations of them that exclude those quantum effects. For these calculations the stretch-mode is the limiting step at *all* temperatures. This finding is therefore very precious in view the results of the single modes in the previous section 6.4 where the stretch mode (mode 1) was indeed found to be the rate-limiting one for all compounds.

The other important quantum aspect is the zero point energy (ZPE) correction. A correction due to the same aspect has already been applied and discussed in section 4.4.5 regarding the hydration energies which were corrected by maximally around 0.1 eV due to the higher net ZPE of protons inside the oxide compared to the gaseous water molecule, therefore rendering the hydrated compounds less stable by this value. In the case concerning the displacement rates the ZPE correction for one internal proton will be determined by the difference of its vibrational modes in the ground state and a corresponding transition state. A description that correctly takes into account this zero point motion has been put forth by WIGNER in 1938 [103] and consists in employing the quantum mechanical partition functions for the nuclear vibrations in the transition state theory treatment instead of the classical ones as was done in section 6.4 (however justified because the described dynamics is classical). For the diffusive displacement mechanisms considered here the ZPE-correction leads to a decrease of the corresponding activation barrier essentially due to the lack of one of the three real normal modes at the transition state. The simplest approach (and correct in the (very) low temperature limit) gives a temperature independent energy correction to the activation barrier equal to

$$\Delta E = \frac{1}{2}\left(\left(\sum_i^2 \hbar\nu_i^*\right)_{TS} - \left(\sum_i^3 \hbar\nu_i\right)_{GS}\right) \tag{6.6}$$

which is just the plain ZPE-difference of a proton in ground-state (GS) and transition-state (TS). Considering the more correct treatment, we recall equation (6.2), the rate expression for a diffusional displacement step. The only modification to perform is to replace the $\frac{q*}{q}$ partition function ratio with its equivalent using the quantum mechanical partition functions of the harmonic-oscillator. The classic expression read $q_\nu = \frac{kT}{h\nu_i}$ whereas the QM equivalent is given by

$$q_\nu = \frac{\exp\left(\frac{h\nu}{2kT}\right)}{1 - \exp\left(\frac{h\nu}{kT}\right)} \tag{6.7}$$

Having a rate expression for the classical and the QM-case each, the effective difference in activation energy between those cases can be written by means of the simple ratio of the two entire rate-expressions:

$$\Delta E_{ZPE} = -kT \cdot \ln\left(\frac{r_{QM}}{r_{cl}}\right), \tag{6.8}$$

The rates and the ratio depend on nothing but the set of vibrational frequencies for GS and TS and the temperature and it takes the explicit form

$$\Delta E_{ZPE} = -kT \cdot \ln\left[\frac{\prod_i^3 \frac{\sinh(h\nu_i/kT)}{h\nu_i/kT}}{\prod_i^2 \frac{\sinh(h\nu_i^*/kT)}{h\nu_i^*/kT}}\right] \tag{6.9}$$

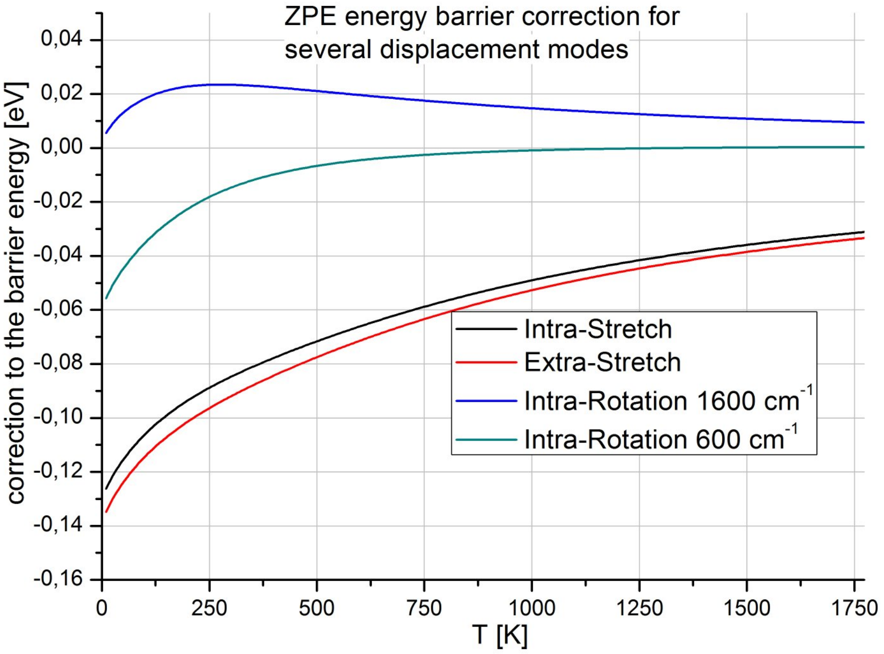

Figure 6.10: ZPE correction to stretch and bending modes as a function of temperature for characteristic frequency sets corresponding to the stretch-activated displacement mode (mode 1) and a bending-activated displacement mode (mode 3).

Figure 6.10 shows the evolution of the ZPE correction with temperature for the two most important types of elementary proton displacement modes. The frequencies that are required for the evaluation of equation (6.9) were obtained by normal mode analysis as described in section ”Vibrational Properties” (4.2.1). The ground state frequencies of an intra-octahedral proton are around 3500 cm^{-1} (3200 cm^{-1} for extra-octahedrals) for the vibrational stretch mode. The vibrational bending modes are between 800 and 1000 cm^{-1} (1000 and 1300 cm^{-1} for extra-octahedrals) depending on the particular compound and the crystallographic site. Typical transition states for the displacement modes 1 and 3 (stretch- and bending-activated) were calculated by the nudged elastic band (NEB) method [104][3]. A local NMA analysis (i.e. the frequency calculation only of the proton in question) at these transition states revealed the two TS-frequencies to be about 1600 and 1350 cm^{-1} for the stretch-displacement transition state. This corresponds to a hardening of the two bending modes at the TS and the vibrational stretch-mode being imaginary now. This frequencies proved valid for both the intra- and extra-octahedral proton sites and most importantly is signifying the loss of the highest 3500 cm^{-1} mode for this TS. The corresponding calculation for a TS of the bending-activated displacement mode (mode 3) mainly differs by the fact that during this rotative movement the high frequency O-H stretch-mode remains. The values of the second vibrational bending mode which is left at this TS are rather broadly spread and depend on the exact local structure. Two extremes (600 and 1600 cm^{-1}) are taken as a min/max estimation in the figure.

The overall extent of the correction as seen in the figure gets larger the more the two frequency domains are different, although no simple expression can be given for which the correction vanishes for all temperatures. Very importantly the value of the energy correction decreases relatively rapidly with increasing temperatures (remembering that the value at T=0 corresponds to the often used estimate of the ZPE-correction). Furthermore its overall level is very dependent on the actual frequency values of GS and TS. As can be seen, displacement modes which keep the high frequency stretching-vibration at their TS (mode 3) are significantly less affected by the ZPE correction. These aspects are important comparing the corrections to the actual activation barriers as presented in table 6.III: typical stretch-activated displacement modes being of the order of 0.3 eV now additionally subjected to a correction of the order -0.1 eV and smaller, or typical bending modes with merely around 0.1 eV barrier however corrected by values of ± 0.01 eV, i.e. in both directions. This behaviour indicates the importance to properly consider the temperature dependence and not to rely on the simple ZPE-correction estimation of equation (6.6).

---

[3] As implemented in VASP this method is capable of finding a transition state in an interpolative manner when two adjacent ground states are known

6.5 Chapter's conclusion and general tendencies for high proton diffusivity

This chapter presented the results for the direct proton diffusion ”experiments” in the completely hydrated compounds. The MD simulations allowed to extract general diffusion coefficients D obtained by the mean-square analysis of the proton trajectories. The parameters prefactor and activation energy of this property were approximately extracted based on simulations at four temperatures in the range from 500°C to 1500°C. However these temperatures remain too elevated for a direct comparison to experimental diffusion coefficients. As it was laid out, the range of temperature where D is measured can have implications on the parameters obtained although the physical system is identical. Nevertheless the MD-values are in any way within the correct order of magnitude both concerning E_a and the prefactor. The dissociation of the proton transport into single elementary steps very illustratively characterizes the process. For each elementary step activation energy and prefactors could be obtained and showed several systematic evolutions with changing chemical environment.

Some key phrases on the general diffusion tendencies are summarized below:

- The extra-octahedral layer is difficult to assess as a whole: on the one hand side it binds protons in a trap-wise manner (section 4.3.1), moreover there is an additional escape barrier (section 6.4.2.3). Combined they are likely to constitute the highest migration barrier in a Brownmillerite like system. However they exist only in compounds on the indium rich side. Remaining in our fully-hydrated frame of reference this means, that in case an extra-layer exists it will be completely occupied by only half (or somewhat less) of the total proton number. Therefore the *diffusivity per proton* cannot be affected more than by a factor 2 at most!

- The blocking layer as it was evidenced by the MD simulation for the BaInOH and 25%-compounds is not supposed to drastically decrease proton conductivity. Section 5.4.2 of the Monte Carlo chapter showed that for a model lattice the decrease in diffusivity is only in the range of 30-40%. A quasi two-dimensional diffusion is still possible in an unrestricted manner. However it cannot be conclusively excluded that such a blocking barrier is of bigger importance in multi-crystallite configurations.

- Trapping at oxygen polyhedra of Ti (presented in section 4.3.2) by definition has to be detrimental on the diffusion coefficient. However obviously there is no simple ”more Ti

Table 6.IV: Simplified scheme of influences on average proton diffusivity in BaInOH based compounds. The proton numbers are given w.r.t. the MD-simulation cell.

		x=0	x=0.25		x=0.5	
		BaInOH	BITh25	BIZh25	BITh50	BIZh50
1	Proton Number	32	24	24	16	16
2	Simple site blocking?	strongest	weaker	weaker	weakest	weakest
3	Blocking layer?	yes (stable)	yes (less stable)	yes (less stable)	no	no
4	Extra-layer?	yes (stable)	yes (less stable)	yes (less stable)	no	no
5	Trapping?	no	yes (at Ti)	yes (at In)	yes (at Ti)	yes (at In)
6	Traps percolate?	-	no	yes	yes	yes
7	Number (fraction) of trapped protons	16 (0.5) (extra-layer)	20 (0.83) (extra-layer + Ti-traps)	16 (0.67) (only extra-layer)	0 (percolation!)	0 (percolation!)

- more traps - less diffusivity" - rule. The aforementioned other structural effects may counteract. Moreover traps in a very high concentration (as in BITh50) lose their meaning as such altogether.

- By tendency, the inverse trapping effect of Zr is supposed to have a less important influence on the diffusivity as it merely blocks some of the potential diffusion pathways.

In light of these last statements a simplified rationalization concerning the differences in net-diffusivity may be constructed. The elements are stoichiometrically determined proton numbers and the just mentioned structural parameters. For the purpose of this simple comparison the consideration is restricted to Ti and Zr as examples for proton trapping (Ti) and proton avoiding (Zr) B-site cations. The structural criteria that come into play are those determined in chapter 4 on the proton structures: the extra/intra-octahedral proton layer, the proton blocking layer and the trapping effect of different substituents. Table 6.IV summarizes those influences:

The first criterion corresponds to the simple mutual site blocking effect of protons which is represented by a temperature independent factor. Its extent will logically decrease with decreasing general proton concentration.

The second aspect is the structural blocking layer which was evidenced for the tetragonal fully hydrated phases (i.e. BaInOH and all 25% substituted) compounds. It affects only potential diffusion pathways and does not trap protons. Its negative influence onto effective diffusion coefficient was estimated to be of the order of -30% by Monte Carlo example runs in section 5.4.2. By cation substitution this effect necessarily diminishes (what however was not quantified in section 4.3.3) to vanish completely for 50% substitution as the layered structure as a whole disapears (XRD experiments show that the hydrated BIZh50 and BITh50 phases are no longer tetragonal).

Entries number 4,5 and 6 represent real trapping aspects, i.e. they decrease the effective concentration of protons that may be considered free to diffuse. For the extra-octahedral layer ”trapping” energies of around 0.335 eV were determined for BaInOH in section 4.3.1. As also revealed in that section, the stabilization decreases for Zr or Ti substitution alike to around 0.25 eV. Like the blocking layer, the extra-octahedral layer vanishes entirely for 50% substitution.

The important concept which increases with increasing substitution is the local trapping next to one kind of the two possible polyhedra: indium/titanium or indium/zirconium. Section 4.3.2 revealed the inverse character of the two substituents with Ti acting as trap and Zr acting as obstacle. Indium in those two cases adopts the opposite role for which it becomes ”trap” in BIZhx. The important distinction is their proportion as well as the question of whether or not the trap-cation *percolates* the lattice: does the trap-cation have continuous polyhedra-paths across the entire structure? For the concerned sub-lattice of the B-site cations (which is simple cubic) the relevant site-percolation threshold is located at ≈33% so in a real material 50% substitution will always yield percolating networks of both In-polyhedra and Ti- or Zr-polyhedra. This was already discussed for the diffusion results for BITh50 in section 6.3.3.

Concerning this proton-cation trapping the situation is therefore rather different for BITh25 and BIZh25, but more or less equal for BITh50 and BIZh50. As given in the table the fraction of protons that is concerned by the combined trapping effects of the extra-layer and the cation-trapping is highest for BITh25 because 25% Ti will not generate percolating Ti-polyhedron networks, whereas the 75% In in BIZh25 do. So in addition to the 16 protons trapped in the extra-layer one can expect aproximately four further protons being trapped to the Ti-polyhedra located in the intra-octaehdral regions (giving the 16+4=20 protons in the table). Consequently in BIZh25 the trapped proton fraction is only 16/24=0.67.

The bottom line of the table hence indicates a very rough guide to how many protons will be affected by trapping effects and thus not contribute notably to the overall long range proton-diffusion.

As can be seen with respect to pure trapping this argumentation yields the worst diffusivity properties for BITh25 followed by BIZh25 and BaInOH. However, already in this simplified picture this ranking is modified by lines 2, 3 and 4 of table 6.IV: The just mentioned restrictions w.r.t. the trapped proton-fraction are thus *softened* in the case of 25% substitution. The two 50% compounds however are least affected by the trapping concept as percolating traps lose the signification of being traps after all. Hence with respect to any localized trapping effects 50/50 substituted have the prerequisites for a good proton diffusion performance.

Relation to MD-results

In relation to the MD-simulations these tendencies may entirely be rationalized except for the special case of BITh50, where the diffusional behaviour was found to be limited by the *artificial* and wrong non-percolation of Ti-polyhedra. A comparison with the table containing the effective diffusion coefficients obtained (table 6.II on page 170) shows:

- By tendency BITh25 has higher activation energies than BaInOH which indicates the detrimental effect of localized cation-proton traps for BIThx to be stronger than the weakening of the extra- or blocking-layers comparing BaInOH and BITh25.
- BITh25 also has higher activation energies than BIZh25 as the latter's diffusivity is not negatively influenced by any cation-trapping as the the non-percolating substituent Zr acts as only as obstacle to proton migration.
- BITh50 and BIZh50 show the lowest activation energies (ignoring the percolation issue for BITh50) and arguably the best diffusion performance of all investigated compounds due to a percolating network of B-site-cation-polyhedra of either sort which makes vanish the very notion of ”trapping” eventually.

Relation to experimental results

Also the qualitative comparison to experimental values of BIThx and BIZhx shows some correct tendencies. Especially the maximum of activation energies for BIThx at 25% in table 6.I on page 164 reflects the tendency of a high fraction of trapped protons whose effective barriers are determined by the pure elementary barriers (stretch-hop etc.) *plus* their trap depths. BIZh25 in comparison shows a considerably lower activation energy in agreement with the absence of a cation-trapping effect.

For the two compounds substituted to 50% however the situation is less clear. Again ignoring the ”percolation issue” for BITh50 one can state that the MD-simulations show those two compounds perform best compared to BaInOH and the 25% substituted ones. However, experimentally BITh50 and BIZh50 perform worse. Especially BIZh50 shows a particularly high activation energy of 0.62 [62] or 0.75 eV [98], respectively. All mentioned structural effects (as they are presented in table 6.IV however predict a rather smooth potential energy surface: no cationic trap effects (due to the In/Zr percolation) and no layered structure (for disordered cations). Moreover are the displacement step barriers (i.e. modes 1, 3 and 4 from figure 6.4 on page 177) not likely to dramatically exceed those of BaInOH, which can also be seen in the MD-simulations. An all conclusive reason can for the moment not be given.

Examining the experimental case, one could argue that for BIZh50 grain-boundary effects may play a more important role than for other compounds, knowing that barium-zirconates in general show extraordinarily high grain-boundary resistivities for proton conductivity [81]. Also the aspect of partial hydration may blur the experimental affirmation, as the condition of *complete* hydration may not be met for the region of the conductivity measurement. Indeed in references [8, 98] BIZh50 is said to be only hydrated to ”60-90%” even at low temperature which complicates the assessment due to the simultaneous presence of oxygen-vacancies, protons and the two kinds of B-site cations; a situation which was ignored altogether in this work and is left to future work.

Chapter 7

Conclusion

Proton conductivity and local structures in oxides were to be studied within the framework of this thesis. The predominant means to do so has been the application of the density functional theory (DFT). In first place it may seem a relatively hopeless undertaking to try to treat a profoundly dynamical and an actually not microscopic property like an ionic conductivity by DFT. However ever growing computational performance allows to go further and further for what the size of the system and the available concepts are concerned. Thus, given the dynamical nature of the problem the decision was made to investigate the oxides of interest by the molecular dynamics (MD) method, nonetheless based entirely on DFT calculations. Furthermore the system size (of course as big as possible) can be considered a *good* compromise between computational effort and realistic depiction of a disordered system in which a multi-particle diffusion is supposed to be studied.

The big merit of having the DFT method as a basis for the entire study is its inherently *virtually* correct description of the chemical aspects of a compound due to its ab initio character. This is a sharp contrast to so called classical MD where the underlaying chemical system is created, modeled and adjusted to fit some experimentally obtained properties. The software with which the entire set of simulations was carried out is the VASP-code supplying the DFT-based MD routines.

The actual chemical object that was investigated is the family of the Brownmillerite structured compounds as well as several related and substituted compounds. They present the interesting property to easily integrate water whose protons subsequently become part of the structure but remain mobile enough to give rise to substantial diffusion coefficients. This fact leads to the pronounced interest in them coming from fuel-cell research. Given their electronic insulating character these kind of materials are now en route to become competitive candidates for the use as electrolyte in proton-conducting solid oxide fuel cells.

This thesis was supposed to contribute to the understanding of the very main aspect of that, being the mechanisms of proton conduction/diffusion inside the Brownmillerite based compounds.

It turns out that, although MD allows very conveniently to actually observe protons diffusing, the problem is more complicated than looking at them given the huge amount of data that is produced during such an MD simulation. Therefore many tools were programmed that allow to extract useful system properties. These tools comprise routines that determine the mean-square displacement, the vibrational spectra or the pair-correlation functions. These three are the classic main aspects that are used to characterize MD-simulations.

Based on them the it was managed to obtain much valuable information about the behaviour of both the hydrated as well as the dehydrated compounds. Their vibrational properties could be deduced and brought into contact with experimental information. the pair correlation functions supplied crucial information about local structures of all sorts: Which cation prefers which oxygen coordination? How strong is the tendency to form hydrogen bonds? Which cation "attracts" protons to a maximum? etc. Especially the last aspect has important consequences given that some cations may act as trap and others not.

The proton and oxygen diffusion coefficients were obtained by the mean-square displacement and reproduce well the experimental values and provide much room for interpretation, given their *not tremendous* differences in different chemical environment.

Related to this, the elementary mechanisms were identified and investigated one by one. Also to this end, a highly adapted exploitation tool was programmed, which for a given MD-simulation is capable of identifying any of 6 different diffusional elementary steps as well as to keep track of the number of protons in the intra- or the extra-octahedral region. By virtue of this analysis it became clearer which chemical environment has what kind of influence on the protonic mobility.

It was possible to relate the observable differences to various structural features whose presence or absence depends on the degree of cation-substitution. These are the confirmation of a genuine blocking layer for proton diffusion for the In-rich compounds as well as the extra-octahedral proton site which gives rise to yet another layer. For increasing degree of substitution it is the localized trapping next to one of the two B-site cations that becomes more and more important, however loses its signification for compositions in the region of 50%. It is argued that the most promising intrinsic proton mobility can be expected for those compounds of about equiatomic composition as real trap-effects will be absent to a great extent.

For what the dehydrated structures are concerned the most important question concerns the local coordination structure of a given cation In^{III}, Ti^{IV}, Zr^{IV}, or Y^{III}. As of before the study this question was unanswered. By the calculations it could unambiguously be answered to be tetrahedral for titanium, octahedral for zirconium and yttrium. Indium turns out to be rather tolerant to all possible coordinations. For the case of Ti a XANES experiment was carried out that in the end could entirely confirm the computational predictions made before.

The general difficulty of the description of diffusivity remains the statistical character of it and the huge computational load that comes with an adequate treatment. Of course, classical molecular dynamics are able to improve the statistical quality of simulations by orders of magnitude. But as already said the application to ”unknown” systems is rather tedious and not secure. However, it is more than conceivable to use the accumulated data based on the DFT-molecular dynamics of this thesis to create empirical potentials of very high quality to be run in a classical molecular dynamics scheme. Having adapted those potentials to the hydrated or dry Brownmillerite compounds the same diffusional problems could then be handled in much bigger systems and for much longer times. In this way, all the mesoscopic aspects that were presented in the Monte Carlo chapter could eventually be implemented for the *real* system. These are for example more or less randomly distributed cations (an aspect not considered in this work) and, of course, partially hydrated compounds.

This latter aspect of partial hydration is *the* big challenge which logically would follow the work on the completely hydrated compounds because they represent much more closely the state the electrolyte is in during the actual fuel-cell operation temperatures.

The problem of their treatment however is that slightly hydrated compounds combine the complexities of the dry and the hydrated state as elucidated in this thesis. Such a system would now contain both oxygen vacancies with all their dynamics and local structures, as well as protons. Not only would such a system be yet more complex but moreover the computational statistics get worse and worse having only a few protons diffusing in a system of comparable size.

Preliminary simulations have nevertheless been performed and they confirm for example that protons no longer preferably associate with Ti-polyhedra in BIT25 because those are present in tetrahedral configuration by virtue of the oxygen vacancies still present. However as was presented in the chapter on the dry compounds (section 3.3.2) there might also be a small number of Ti-pyramides, which in turn *do* act as proton traps. So the trapping question would be determined by the *exact* proportion of proton concentration (”slightly hydrated”) and temperature dependent Ti-pyramid fraction.

Bibliography

[1] S. Noirault, *Nouvelles phases oxydes céramiques conductrices anionique et protonique pour pile à comustible*, PhD thesis, Université de Nantes, 2008.

[2] V. Jayaraman *et al.*, Solid State Ionics **170**, 17 (2004).

[3] G. B. Zhang and D. M. Smyth, Solid State Ionics **82**, 161 (1995).

[4] J. B. Goodenough, J. E. Ruiz-Diaz, and Y. S. Zhen, Solid State Ionics **44**, 21 (1990).

[5] M. Yoshinaga, M. Yamaguchi, T. Furuya, S. Wang, and T. Hashimoto, Solid State Ionics **169**, 9 (2004), Proceedings of the Annual Meeting of International Society of Electrochemistry.

[6] T. Delahaye, *Réalisation et optimisation délectrolytes et danodes pour piles à combustible à oxyde solide fonctionnant à température intermédiaire*, PhD thesis, Université de Nantes, 2006.

[7] A. Rolle, P. Roussel, N. V. Giridharan, E. Suard, and R.-N. Vannier, Solid State Ionics **179**, 1986 (2008).

[8] I. Ahmed *et al.*, Solid State Ionics **177**, 1395 (2006).

[9] S. Adler *et al.*, Solid State Ionics **68**, 193 (1994).

[10] W. Fischer, G. Reck, and T. Schober, Solid State Ionics **116**, 211 (1999).

[11] V. Jayaraman *et al.*, Solid State Ionics **170**, 25 (2004).

[12] J.-R. Martinez, C. E. Mohn, S. Stølen, and N. L. Allan, Journal of Solid State Chemistry **180**, 3388 (2007).

[13] H. Mehrer, *Diffusion in Solids* (Springer, 2007).

[14] P. Argyrakis, A. Milchev, V. Pereyra, and K. W. Kehr, Phys. Rev. E **52**, 3623 (1995).

[15] K. W. Kehr and T. Wichmann, Diffusion coefficients of single and many particles in lattices with different forms of disorder, in *Proceedings of the International Seminar on Current Developments in Disordered Materials, Kurukshetra University, India, January 1996*, 1996.

[16] T. Takahashi and H. Iwahara, Rev. Chim. Miner. **17-4**, 243 (1980).

[17] H. Iwahara, T. Esaka, H. Uchida, and N. Maeda, Solid State Ionics **3-4**, 359 (1981).

[18] K. D. Kreuer, Solid State Ionics **136-137**, 149 (2000).

[19] K. D. Kreuer, Solid State Ionics **125**, 285 (1999).

[20] K. D. Kreuer, Chem. Mater. **8**, 610 (1996).

[21] K. D. Kreuer *et al.*, Solid State Ionics **145**, 295 (2001).

[22] K. D. Kreuer, A. Fuchs, and J. Maier, Solid State Ionics **77**, 157 (1995), Solid State Protonic Conductors VII.

[23] W. Münch, K. D. Kreuer, G. Seifert, and J. Maier, Solid State Ionics **136-137**, 183 (2000).

[24] W. Münch, K. D. Kreuer, G. Seifert, and J. Majer, Solid State Ionics **125**, 39 (1999).

[25] W. Münch, G. Seifert, K. D. Kreuer, and J. Maier, Solid State Ionics **97**, 39 (1997).

[26] W. Münch, G. Seifert, K. D. Kreuer, and J. Maier, Solid State Ionics **86-88**, 647 (1996), Proceedings of the 10th International Conference on Solid State Ionics.

[27] W. Münch, K. D. Kreuer, U. Traub, and J. Maier, Journal of Molecular Structure **381**, 1 (1996), Proceedings of the XIth international workshop "Horizons in hydrogen bond research".

[28] M. A. Gomez, M. A. Griffin, S. Jindal, K. D. Rule, and V. R. Cooper, The Journal of Chemical Physics **123**, 094703 (2005).

[29] M. A. Gomez *et al.*, The Journal of Chemical Physics **126**, 194701 (2007).

[30] M. A. Gomez *et al.*, The Journal of Chemical Physics **132**, 214709 (2010).

[31] M. A. Gomez, M. Chunduru, L. Chigweshe, and K. M. Fletcher, The Journal of Chemical Physics **133**, 064701 (2010).

[32] A. Bilic and J. D. Gale, Chemistry of Materials **19**, 2842 (2007).

[33] A. Bilic and J. D. Gale, Solid State Ionics **179**, 871 (2008), Solid State Ionics 16: Proceedings of the 16th International Conference on Solid State Ionics (SSI-16), Part I.

[34] M. E. Björketun, P. G. Sundell, and G. Wahnström, Faraday Discussion **134**, 247 (2007).

[35] P. G. Sundell, M. E. Björketun, and G. Wahnström, Phys. Rev. B **73**, 104112 (2006).

[36] M. E. Björketun, P. G. Sundell, and G. Wahnström, Phys. Rev. B **76**, 054307 (2007).

[37] M. E. Björketun, P. G. Sundell, G. Wahnström, and D. Engberg, Solid State Ionics **176**, 3035 (2005), Selected Papers from the 12th International Conference on Solid State Proton Conductors (SSPC-12).

[38] Q. Zhang, G. Wahnstrom, M. E. Björketun, S. Gao, and E. Wang, Physical Review Letters **101 (215902)**, 1 (2008).

[39] S. Stølen and T. Grande, *Chemical Thermodynamics of Materials* (Wiley, 2004).

[40] E. Bakken *et al.*, Phys. Chem. Chem. Phys. **5**, 2237 (2003).

[41] C. E. Mohn, N. L. Allan, C. L. Freeman, P. Ravindran, and S. Stølen, Journal of Solid State Chemistry **178**, 346 (2005).

[42] C. E. Mohn, N. L. Allan, C. L. Freeman, P. Ravindran, and S. Stolen, Phys. Chem. Chem. Phys. **6**, 3052 (2004).

[43] G. Kresse and J. Hafner, Phys. Rev. B **48**, 13115 (1993).

[44] G. Kresse and J. Hafner, Phys. Rev. B **49**, 14251 (1994).

[45] G. Kresse and J. Furthmüller, Phys. Rev. B **54**, 11169 (1996).

[46] P. E. Blöchl, Phys. Rev. B **50**, 17953 (1994).

[47] G. Kresse and J. Joubert, Phys. Rev. B **59**, 1758 (1999).

[48] J. P. Perdew, K. Burke, and M. Ernzerhof, Physical Review Letters **77**, 3865 (1996).

[49] P. E. Blöchl, O. Jepsen, and O. K. Andersen, Phys. Rev. B **49**, 16223 (1994).

[50] R. Bader, *Atoms in Molecules: A quantum theory* (Oxford University Press, 1990).

[51] P. Cassam-Chenai and D. Jayatilaka, Theoretical Chemistry Accounts **105**, 213 (2000).

[52] E. Sanville, S. D. Kenny, R. Smith, and G. Henkelman, Journal of Computational Chemistry **28,5**, 899 (2007).

[53] G. Henkelman, A. Arnaldsson, and H. Jonsson, Computational Material Science **36**, 254 (2006).

[54] M. J. Saxton, Biophysical Journal **72**, 1744 (1997).

[55] J. Horbach, W. Kob, and K. Binder, J. Phys. Chem. B **103**, 4104 (1999).

[56] D. Frenkel and B. Smit, *Understanding Molecular Simulation* (Academic Press, 2002).

[57] J. Haile, *Molecular Dynamics Simulation - Elementary Methods* (Wiley, 1992).

[58] L. Ismer, *First principles based thermodynamic stability analysis of the secondary structure of proteins*, PhD thesis, Universitaet Paderborn, 2008.

[59] M. Kanzaki and A. Yamaji, Materials Science and Engineering B **41**, 46 (1996).

[60] C. A. J. Fisher, M. S. Islam, and R. J. Brook, Journal of Solid State Chemistry **128**, 137 (1997).

[61] W. Paulus *et al.*, Journal of the American Chemical Society **130 (47)**, 16080 (2009).

[62] F. Giannici, A. Longo, A. Balerna, K.-D. Kreuer, and A. Martorana, Chemistry of Materials **21**, 2641 (2009).

[63] J. R. Günter and G. B. Jameson, Acta Crystallographica Section C **40**, 207 (1984).

[64] J. A. Bland, Acta Crystallographica **875**, 875 (1961).

[65] B. Ravel and M. Newville, Journal of Synchrotron Radiation **12**, 537 (2005).

[66] F. Farges, G. E. Brown, and J. Rehr, Phys. Rev. B **56**, 1809 (1997).

[67] B. Ravel and E. Stern, Physica B **208**, 316 (1995).

[68] R. D. Shannon, Acta Crystallographica **A32**, 751 (1976).

[69] Y. Zhang, Inorg. Chem. **21**, 3886 (1982).

[70] J. T. Last, Phys. Rev. **105**, 1740 (1957).

[71] M. Karlsson *et al.*, Chemistry of Materials **20**, 3480 (2008).

[72] S. Noirault, E. Quarez, Y. Piffard, and O. Joubert, Solid State Ionics **180**, 1157 (2009).

[73] E. Quarez, S. Noirault, A. L. G. L. Salle, P. Stevens, and O. Joubert, Journal of Power Sources **195**, 4923 (2010).

[74] F. Giannici, A. Longo, K.-D. Kreuer, A. Balerna, and A. Martorana, Solid State Ionics **181**, 122 (2010).

[75] R. Wahl, D. Vogtenhuber, and G. Kresse, Phys. Rev. B **78**, 104116 (2008).

[76] D. Beshers, Acta Metallurgica **6**, 521 (1958).

[77] G. Cannelli, R. Cantelli, and F. Cordero, Phys. Rev. B **32**, 3573 (1985).

[78] I. Maroef, D. L. Olson, M. Eberhart, and G. R. Edwards, International Materials Reviews **47**, 192 (2002).

[79] B. Groß, S. Marion, R. Hempelmann, D. Grambole, and F. Herrmann, Solid State Ionics **109**, 13 (1998).

[80] B. Groß *et al.*, Phys. Chem. Chem. Phys. **2**, 297 (2000).

[81] K. D. Kreuer, Annu. Rev. Mater. Res. **33**, 333 (2003).

[82] T. Norby and Y. Larring, Current Opinion in Solid State & Material Science **2**, 593 (1997).

[83] T. Schober and J. Friedrich, Solid State Ionics **113-115**, 369 (1998).

[84] T. Schober, J. Friedrich, and F. Krug, Solid State Ionics **99**, 9 (1997).

[85] G. B. Zhang and D. M. Smyth, Solid State Ionics **82**, 153 (1995).

[86] W. G. Hoover, Phys. Rev. B **31 - 3**, 1695 (1985).

[87] S. Baroni, P. Giannozzi, and E. Isaev, Reviews in Mineralogy and Geochemistry **71**, 1 (2009).

[88] B. Grabowski, L. Ismer, T. Hickel, and J. Neugebauer, Phys. Rev. B **79**, 134106 (2009).

[89] J. G. Dash, D. P. Johnson, and W. M. Visscher, Physical Review **168,3**, 1087 (1968).

[90] L. C. Allen, Journal of the American Chemical Society **111**, 9003 (1989).

[91] Y. Limoge and J. L. Bocquet, Phys. Rev. Lett. **65**, 60 (1990).

[92] T. Wichmann and K. W. Kehr, Journal of Physics: Condensed Matter **7**, 717 (1995).

[93] P. Heitjans and J. Kärger, *Diffusion in Condensed Matter* (Springer, 2005).

[94] K. Mussawisade, T. Wichmann, and K. W. Kehr, Journal of Physics: Condensed Matter **9**, 1181 (1997).

[95] S. Alexander, J. Bernasconi, W. R. Schneider, and R. Orbach, Rev. Mod. Phys. **53**, 175 (1981).

[96] S. C. van der Marck, International Journal of Modern Physics C **9-4**, 529 (1998).

[97] R. Kutner, Physics Letters A **81**, 239 (1981).

[98] M. Karlsson *et al.*, Chemistry of Materials **22**, 740 (2010).

[99] I. Chorkendorff and J. Niemantsverdriet, *Concepts of Modern Catalysis* (Wiley-VCH Verlag GmbH, 2007).

[100] A. S. Nowick and A. V. Vaysleyb, Solid State Ionics **97**, 17 (1997).

[101] E. Matsushita, Solid State Ionics **145**, 445 (2001).

[102] A. Samgin, Solid State Ionics **176**, 1837 (2005).

[103] E. Wigner, Trans. Far. Soc. **34**, 29 (1938).

[104] G. Henkelman, B. P. Uberuaga, and H. Jonsson, Journal of Chemical Physics **113, 22**, 9901 (2000).

Remerciements

Ce travail a été effectué à l'Institut des Matériaux Jean Rouxel de Nantes et je veux tout d'abord remercier le directeur de l'IMN, Monsieur Guy Ouvrard de m'avoir accueilli au sein de son laboratoire. Une partie de la thèse s'est également deroulée au sein du site de Recherche et Développement de EDF à Moret-sur-Loing et je remercie le directeur du département Métaux, Matériaux et Composites, Monsieur Christophe Varé de m'avoir accueilli. De plus, je tiens à préciser que sqns le soutien techniaue de EDF (la grande majorité des calculs ont été fait au centre de calculs de EDF) ce travail n'aurait pas pu aboutir.

Bien sûr, ce sont mes encadrants Florent Boucher (chargé de recherche, IMN), Olivier Joubert (maître de conférences, IMN) et Philippe Baranek (ingénieur de recherche, EDF R&D) qui sont les destinataires des plus grands mercis pour leur conseil, leur soutien et leur inspiration. J'aimerais remercier particulièrement mon directeur de thèse, Florent Boucher, pour son soutien continu, son aide à de nombreux niveaux ainsi que pour sa patience.

Je souhaite également sincèrement remercier tous les membres de mon jury de thèse pour avoir accepté de juger mon travail : Guy Ouvrard (Professeur de l'université de Nantes) qui a accepté de prendre la présidence, les deux rapporteurs Truls Norby (Professeur de l'université d'Oslo) et Fabrizio Cleri (Professeur de l'université de Lille) ainsi que les examinateurs Deborah Jones (Directeur de recherche, ICG, Montpellier) et Matthieu Marrony (Docteur Ingenieur, EIfER, Karlsruhe).

Une pensée également pour tous les collègues, thésards, post-docs (Franois, Samuel, Kalid, Marine, Aymeric, Nico, JB...) qui ont su rendre l'atmosphère de travail à l'IMN encore plus agréable. Merci aussi à Stéphanie Belin du synchrotron Soleil et Eric Quarez pour du soutien au niveau expérimental. Il ne faut pas non plus oublier tout le personnel technique (et plus particulièrement le service informatique) et administratif de l'IMN qui ont toujours su garantir un très bon fonctionnement au jour le jour.

Un grand merci à Erminia, Daniel, Mathias et Nadège pour leur accueil en pays nantais. Und dann möchte ich mich noch bei meinen Eltern, Dorethee und Wolfgang bedanken, die mich über diese drei Jahre hinweg auch über die große Entfernung immer unterstützt haben.

Und natürlich will ich auch meiner Marika danken, die mir die ganze "thèse" über und immernoch so unglaublich viel hilft!

Resumé en langue française de la thèse de
M. Karsten RASIM

Conductivité protonique et structures locales par simulations *ab initio* d'oxydes utilisés comme électrolyte dans les piles à combustible

Table des matières

Chapitre 1

Chapitres d'introduction et d'état de l'art

1.1 Introduction générale

Cette thèse porte sur la description de matériaux qui sont aptes à être utilisés comme électrolytes de pile à combustible. Elle concerne en particulier les piles dites PC-SOFC (proton conducting solid oxide fuel cells - piles à combustible à oxyde solide à conduction protonique).

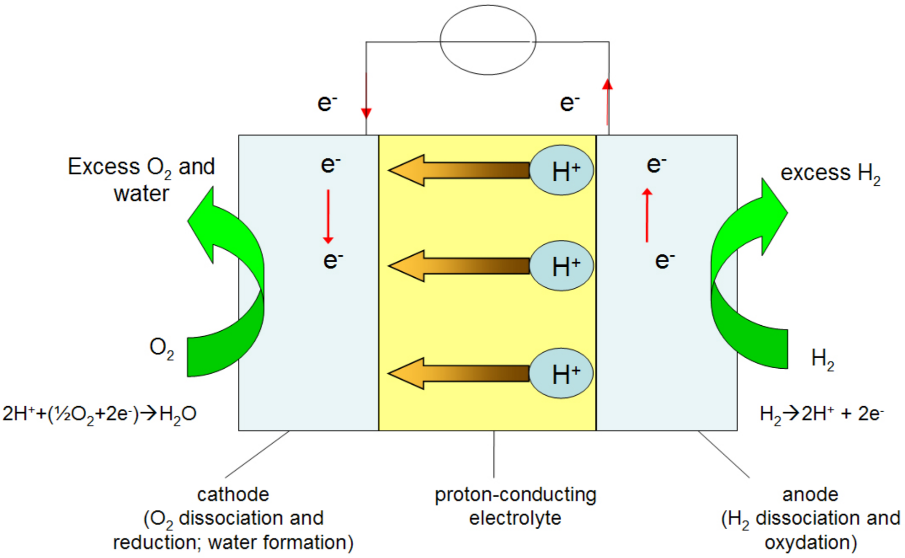

FIGURE 1.1 – Fonctionnement schématique d'une pile à combustible à conduction protonique.

L'image 1.1 illustre le mode de fonctionnement principal. Contrairement aux SOFC classiques les porteurs de charge ioniques ne sont pas les ions O^{2-} mais les protons H^+. Néanmoins, en contraste avec des piles de type électrolyte polymère l'électrolyte est un oxyde solide qui doit être un bon conducteur protonique - une propriété qui n'est pas abondante chez les oxydes et ce que représente un défi pour cette application. La propriété clé de la performance d'un électrolyte de pile à combustible est sa conductivité ionique et dans ce cas la conductivité protonique. Le but de ce thèse est de décrire le processus de la conduction protonique et d'approfondir les connaissances concernant les contributions qui jouent des rôles principaux.

La plupart de ces travaux ont été menés par le biais d'approches de modélisation basées sur la théorie de la fonctionnelle de la densité (Density Functional Theory - DFT). Bien qu'il reste des limitations en ce qui concerne l'applicabilité des résultats obtenus sur des cas réaliste, les récents développements au niveau de la puissance de calcul et méthodique permettent de modéliser des systèmes de plus en plus macroscopiques.

Un exemple est notamment la conductivité ionique des matériaux massifs qui est déterminé à une échelle intermédiaire entre la taille d'une cellule élémentaire et un grain de matière. Dans le cadre de cette thèse la conductivité (fortement liée à la diffusion) protonique au sein de quelques composés expérimentalement intéressants doit être étudiée. Pour çe faire, le choix à été fait de se baser sur des algorithmes de dynamique moléculaire (DM) ab initio afin d'étudier la diffusivité de la manière la plus directe possible.

Les grands axes de cette étude distinguent les matériaux complètement hydratés ou déshydratés donc les deux cas extrêmes d'un point de vue chimique. Néanmoins dans les deux cas la problématique peut être adressée dans le cadre du terme désordre. Prenant comme modèle idéale la structure des pérovskites, le désordre pour les composés secs s'impose par la présence de deux sortes de cations sur le site B (de valence +IV et +III) qui, tout en étant distribué de manière aléatoire eux mêmes, entrainent la présence de lacunes d'oxygènes à cause du principe de neutralité des charges. Quant aux composés hydratés, ils ne présentent plus de lacunes d'oxygène suite à l'hydratation par des molécules d'eau mais, c'est à présent les protons qui se trouvent dans les sites interstitiel (qui sont distribuées de manière désordonnée). Un concept utile pour la description de cet aspect va être la notion de piège ou d'obstacle à protons à cause du désordre cationique sur les sites B (qui restent indifférents à l'hydratation).

Les matériaux qui seront décrit plus en détail dans la suite sont nommé de la manière suivante dans ce resumé : le composé $Ba_2In_2O_5$ va servir comme reférence et sera appellé BaInO et BaInOH dans sa forme sèche et complètement hydratée, respectivement. Tous les autres composés basés sur ce systeme sont nommés en fonction de leur cation du site A, leur substituant S et l'état d'hydratation. La notation est <A>I<S>(h)x avec A = (B...barium, S...strontium), I...indium, <S> (T...titanium, Z...zirconium, Y...yttrium), h (absent - composé déshydraté ; présent - composé hydraté) et le x correspond aux taux de substitution de l'indium en % par les substituents (Ti, Zr ou Y).

1.2 Les Brownmillerites en tant qu'électrolyte ionique - état de l'art

Les matériaux de type Brownmillerites présentent une structure, notée $A_2B_2O_5$, qui est en proche relation avec la structure très répandue des pérovskites, notée ABO_3. Pour la suite de la thèse le matériau d'intérêt primordial sera le composé $Ba_2In_2O_5$ qui représente le composé de départ pour toutes les considérations de substitution cationique. La différence des Brownmillerites par rapport aux pérovskites est que le cation du site B se trouve dans deux coordinences distinctes : 50 % en tétraédrique et 50 % en octaédrique. Autrement formulé, la moitié des cations In(3+) se trouve en direct voisinage avec un arrangement de lacunes d'oxygène ordonné.

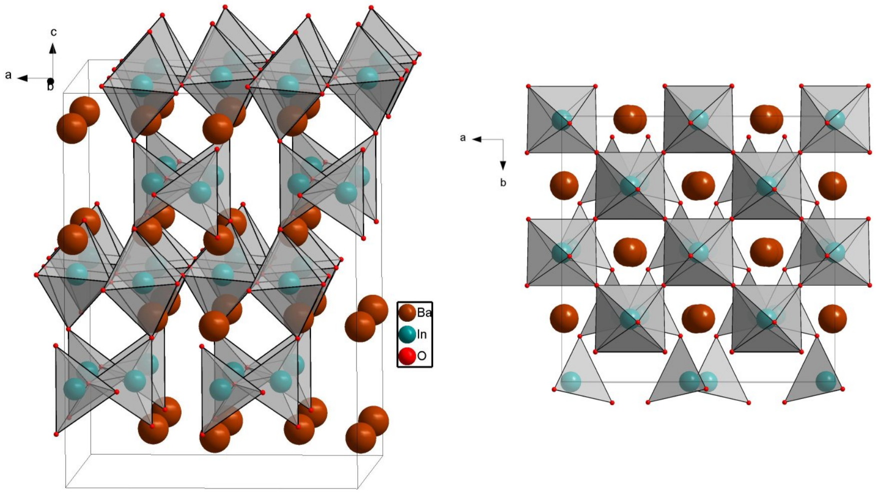

FIGURE 1.2 – Structure du matériau de référence $Ba_2In_2O_5$, à gauche vue de côté, à droite vue du haut.

La figure 1.2 présente une cellule de simulation typique du matériau qui contient 144 atomes. Pour la suite le terme « cellule de simulation » doit toujours décrire la cellule avec laquelle toutes les simulations ont été réalisées, à la fois des calculs statiques et les simulations de dynamique moléculaire. Quant au matériau, il cristallise dans une symétrise orthorhombique (group d'espace Icmm - 74 [1]) avec des paramètres de maille a=6.095 Å, b= 16.272 Å et c=5.96 Å.

L'intérêt principal de ce matériau est dû à son transformation d'une phase ordonnée vers une phase désordonnée à la température de 933 °C. A partir de ce point l'arrangement des tétraèdres et octaèdres commence à céder et conduit à une distribution aléatoire des lacunes d'oxygène ; en même temps ceci entraîne une forte augmentation (de plusieurs ordres de grandeur) de la conductivité ionique à cause de la grande mobilité des lacunes désordonnées.

A propos de la structure de çe matériau il existe une publication du groupe de Mohn et Stolen [2, 3] qui éclair beaucoup la problématique des calculs des structures avec un grand nombre de degrés de liberté configurationels, ici dû à la forte concentration des lacunes intrinsèques d'oxygène. Avec un grand nombre (aux alentours de 100) de configurations locales (i.e. la coordinence de l'indium - tetraédrale, pyramidal, octaédrale) les auteurs remontent à des relations énergétiques entre ces configurations et établissent des plages de température dans lesquelles certaines de ces structures locales sont stables et leur lien avec la transition de phase ordre-désordre mentionnée auparavant. Néanmoins cette approche va devenir inévitablement trop complexe pour traiter des systèmes avec encore plus de degrés de liberté - comme c'est le cas pour les Brownmillerites dans cette thèse qui sont substitués par d'autres cations sur leurs sites B. C'est pourquoi le choix d'un approche directe via la dynamique moléculaire a été adopté. Ce choix permet non seulement de faire un échantillonnage au niveau des structures locales (par exemple les préférences de coordinence des différents cations), mais aussi de remonter aux propriétés vibrationnelles ainsi que - de manière directe - aux propriétés diffusives soit pour les composés secs et hydratés.

1.3 Approches théoriques et outils de calcul

Tous les calculs de cette thèse qui s'intéressent à décrire directement les matériaux basés sur les Brownmillerites ont été faits par le moyen de la théorie de la fonctionnelle de la densité. De plus quelques considérations supplémentaires concernant des genéralités de la diffusion au sein des réseaux désordonnés ont été effectuées à l'aide d'une approche « Monte Carlo » cinétique qui sera décrit dans la section 2.3 de ce résumé. En ce qui concerne l'intégralité de calculs DFT ils ont été effectués à l'aide du code VASP (Vienna ab initio simulation package) qui représente un logiciel très avancé. Le code intègre une approche d'ondes planes pour la description des fonctions d'onde dans le cadre de la méthode « projector augmented wave » (PAW). Les potentiels atomiques pour la description d'une espèce chimique sont fourni par le programme pour tout le tablau périodique. L'approximation physique cruciale dans une approche DFT étant la fonctionnelle de corrélation-échange, il a été choisi d'utiliser des fonctionnelles du type GGA (« generalized gradient approximation »).

La partie dynamique moléculaire (DM) se déroulait également dans le cadre du code VASP, qui propose une routine de DM à volume et température constante (l'ensemble NVT). La dynamique est de type « Born-Oppenheimer » qui consiste effectuer un calcul électronique de DFT à chaque pas de temps de la dynamique des atoms. Le traitement des données issus de la DM a été effectué par des programmes écris dans la langue de programmation « C ». Ils calculent les propriétés suivants à base de trajectoires des particules de la boite de simulation : la fonction de corrélation de pairs, la fonction d'auto-corrélation, le déplacement moyen carré. De plus, des routines capables d'analyser en détail les modes de déplacement des protons (et des oxygènes dans le matériaux déshydratés) ont étés conçus. L'ensemble de ces traitements donne donc accès aux coefficients de diffusion, aux spectres de vibrations, aux relations de pairs, ainsi qu'à la quantification de plusieurs modes de déplacement des protons.

Chapitre 2

Les Résultats

2.1 Structure et dynamique des composés complètement déshydratés

2.1.1 Introduction

En parallèle du traitement des composées complètement hydratés de type Brownmillerite il a été jugé utile d'étendre les calculs aux matériaux complètement déshydratés. Ceci pour deux raisons principales :

1. la détermination des énergies d'hydratation, présentées dans la section 2.2.4, est basée sur les moyennes d'énergie totale d'un composé hydraté ainsi que son équivalent déshydraté. Cette approche nécessite donc des calculs de type dynamique moléculaire pour les deux états du matériau.
2. l'état déshydraté même est d'un intérêt particulier vu son fort taux de lacunes d'oxygène. Ces lacunes entraînent un désordre au niveau des polyèdres de coordinence des cations sur le site B. L'intérêt repose sur la préférence d'un cation du site B donné à se trouver dans une coordinence particulière. Dû au caractère local de ce comportement, cette information reste inaccessible pour les expériences de diffraction comme par exemples la diffraction des rayons-X (DRX). La préférence peut être de type tétraédrique, pyramidal ou octaédrique. L'observation de la repartition des cations dans les polyèdres de coordinence pendant un calcul DM permet donc de déterminer cette préférence pour l'ensemble des cations du site B (In, Ti, Zr et Y) qui ont été étudiés pendant les travaux de thèse.

2.1.2 Étude statique concernant les préférences de coordinence des cations

La question qui est à l'origine de cette étude est celle sur la répartition des lacunes dans les composés dans lesquels l'indium est partiellement remplacé par d'autres cations, notamment le Ti, Zr ou Y. Dû au bilan stoechiométrique $Ba^{2+}(In^{3+}/Ti^{4+},Zr^{4+},Y^{3+})O^{2-}$ des taux de substitution assez faibles (de l'ordre de 25 %) entraînent un nombre important de lacunes structurales d'oxygène. Par diffraction des rayons X il a été trouvé que suite à la substitution la structure cristallin a tendance à changer du type orthorhombique vers cubique. De plus il n y a aucun indice d'une mise en ordre des cations. Néanmoins il est très probable d'assumer un ordre local au niveau des cations qui se manifestera par une préférence des lacunes à se trouver à coté d'un des deux types de cations. Autrement dit, de localement trouver les deux cations du site B préférablement en coordinence tétraèdrique, pyramidale ou octaédrique selon l'absence ou présence des lacunes.

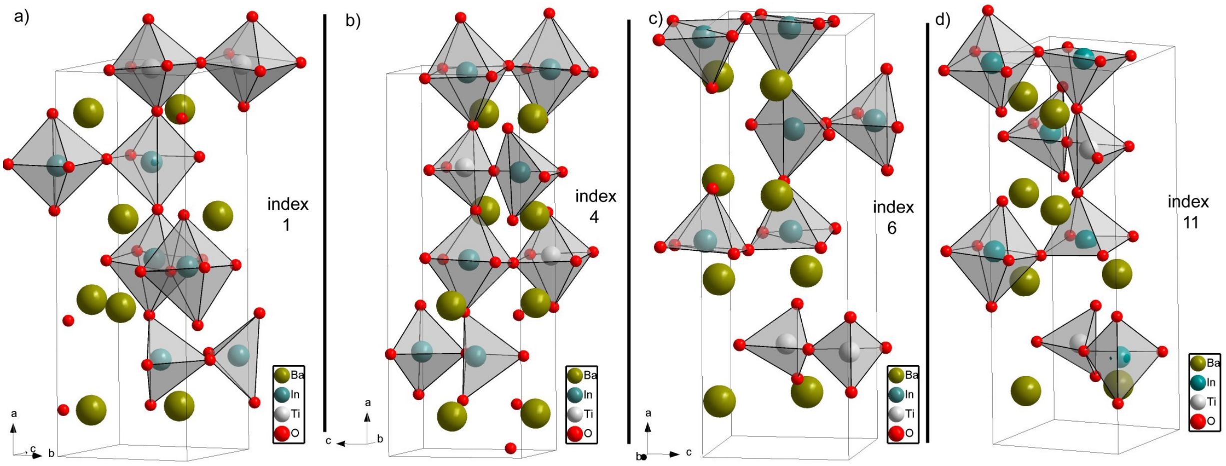

FIGURE 2.1 – Quatre exemples de cellules de simulation pour le composé BIT25 pour différentes structures de coordination locale du cation Ti^{4+}.

L'approche adoptée initialement était de simplement comparer un nombre de plusieurs réalisations de structures locales d'un composé donné à un certain composition. La figure 2.1 par exemple illustre quelques choix de cellule de simulation pour le composé BIT25 ($Ba_2In_{1,5}Ti_{0,5}O_{5,5}$) où le cation Ti^{4+} est placé dans plusieurs polyèdres de coordinence locale possible.

Le grandeur clé est l'énergie totale issu des calculs DFT de ces structures.

L'image 2.2 à gauche regroupe les résultats des calculs pour un nombre de composés à 25 % substitution de l'In par Ti (BIT25), Zr (BIZ25), Ti (SIT25 avec du Sr à la place du Ba) et Y (BIY25). L'axe des ordonnées est l'énergie totale en eV pour la configuration correspondante.

En résumé les différences en énergie démontré du côté droite de l'image 2.2 peuvent en être tiré. Elles indiquent une préférence locale dont la différence en énergie est de l'ordre de la centaine de meV, ce qui est suffisamment important pour être disriminant. Les substituants se comportent différemment : alors que Zr et Y préfèrent une coordinence octaédrique (et en contre-partie laissent l'indium en coordinence plus basse) le titane préfère la coordinence tétraédrique dû à la petite taille du cation Ti^{4+}. Des calculs supplémentaires (non présentés ici) démontrent que la répulsion O^{2-} - O^{2-} autour d'un cation Ti^{4+} serait trop grande dans

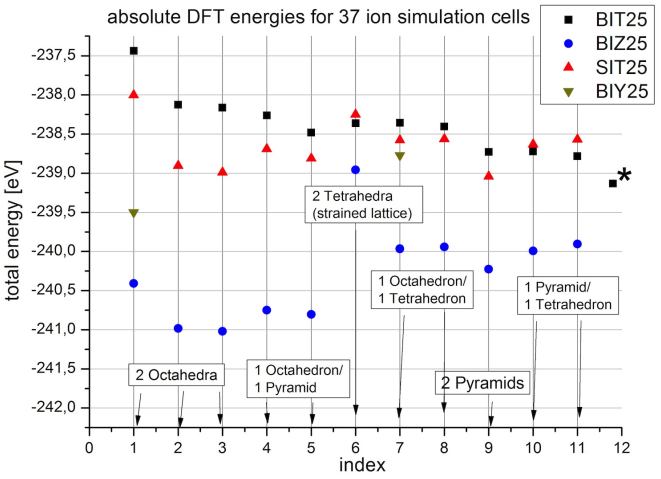

Ti-Tetra	⇒	Ti-Pyra	⇒	Ti-Octa
	+0.35 eV		+0.3 eV	
Zr-Octa	⇒	Zr-Pyra	⇒	Zr-Tetra
	+0.3 eV		+0.7 eV	
Y-Octa	⇒	Y-Tetra		
	+0.5 eV			

FIGURE 2.2 – a) Energies absolues de la cellule de simulation pour plusieurs configurations locales des substituants Ti, Zr et Y et b) relations (en eV) entre les différentes situations de coordinence pour Ti, Zr et Y.

une configuration octaédrique ce qui favorise une coordination quatre avec des distances Ti-O assez petites comprises entre 1.6 et 1.8 Å.

Des calculs en dynamique moléculaire (expliqués de manière détaillée dans le texte principal) confirment les résultats des préférences des structures locales obtenues en calculs statistiques également à température élevée (du moins jusqu'à 800 °C).

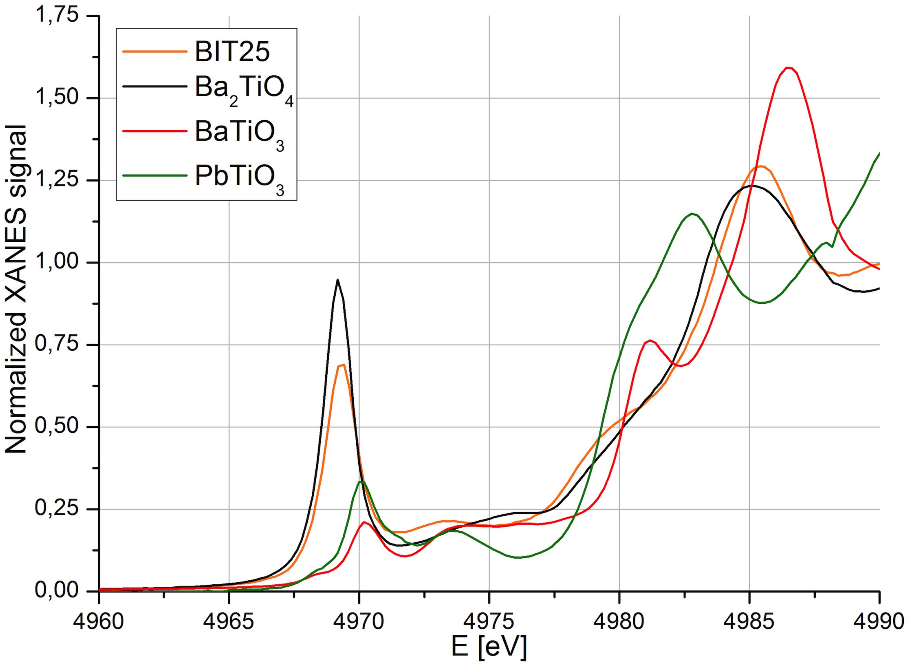

FIGURE 2.3 – Spectres XANES pour le seuil du Ti du composé BIT25 ainsi que pour des composés de référence pour lesquels le Ti se trouve dans des coordinences connues.

Dans le cadre de cette problématique des mesures d'absorption des rayons X ont étés effectuées au synchrotron SOLEIL, Paris. La méthode appliquée (XANES - anglais pour « X-ray

Absorption Near Edge Spectrum ») permet de directement examiner la coordinence locale d'un cation donné ; dans notre cas du Ti^{4+}. Grâce à ces mesures la prédiction des calculs sur la coordinence du Ti^{4+} a pu être complètement confirmée. L'image 2.3 présente les spectres XANES du Ti^{4+} dans le composé BIT25 comparée a des substances de référence pour lesquelles la coordinence du Ti^{4+} est connue. En particulier le composé Ba_2TiO_4 qui a 100 % de ses cations de Ti dans des tétraèdres, est important vu sa similarité avec le BIT25 ce qui permet de conclure sur la coordinence tétreédrique pour le Ti^{4+} en tant que substituant.

2.1.3 Relations de charge de Bader en fonction des paramètres de composition

Grâce à la nature des calculs DFT, la répartition de charges au sein d'une cellule de simulation d'un composé donné (déterminée par sa composition et sa structure locale) est accessible presque immédiatement. En notant que cette répartition de charges est une grandeur bien définie, la « charge » dans un sens chimique associée à un ion donné est une question d'interprétation. Il existe donc plusieurs approches pour attribuer une charge à un ion dans une structure.

Le concept de charge de Bader repose sur un concept assez simple qui consiste à segmenter l'espace dans une cellule de simulation selon un critère mathématique. Dans presque tout les cas, le centre de chaque segment coïncide avec un ion. Toute charge qui se trouve à l'intérieur d'un segment est donc attribuée à l'ion en question et est appelé sa « charge de Bader ». Laissons de côté l'interprétation de valeur absolue de cette charge, d'une manière comparative, il est possible de classifier une série de composés. Le critère intéressant ici est le transfert de charges sur les ions d'oxygène qui permet d'établir un simple classement d'ionicité ; par exemple en fonction du taux de substitution de l'indium par le titane ou le zircone.

L'image 2.4 présente l'ensemble des résultats obtenus pour les transferts de charges Bader pour les composés étudiés. Il est montré la moyenne du transfert de charge sur les ions d'oxygène pour les quatre groupes de matériaux BIT, BIZ, BIY et SIT. Le taux de substitution de l'indium par un cation de type Ti, Zr ou Y dans les structures augmente de gauche à droite. Si on considère qu'un transfert de charge important correspond à une grande ionicité on observe une ionicité décroissante avec le taux de Ti dans le BIT et le SIT (bien qu'un décalage entre les deux séries de valeurs soit observé). Au contraire, un taux croissant de Zr ou Y conduit à une augmentation d'ionicité.

Pour le cas du Ti^{4+} on remarque que son comportement n'est pas en accord avec l'échelle

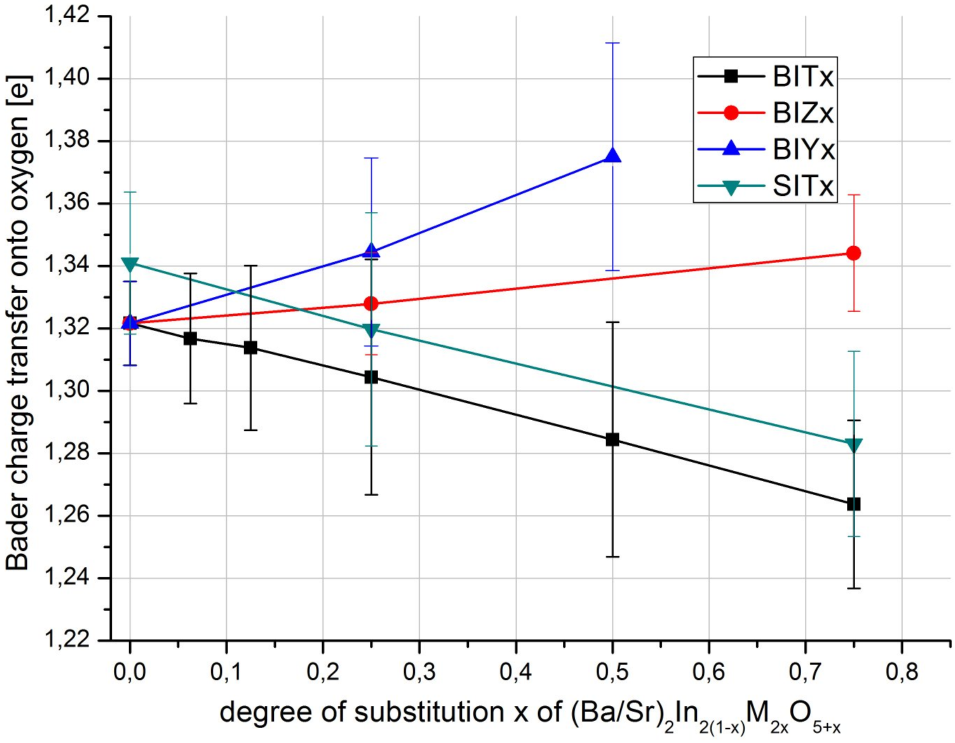

FIGURE 2.4 – Évolution du transfert de charges Bader vers les ions oxygène en fonction du taux de substitution pour les familles de composés BITx, BIZx, BIYx et SITx.

d'électronégativité tabulée d'après Pauling ou Allred/Rochow dans lesquelles l'indium est plus électronégatif que le titane. Par contre il existe bien d'autres échelles (par exemple celle de ZHANG [4]) pour laquelle les relations entre les ions sont en accord avec les résultats obtenus ici.

L'établissement d'un classement d'électronégativité basé sur les charges de Bader semble intéressant et sa poursuite sera sans doute utile d'un point de vue chimique conceptuelle.

Les considérations et résultats liés au charges de Bader vont plus tard être mis en relation avec les énergies d'hydratation (obtenues par une série de calculs en dynamique moléculaire) pour lesquelles une corrélation avec l'ionicité du réseau déshydraté peut être établi.

2.1.4 Propriétés vibrationnelles

En ayant entrepris des longs calculs de dynamique moléculaire, un autre aspect se prête à cette étude : celui des spectres vibrationnels. Néanmoins, dans le cadre du code de simulation VASP il n'est pas possible d'accéder aux intensités de chaque mode vibrationnel mais seulement à sa densité d'état. Donc, une directe équivalence avec les spectres expérimentales d'absorption d'infrarouge n'est pas possible. Toutefois, des informations intéressantes peuvent en être tirées.

La méthode qui permet de remonter à la densité d'état (density of states - DOS) vibrationnelle est la transformation de Fourier de la fonction d'auto-corrélation des vitesses (en anglais « velocity auto-correlation function - VAF). Elle est définie comme suit :

$$\Psi(\tau) = \frac{1}{n}\sum_{i}^{n} \frac{\langle \vec{v}_i(t_0+\tau)\cdot \vec{v}_i(t_0)\rangle}{\langle \vec{v}_i(t_0)^2\rangle}. \tag{2.1}$$

Dans le cas présent, les DOS sont données pour chaque espèce chimique du composé donné. La fonction dépend de τ et est formée par la prise des moyennes sur toutes les produits $\mathrm{v}(\mathrm{t}_0+\tau)\mathrm{v}(\mathrm{t}_0)$ avec un t_0 qui se déplace selon le vrai axe de temps de la simulation (la section 2.2.4.3. du texte principal contient plus de détails).

La VAF est une fonction qui contient toutes les informations concernant la dynamique d'un système moléculaire (déplacement et vibration) et a été introduite par KUBO and GREENWOOD [5] dans le cadre de leur théorie de transport. En particulier son caractère oscillatoire fourni l'information sur toutes les fréquences présentes dans le système.

Une approche supplémentaire aux propriétés vibrationnelles est l'analyse de la matrix de Hess qui permet de remonter aux modes propres (leurs fréquences et leurs vecteurs propres) des atomes dans un réseau cristallin. En contraste avec la VAF, cette dernière méthode est intégrée dans le code VASP.

Sur le groupement d'images 2.5 sont montrés sur un seul graphique : l'analyse de la VAF pour chaque espèce en traits colorés et la distribution des fréquences (pour toutes les espèces confondues) en colonnes grises, issue de l'analyse des modes propres. Les propriétés vibrationnelles sont présentées pour la série de composés BITx (complètement déshydraté et avec des taux de substitution de 0 %, 6,25 %, 25 % et 50 % ainsi que pour du $\mathrm{BaTiO_3}$)

2.2 Structures et relations énergétiques des composés complètement hydratés

2.2.1 Introduction

Cette deuxième grande partie va s'intéresser aux composés complètement hydratés qui se forment de manière thermodynamiquement stable sous l'atmosphère humide. Leur étude est importante car les structures (globales et locales) sont à l'origine de la question « comment des protons se déplacent-ils ? » dans l'optique de faciliter ce transport et donc la conductivité protonique.

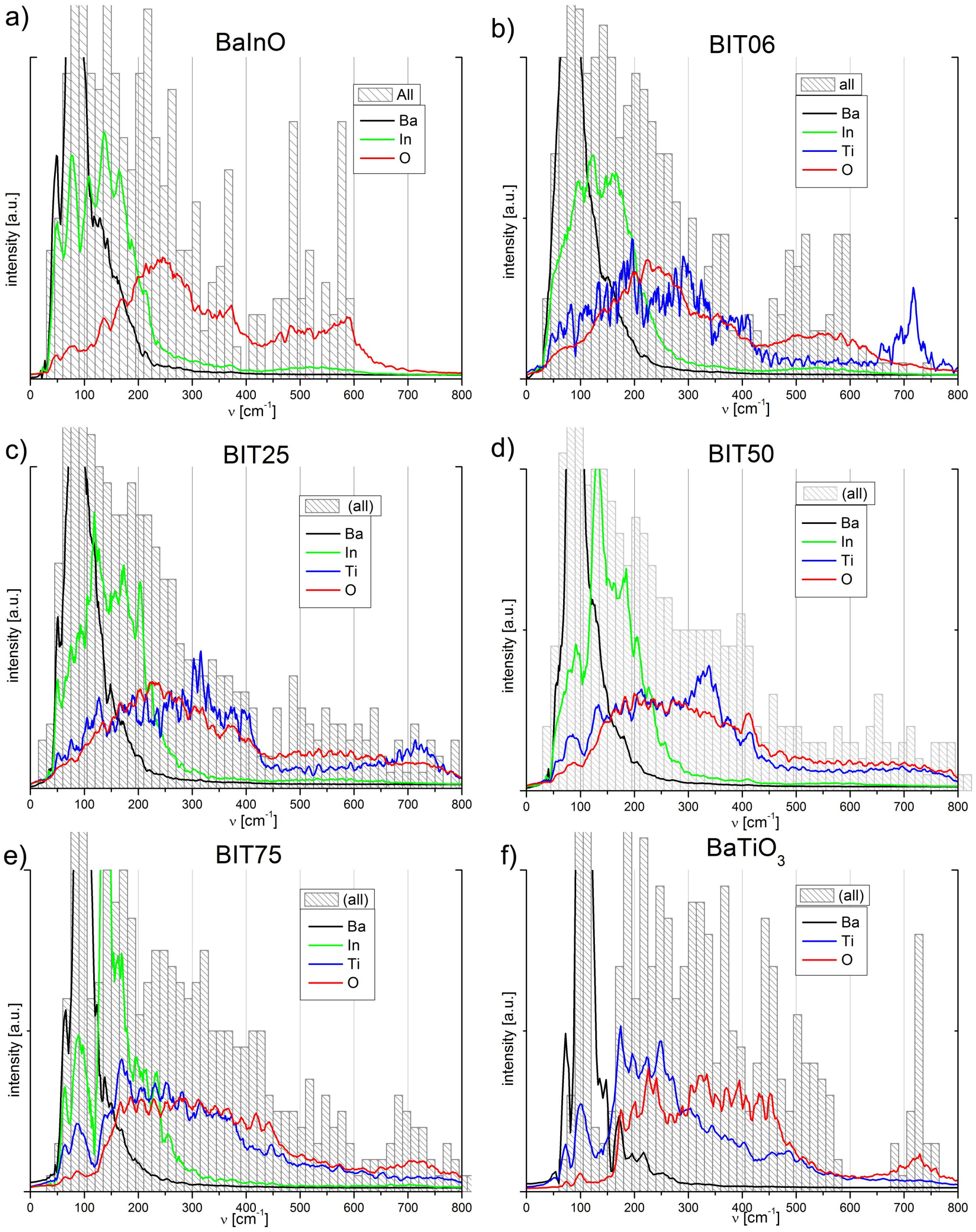

FIGURE 2.5 – Densités d'états vibrationels des composés déshydratés obtenues par analyse des modes propres (colonnes grises) et de la dynamique moléculaire (traits colorés).

Suite à la réaction :

$$H_2O(g) + O_o + V_o^{\bullet\bullet} \rightarrow 2OH^{\bullet} \tag{2.2}$$

les lacunes d'oxygènes sont remplies par des ions O^{2-} et tous les protons sont liés à un oxygène de manière covalente et distribués aléatoirement sur le réseau. Ainsi ce sont les protons qui sont maintenant à l'origine du caractère désordonné du composé (en plus du désordre des cations qui substituent l'indium).

L'étude structurale suivante est segmentée en trois aspects qui sont : (I) la description des deux classes de site cristallographique pour les protons intra- et extra-octaédraux, (II) la quantification de la préférence de site des protons vis-à-vis des polyèdres de coordinence de In, Ti, Zr et Y et finalement (III) la mise en évidence du caractère bloquant d'un plan cristallographique précis dans les composés à des taux de substitution cationique jusqu'à 25 %.

2.2.2 Étude structurale des composés complètement hydratés

2.2.2.1 Protons sur des sites intra- et extra-octaédraux

Un aspect très intéressant chez les composés complètement hydratés est l'équilibre dynamique entre les protons qui occupent les site intra- et extra-octaèdraux. Ces deux sites sont une particularité du composé de type Brownmillerite hydraté jusqu'à un taux de substitution cationique de 25 %. Ces deux sites possibles sont illustrés dans l'image 2.6 ainsi que le fait que les positions « extra » s'arrangent sous la forme d'une couche tous les deux plans d'octaèdres.

Le fait d'observer ces positions extra en diffraction des rayons-X montre qu'il doit s'agir d'une stabilisation énergétique comparé à l'état d'une distribution homogène des protons à travers le réseau. Il faut à présent déterminer à quel point les positions extra-octaèdrales sont stabilisées. Combiné avec le fait d'être arrangé dans un plan ordonné les protons extra-octaédrales sont d'importance pour le transport puisqu'ils peuvent être vus comme piège 2-dimensionnel pour les autres protons.

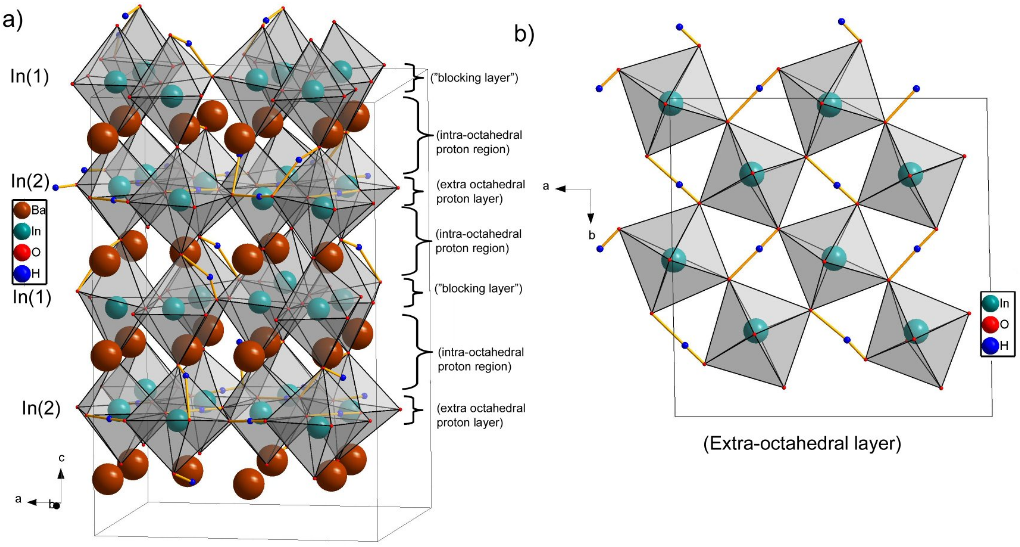

FIGURE 2.6 – Structure cristalline du composé complètement hydraté BaInOH. Les protons occupent deux types de site nommés intra- et extra-octahédral sous forme de couches alternantes.

À l'aide des simulations en dynamique moléculaire il a donc été possible de directement observer les taux d'occupation à des températures différentes et de remonter ainsi aux valeurs énergétiques de cette stabilisation en fonction de l'environnement chimique (son substituant et sa concentration). Ceci est possible dans le cadre de la statistique d'occupation de type Fermi. Cette approche est capable de décrire ce type de situations où un nombre de particule donné se voit être distribué sur deux types de site qui sont différent en énergie.

Après quelques opérations mathématiques le terme qui permet de décrire la relation entre intra- et extra-protons est :

$$c_{extra} = \frac{c_T}{1 + \exp\left(\frac{\Delta G - \mu(T, c_T, c_P)}{kT}\right)} \tag{2.3}$$

ou cextra est la concentration des extra-protons et c$_T$ la fraction des *sites* extra-octaédraux. Le potential chimique μ est une expression complexe qui est issu de la condition que le nombre constant des protons dans le composé est donné par deux expressions de type Fermi (une pour la concentration des extra-protons et une pour la concentration des intra-protons)

$$\mu = kT \ln\left\{\left[((xc_T + xc_P - x - c_T + c_P)^2 - 4x(c_P - 1)c_P)^{1/2} - xc_T - xc_P + x + c_T - c_P\right]/(2(c_P - 1))\right\} \tag{2.4}$$

avec $x = \exp\left(\frac{\Delta G}{kT}\right)$.

Après quelques affinements (qui sont expliqués plus en détail dans le texte principal) on arrive à une procédure de fit qui permet de relier les concentrations de protons extra-octaédraux observées à différentes températures (par DM) à la stabilisation énergétique Δ E. Ceci est démontré dans l'image 2.7 pour quatre composés différents à 25 % de substitution.

Il est à noter, que ce genre de considération est fondamentalement différente de ce que a été décrit dans la section 2.1.2 concernant les polyèdres de coordination, où l'écart énergétique était tiré de deux simples calculs DFT statiques. Le traitement des sites de protons inclut de manière implicite toute contribution complexe qui ne serait pas accessible par des calculs statiques vu le très grand nombre de configurations possibles pour 24 protons par cellule de simulation sur un réseau de 84 ions oxygène.

En ce qui concerne les valeurs énergétiques, la comparaison avec le composé de référence BaInOH (Δ E = -0,34 eV, image non donnée) montre une déstabilisation du site extra-octaédral pour les composés substitués par du Ti ou du Zr, et ce malgré le fait qu'il reste le site le plus fréquemment rencontré. L'yttrium par contre laisse la stabilité de la position extra inchangée par rapport au composé non-substitué. Ceci peut s'expliquer par la similarité de taille et degré d'oxydation (3+) de l'In et Y. Zr et Ti perturbent le réseau de manière plus significative.

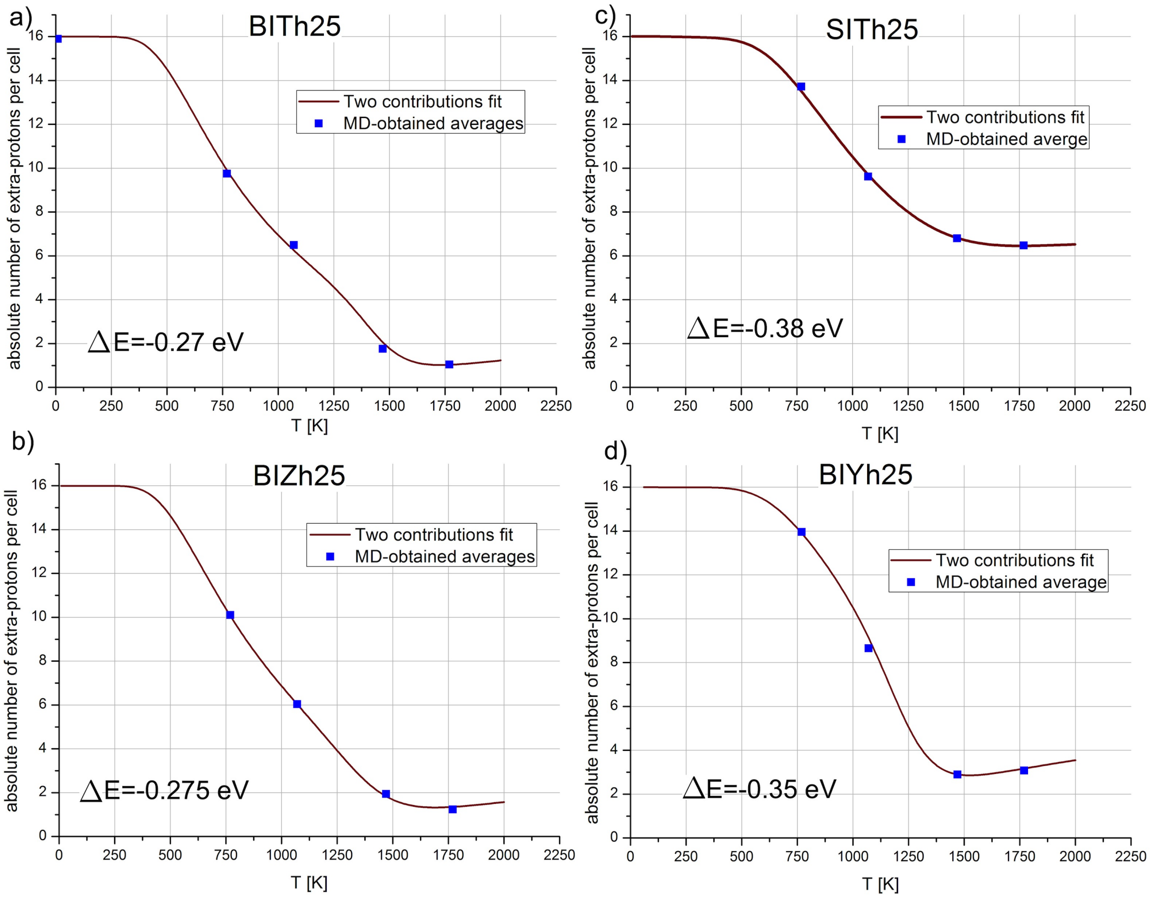

Figure 2.7 – Concentration d'équilibre (nombre par cellule de simulation) de protons extra-octahédraux dans quatre composés en fonction de la température. Les valeurs observées sont présentées en points bleus, la fonction de fit en trait rouge.

2.2.2.2 Piégeage des protons dû à la substitution cationique

L'aspect du piégeage des protons sur des sites crystallographique précis est d'un grand intérêt pour le transport diffusif. En fonction de la concentration des protons et des pièges cet effet va influencer négativement le coefficient de diffusion. Néanmoins le piégeage est seulement un des facteurs qui déterminent la diffusion.

Comme pour le cas des protons sur les différents sites intra et extra, la question de piégeage sur des polyèdres de coordination des substituants, peut facilement être adressée par une observation détaillée des calculs de dynamique moléculaire. Cet aspect est une bonne illustration de l'utilité des calculs dans ce domaine car l'obtention de structure locale de protons au sein d'oxydes désordonnés serait extrêmement difficile par des moyens expérimentaux (comme la diffusion des neutrons).

Un moyen d'exploitation est de se servir des fonctions de corrélation de paires (FCP) pour un couple d'espèces chimique (notamment cation-proton et cation-oxygène). Cette fonction est obtenue par l'enregistrement des distances entre chaque couple possible des deux espèces pendant toute la simulation DM. Ensuite ce comptage est normalisé afin de retrouver la valeur « 1 » pour les distances qui représentent une distribution complètement désordonnée. D'autres valeurs que « 1 » à certaines distances signifient donc la présence d'un ordre local (pour de petites distances) ou global (pour de longues distances). En faisant une comparaison de deux FCPs (In-proton et substituant-proton) cette fonction est bien adaptée pour indiquer à quel point le proton est plus ou moins souvent présent à coté d'un polyèdre d'indium ou d'un polyèdre d'un substituant (Ti, Zr, Y) ; donc de savoir si le proton est piégé ou pas et le cas échéant à côté de quel cation.

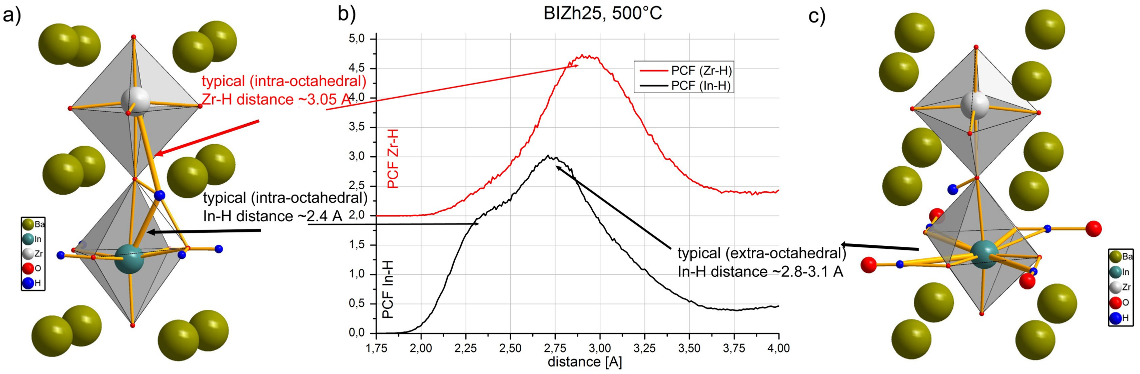

FIGURE 2.8 – Présentation de détail d'un FCP du couple Zr-H (partie du haut) et In-H (partie du bas) pour le composé BIZh25. Les deux représentations structurales du côté expliquent la provenance des pics.

L'image 2.8 présente des cas typiques de FCP cation-proton par exemple pour le composé BIZh25 avec leurs explications structurales. On remarque des différences significatives au niveau de l'emplacement et de la forme des pics de premier voisin. Ceci indique bien une influence importante du cation substitué sur le comportement des protons. Comme il peut être tiré de la figure, pour le cas du Zr comme substituant c'est le polyèdre d'indium qui attire le proton. Néanmoins la notion de piège ne serait pas appropriée vu que l'indium représente 75 % des cations du site B et que les octaèdres d'indium percolent. La figure suivante 2.9 montre la comparaison directe entre deux cas extrêmes, qui sont les composés BITh50 et BIZh50 (substitution par du Ti ou Zr à 50 %). Le BITh50 est présenté du coté gauche avec son FCP In-H (en haut) et Ti-H (en bas), le BIZh50 du coté droite. Chaque FCP est montrée à quatre températures différentes allant de 500 °C à 1500 °C .

On remarque un comportement inversé des deux composés, les protons préfèrent des sites associés à des polyèdres de Ti dans BIT mais évitent ceux de Zr dans BIZ. De plus, la variation avec la température montre, que énergetiquement cette préférence est importante et peut être estimée de l'ordre de quelques 0,1 eV.

Déjà ici, il est important de noter que l'influence sur le transport des protons va non seule-

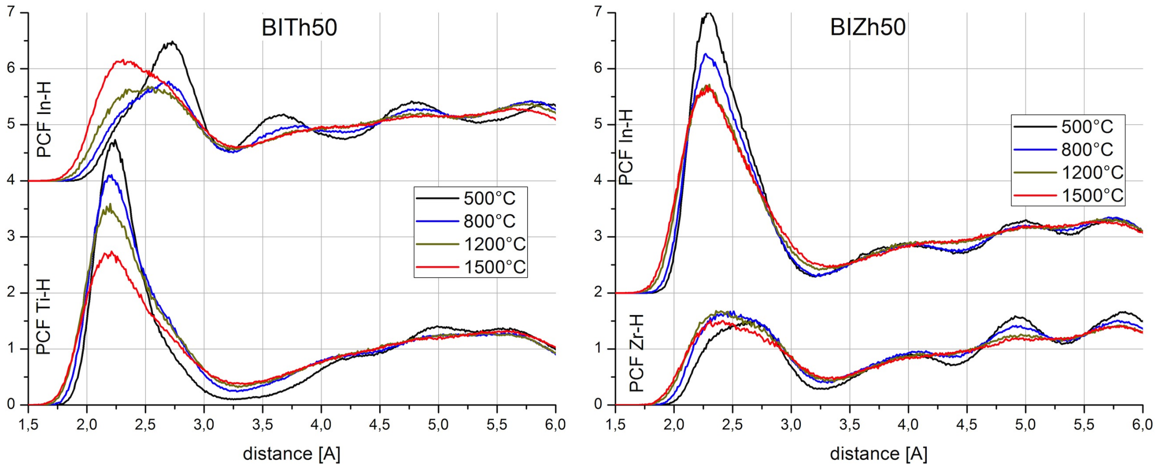

FIGURE 2.9 – Fonctions de corrélation de paires pour a) BITh50 et b) BIZh50. Les deux couples In-H et substituant-H sont présentés pour quatre températures.

ment dépendre du fait qu'un cation donné attire ou repousse un proton, mais aussi de la concentration des cations en question ainsi que des protons mêmes. Par exemple, malgré une très forte préférence de se placer à côté d'un Ti dans BITh50, le proton ne sera pas piégé car les polyèdres de Ti (à 50 %) sont percolants et permettent donc un déplacement à longue portée.

2.2.3 La couche bloquante vis-à-vis du transport protonique

Un troisième aspect structural des composés complètement hydratés et substitués jusqu'à 25 % est la présence d'une couche bloquante pour la diffusion protonique. Dans leur étude théorique du composé $Ba_2In_2O_4(OH)_2$ MOHN et al. [3] ont déjà mis en évidence des sites énergétiquement très défavorables en ayant analysé les énergies totales d'un très grand nombre de configurations locales. Les simulations menées ici ont pu mettre en relation cet aspect avec le comportement diffusif des protons. L'exploitation des données se servait encore une fois des fonctions de corrélation de paires mais cette fois celles du couple oxygène-proton. En plus l'évaluation a été faite en fonction de l'ion oxygène en particulier afin de identifier ceux avec le plus/moins de contact avec des protons. De manière qualitative la figure 2.10 présente le résultat clé de cette évaluation (sur l'exemple de BaInOH) en donnant en rouge les oxygènes, qui pendant toute une simulation de DM à 500 °C n'ont pas eu un seul contact avec un proton malgré le fait que les protons quant à eux ont montré un déplacement moyen plus grand que 2-3 polyèdres de coordination. Pendant tout le calcul seuls les ions d'oxygène montrés en vert étaient liés de manière covalente à des protons.

La caractère planaire des sites bloquants font en sorte que la diffusion des protons se fait exclusivement dans une couche sur deux avec littéralement aucune possibilité pour les protons

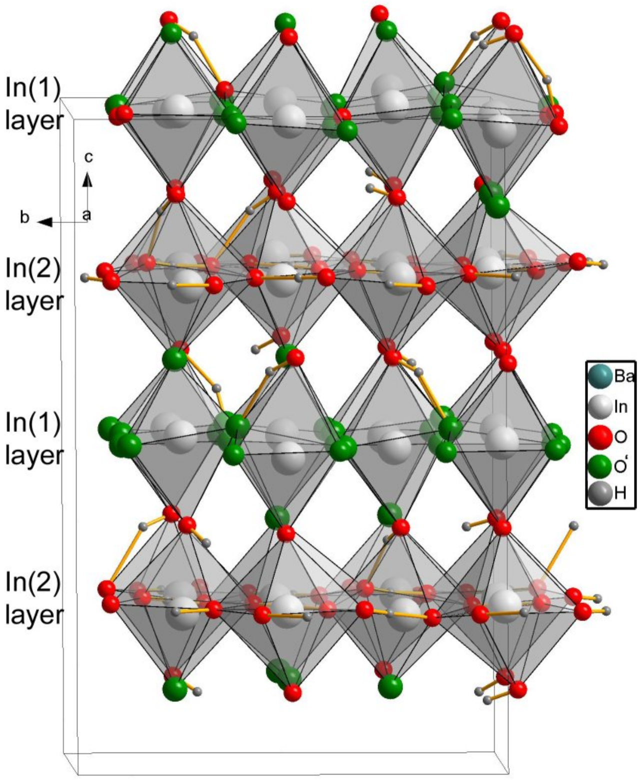

FIGURE 2.10 – Illustration de la structure complètement hydratée BaInOH. Les ions oxygène sans aucun contact avec un proton pendant toute la durée de simulation DM sont marqués en rouge, les autres en vert.

de changer de plan. Il reste à noter que ce comportement (illustré en figure 2.10 pour BaInOH) est relativement inchangé (bien que un peu moins prononcé) pour tous les composés substitués par d'autres cations jusqu'à 25 %. Ceci est aussi une analogie avec la présence des protons extra-octaédrales qui également restent stables jusqu'à ce taux.

2.2.4 Les énergies d'hydratation

Avec les propriétés de transport, les énergies d'hydratation font partie des paramètres les plus importants qui caractérisent les oxydes étudiés ici. C'est l'énergie d'hydratation qui détermine avec quelle facilité un oxyde va s'hydrater en atmosphère humide et jusqu'à quelle température la structure restera dans cet état. Dans le cadre de modélisation thermodynamique les deux grandeurs importantes sont l'énergie et l'entropie d'hydratation. Sans rentrer dans le détails, leur détermination de manière expérimentale est souvent accomplie par des procédures de fit des courbes d'analyse thermogravimetrique (ATG). Par contre concernant les calculs ab initio, si l'approche pour calculer la partie énergétique est (au moins en principe) bien définie, la détermination de l'entropie (c-à-d la différence d'entropie entre le composé hydraté et le composé sec plus des molécules d'eau) n'est pas aussi évidente. Effectivement il n y a pas de méthode simple pour remonter à ce type de entropie qui contient des parties vibrationnelles et configurationelles. Mais la description du terme énergétique reste difficile vu la complexité du système en question. C'est le très grand nombre de configurations possibles au sein d'un composé désordonné (et décrit par une cellule de simulation qui contient 200 atomes) qui rend impossible une simple comparaison d'énergies totales entre une cellule hydratées et une cellule déshydratées.

Par contre les calculs en dynamique moléculaire permettent de prendre des moyennes d'énergies totales pendant toute la durée d'une simulation. Ainsi, si la dynamique « explore » un nombre suffisamment grand de micro-configurations, ces moyennes peuvent être regardées comme moyennes thermodynamiques qui contiennent toute la complexité structurale des états secs et hydratés.

L'énergie d'hydratation peut être définie comme :

$$E_H(T) = \langle U_{hydr}(T) \rangle - \langle U_{dry}(T) \rangle - U_{H2O}(T) \tag{2.5}$$

en tant que gain (ou perte) d'énergie en eV du fait de l'incorporation (ou de la perte) des constituants d'une molécule d'eau. Les énergies sont donc des valeurs moyennées à travers un calcul complet de dynamique moléculaire à une température constante. Les températures choisies pour la DM sont assez élevées afin d'accélérer l'équilibration thermique et ne sont pas directement comparable avec des températures réelles car les composées se déshydratent déjà aux alentours de 300-400 °C.

A une température donnée, plus la valeur (négative) de Eh va être élevée, plus le taux de protons qui restent dans la structure va être important. Il est donc particulièrement intéressant d'établir des tendances chimiques qui influencent la valeur de cette énergie.

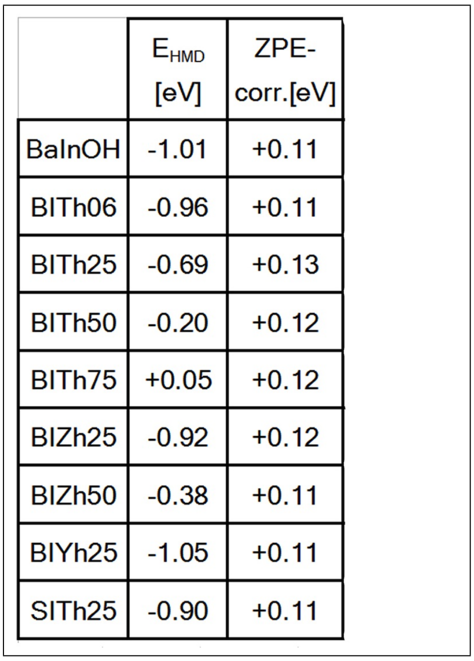

	E_{HMD} [eV]	ZPE-corr.[eV]
BaInOH	-1.01	+0.11
BITh06	-0.96	+0.11
BITh25	-0.69	+0.13
BITh50	-0.20	+0.12
BITh75	+0.05	+0.12
BIZh25	-0.92	+0.12
BIZh50	-0.38	+0.11
BIYh25	-1.05	+0.11
SITh25	-0.90	+0.11

FIGURE 2.11 – Les énergies d'hydratation par molécule d'eau (en eV)

Quant à la détermination des énergies d'activation il est important de noter que l'application de l'équation 2.5 donne des énergies d'hydratation différentes à différentes températures. Ceci est compréhensible du fait que les deux systèmes sont assez différents (le composé hydraté / le composé déshydraté plus la molécule d'eau). Comme décrit en détail dans le texte principal, la raison de ce comportement est une différence de capacité de chaleur (c_v) de ces deux configurations. Il a donc été choisi, de tracer une énergie d'hydratation en fonction de la température de simulation et de prendre la valeur extrapolée à température zéro comme valeur de résultat. Le tableau 2.11 montre les valeurs ainsi déduites pour tous les composés étudiés.

La colonne « ZPE correction » représente la correction due à la vibration à température zéro qui n'est pas inclue dans un calcul DFT. La correction est nécessaire pour compenser la différence entre le nombre total de modes vibrationnels entre composé hydraté et composé sec plus molécules d'eau. La méthode est basée sur l'analyse complète de la densité d'états vibrationnelle des deux systèmes auxquels une énergie vibrationnelle au point zéro peut être attribuée (par cellule de simulation). Du fait que le nombre absolu de modes vibrationnels est plus élevé dans le composé hydraté que dans le composé sec plus les molécules d'eau la correction diminue le gain en énergie lors de l'hydratation.

On constate les énergies d'hydratation les plus élevées pour le composé de référence, BaInOH et pour le composé substitué par du yttrium, BIYh25. Toute autre composé se retrouve avec des énergies d'hydratation significativement moins favorables. En simplifiant, les contributions principales sont des changements structuraux en allant d'un système ordonné (e.g. BaInOH) vers des systèmes désordonnés (BIThx, BIZhx) ainsi que des considérations de basicité (e.g. en allant de BaInOH vers BIYh25, qui est un composé plus ionique, c.f. figure 2.4). Une explication plus détaillée se trouve dans la prochaine section.

2.2.5 Les énergies d'hydratation et leur relations avec l'électronégativité du composé

Un grand nombre d'études expérimentales cherchent à corréler les énergies d'hydratation avec le concept chimique de la « basicité » [6, 7, 8]. En effet par définition dans le milieu aqueux, un composé avec une grande basicité va avoir une tendance importante à l'intégration de protons (ou de molécules d'eau). Dans les solides la basicité va donc être liée à la répartition de charges ioniques dans le réseau du composé. On s'attend à ce que plus le transfert de charge sur un ion d'oxygène est élevé dans l'état sec, plus l'affinité d'accueil d'eau (des protons dans ce cas) sera grande.

Naturellement les calculs ab initio se prêtent à étudier cette corrélation attendue à l'aide de la comparaison des énergies d'hydratation obtenues par dynamique moléculaire (qui sont issues de valeurs moyennées des énergies totales des composés secs et hydratés) et des transferts de charges « Bader » dans les composés complètement déshydraté qui ont étés présentés plus haut.

Le diagramme 2.12 établit cette comparaison pour les composées BITx, BIZx et BIYx. En

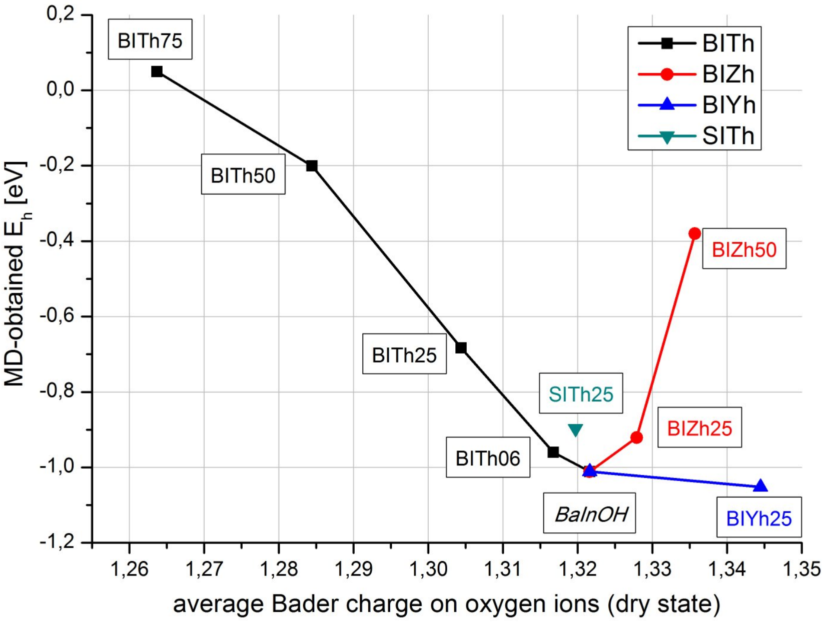

FIGURE 2.12 – Valeurs de l'énergie d'hydratation pour toutes les familles de composés en fonction du transfert de charges Bader (introduit dans la section 2.1.3).

identifiant un grand quantité de transfert de charge sur l'oxygène avec une grande basicité (c-à-d l'affinité de cet oxygène à être protoné) on s'attendra à une évolution qui fait augmenter la valeur absolue de l'énergie d'hydratation avec un transfert de charge Bader croissant. Ceci est effectivement observé pour la famille du BITx (indiqué par le trait noir) qui passe par les quatre composés BIT(h)x étudiés. Malgré le petit nombre de composés de type BIYx étudié, le comportement qualitative est également en accord avec l'attente (trait en bleu). Par contre pour le barium-indate substitué par du zircone (trait en rouge) on observe le comportement inverse : l'énergie d'hydratation absolue diminue avec le transfert de charges de Bader sur les oxygènes.

Ici le taux croissant de Zr (qui entraîne une augmentation du transfert de charge moyen sur l'oxygène ainsi qu'une augmentation de sa basicité), va avec une diminution de l'énergie d'hydratation de manière significative. Ceci présente une claire déviation du pouvoir prédictif de la basicité pour l'énergie d'hydratation. Une explication peut par contre en être trouvée dans les aspect structuraux abordés dans la section auparavant. Plus précisément c'est la préférence de sites des protons au sein des différents cations (In, Zr, Ti et Y) dans les composés. En particulier, il avait été trouvé qu'au sein des BIThx les protons se trouvaient préférablement à côté des polyèdres du Ti qui sont des cations « moins ioniques » donc « moins basiques » comparé à l'indium. Dans les BIZhx par contre les protons ne se trouvent pas associés aux polyèdres des cations les plus basiques qui sont les Zr. Donc malgré le fait que Zr fait en moyenne augmenter l'ionicité/basicité du réseau, les protons ne « ressentent » pas cette basicité par ce que des aspects énergétiques-structuraux interviennent.

En conclusion il a été démontré surtout à l'aide de l'étude comparative de BIT et BIZ comment et avec quel résultat des propriétés électroniques (ionicité) et des propriétés structurelles/locales déterminent l'énergie d'hydratation et qu'avec uniquement une des deux grandeurs une prédiction de leurs comportements n'est pas possible.

2.3 La méthode « Monte Carlo cinétique » appliquée au transport protonique

2.3.1 Les modèles de barrières et pièges aléatoires et les effets « multi-particules »

Ce chapitre s'intéresse à des travaux basés sur la méthode « Monte Carlo cinétique » qui permet d'obtenir des informations sur le comportement général de la diffusion de particules sur les réseaux désordonné comme dans le cas de la diffusion protonique dans les Brownmillerites (particulièrement dans le cas d'une substitution cationique).

C'est une méthode de physique statistique qui intègre essentiellement une approche de marche aléatoire (« random walk »). Dans le cas présent, le réseau a été modélisé afin d'imiter le réseau de diffusion d'un (ou de plusieurs) protons au sein des matériaux étudiés. Cet aspect est présenté dans l'image 2.13 ; depuis une position donnée un proton peut effectuer trois types de sauts différents (numérotés de 1 à 3) qui sont liés aux modes vibrationnels d'une élongation de liaison (« stretch jump » - numéro 1) ou d'un basculement (en restant au polyèdre initial - numéro 2, ou en changeant le polyèdre d'association - numéro 3).

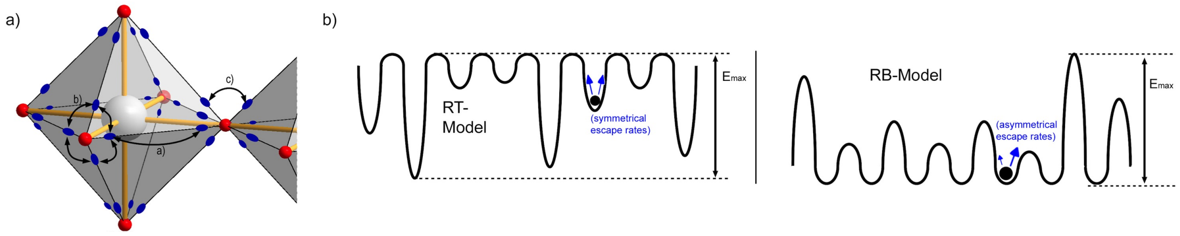

FIGURE 2.13 – a) Un octaèdre avec ses 24 sites possibles de protons et les trois types de déplacement qu'un proton peut effectuer en partant d'un site donné : 1) saut selon un mode de vibration de type « stretch » 2) rotation autour d'un oxygène 3) basculement vers un octaèdre voisin et b) Illustration des principes de piège aléatoire (« RT-Model ») et barrière aléatoire (« RB-Model »).

L'élément Monte Carlo (MC) correspond à d'attribuer à chaque saut qu'une particule peut effectuer une énergie d'activation et à appliquer un algorithme de Métropolis. A chaque pas de MC Un saut/événement est effectué quand un numéro aléatoire P entre 0 et 1 satisfait la condition

$$0 \leq P \leq \exp\left(-\frac{E_{trap} + E_{barrier}}{kT}\right). \tag{2.6}$$

Ici le côté droit représente un facteur de Boltzmann qui intègre le profondeur d'un piège et, le cas échéant, la hauteur d'une barrière. Ce facteur a par définition des valeurs entre 0 et 1.

En même temps la simulation prend en compte des pré-facteurs approximés pour chaque type de saut ce qui fournit des grandeurs commodes en terme d'unité. Pour un ensemble de plusieurs trajectoires le déplacement est moyenné afin de remonter aux coefficient de diffusion. La routine MC a été écrite dans la langue de programmation « C » et vu sa (relative) simplicité a pu être réalisée à l'aide d'un ordinateur ordinaire. Tout au contraire du cas de la dynamique moléculaire ab initio, les simulations MC ne sont pas limitées concernant leur poids statistique, c-à-d afin de remonter à un coefficient de diffusion des milliers de simulations équivalentes ont pu être moyennées et elles avaient toutes une durée de milliers de pico-seconds chacune (comparé à des dizaines de pico-seconds pour les calculs DM).

Les questions adressées ici étaient : comment le coefficient de diffusion se comporte à travers une large région de températures similaire à celle des calculs de dynamique moléculaire et quelle est l'influence du désordre et quelle influence certains aspects de ce désordre ont sur le changement du coefficient.

Tout d'abord il est nécessaire de constater, que l'énergie d'activation effective de diffusion sur un réseau désordonné n'est pas constante en fonction de la température. La représentation d'Arrhenius presque toujours utilisée pour le démontrer a une courbure et les paramètres à extraire ne sont pas bien définis.

La manière exacte de cette déviation d'une droite est une fonction du caractère du réseau. Des considérations analytiques (c.f.) démontrent que sur des réseaux simples le comportement est opposé pour deux cas extrêmes : une distribution de barrières (c.f. fig. 2.13 b) côté droite) aléatoires conduit à une courbure convexe alors qu'une distribution de puits (c.f. fig. 2.13 b) côté gauche) entraîne une courbure concave de la représentation d'Arrhenius du coefficient de diffusion effectif. Par conséquence chaque détermination d'une énergie d'activation et d'un pré-facteur dépend de la plage de températures de laquelle les données proviennent.

Dans le cadre de ce résumé seulement quelques exemples choisis sont présentés afin d'illustrer l'approche et le type de résultats qui peuvent être obtenus.

2.3.2 Exemple I - Le réseau de pièges aléatoires pour une particule

Cette étude est une des plus simples à mener dans le cadre de l'approche MC pour une particule (par ailleurs elle est encore entièrement traitable de manière analytique). Cette particule est placée dans un réseau de pièges aléatoires dans lequel chaque site est associé à un niveau énergétique entre zéro est un valeur maximale. L'évolution en température de ce système est caractérisé par des énergies d'activation (du coefficient de diffusion) qui sont dépendantes de la plage de température. La représentation d'Arrhenius est courbée de manière convexe ; à basses températures les valeurs de ces énergies sont proches des énergies des pièges les plus profonds. A plus hautes températures l'énergie d'activation effective s'approche des valeurs des pièges les moins profonds de manière asymptotique.

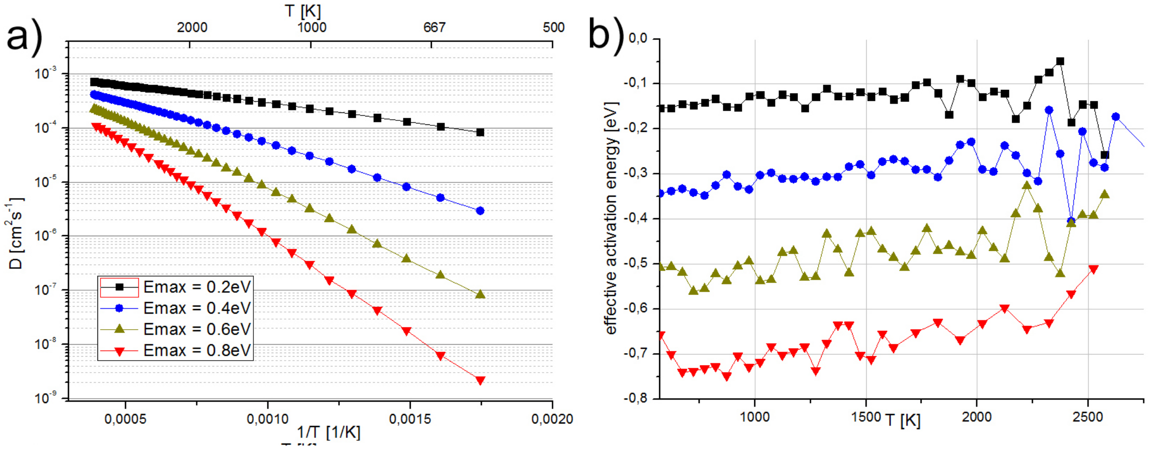

FIGURE 2.14 – a) Représentation d'Arrhenius du coefficient de diffusion pour une particule sur un réseau de pièges aléatoires b) Evolution des énergies d'activation ponctuelles en fonction de la température.

La figure 2.14 donne une illustration du coefficient de diffusion (gauche) d'un proton et des énergies d'activation (droite). Le paramètre Emax détermine le valeur maximale de la distribution uniforme des profondeurs de pièges. Cet exemple le plus simple, démontre déjà que l'aspect du désordre à une grande importance quant aux études (à la fois expérimentale et par calcul), particulièrement en ce qui concerne l'attribution d'une seule énergie d'activation.

2.3.3 Exemple II - L'effet de la concentration des protons dans un réseau de pièges aléatoires

Ce cas utilise l'approche MC sous la condition d'avoir plusieurs particules qui se déplacent de manière simultanée sur un réseau donné. Les calculs qui ont fourni la figure 2.15 étaient basés sur les mêmes réseaux que dans l'exemple (I) avec une profondeur de piège maximale de 0,4 eV.

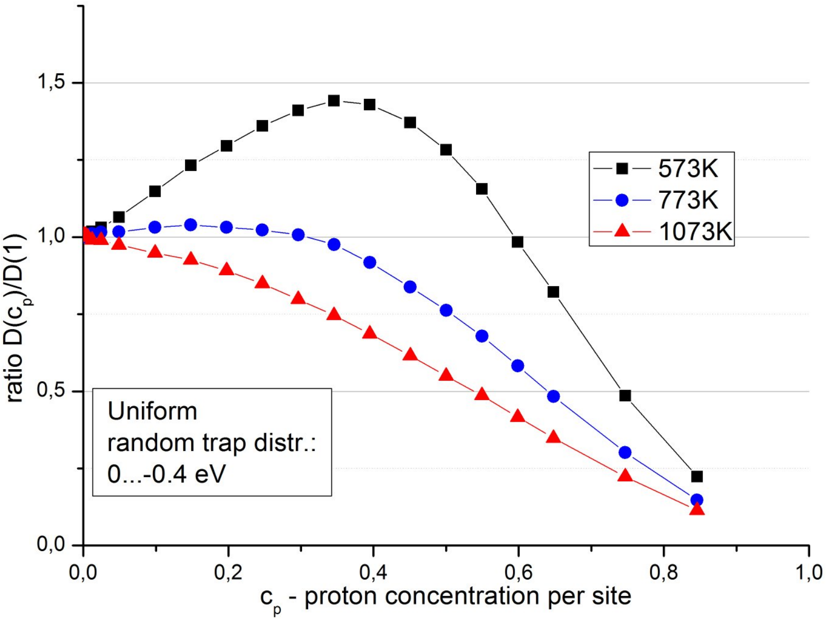

FIGURE 2.15 – Coefficient de diffusion rapporté au cas dilué de particules en fonction de leur concentration pour trois températures. Le réseau est défini par des pièges aléatoires.

Sans l'expliquer en détail le graphique montre le comportement assez complexe du coefficient de diffusion en fonction de la concentration des protons. La tendance attendue est une diminution de la diffusivité dû au blocage des sites avec une augmentation de la concentration des protons. Néanmoins il existe des régimes où cette tendance est inversée et un gain de diffusivité (ligne noire à 573 K pour des concentrations comprises entre 0,25 et 0,35) est constaté. La raison de ce comportement repose sur l'occupation des pièges les plus profonds par uniquement quelques particules qui, de cette manière, facilitent la diffusion pour les autres. De plus, en contraste avec le cas d'une particule, ces relations ne sont plus traitables de manière mathématiquement analytique.

2.3.4 Exemple III - L'effet d'une couche bloquante à la diffusion protonique

Comme il a pu être mis en évidence dans la section 2.1.2 les composés avec un taux de substitution ≤ 25 % présentent la particularité d'avoir une couche d'octaèdres qui pendant toute la simulation n'associent pas à un seul proton ; qui représentent donc une couche isolante pour le transport protonique. Il a été intéressant donc, d'étudier l'effet global d'un tel arrangement sur le coefficient de diffusion par une simulation Monte Carlo. Le résultat est montré dans la partie droite de l'image 2.16 ou le coefficient de diffusion (D) d'un réseau parfait (et des pièges et barrières typiques) est comparé avec ce même réseau mais modifié. Pour ce calcul Monte

Carlo il a été attribué à la région verte des barrières beaucoup plus élevées afin de simuler le caractère bloquant. Ces calculs fournissent donc un ordre de grandeur de la diminution du coefficient de diffusion dû à la présence d'une couche qui bloque de manière plus (trait rouge) ou moins (trait bleu) rigoureuse. Dans cet exemple cette diminution est donc de presque un facteur deux, sachant que la géométrie/topologie du réseau (c-à-d l'emplacement et/ou la densité des plans bloquants) détermine la valeur exacte.

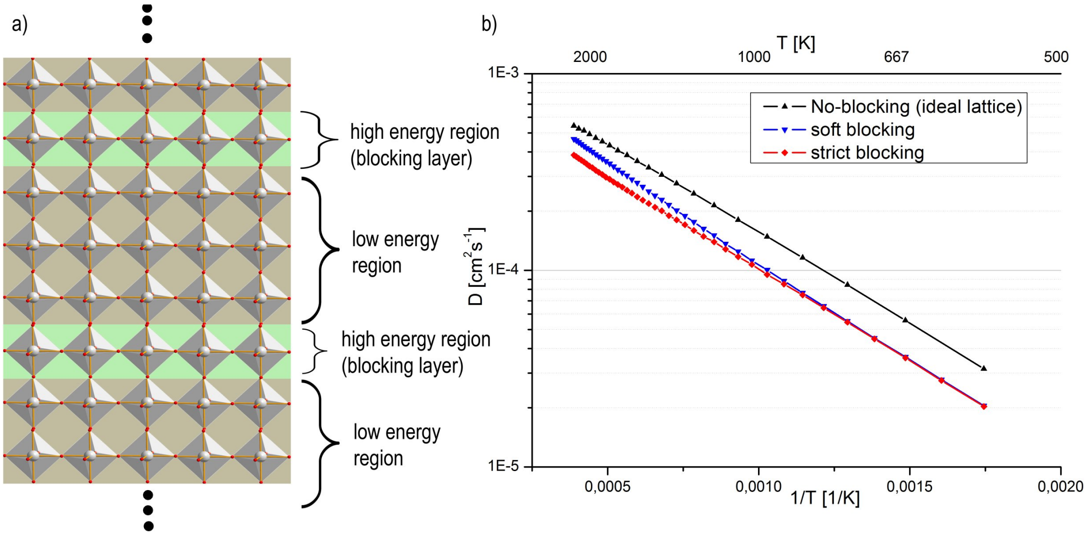

FIGURE 2.16 – a) Illustration du réseau modèle pour une couche blocante et b) évolution du logarithme du coefficient de diffusion en fontion de 1/T pour le cas non-bloquant (trait noir) et deux cas plus ou moins fortement bloquants (traits rouge et bleu).

Pour conclure cette partie sur les calculs supplémentaire de type Monte Carlo il peut être constaté qu'il a été possible d'éclairer le caractère de la diffusion sur des réseaux désordonné et de souligner le fait que la description avec une seule énergie d'activation ainsi qu'un seul pré-facteur n'est pas approprié pour ces systèmes.

2.4 Le transport diffusif des protons

2.4.1 Énergies d'activation du coefficient de diffusion obtenues par DM comparées aux valeurs expérimentales

Cette dernière section concerne le sujet principal de la thèse, qui est l'observation et l'interprétation du déplacement des protons dans les différents composés à l'aide de la dynamique moléculaire. La grandeur la plus importante est le coefficient de diffusion (CdD) qui peut être extrait de simulations en observant le déplacement carré moyen (DCM) de l'ensemble des protons. Le CdD est donné par :

$$D = \frac{\langle \Delta^2 \vec{r}(\tau) \rangle}{6\tau} \tag{2.7}$$

où le terme $\vec{r}(\tau)$ représente le DCM qui est extrait de l'observation des protons pendant une simulation de dynamique moléculaire.

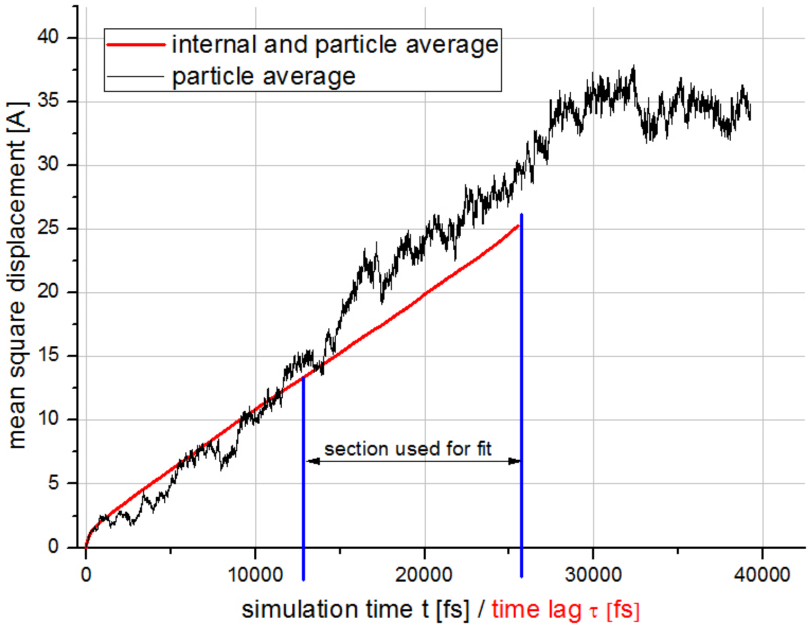

FIGURE 2.17 – Évolution du déplacement carré moyen avec le temps en donnée brute (trait noir) ainsi que sous forme moyennée (trait rouge). Pour cette dernière l'axe du temps ne correspond plus au vrai temps de simulation mais à un décalage τ qui regroupe pour chacunes des ses valeurs tous les Δ-t existants de même valeur pendant une simulation DM.

La procédure de l'obtention du CdD comprend une un fit linéair (trait rouge) du déplacement brût (trait noir) de l'ensemble des protons et est illustrée dans l'image 2.17. Le terme « moyenne interne » signifie de moyenner sur un grand nombre de quasi-trajectoires qui sont générées par le déplacement de l'origine temporel et laissant chacune de celles-ci contribuer à la moyenne (trait rouge).

De manière générale il faut noter, que le transport protonique dans les composés en question est assez complexe en raison du caractère désordonné du réseau et (le cas échéant) de l'assez grande concentration de protons qui peuvent s'influencer leur diffusion. Le composé BaInOH (sans substituent cationique) propose une multitude de sites cristallographiques différents pour le proton. Bien sûr le fait de substituer l'indium sur le site B ajoute encore une autre forme de désordre qui a été expliquée dans la section 2.1.2.

Ceci est une énorme complication par rapport au cas de la pérovskite légèrement protonée qui est le sujet d'un grand nombre de travaux antérieurs [9, 10, 11, 12]. Le réseau sur lequel les protons diffusent est inhomogène et caractérisé par des pièges et des barrières de profondeur/hauteur différentes est distribués de manière aléatoire (du moins pour le cas de la substitution cationique).

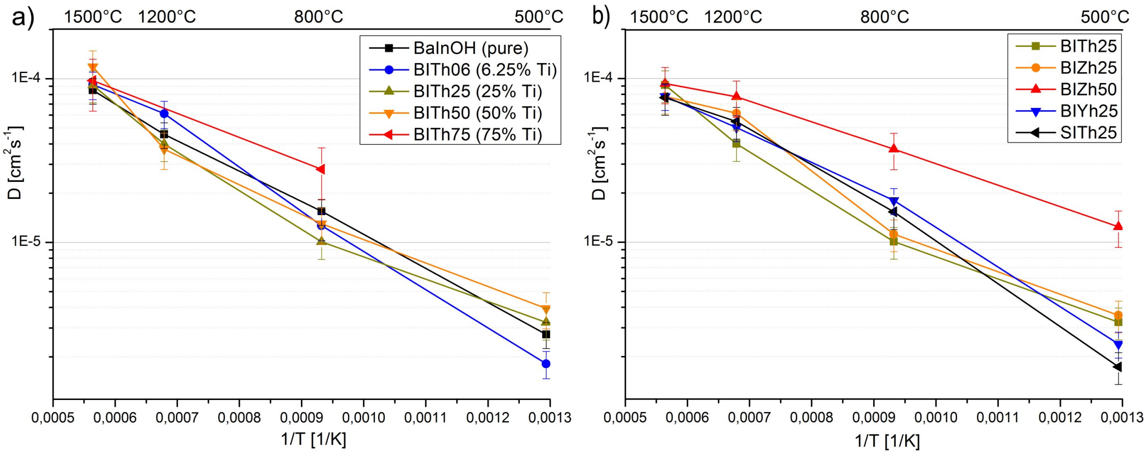

FIGURE 2.18 – Coefficients de diffusion (en échelle logarithmique) en fonction de 1/T pour tous les composés étudiés. a) Substitution par du Ti à différents taux et b) subsitution à un taux de 25 % par plusieurs cations (Ti, Zr, Y).

En prenant ceci en compte, l'étude préalable (présentée plus haut) à l'aide des réseaux modèles dans le cadre de l'approche Monte Carlo cinétique a eu le rôle d'illustrer ce problème. En principe, la diffusion sur un réseau désordonné ne peut pas être décrite par une seule énergie d'activation et pré-facteur sur toute la gamme de température. Néanmoins l'observation d'uniquement quatre températures différentes (entre 500 °C et 1500 °C) n'a pas permis de rigoureusement établir une courbure de la représentation d'Arrhenius du CdD. La figure 2.18 montre les CdD de tous les composés à toutes les températures considérées avec des barres d'erreur qui sont issues d'une étude supplémentaire de type « Monte Carlo » (expliquée en détail dans le texte principal à la section 2.4)

En règle générale les valeurs du CdD sont tout à fait comprise dans la région expérimentalement obtenue pour la diffusion protonique dans des oxydes [13, 14, 15, 16].

A l'exception de BIZh50 les deux graphes de la figure 2.18 ne démontrent pas d'écarts significatifs entre les différents composés. Les différentes contributions (favorables ainsi que défavorables) qui sont apportées par la substitution semblent se compenser. Néanmoins il semble clair, que l'approche a bien atteint ses limites en ce qui concerne la fiabilité statistique avec une seule simulation par température et (surtout à la plus basse température) des déplacements moyens carrés de seulement quelques Angström pour chaque proton.

Bien sûr il est néanmoins possible d'extraire le couple habituel de caractérisation de diffusion, i.e. l'énergie d'activation et le pré-facteur. Un fit linéaire de la représentation d'Arrhenius ou

TABLE 2.I – Plan simplifié des influences sur la diffusivité des protons dans des composés basés sur du BaInOH. Les nombres de protons sont donnés par cellule de simuulation.

		x=0	x=0.25		x=0.5	
		BaInOH	BITh25	BIZh25	BITh50	BIZh50
1	nombre de protons	32	24	24	16	16
2	Blocade des sites ?	fréquent	moins fréquent	moins fréquent	le moins fréquent	le moins fréquent
3	Couche bloquante ?	oui (stable)	oui (moins stable)	oui (moins stable)	non	non
4	Couche-extra-oct. ?	oui (stable)	oui (moins stable)	oui (moins stable)	non	non
5	Piègeage ?	non	oui (au Ti)	oui (au In)	oui (au Ti)	oui (au In)
6	Pièges percolent ?	-	non	oui	oui	oui
7	Nombre (fraction) de protons piégés	16 (0.5) (couche-extra)	20 (0.83) (couche-extra + pièges-Ti)	16 (0.67) (couche-extra seulement)	0 (percolation !)	0 (percolation !)

un fit exponentiel des valeurs absolues fournissent des énergies d'activation entre 0,25 et 0,6 eV et des pré-facteurs de l'ordre 0,5-5 · 10-3 cm^2s^{-1}.

Comme déjà évoqué le composé BIZh50 montre systématiquement des CdD supérieurs (et une énergie d'activation de seulement 0,25 eV) à ceux des autres composés.[1] Effectivement il peut être logique de s'attendre à de très bons CdD pour des structures avec des taux de substitution dans la région 50/50 comme c'est le cas pour BIZh50. La clé est l'interaction entre les contributions de tous les aspects structuraux à la diffusivité des protons. Le tableau 2.I les regroupe donc à l'aide de l'exemple des composés BaInOH et des familles de BIThx et BIZhx.

En commençant avec la référence BaInOH il est noté l'impact de la substitution à 25 et 50 % sur les aspects structuraux (la couche bloquante, le plan des protons extra-octaèdrales et le piégeage de protons individuels à côté des polyèdres d'un des deux cations du site B. Une information qualitative qui est apporté en ligne « 6 » est de savoir si le réseau des polyèdres de cations du site B percolent à travers le réseau ou pas. Ceci est énormément important en vue d'une diffusion à longue portée, ou un site de piège qui par contre est pércolatif n'empêche plus

---

[1] Comme expliqué en section 6.3.3 du texte principale, selon toute vraisemblance le composé BITh50 devrait avoir un comportement similaire à celui de BIZh50 et ne le montre pas à cause d'une cellule de simulation mal choisi.

la diffusion. Cette considération est basée sur le réseau défini par les polyèdres de coordinence qui est un réseau simple-cubique. Le seuil de percolation de site correspondant est de 0.31 ce qui place les taux de substitution de 25 % en dessous et les 50 % au dessus de ce seuil.

Le résultat de ce tableau récapitulatif est donc, qu'au moins en ce qui concerne l'empêchement par les pièges, les composés à 50 % laissent attendre les performances les plus élevées de leur coefficient de diffusion. Idéalement il ne seront pas affectés par un concept de piégeage quiconque à cause de l'absence du plan extra-octaédral et le fait que les deux sous-réseaux (In/Ti ou In/Zr) percolent. En plus, ces composés profitent de l'absence de la couche bloquante et de la plus basse concentration de protons qui conduit à une faible interaction repulsive proton-proton.

Il est à noter impérativement que la situation ici reste assez idéalisée surtout dues aux conditions d'hydratation complète, qui sont toujours imposées lors des calculs. Une équivalence directe avec les conductivités/diffusivités réelles à des températures au dessus de 200 - 250 °C ne peut pas être établie à cause de l'état partiellement déshydraté. Ceci est d'un complexité particuliere, vu la présence simultanée de lacunes d'oxygène (et leur préférence de site à côté d'un des deux cations) et de protons. Les sites préférés de ces derniers par contre ne sont plus seulement déterminés par le cation (In/Ti, In/Zr, In/Y) mais aussi par les lacunes. Des calculs préliminaires montrent que dans un composé partiellement hydraté, le proton ne se trouve plus à coté des polyèdres du Ti parce qu'ils sont maintenant des tétraèdres qui ne peuvent plus accueillir des protons en liaison covalente.

2.4.2 Les modes de déplacement des protons au sein des structures Brownmillerite

Afin de mieux caractériser le transport des protons dans le réseau, les simulations DM sont étudiées plus en détail. A l'aide des routines (programmés en « C ») qui « suivent » chaque proton pendant la simulation il est possible de distinguer plusieurs modes de déplacement. Leur caractère est présenté dans l'image 2.19 en relation avec le polyèdre de coordination auquel le proton est associé. Il est important de noter, que les modes notés 1, 3 et 4 sont présents (et connus) dans le cadre des travaux antérieurs (notamment par Kreuer et al. [6, 9, 17]) dans les pérovskites légèrement protonées. Les modes 2, 5 et 6 dans la figure apparaissent uniquement dans les composés de type Brownmillerite complètement hydratés et (pour 5 et 6) permettent aux protons de changer son type de site entre intra- et extra-octaédrale.

La description quantitative à partir du simple « comptage » d'événements est fait avec la

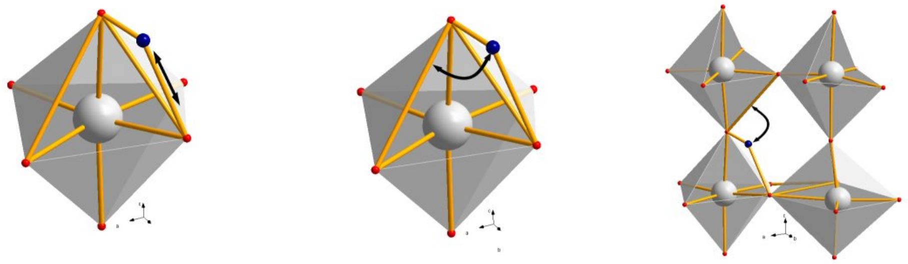

Mode 1: intra-octahedral stretch Mode 3: intra-octahedral rotation Mode 4: intra-octahedral flip

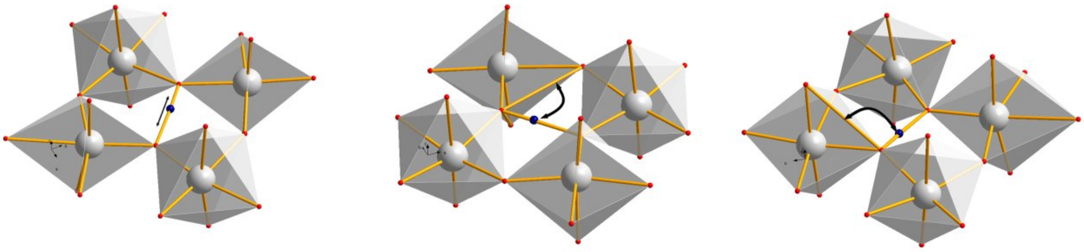

Mode 2: extra-octahedral stretch Mode 5: extra/intra-octahedral in-plane bend Mode 6: extra/intra-octahedral out-of-plane bend

FIGURE 2.19 – Illustration des modes de déplacement d'un proton pour le cas d'un proton intra-octaédral (Modes 1, 3 et 4) et le cas d'un proton extra-octaédral (Modes 2, 5 et 6).

théorie de l'état de transition (en anglais « transition state theory - TST »). A partir d'un comptage il est donc possible de remonter à l'énergie d'activation ainsi qu'au pré-facteur d'un mode de déplacement donné. Dans le cas d'un processus de saut pour lequel un axe vibrationnel sert comme coordonnée de transition la théorie donne une simple expression qui relié le taux d'un événement ses paramètres :

$$r = \frac{kT}{h} \exp\left(\frac{\Delta S(T)}{k}\right) \exp\left(-\frac{E_a}{kT}\right) = \frac{kT}{h} \exp\left(-\frac{\Delta G}{kT}\right) \tag{2.8}$$

où r est égal au taux, Δ-S et Δ-H sont l'entropie est l'enthalpie d'activation. Quant aux résultats détaillés on fait référence au tableau 6.III dans le texte principal qui regroupe ces paramètres pour les différents composés et les modes 1, 3 et 4 ainsi qu'au sections suivantes 6.4.2.2. et 6.4.2.3 qui présentent les modes 2, 5 et 6.

En ce qui concerne les modes 1, 3 et 4 il a été trouvé, que pour la plupart des composés le mode 1 coïncide avec la rupture d'une liaison covalente O-H. Les énergies d'activation sont de l'ordre 0,3 eV pour le matériau de référence BaInOH avec une tendance à diminuer avec un taux croissant de Ti ou Zr. Le mode 2 semble moins intéressant vu qu'il n'est pas capable d'être à l'origine d'un déplacement macroscopique du proton. Dans toute sa gamme d'existence (c-à-d dans les composés proches de la structure Brownmillerite complètement hydratée) ce mode est toujours associé à des taux très élevés. Les modes 5 et 6 sont les déplacements qui montrent les énergies d'activation les plus élevées. Comme expliqué en détail dans la section 6.4.2.3. du texte principal, leurs valeurs sont aux alentours de 0.5 eV lorsqu'un proton extra-octaédral est converti en un proton intra-octaédrale. L'importance de ce mode pour la diffusion à longue portée par contre est limitée, car seuls les protons extra-octaédraux sont concernés tandis que les protons intra-octaédraux sont plus libre de diffuser.

2.4.3 Aspects quantiques du déplacement du proton

Dû à sa très petite taille et masse il est important de quantifier à quel point le comportement dynamique d'un proton dans un oxyde doit être décrit comme quantique. D'un point de vue général la modélisation de type DFT peut être a priori considéré comme « quantiquement correct » (dans les limites de ses approches au niveau de l'échange/corrélation électronique). Ceci par exemple concerne des propriétés statiques comme la distribution de charges dans le réseau cristallin et la liaison chimique.

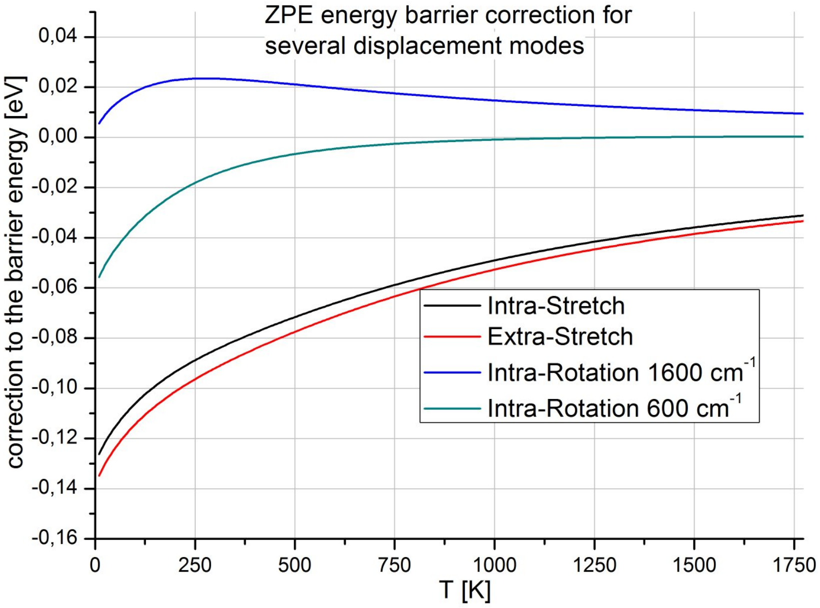

FIGURE 2.20 – Ordres de grandeurs des corrections des énergies d'activation dues aux vibrations au point zéro en eV. Les quatre cas correspondent aux différents modes de déplacements. Déplacement par élongation de la liaison O-H (traits noir et rouge) ou par rotation autour d'un oxygène (traits bleu et vert).

En s'intéressant à la dynamique de transport par contre il existe des effets quantiques dynamiques qui ne sont par définition pas inclus dans l'approche dynamique moléculaire - DFT. Il s'agit de (I) la vibration à température zéro Kelvin et (II) l'effet tunnel. D'une manière avantageuse ils appartiennent au groupe des effets quantiques qui en général ne sont d'une grande importance qu'à basses températures.

L'effet tunnel permet au proton de se déplacer à travers des barrières de potentiels de manière non thermiquement activée. Quant au déplacement protonique l'effet tunnel est important dans les macromolécules à basses températures ainsi que dans de la glace. Pour le cas des oxydes de type pérovskite [18] démontre par des calculs dynamiques (quantiquement rigoureux) que les taux de déplacements thermiquement activés (donc traitables dans le cadre de DM) au dessus de la température ambiante sont significativement plus grands que les déplacements grâce à l'effet tunnel. Le déplacement par effet tunnel peut donc considéré comme négligeable.

Le cas des vibrations à température zéro est plus compliqué et elles peuvent être prises en compte a posteriori par des corrections aux énergies d'activations des processus élémentaires de déplacement. Ces corrections sont accessiblee par l'utilisation des fonctions de partition vibrationnelles quantiques dans le cadre de la théorie de l'état de transition. La correction dépend des fréquences des vibrations en question ainsi que de la température. La figure 2.20 montre l'ordre de grandeur des corrections pour trois types de déplacement principaux avec leur fréquences typiques en fonction de la température. Il peut être conclu, qu'aussi pour le cas des vibrations au point zéro, les corrections sont d'un ordre de grandeur pas trop important et que le traitement de la diffusion protonique avec de la dynamique moléculaire Born-Oppenheimer reste justifié.

Chapitre 3

Conclusion générale

Le but de cette thèse a été d'approfondir les connaissances des mécanismes et processus de la conduction protonique au sein des oxydes de type Brownmillerite. Ceci a pu être effectué notamment par le moyen de la modélisation « ab initio », donc des calculs de physique/chimie quantique. Ce sont ces calculs qui en ce moment connaissent une véritable augmentation de leur utilisation grâce au fait, d'être de plus en plus capable de fournir des prédictions et explications sur des systèmes de matériaux chimiquement intéressants. Ceci représente une vraie différence avec la situation d'il y a seulement une dizaine d'années, où la puissance de calculs limitait de manière significative la valeur de ces modélisations pour « le chimiste », qui lui est intéressé par les propriétés des matériaux.

Avec la possibilité technique de choisir des cellules de simulation d'une taille de 200 atomes au niveau théorique de calculs ab initio il a été envisageable d'étudier des systèmes désordonnés cationiquement de manière explicite. Cette approche était incontournable afin de remonter aux propriétés de conductivité des matériaux d'électrolyte protonique, qui sont en grande partie déterminées *par* ce désordre. De plus, l'approche de dynamique moléculaire a permis, de rigoureusement et d'une manière très directe d'observer quels aspects structuraux ont quelle influence sur la diffusion des protons. Ceci a mis en évidence l'importance des concepts de pièges et barrières à la diffusion. Notamment c'est leur distribution et quantité qui (dans l'optique de matériaux désordonnés) détermine plus en détail à quel point on peut s'attendre à un bon conducteur ionique/protonique.

De même les études préalables aux calculs de diffusion ont clarifié la structure générale à la fois des composés secs et hydratés. Ceci concerne surtout la question des structures locales des oxydes fortement lacunaires et la préférence des coordinences particulières d'un cation donné qui substitue l'indium. Il s'est également avéré qu'il existe un lien très fort entre ces préférences de l'état sec et des détails structuraux au sein des composés protonés. Ce lien se manifeste par exemple pour le substituant titane qui, dans les composés secs préferentiellement est proche de une ou deux lacunes d'oxygnène et dans l'état hydraté agit en tant que piège pour les protons. Ce dernier fait a pû être directement confirmé expérimentalement par des mesures XANES.

En ce qui concerne une possible continuation des travaux de cette thèse, une approche en dynamique moléculaire *classique* peut être proposée. La problèmatique principale de cette dernière est la validité des potentiels empiriques qui servent à décrire les espèces chimiques. La manière la plus fréquente d'en créer est de les adapter à l'aide des données obtenues en calcul ab initio. Par conséquent ceci pourrait être fait à partir du grand nombre de données ab initio générées pendant cette thèse. La dynamique moléculaire classique serait ensuite capable de s'étendre vers des aspects presque macroscopiques qui, à présent, ne sont pas encore accessible directement par des calculs ab initio. Entre outre, le désordre des cations pourrait être caractérisé de manière rigoureuse ainsi que le comportement de la diffusion à des échelles de temps/d'espace plus importantes.

Bibliographie

[1] V. Jayaraman *et al.*, Solid State Ionics **170**, 17 (2004).

[2] C. E. Mohn, N. L. Allan, C. L. Freeman, P. Ravindran, and S. Stolen, Phys. Chem. Chem. Phys. **6**, 3052 (2004).

[3] C. E. Mohn, N. L. Allan, C. L. Freeman, P. Ravindran, and S. Stølen, Journal of Solid State Chemistry **178**, 346 (2005).

[4] Y. Zhang, Inorg. Chem. **21**, 3886 (1982).

[5] R. Kubo, Journal of the Physical Society of Japan **12-6**, 570 (1957).

[6] K. D. Kreuer, Annu. Rev. Mater. Res. **33**, 333 (2003).

[7] K. D. Kreuer, Solid State Ionics **136-137**, 149 (2000).

[8] T. Norby and Y. Larring, Current Opinion in Solid State & Material Science **2**, 593 (1997).

[9] W. Münch, K. D. Kreuer, G. Seifert, and J. Maier, Solid State Ionics **136-137**, 183 (2000).

[10] W. Münch, K. D. Kreuer, G. Seifert, and J. Majer, Solid State Ionics **125**, 39 (1999).

[11] M. E. Björketun, P. G. Sundell, and G. Wahnström, Phys. Rev. B **76**, 054307 (2007).

[12] M. E. Björketun, P. G. Sundell, and G. Wahnström, Faraday Discussion **134**, 247 (2007).

[13] F. Giannici, A. Longo, K.-D. Kreuer, A. Balerna, and A. Martorana, Solid State Ionics **181**, 122 (2010).

[14] M. Karlsson *et al.*, Chemistry of Materials **22**, 740 (2010).

[15] V. Jayaraman *et al.*, Solid State Ionics **170**, 25 (2004).

[16] G. B. Zhang and D. M. Smyth, Solid State Ionics **82**, 153 (1995).

[17] W. Münch, G. Seifert, K. D. Kreuer, and J. Maier, Solid State Ionics **97**, 39 (1997).

[18] Q. Zhang, G. Wahnstrom, M. E. Björketun, S. Gao, and E. Wang, Physical Review Letters **101 (215902)**, 1 (2008).